A STUDY ON THE PERFORMANCE OF LASER BASED BENDING

A Thesis Submitted in Partial Fulfillment of the Requirements for the Degree of

DOCTOR OF PHILOSOPHY

by

Besufekad Negash Fetene

(Roll No. 126103039)

Department of Mechanical Engineering

Indian Institute of Technology Guwahati

Guwahati-781039

INDIA

July 2018

Department of Mechanical Engineering,
Indian Institute of Technology Guwahati,
Guwahati-781039,
INDIA

CERTIFICATE

It is certified that the work contained in the thesis entitled "**A Study on the Performance of Laser Based Bending**" is submitted by **Mr. Besufekad Negash Fetene** to the Indian Institute of Technology Guwahati for the award of the degree of Doctor of Philosophy has been carried out under my supervision in the Department of Mechanical Engineering, Indian Institute of Technology Guwahati. This work has not been submitted elsewhere for the award of any other degree or diploma.

Date: July 6th, 2018

Dr. U. S. Dixit
Professor
Department of Mechanical Engineering,
Indian Institute of Technology Guwahati,
Guwahati-781039,
INDIA

DECLARATION

I declare that,

a. The work contained in this thesis is original and has been done by me under the guidance of my supervisor.
b. The work have not been submitted to any other institute for any degree or diploma.
c. I have followed the guidelines provided by the institute in preparing the thesis.
d. I have confirmed to the norms and guidelines given in the ethical code of conduct of the institute.
e. Whenever I used materials (data, theoretical analysis, figure and text) from other sources I have given due credit to them by citing them in the text of the thesis and giving their detail in references. Further, I have taken permission from the copyright owner of the sources, whenever necessary.

Signature of student
(Besufekad Negash Fetene)

Dedicated To God

Acknowledgements

I start this thanking Almighty God Jesus Christ for keeping me healthy and giving patience throughout my thesis work. I would like to express my sincere gratitude towards all those who have helped me in various ways directly and indirectly during the tenure of my PhD work at IIT Guwahati. Each step of the PhD work was supported by many people and each one have played important role. I am grateful to express my deep gratitude to all of them.

I would like to acknowledge Government of Ethiopia for providing financial support to conduct my PhD work. I thank Indian government and Indian Institution of Technology Guwahati for all sorts of infrastructural facilities. Special thank for Central Workshop, Material Science Laboratory, Advance Manufacturing Laboratory, and Central Instruments Facility of IITG for providing instruments to carry out the research work. I would also like to thank DST-FIST (2009–2014) scheme of Government of India for providing CO_2 laser facility.

I express my sincere gratitude and appreciation to my supervisor, Prof. U.S. Dixit, Department of Mechanical Engineering, IIT Guwahati, for his valuable advice, expert guidance, patience and encouragement, and for all the support he has given me from the beginning to end of the PhD work. Without his support and advice, it would have not been possible for me to carry out this research work. Regardless of his work-load, he always managed time to discuss every difficult phases for my PhD work with moral support. I really feel privileged for having the opportunity to work under him as my PhD supervisor. I shall always be grateful to him.

I would like to thank my doctoral committee members, Prof. P. S. Robi, Prof. A. K. Das and Dr. P. Biswas, for their valuable suggestions and encouragement during the period of my research work. I am also grateful to the former and present heads of the Department of Mechanical Engineering, Prof. P. Mahanta, Prof. A.K. Dass and Prof. S. K. Dwivedy for extending various facilities during the tenure of my doctoral program.

I wish to express my sincere thanks to Mr. Jiten Basumatary, Mr. Dilip Chetri, Mr. Bijoy Choudhury, Mr. Dipak Deka, Mr. Upen Gohain, Mr. Dhaneswar Khaklary,

Mr. Minesh Medhi, Mr. Mrinal Sarma, Mr. Saiffuddin Ahmed and Mr. Sanjib Sarma for helping me during the experimental studies.

I express my sincere thanks to my friends Mr. Vikash Vanik, Mr. Rajkumar Shufen, Mr. Polash Dutta, Mr. Aghyad Eideh, Mr. Rosang Pongen, Dr. Vinod Yadav, Mr. Faladrum Sharma, Mr. Amit Raj, Dr. Ravi Kant, Mr. Dawit Gudeta, Mr. Woldetinsay Gutu, Dr. Hailu Gebretsadik and Mr. Zinabu Haile. I shall always be grateful to my IITG and childhood friends for their great encouragement and wishes.

I express my deep gratitude to my wife "Meseret Sahle" for immense support during the course of my PhD program. Her patience, goodwill, caring nature and encouraging words kept me driving and helped me to focus on my work. I will be grateful to her for sharing every responsibility without my presence during PhD period. Last but not the least; I am thankful to all my family members and any one related to this work up to any extent in due course of time.

July 6th, 2018

Besufekad Negash Fetene
IIT Guwahati

Abstract

Laser based bending is a process of bending of different workpieces by using a controlled moving or stationary laser heat source, which induces thermal stress to achieve the desired bending. Recently, laser bending has received attention for a wide variety of applications in industries due to its excellent bend quality with high productivity and flexibility. Researchers studied the effects of different process parameters related to the laser source, material and workpiece geometry on laser bending of sheets. In this thesis, experimental study and finite element method (FEM) simulations of various kinds of laser based bending are reported. The FEM was used to predict bend angle, edge effect, temperature variation, stress and strain. The focus of the work was to study the performance and robustness of the process for filling the research gap in the literature.

First, the bending of small sized steel sheets was carried out with stationary and moving laser heat sources. Effect of laser power, workpiece geometry (length and width), laser spot diameter and laser scan speed on the achievable bend angle in a single pass is studied numerically as well experimentally. Afterward, the multi-pass laser bending of steel strips was studied. Effects of process parameters on bend angle, edge effect, temperature distribution, stress, plastic strain, flexure strength, microhardness and microstructure was studied. It was encouraging to note that FEM could predict the bend angle with the maximum error of 11%.

Laser bending of friction stir welded aluminium alloy sheets was also studied. Considering the difficulty in obtaining the temperature dependent material properties, an inverse methodology was employed. The inverse methodology is based on the measurement of bend angle and temperature at two locations during laser bending. To reduce the computational time, the techniques of forced cooling and mesh optimization were used. The deviation between experimental and numerical simulation results was less than 10% in all except one case of 16% deviation.

Two techniques were employed for enhancing the absorptivity of sheet metal such as surface coating and surface roughening. One was employing cement coating in place of graphite coating. However, usually the coating gets removed after irradiation, which poses problem in multi-pass laser bending. Hence, another

technique of roughening the surface by friction stir processing was employed. Laser bending of uncoated raw, cement-coated and friction stir processed sheets of aluminum alloy and mild steel were compared. Among them cement coating performed the best, but friction stir processing was also not far behind. Microhardness and microstructure were also studied.

For obtaining large bend angle in a single-pass, laser assisted bending was carried out by applying mechanical and magnetic forces. Mechanical force was applied by hanging a weight at the free end of the cantilevered strip. The magnetic force was applied by means of permanent magnets and with proper design of setup it was used even for laser assisted bending of a non-magnetic material. For quicker estimation of bend angles, the application of an artificial neural network (ANN) model was also explored. ANN was trained by FEM model and validated through experiments. This was demonstrated for laser assisted bending by mechanical load. The same technique can be applied for other bending processes. ANN not only predicted the most likely values, but upper and lower bounds also. FEM modelling of magnetically assisted laser bending was also carried out. The simulation results agreed well with experiments.

Overall, this thesis accomplished the following tasks. Laser bending of small sized sheets, strips and friction stir welded sheets was studied. Laser assisted bending by mechanical and magnetic forces was studied. The study focused on the following aspects: (1) feasibility of achieving sufficient bending with good repeatability for a variety of jobs, (2) predictability of the bending processes by FEM and ANN tools, and (3) post-bend properties. In order to improve the performance and reliability of laser based bending, techniques to enhance the absorptivity were also developed. Appropriate measures were also employed for reducing the computational time of FEM based models of the processes. As the process is stress-controlled (instead of displacement-controlled), prediction models are very important for making the process industry-friendly.

Contents

Abstract..... xi

Contents..... xiii

List of Figures..... xix

List of Tables..... xxvi

Nomenclature..... xxxi

1 Background and Scope..... 1

1.1 Introduction..... 1

1.2 Laser Bending..... 2

1.3 Application of Laser Bending..... 4

1.4 Advantages and Disadvantages..... 5

1.5 Scope of the Present Thesis..... 6

1.6 Organization of the Thesis..... 6

2 Literature Survey and Detailed Objectives..... 9

2.1 Introduction..... 9

2.2 Laser Bending Mechanism..... 9

2.2.1 Temperature gradient mechanism..... 10

2.2.2 Buckling mechanism..... 11

2.2.3 Upsetting mechanism..... 12

2.3 Material Processed by Laser Forming Process..... 13

2.3.1 Carbon steel..... 14

2.3.2 Stainless steel..... 14

2.3.3 Aluminum and aluminum alloys..... 14

2.3.4 Aluminum foam..... 15

2.3.5 Nickel alloy..... 15

2.3.6 Brittle materials..... 15

2.3.7 Magnesium and magnesium alloys..... 16

2.3.8 Plastics..... 17

2.4 Curvilinear Laser Bending Process..... 17

2.5 Process Parameters in Laser Bending..... 18
2.5.1 Effects of laser power..... 18
2.5.2 Effects of scan speed..... 19
2.5.3 Effects of laser beam diameter and geometry..... 20
2.5.4 Effects of number of laser passes..... 20
2.5.5 Effects of workpiece geometries..... 21
2.5.6 Effects of absorptivity on laser bending..... 22
2.5.7 Effects of thermal properties..... 23
2.5.8 Effects of mechanical properties..... 24
2.5.9 Effects of force cooling..... 24
2.5.10 Effects of external load..... 25
2.5.11 Effects of clamp..... 27
2.6 Edge Effect in Laser Bending Process..... 28
2.7 Process Modelling of Laser Forming Process..... 29
2.7.1 Analytical models on laser bending..... 29
2.7.2 Numerical models on laser bending..... 34
2.7.3 Soft computing models..... 37
2.7.4 Inverse modelling..... 39
2.8 Process Optimization of Laser Forming Process..... 40
2.9 Effect of Laser Forming on Mechanical and Microstructural Properties..... 41
2.9.1 The effects of laser forming on microstructural properties.... 41
2.9.2 The effects of laser forming on mechanical properties..... 42
2.10 Major Gaps from the Literature..... 43
2.11 Scope and Objectives of the Present Thesis..... 45
3 Details of Experimental and Simulation Procedures..... 49
3.1 Introduction..... 49
3.2 Chemical Compositions of the Materials..... 49
3.2.1 Field Emission Scanning Electron Microscopy (FESEM) and Energy Dispersive X-Ray Spectroscopy (EDS) 49

3.3 Experimental Study on Laser Machine and other Instruments..... 52
3.3.1 CO_2 laser machine..... 53
3.3.2 Sample preparation..... 54
3.3.3 Temperature measuring instrument..... 56
3.3.4 Coordinate measuring machine (CMM)..... 57
3.4 Study on Mechanical Properties of Workpiece..... 58
3.4.1 Universal testing machine..... 59
3.5 Study on Metallographic Sample Preparation and Examination..... 62
3.5.1 Precision hack saw..... 63
3.5.2 Sample molding press machine..... 63
3.5.3 Polishing Machine..... 64
3.5.4 Optical microscope…..... 65
3.5.5 Microhardness testing..... 66
3.5.6 Non-contact profilometer..... 66
3.6 Experimental Setup of Friction Stir Welding (FSW) and Friction Stir Processing (FSP)..... 67
3.6.1 Fabrication of friction stir welding and processing tools..... 68
3.6.2 Preparation of sheets by friction stir welding and friction stir processing..... 69
3.7 FEM Model of Laser Bending..... 70
3.7.1 Thermal and mechanical properties of the materials..... 72
3.7.2 Thermal and mechanical analysis..... 72
3.7.3 Mesh sensitivity and time increment analysis..... 74
3.8 Measurement of Edge Effect and Springback Effect..... 83
3.8.1 The edge effect..... 83
3.8.2 Springback effect…..... 84
3.9 Conclusion..... 84
4 Laser Bending of Small Sized Sheet..... 87
4.1 Introduction..... 87
4.2 Experiment and FEM Simulation..... 88
4.3 Results of Experimental and Numerical Studies..... 90

4.3.1 Effect of laser power..... 90
4.3.2 Effect of laser beam diameter..... 93
4.3.3 Edge effect..... 93
4.4 Temperature Distribution by Simulation..... 95
4.5 Conclusion..... 98
5 Single and Multi-Pass Laser Bending of Strips..... 101
5.1 Introduction..... 101
5.2 Experiment and FEM Simulation..... 102
5.2.1 Experimental setup and procedure..... 102
5.2.2 Design of experiment..... 103
5.2.3 FEM simulations..... 103
5.3 Results and Discussion..... 104
5.3.1 Experimental and FEM results..... 104
5.3.2 Microhardness..... 109
5.3.3 Flexural test..... 111
5.3.4 Main effects of factors on bend angle and flexural strength.. 112
5.3.5 Microstructure..... 116
5.4 Conclusion..... 119
6 Laser Bending of Friction Stir Welded Sheets..... 121
6.1 Introduction..... 121
6.2 Methodology for Inverse Estimation of Material Properties..... 122
6.2.1 Heuristic algorithm for optimization..... 124
6.2.2 Determination of mechanical properties..... 129
6.3 Results for Inverse Determination of Material Properties..... 129
6.4 Result and Discussion of Laser Bending in Friction Stir Weld Plate..... 132
6.4.1 Tensile test results..... 133
6.4.2 Fracture test..... 136
6.5 Validation of FEM Result..... 137
6.6 Conclusion..... 144
7 Laser Bending of Friction Stir Processed and Cement Coated Sheet... 147

7.1 Introduction..... 147
7.2 Experimental Procedure..... 148
7.3 Results and Discussion..... 151
7.3.1 Tensile strength..... 151
7.3.2 Surface roughness..... 152
7.3.3 Bend angle..... 155
7.3.4 Microhardness..... 158
7.3.5 Microstructure..... 161
7.4 Conclusion..... 163
8 Laser Assisted Bending by Mechanical Load..... 165
8.1 Introduction..... 165
8.2 Details of Experiment..... 166
8.3 Neural Network Modelling..... 168
8.3.1 Selection of training and testing data set for MLP neural network..... 168
8.3.2 Implementation of MLP neural network..... 170
8.3.3 Selection of training and testing data set for RBF neural network..... 173
8.3.4 Implementation of RBF neural network..... 173
8.3.5 Upper and lower bound estimation..... 174
8.4 Results and Discussion..... 175
8.4.1 Validation of FEM model..... 175
8.4.2 Results of neural network model..... 176
8.2.3 Parametric study..... 180
8.2.4 Inverse analysis..... 184
8.5 Conclusions..... 185
9 Laser Assisted Bending by Magnetic Force..... 187
9.1 Introduction..... 187
9.2 Procedure of Experiments..... 188
9.2.1 Preparation of magnetic and nonmagnetic workpiece..... 188
9.2.2 Measurement of magnetic force..... 188

9.2.3 Measurement of the temperature during laser heating of workpiece..... 189
9.2.4 Experiments on laser assisted bending..... 190
9.3 Result and Discussion..... 192
9.3.1 Measurement of magnetic force..... 192
9.3.2 Validation of FEM model..... 194
9.3.3 Simulation results..... 199
9.3.4 Edge effect..... 203
9.3.5 Simulation of evolution of the bend angle with time..... 205
9.3.6 Microhardness..... 206
9.3.7 Temperature distribution..... 208
9.4 Conclusion..... 210
10 Epilogue..... 211
10.1 Introduction..... 211
10.2 Effect of Laser Parameters on Bending of Small Sized Sheet..... 212
10.3 Effect of Single and Multi-pass on Laser Bending of Mild Steel Strips..... 212
10.4 Effect of Laser Parameters as well as Welding Parameter on Laser Bending of Friction Stir Welded Sheets..... 212
10.5 Effect of Laser Absorptivity on Bending of Friction Stir Processed and Cement Coated Sheets..... 213
10.6 Laser Assisted Bending by Mechanical Load..... 213
10.7 Laser Assisted Bending by Magnetic Force..... 214
10.8 Overall Conclusion..... 214
10.9 Scope for Future Work..... 215
References..... 217
Appendices..... 243
Publications from This Thesis..... 253

List of Figures

Figure 1.1	Schematic diagram of laser forming	3
Figure 2.1	Bending mechanisms	13
Figure 2.2	Schematic illustration of laser forming: (a) temperature gradient mechanism, (b) buckling Mechanism and (c) upsetting mechanism	13
Figure 2.3	A laser assisted bending using transparent sapphire tool	26
Figure 2.4	A laser assisted bending by moving mechanical load	26
Figure 2.5	Laser assisted bending by applying a load at the free end of a cantilevered sheet	26
Figure 2.6	Schematic of clamped and unclamped configurations	27
Figure 2.7	A proposed scheme of reducing edge effect by applying two unequal forces at the free end	28
Figure 2.8	Flow chart of research plan	47
Figure 3.1	Field emission scanning electron microscope	50
Figure 3.2	Energy dispersive X-ray spectrum of (a) aluminium alloy 5052-H32 (b) mild steel (AH36) and (c) HSS (H13)	52
Figure 3.3	Orion 3015 2.5 kW CO_2 laser machine: (a) photograph and (b) Schematic diagram of CO_2 laser bending process	54
Figure 3.4	Experimental setup for measuring temperature from bottom side of the workpiece by using thermocouple	56
Figure 3.5	Experimental setup for measuring temperature from bottom side of the workpiece by using pyrometers	57
Figure 3.6	CMM machine (Make: Zeiss^{TM}; model: Vista)	58
Figure 3.7	A schematic of bend angle measurement	58
Figure 3.8	Universal testing machine for (a) Tensile test and (b) Flexural test	60

Figure 3.9	Uniaxial tensile test specimens for longitudinal and transverse directions: (a) FSW workpiece and (b) FSP workpiece	61
Figure 3.10	Tensile test samples after testing	62
Figure 3.11	Basic steps for microstructure and microhardness sample preparation	62
Figure 3.12	Precision hack saw	63
Figure 3.13	Molding machine	64
Figure 3.14	Double disc polishing machine	64
Figure 3.15	Silicon carbide abrasive paper in the range of 400-2000 grit size for specimen polishing, velvet cloth and polished samples	65
Figure 3.16	Optical microscope	65
Figure 3.17	Microhardness tester	66
Figure 3.18	Non-contact profilometer	67
Figure 3.19	Photograph of Friction stir welding (FSW) machine	68
Figure 3.20	Friction stir welding and friction stir processing tools	69
Figure 3.21	Schematic diagram of the friction stir welding process	70
Figure 3.22	Schematic representation of workpiece meshing with region	75
Figure 3.23	The small size workpiece mesh model	76
Figure 3.24	The mesh model for strip	78
Figure 3.25	The friction stir welded plate mesh model	79
Figure 3.26	Schematic representation of workpiece meshing with region	80
Figure 3.27	Overview of the experimental work	85
Figure 4.1	The workpieces for stationary and movable heat source with size of (a) 25 mm × 20 mm × 2 mm and (b) 15 mm × 10 mm × 2 mm	89
Figure 4.2	Effect of laser power on the bend angle for stationary and moving heat sources on 25 mm × 20 mm × 2 mm workpiece for (a) 8 mm beam diameter and (b) 4 mm beam diameter	91
Figure 4.3	Effect of laser power on the bend angle for stationary and moving heat sources on 15 mm × 10 mm × 2 mm workpiece for (a) 8 mm laser diameter and (b) 4 mm laser diameter	92

Figure 4.4	The effects of stationary heat source on bend angle along width direction by using 4 mm laser diameter on 25 mm × 20 mm × 2 mm workpiece	94
Figure 4.5	Effect of laser power on bend angle for 25 mm × 20 mm × 2 mm workpiece for (a) 250 W laser power and (b) 100 W laser power	95
Figure 4.6	Variation of top and bottom surface center point temperature with laser power for 25 mm × 20 mm × 2 mm workpiece	96
Figure 4.7	Variation of top and bottom surface center point temperature with beam diameter for 25 mm × 20 mm × 2 mm workpiece	96
Figure 4.8	Temperature distributions at the top and bottom surface center point and variation of bend angle with time for the workpiece of size (25 mm × 20 mm × 2 mm) for (a) moving heat source and (b) stationary heat source	97
Figure 5.1	Comparison between experimental and simulation results for bend angle variation at different process parameters for (a) 20 mm width (b) 30 mm width and (c) 40 mm width	106
Figure 5.2	Variation of temperature and bend angle with time	107
Figure 5.3	*X*-direction (along length) stress at top and bottom surfaces of the workpiece	108
Figure 5.4	Plastic stain in *X*-direction at top and bottom surface center points of the workpiece	109
Figure 5.5	Microhardness profile across thickness of the laser bending process for (a) different thickness and (b) number of passes	110
Figure 5.6	Flexural stress variation with deflection for three different parameters and base material	112
Figure 5.7	Plot of main effects for bend angle	114
Figure 5.8	Plot of main effects for flexural strength	114
Figure 5.8	Optical microstructures at the cross section perpendicular to the scanning (along thickness direction) (×10 magnification)	117
Figure 5.9	Optical microstructures at the center of laser irradiated mild steel surface from top side (×40 magnification): (a) after fifth laser	118

	pass (b) after third laser pass (c) after first laser pass and (d) base plate (before laser bending)	
Figure 5.10	Optical microstructures of laser irradiated surface after 5th laser pass of mild steel strip along laser scan line (×40 magnification) for strip thicknesses of (a) 1 mm, (b) 1.5 mm and (c) 2 mm	119
Figure 6.1	Top and bottom view of the workpiece showing the laser beam path and location of pyrometers	123
Figure 6.2	Two-dimensional graphical representation of search procedure	127
Figure 6.3	Flow chart of optimization techniques	128
Figure 6.4	Temperature versus thermal diffusivity	130
Figure 6.5	Temperature versus specific heat	131
Figure 6.6	Temperature versus density	131
Figure 6.7	Mechanical properties of aluminum alloy (5052-H32) at various temperatures: (a) Yield stress and (b) Young's modulus	132
Figure 6.8	The scanning scheme on friction stir welded sheets: (a) along welding direction on the top surface, (b) along welding direction on the bottom surface, (c) across welding direction on the top surface and (d) across welding direction on the bottom surface	133
Figure 6.9	The engineering stress and strain of aluminum alloy 5052-H32 base metal sheet and the friction stir welded zone in transverse direction	134
Figure 6.10	The engineering stress and strain of aluminum alloy 5052-H32 base metal sheet and the friction stir welded zones in longitudinal direction	135
Figure 6.11	Fractured tensile specimen (friction stir welded aluminum alloy 5052-H32) at different tool rotations and welding speeds	136
Figure 6.12	FESEM image of fracture test samples: (a) tool rotation 1500 RPM and welding speed 36 mm/min and (b) tool rotation 1500 RPM and welding speed 132 mm/min	137

Figure 6.13	Simulation and experiment results of bend angles for friction stir welded sheet (weld zone thickness 1.75 mm and scanning along weld direction on the bottom surface)	138
Figure 6.14	Simulation and experiment results of bend angles for friction stir welded sheet (weld zone thickness 1.75 mm and scanning along weld direction on the top surface)	139
Figure 6.15	Simulation and experiment results of bend angles for friction stir welded sheet (weld zone thickness 1.75 mm and scanning across weld direction on the bottom surface)	139
Figure 6.16	Simulation and experiment results of bend angles for friction stir welded sheet (weld zone thickness 1.75 mm and scanning across weld direction on the top surface)	140
Figure 6.17	Simulation and experiment results of bend angles for friction stir welded sheet (weld zone thickness 1.95 mm and scanning along weld direction on the bottom surface)	141
Figure 6.18	Simulation and experiment results of bend angles for friction stir welded sheet (weld zone thickness 1.95 mm and scanning along weld direction on the top surface)	141
Figure 6.19	Simulation and experiment results of bend angles for friction stir welded sheet (weld zone thickness 1.95 mm and scanning across weld direction on the bottom surface)	142
Figure 6.20	Simulation and experiment results of bend angles for friction stir welded sheet (weld zone thickness 1.95 mm and scanning across weld direction on the top surface)	142
Figure 6.21	Variation of bend angle along width direction for weld zone thicknesses 1.75 mm (scanning on the top surface along the weld direction) for sheets produced by different FSW conditions	143
Figure 6.22	Variation of bend angle along width direction for weld zone thicknesses 1.85 mm (scanning on the top surface along the weld direction) for sheets produced by different FSW conditions	143

Figure 6.23	Variation of bend angle along width direction for weld zone thicknesses 1.95 mm (scanning on the top surface along the weld direction) for sheets produced by different FSW conditions	144
Figure 7.1	Photographs of sheets ready for bending: (a) aluminum alloys (5052-H32) and (b) mild steel (AH36)	149
Figure 7.2	A schematic of the indented sheet after microhardness test	150
Figure 7.3	Experimental result of true stress verses true strain (a) aluminum alloy (5052-H32) and (b) mild steel (AH36)	152
Figure 7.4	The centreline average surface roughness values of friction stir processed sheet at different sections	153
Figure 7.5	Results of 3D non-contact surface profilometer for friction stir processed aluminum: (a) surface topography and (b) scan profile showing the width and the height of the groove	154
Figure 7.6	Results of 3D non-contact surface profilometer for friction stir processed mild steel (AH36): (a) surface topography and (b) scan profile showing the width and the height of the groove	155
Figure 7.7	Effect of number of laser pass on bend angle for (a) aluminum alloy (5052-H32) and (b) mild steel (AH36)	156
Figure 7.8	Variation in bend angle along the laser path after 6^{th} laser pass for (a) aluminum alloy (5052-H32) and (b) mild steel (AH36)	157
Figure 7.9	Microhardness profile of laser applied FSP sheet at the middle of the thickness (a) aluminium alloy (5052-H32) and (b) mild steel (AH36)	158
Figure 7.10	Microhardness profile after 6^{th} laser pass on FSP, cement coated and raw sheets along thickness direction for (a) aluminum alloy (5052-H32) and (b) mild steel (AH36)	159
Figure 7.11	Optical microstructures at the center of friction stir processed steel sheet (×20 magnification): (a) before laser bending, (b) after first laser pass, (c) after third laser pass and (d) after sixth laser pass	160

Figure 7.12	Optical microstructures after 4th laser pass of friction stir processed mild steel (AH36) sheet along thickness direction (×20 magnification): (a) near top, (b) middle and (c) near bottom	161
Figure 7.13	The mean grain size distribution for friction stir processed steel sheet after (a) first laser pass, (b) third laser pass and (c) sixth laser pass	162
Figure 8.1	A schematic diagram of laser assisted mechanical bending	165
Figure 8.2	Experimental setup in the laser machine	167
Figure 8.3	MLP neural network architecture	170
Figure 8.4	Flowchart for the training process	172
Figure 8.5	RBF neural network architecture	174
Figure 8.6	Experimental versus FEM result	176
Figure 8.7	Testing results for MLP neural network	176
Figure 8.8	Testing results for RBF neural network	177
Figure 8.9	Experimental versus RBF predicted bend angles for validation inputs	178
Figure 8.10	FEM versus RBF predicted bend angles for validation inputs	178
Figure 8.11	Upper and lower bound predictions of the testing data	179
Figure 8.12	Upper and lower bound predictions of the validation data	179
Figure 8.13	Power versus bend angle	180
Figure 8.14	Mechanical load versus bend angle	181
Figure 8.15	Scan speed versus bend angle	181
Figure 8.16	Scan-line distance versus bend angle	182
Figure 8.17	Time variation of bend angle with the top and bottom surface temperatures of workpiece for (a) 800 W and (b) 700 W	183
Figure 9.1	Experimental setup to measure the magnetic force on workpieces which are made of (a) mild steel and (b) stainless steel	189
Figure 9.2	Experimental setup for measuring the temperature from bottom side of the workpiece	190

Figure 9.3	Photograph of the experimental setup for magnetic material (mild steel): (a) magnet holder fixed at the bottom and (b) magnet holder fixed at the top	191
Figure 9.4	Photograph of the experimental setup for nonmagnetic material (stainless steel): (a) magnet holder fixed at the bottom and (b) magnet holder fixed at the top	191
Figure 9.5	Variation of magnetic force with air gap for (a) mild steel and (b) stainless steel	193
Figure 9.6	Simulated and experimental time histories of temperature for (a) mild steel and (b) stainless steel	195
Figure 9.7	Bend angle results at various scan speed for mild steel: (a) upward magnetic force, (b) downward magnetic force and (c) without magnetic force	197
Figure 9.8	Bend angle results at various scan speed for stainless steel: (a) upward magnetic force, (b) downward magnetic force and (c) without magnetic force	198
Figure 9.9	Laser bending of mild steel: (a) upward magnetic force, (b) downward magnetic force and (c) without magnetic force	201
Figure 9.10	Laser bending of stainless steel: (a) upward magnetic force, (b) downward magnetic force and (c) without magnetic force	202
Figure 9.11	Variation of bend angle along the scan direction for (a) mild steel workpiece without magnetic force, (b) mild steel workpiece with upward magnetic force, (c) stainless steel workpiece without magnetic force and (d) stainless steel workpiece with upward magnetic force	203
Figure 9.12	Effect of magnetic assisted bending on edge effect at different scan speeds for (a) stainless steel workpiece and (b) mild steel workpiece	204
Figure 9.13	Evolution of bend angle with time in magnetically assisted bending as obtained by FEM simulation for (a) mild steel and (b) stainless steel at different scan speeds	205

Figure 9.14	Average microhardness profile of laser irradiated workpiece: (a) mild steel and (b) stainless steel	207
Figure 9.15	Average microhardness profile for downward magnetic force, upward magnetic force and without magnetic force for: (a) mild steel and (b) stainless steel	207
Figure 9.16	Effect of scanning speed on temperature distribution	208
Figure 9.17	Temperature history for laser assisted and laser bending process	209
Figure 9.18	Temperature history for different thickness	209

List of Tables

Table 2.1	Effect of absorptivity on laser bending process.	23
Table 3.1	Laser and material parameters for different experiments	55
Table 3.2	Mesh sensitivity study for fine mesh region for stationary heat source, workpiece size of 25 mm × 20 mm × 2 mm, laser power of 225 W and laser beam diameter of 8 mm	77
Table 3.3	FEM models for workpiece of different size	77
Table 3.4	Effect of element size for refined zone on bend angle (20 mm width)	78
Table 3.5	FEM mesh size for workpiece of different widths	79
Table 3.6	Effect of element size in refine zone on bend angle for laser power of 800 W, scan speed of 400 mm/min and laser beam diameter of 7.76 mm	80
Table 3.7	Effect of element size in Region I (refined zone)	81
Table 3.8	Effect of element size in Region III	81
Table 3.9	Effect of element size in Region II	81
Table 3.10	Effect of element size in Region I on bend angle for laser power of 1000 W and scan speed 1000 mm/min (number of divisions along length in each Region II and III fixed at 5)	82
Table 3.11	Mesh sensitivity analysis for coarse bias mesh in region between refined zone and free end for laser power of 1000 W and scan speed of 1000 mm/min (element size in refined zone: 0.5 × 0.5 × 0.333 mm^3, number of elements in region between refined zone and fixed end fixed at 5)	83
Table 4.1	Process parameters	89
Table 4.2	Fourier number for 25 mm × 20 mm × 2 mm for 8 mm laser diameter	98
Table 5.1	Process parameters and corresponding levels	103

Table 5.2	Experimental and simulated bend angle	105
Table 5.3	Relation between temperature gradient and bend angle for P= 600 W, v = 800 mm/min, D = 9.4 mm, w = 40 mm and t = 2 m	108
Table 5.4	The flexural strength of laser scanned specimens	112
Table 5.5	ANOVA table for bending test	115
Table 5.6	ANOVA table for flexural strength	115
Table 5.7	Additional test for conformation	116
Table 6.1	Experimental results of temperature at the bottom of the aluminum alloy 5052-H32 workpiece at two locations, P_1 and P_2	124
Table 6.2	Ranges of the initial parameters	125
Table 6.3	Variation of thermal properties, density and laser beam radius with temperature (absorptivity fixed at 0.4 based on earlier experiments, beam radius 0.0039 mm)	130
Table 6.5	Yield stress and modules of elasticity for aluminum alloy 5052-H32 base material and friction stir welded zone based on longitudinal direction	135
Table 7.1	Mechanical properties for aluminum alloy (5052-H32) and mild steel (AH36) before and after FSP	151
Table 8.1	Process parameters and their levels in the experiment	167
Table 8.2	Errors in upper and lower limit predictions of small angle cases in testing data	180
Table 8.3	Inverse prediction of laser power using RBF	184
Table 8.4	Inverse prediction of mechanical load using RBF	185
Table 9.1	Experimental process parameters	192
Table 9.2	Magnetic attraction force for different materials and thicknesses	194
Table 9.3	Deviations between experimental and simulated bend angles (with downward magnetic force)	199

Nomenclature

Roman letters

c_1 and c_2	Constants dependent on materials properties
c_p	Specific heat capacity
d_s	Scan-line distance
D	Laser beam diameter
D_L	Laser beam diameter before lens
D_t	Thermal diffusivity
E	Young's modulus
E_1	Pyrometer one
E_2	Pyrometer two
f	Focal length
h	Convective heat transfer coefficient
H	Standoff distance
k	Thermal conductivity
l	Length of workpiece
l_h	Half length of heated zone
L	Mechanical load
M^2	Beam quality factor
n	Number of data
N	Number of passes
P	Laser power
P_o	Probability
q	Thermal heat flux density of laser beam
r	Radius of the laser beam
R^2	Coefficient of determination
S_F	Flexural strength
t	Thickness of the workpiece

t_h	Thickness of heated volume
T_a	Ambient temperature
T_{max}	Maximum temperature
T_{pred}	Maximum predicted temperature
T_s	Sheet surface temperature
v	Scan speed
w	Width of workpiece
w_o	Laser beam waist

Greek letters

α_b	Bend angle
α_{ave}	Average bend angle
α_{max}	Maximum bend angle
$\alpha_{min,}$	Minimum bend angle
α_{bpi}	Predicted bend angle
α_{bti}	Target bend angle
α_{th}	Coefficient of thermal expansion of the workpiece
β	Tolerance parameter
η	Absorption coefficient
ρ	Density
μ	Poisson's ratio
σ_y	Yield stress
λ	Wave length

List of abbreviations

ANN	Artificial Neural Network
BM	Buckling Mechanism
CMM	Coordinate Measuring Machine
CNC	Computer Numerical Control
CO_2	Carbon di-oxide
CW	Continuous Wave
DOF	Degree of Freedom
EDS	Energy Dispersive X-Ray Spectroscopy

FE	Finite element
FEA	Finite element analysis
FEM	Finite element method
FESEM	Field Emission Scanning Electron Microscopy
FSP	Friction stir process
FSW	Friction stir welding
HAZ	Heat affected zone
MLP	Multilayer perceptron
MSS	Mean Sum of Squares
Nd:YAG	Neodymium-doped yttrium aluminum garnet
OA	Orthogonal array
RBF	Radial basis function
RMS	Root mean squared
RVBA	Relative variation in bend angle
SS	Sum of Squares
TGM	Temperature Gradient Mechanism
UM	Upsetting Mechanism
UTM	Universal Testing Machine

Chapter 1

Background and Scope

1.1 Introduction

For most manufacturers today, the key to success is to be able to satisfy customer needs by providing better quality products at the lowest possible cost and within the shortest possible time. One of the greatest inventions of 20th century that influenced manufacturing sector to a great extent is light amplification by stimulated emission of radiation (laser). Due to their power and economic advantages, laser beam sources, are now an integral part of technology in many manufacturing companies. The first laser was built in 1960 by T. H. Maiman at Hughes Research Laboratories, based on theoretical work by C. H. Townes and A. L. Schawlow. The word laser was first coined by Gordon Gould in 1957, when he suggested a conceptual design.

Due to increasing complexity of part geometry and requirement of highly accurate products, laser is applied in a number of manufacturing processes. Industrial applications of laser include bending, shaping, cutting, drilling, ablation, scribing, structuring, joining (welding), hardening, alloying, dispersing, coating and marking. The focus of this thesis on laser forming and in particular, on laser based bending. For the purpose of this thesis, the term laser based bending connotes the bending of a sheet by laser irradiation with or without the application of an external load. Laser based bending can be classified into laser bending and laser assisted bending. Laser bending uses only laser irradiation to bend the sheet whilst laser assisted bending uses an external load as well.

Before laser bending, flame bending was used for the adjustment of welded construction in ship building industry. Bending of metal plates with the application of flame heating was initiated to shape metal plates of ship-hull. The process is time taking, requires skilled person and it is difficult to focus the flame on a small area (Vásquez-Ojeda and Ramos-Grez, 2009, Vollertsen and Sakkiettibutra, 2010, Dutta and Manna, 2011). Due to uncontrolled flame, it may produce defective product. It is

very important to control the flame in a bending process. To mitigate these problems, laser beam was applied instead of a gas flame to bend workpiece. First application of the laser bending was patented in by Martin (1979).

There are many types of lasers available for research, medical, industrial and commercial uses. Lasers are often described by the kind of lasing medium they use. Some of these are as follows:

- **Solid state** lasers have lasing material distributed in a solid matrix. In these lasers, glass or crystalline materials are used, e.g., ruby laser, Nd:YAG laser, etc.
- **Liquid** laser is a laser that uses the liquid as a lasing material. In liquid lasers, light supplies energy to the lasing material. An example is a dye laser that uses an organic dye as a lasing material.
- **Gas** lasers have gas as lasing medium, e.g., He-Ne laser, argon ion lasers, CO_2 laser, **excimer** lasers etc.
- **Semiconductor** lasers are sometimes called diode lasers. These electronic devices are generally very small, very cheap, of compact size and consume low power. Semiconductor lasers are different from solid-state lasers. In solid-state lasers, light energy is used as the pumping source, whereas in semiconductor lasers, electrical energy is used as the pumping source.

Lasers are also characterized by the duration of laser emission. Two popular classes are the continuous wave (CW) laser and the pulsed laser. In the CW laser, the light is emitted as a steady continuous beam, generally, with less intensity. Gas lasers belong to this category. On the other hand, the pulsed lasers produce powerful bursts of light of short duration. Q-switched laser, crystals, glass and liquid types of lasers belong to this category. Normally the solid-state lasers operate intermittently, mainly due to the large amount of heat developed in the crystal. However, some solid-state lasers can operate in CW mode as well.

1.2 Laser Based Bending

Laser based bending is a process of bending the workpiece by using a controlled laser heat source. There are predominantly two ways to bend sheets with

the help a laser. One way is to carry out laser line heating of the sheet to induce thermal stresses in it. This process, called laser bending, is a non-contact bending process and is suitable for obtaining small bend angles. The other way is to carry out mechanical bending along with laser heating for localised softening of the material. To distinguish it from laser bending, this method is called laser assisted bending. It helps to get larger bend angles with a single laser scan in a particular direction.

Figure 1.1 shows the schematic diagram of a straight-line irradiation of laser bending. During experiments, one end of the workpiece is clamped over laser machine bed using a fixture. The laser beam is irradiated in a direction parallel to the free edge of clamped specimens. The localized nature of laser irradiation yields high temperature gradients between the irradiated surface and the surrounding material that force the material to expand non-uniformly, resulting in a differential thermal expansion between the top and bottom surfaces. The non-uniform expansion of the material leads to non-uniform thermal stresses, which results in plastic deformation at locations where thermal stresses exceed the yield stress of material. After the laser beam irradiation, the heated specimens are allowed to cool naturally or by forced cooling. During cooling, the upper material layers shrink more than the lower ones, resulting in permanent sheet bending towards the laser beam.

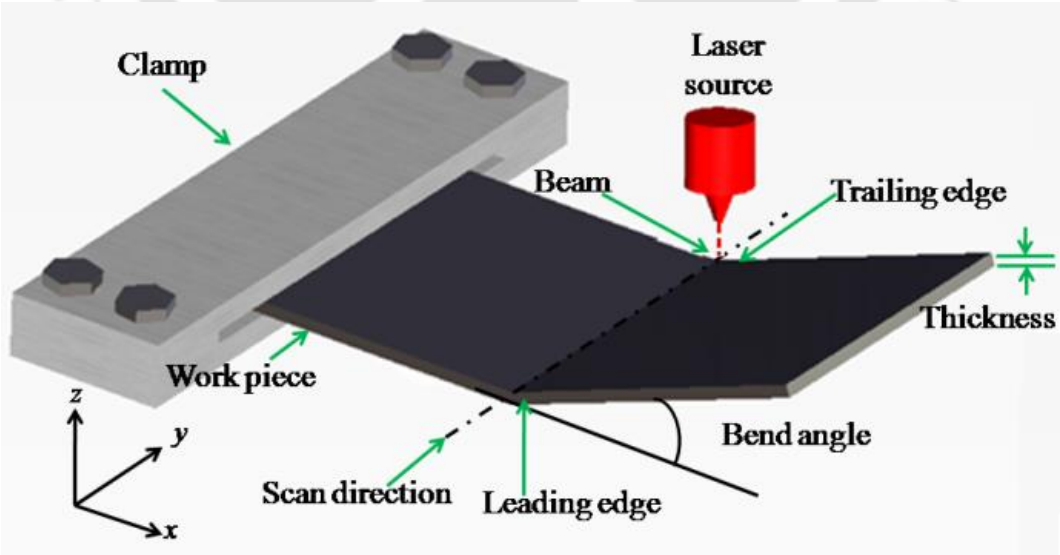

Figure 2.1 Schematic diagram of laser forming

In general, a number of scans or passes of laser beam may be required to get the required bending. With the help of overlapping of multiple passes or by increasing the number of adjacent parallel scan lines, bends and curvatures of a desired angle and radius can be obtained. The thermal stress is induced in the workpiece without melting the workpiece. The behavior of laser bending of workpiece is controlled by a combination of laser parameters (power, scan speed and laser beam diameter), geometry of workpiece (length, width and thickness) and material properties (mechanical and thermal). The laser bending process has been investigated for plates (Lawrence et al. 2001), sheets (Geiger 1994), foils (Liu et al. 2009) pipes and tubes (Hao and Li 2003a, b) for a wide range of materials, *viz*., metals, non-metals, composites, plastics and ceramics.

Based on the direction of bending of the workpiece after the incident of the laser beam, laser bending is divided into two types:

1. Positive laser bending: If the bending of the workpiece occurs towards the incident beam then it is called positive laser bending. It is the most common type of laser bending.
2. Negative laser bending: If the bending of the workpiece occurs away from the incident beam then it is called negative laser bending.

1.3 Applications of Laser Based Bending

The unique characteristics of lasers have made them important tools in various applications after the first demonstration of HeNe laser in 1960. Laser bending is used as an accurate and cost effective process to adjust or align the mating parts in welding constructions, ship building industry and straightening the distorted parts, e.g., car body parts (Ueda 2009, Ueda 2011, Hennige 1997, Zhang and Xu 2005a, Qi and Namba 2011).

Laser bending has many applications in the fields ship building (naval), aerospace, micro-electromechanical system (MEMS), chemical and sensor industries (Zhou et al. 2013, Watkins et al. 2001, Vollertsen et al. 1995, Chen et al. 1998, Tam et al. 2001, Ocana et al. 2007). It can be also used to bend brittle material (Wu et al. 2010a, b, Bammer et al.2011).

1.4 Advantages and Disadvantages of Laser Based Bending

Laser-based techniques have the following decisive advantages over conventional processing methods. Different researchers highlighted the following advantages of laser based bending (Vollertsen et al. 1995, Chen and Xu 2001, Magee and Vin 2002, Zihang and Xu 2005, Barletta 2006, Casamichel et al. 2007, Shen 2008 and Shidid et al. 2013):

- Excellent beam control with fully automation can be achieved.
- Laser bending is a contact free method and does not require tools and dies (zero-force processing) for laser bending. It reduces the cost of small batch production. Tools and die are used for laser assisted bending to create large bend angles in difficult-to-form materials.
- The process can be used for obtaining precise, accurate and small bend angles, particularly micro-bending, which may not be possible with mechanical bending.
- Process can be implemented for bending without any size constraints. It can be used for bending of small parts required for miniaturization as well as large parts for aerospace and ship building industry.
- There is low thermal input to the workpiece, due to the very high energy density at the processing point. The bending can be performed without melting the workpiece.
- High processing speed is possible due to the elimination of lead-time associated with the design, manufacturing and placement of tools and dies.
- The laser can bend brittle and hard materials e.g., magnesium alloy, titanium alloy, aluminum alloy, nickel alloy and ceramic.
- It can be easily integrated into conventional manufacturing processes.
- It can generate complex shapes with suitable laser irradiation strategies.
- It has high-energy efficiency due to controlling mechanisms as compared to other heat based bending processes like flame bending.
- Transportation of the laser beam through flexible fibre optical cables is possible. It facilitates forming operation in complex area where mechanical tooling is not accessible.

Any of these aspects may argue strongly in favour of laser based bending. However, they are some limitation too. They are as follows:

- Process efficiency depends on radiation absorptivity of material. However, coating the workpiece can mitigate this problem to a great extent.
- Sheet metals of high thickness are difficult to bend.
- For mass production, laser bending process is not advisable due to slow operation as compared to traditional punch and die technique.
- Great care needs to be taken to avoid oxidation.
- High initial investment of laser machine makes the process more expensive than flame bending.

1.5 Scope of the Present Thesis

The primary objective of the present thesis is to study the performance of laser based bending process of ductile materials. The influence of the laser process parameters, *viz.*, power, scan speed and laser beam diameters and workpiece parameters, *viz.*, length, thickness, width, material properties including absorptivity have great influence on the accuracy and efficiency of the process. This study is mainly focused on laser and laser assisted bending of aluminum alloy (5052-H32), mild steel (AH36), stainless steel (SUS304), friction stir welded aluminum alloy (5052-H32) and friction stir processed aluminum alloy (5052-H32). The thesis explores efficient techniques to manufacture large and precise bend angle with good surface quality and minimum edge effect. For this purpose, laser assisted bending, using mechanical load in the form of dead weight and magnetic force, is also explored. Microhardness, microstructure and average mean grain size also form the part of the study.

1.6 Organization of the Thesis

The work performed in the present thesis consists of ten chapters. This chapter has presented an introduction of laser bending and scope of the thesis. Chapter 2 presents a literature review on the laser bending process and a detailed summary on the techniques used to predict the quality of the laser bend. It discusses a number of processes of laser bending, effect of process parameters on laser bending, mechanisms

of laser bending, materials processed by laser forming process, edge effect in laser bending process and process modelling of laser forming processes.

Chapter 3 describes the detailed plan regarding of experiments and simulations of laser bending. The experimental set up, testing machine and details of numerical simulation have been explained. Chapter 4 describes numerical and experimental study on multi-pass laser bending of AH36 steel strips. The effect of different process parameters such as laser power, scan speed, laser beam diameter, number of laser pass, thickness and width of workpiece are discussed. Chapter 5 presents bending of small sized sheet by applying stationery and movable heat source.

Chapter 6 present laser bending of friction stir welded aluminum alloy 5052-H32 sheets. Inverse determination of thermal and mechanical properties was conducted in this chapter. Chapter 7 discusses the laser bending of raw (uncoated), cement-coated and friction stir processed sheets (aluminum 5052-H32 and mild steel sheets). The effects of friction stir processing and cement coating on laser bending are investigated. The properties of the bent sheets, *viz*., micro-hardness, microstructure and grain size distribution, are studied. Chapter 8 and Chapter 9 present laser assisted bending by using mechanical load in the form of dead weight and magnetic force, respectively. Conclusions and scope for future work are presented in Chapter 10 followed by references and appendices.

Chapter 2

Literature Survey and Detailed Objectives

2.1 Introduction

Recently, the forming of sheet by the application of heat through a laser beam has drawn the attention of various researchers. The laser is an energy source that has recently become an important manufacturing tool. The laser bending has been modelled analytically as well as numerically. In this chapter, the review of literature is presented on the laser bending process. A lot of information in this chapter has been taken from earlier review papers (Shen and Vollertsen, 2009; Dixit et al. 2015).

2.2 Laser Bending Mechanism

The laser bending mechanism is characterized based on the bending direction. The desired laser bending direction of the sheet can be controlled by proper selection of workpiece geometries (thickness, length and width of the workpiece), laser beam parameters (laser power, scan speed and laser spot diameter) and material properties (Vollertsen and Rodle, 1994).

Geiger and Vollertsen (1993); Vollertsen and Roodle (1994) and Shen and Vollertsen (2009) reported three fundamental mechanisms for describing the thermo-mechanical behaviour during laser forming process. These mechanisms depend on the geometries of the workpiece and laser process parameters. They are

1. Temperature gradient mechanism (TGM),
2. Buckling mechanism (BM),
3. Upsetting mechanism (UM).

Guan et al. (2005) mentioned that the bending of the sheet material occurs because of temperature variation between top and bottom of the workpiece through the thickness direction. This temperature variation induces stress due to the differential expansion of adjacent layer that are at different temperatures.

2.2.1 Temperature gradient mechanism (TGM)

TGM is the most commonly appeared mechanism for sheet metal bending. It generates when the diameter of laser beam is much smaller compared to workpiece thickness. Vollertsen and Rodle (1994), Merklein et al. (2001), Hu et al. (2002) and Kant and Joshi (2012a) observed that the diameter of laser beam, scan speed and thickness of the workpiece affect the bending direction. TGM is initiated when the diameter of laser beam is smaller than the workpiece thickness (laser beam diameter is of the order of workpiece thickness) and scan speed is fast to generate a steep temperature gradient (Li and Yao, 2001a).

TGM operates in the following two stages, *viz.*, heating and natural cooling of the workpiece:

- Heating stage: During heating, thermal expansion occurs in the heated area that results in bending towards the reverse side of the laser source. The expansion due to thermal gradient is resisted by the neighbouring material that causes compressive stresses in the heated region. Once the thermal stresses reach the temperature dependent flow stress, plastic deformation is produced near the top surface but not in the vicinity of bottom surface as the temperature is low.
- Cooling stage: During cooling, the bending direction is towards the laser beam. This is due to contraction and shortening of the material at the upper layers, which finally bends the sheet towards the laser beam.

Lawrence et al. (2001) conducted experiments on a single-pass laser bending. They observed that for single pass, the bend angle ranging between 0.1º to 3º was achieved. Wang et al. (2016) studied the thickening phenomenon in laser bending zone of a metal laminated plate. A thickening behaviour of stainless steel/carbon steel laminated plate (SCLP) was investigated in laser bending zone. SCLP comprised the matrix layer of carbon steel cladded on both side by stainless steel plates. Researchers argued that the thickening is caused due to thermal as well as plastic deformation effect.

2.2.2 Buckling mechanism (BM)

Buckling mechanism (BM) is responsible for bending of thin sheets at low scan speed. BM is achieved by using a beam diameter larger than the sheet thickness (approximately ten times of the sheet thickness) (Hu et al. 2002). The BM occurs when the temperature gradient across thickness is negligible (Li and Yao 2001b; Hu et al. 2002 and Shi et al. 2006b). It occurs when a thin sheet having higher thermal conductivity is scanned using a bigger spot diameter and slow laser scan speed, resulting in a high thermo-elastic strain in the metal (Vollertsen et al. 1995 and Dearden and Edwardson, 2003). It is used to deform thin metal sheets. During BM, a bend angle in the range of 1° to 15° can be generated in a single laser scan, which is considerably larger than that during TGM (Lawrence et al. 2001).

The bending process in BM comprises the following steps:

- Heating stage: Primarily the material is heated, which in turn leads to thermal expansion of the material and results in compressive stresses in the heated region. The sheet develops bulging as the compressive stresses increase and the flow stress of the heated workpiece is reduced. As the flow stress in the top of the buckled sheet is reduced further, the metal bends plastically in this region.
- Cooling stage: The temperature is reduced and the flow stress in heated region becomes relatively high. This results only in elastic bending of the sheet in that region.

The process itself does not define the direction of the bend angle. BM can cause the bending in both ways towards and away from laser source depending on a number of factors (Edwardson et al. 2001; Hennige et al. 1997; Shi et al. 2006a and Jamil et al. 2011a). The main factors are laser parameters, workpiece geometry, internal and external stresses (gravitation forces). Pre-existing residual stresses and pre-bending orientation of the sheet determine the direction of the bend angle. However, it is possible to bend a sheet metal in a defined way using the BM.

Chakraborty et al. (2016) developed experimental and finite element (FE) simulations to form bowl shaped surfaces with a stationary laser beam irradiating at the centre of flat circular sheet-blanks. Flat circular blanks of 25 mm diameter and 1

mm thick AISI 304 steel sheet were irradiated at the centre with a 2 kW Yb fibre laser. Irradiation time was varied from 1 to 4 s, laser spot diameter was varied from 6 to 12 mm and keeping power as 300 W. At constant laser beam diameter and laser power, sheet blanks bent more for higher irradiation time. Higher laser beam diameters (approximately 10 times of the sheet thickness) activated buckling mechanism of laser forming.

2.2.3 Upsetting mechanism (UM)

Upsetting mechanism (UM) is activated when the beam diameter is much smaller than the sheet thickness of the workpiece. Additionally, a high thermal conductivity of the sample material facilitates the activation of UM (Pretorius, 2009). In the upsetting mechanism, the workpiece becomes short in length and thicker along thickness direction in the laser irradiated region. Hence, it is also known as shortening mechanism (Shen 2008). The UM appears when the thick plate is irradiated with slow laser scan speed with small laser spot diameter (Shi et al. 2012). The process parameters are similar to BM but the heated area is much smaller than the sheet thickness; therefore the buckling is prevented by the workpiece. The low processing speed will result in almost homogeneous heating across the thickness of the sheet. In the heated area, the flow stress decreases and the thermal strains approach the elastic strains at the yield stress. Additional heating leads to a plastic compression of the heated material as the surrounding bulk material restricts the free expansion. Therefore, a large amount of the thermal expansion is converted into plastic compression. The sheet is compressed with an almost constant strain along the thickness, causing a shortening of the sheet and an increase in thickness (Li and Yao 2001a; Lawrence et al. 2001; Hu et al. 2002 and Shi et al. 2006b). The laser bending mechanisms are summarized in Fig. 2.1. The schematic diagram of the laser bending mechanisms is shown in Fig. 2.2.

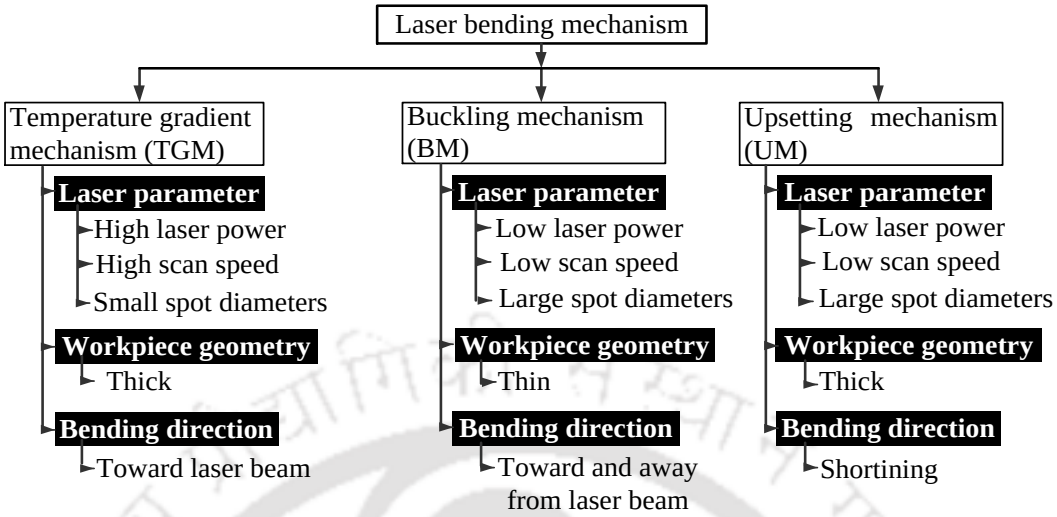

Figure 2.1 Bending mechanisms

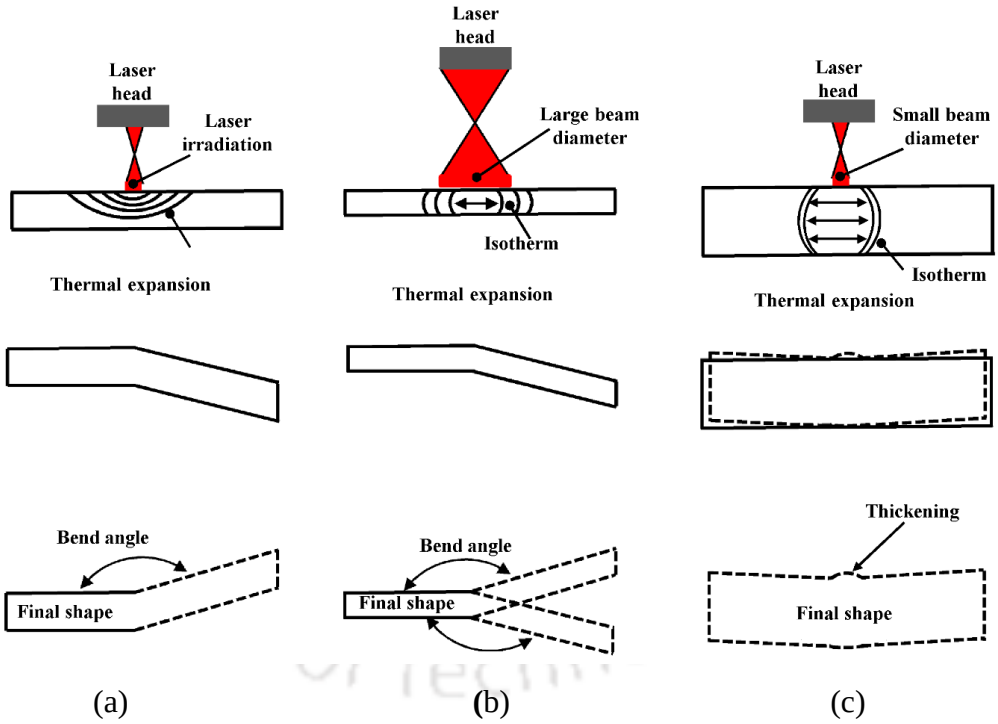

Figure 2.2 Schematic illustration of laser forming: (a) temperature gradient mechanism, (b) buckling Mechanism and (c) upsetting mechanism

2.3 Materials Processed by Laser Bending Process

Researchers in laser bending have investigated different materials, which have been useful for the manufacturing industries. The process of laser bending has been

applied to various industrial materials. A brief description is provided in the following subsections.

2.3.1 Carbon steel

Dearden and Edwardson (2003) generated 3-D complex shaped in the mild steel sheet by using Nd:YAG, Q-switched laser. Chen et al. (2008) studied the bend angle in laser forming of cold-rolled grade 1008-1012 steel by using continuous wave fiber laser. TGM and BM laser bending were studied for the multi-path and multi-scan irradiations. Shen and Yao (2009) carried out a detailed investigation of the mechanical properties of low carbon steel sheets after laser bending. They observed an enhancement in the fatigue life due to the compressive strains induced by the process. Safari and Farzin (2013) studied laser bending of tailor-machined blanks of mild steel by using continuous wave CO_2 laser at the maximum power of 2 kW.

2.3.2 Stainless steel

Chen et al. (1999) used line shaped pulsed laser to bend full-hard 301 stainless steel workpiece. Gollo et al. (2011) investigated the effect of process parameters on bend angle in laser bending by using pulsed Nd:YAG lasers for St12 and 304 alloy steel sheets. They applied Taguchi experimental design. Lambiase et al. (2013) reported the effect of the passive water-cooling during diode laser (maximum power 1.055 kW) bending of stainless steel 304. Maji et al. (2014a) generated dome shapes of AISI 304 sheet by using fibre laser having continuous wave. Shen et al. (2014) investigated pulsed laser (wavelength 1.07 μm) bending of the stainless steel under water. Chakraborty et al. (2015a) studied laser forming of stainless steel sheet under coupling mechanism and proposed a scanning strategy for forming of deep pillow shaped surfaces.

2.3.3 Aluminum and aluminum alloys

Chan and Liang (2000a) investigated the deformation behavior of Al6013/SiCp aluminum alloy composite sheet for two types of laser scanning— (1) parallel and (2) transverse to the rolling direction. A larger bend angle was obtained when transverse scanning along rolling direction was performed. Similar result was

obtained by Chan and Liang (2000b) for two aluminum based metal matrix composites (Al2009/20 vol.% SiCw and Al2009/20 vol.% SiCp). (Here, w indicates whiskers and p indicates particles). Labeas (2008) developed a model for the laser bending of aluminum sheets.

2.3.4 Aluminium foam

Quadrini et al. (2010) carried out experiments on laser bending of open-cell foam panels of rectangular specimens of AlSi7Mg with the size of 100 mm × 35 mm × 10 mm with diode laser (940 nm wavelength). They achieved a crack-free bend angle of 50° in 150 scans. This could not be achieved by mechanical bending. A larger bend angle was obtained for low-density foam as compared to for high-density foam. Guglielmotti et al. (2009) have also demonstrated the use of laser to bend aluminium foam sandwich panels.

2.3.5 Nickel alloy

Yau et al. (1998) observed that the bend angle of thin A42 nickel alloy steel sheet increases linearly with increasing number of irradiations. Jamil et al. (2015) studied laser bending of pre-stressed thin-walled nickel micro-tubes. They observed that short pulses with high power laser beams are more effective. There is minimum thinning at the extrudes, which is beneficial for thin-walled micro-tube bending.

2.3.6 Brittle materials

Forming of brittle materials for example, low formability material like aluminum oxide Al_2O_3, borosilicate glass, single and mono crystal silicon and ceramics is a challenging task. It is difficult to deform by using mechanical bending operation with conventional tools and dies that generate crack on the worksheet. However, laser and laser assisted bending have been successfully employed to bend brittle materials. Xu et al. (2013) studied the laser bending mechanism of the silicon sheet. They observed the plastic deformation resulting in the permanent bending of the workpiece. The working temperature crossed the brittle-ductile transition threshold. Wang et al. (2011) reported laser bending of a single-crystal silicon sheet by using Nd:YAG laser. The silicon sheet was prepared in the size of 10 mm × 5 mm

× 0.2 mm. The pulsed laser bending mechanism of thin silicon-sheet was a combination of BM and TGM. For the silicon sheets, a bend angle of up to 6.5° was obtained after six laser passes. Wu et al. (2010b) studied laser bending of three different brittle materials, borosilicate glass and Al_2O_3 ceramic by using continuous wave CO_2 laser irradiation and mono-crystalline silicon by using Nd:YAG pulsed laser irradiation. They observed fracture-free bending of these brittle materials. For mono-crystalline silicon and Al_2O_3 ceramic materials, the bending was towards the laser beam direction (positive bending). On the other hand, for borosilicate glass workpiece, both positive and negative bend angles were obtained. The bend angles increased with increasing the width (along scan direction). A bend angle up to 40° was obtained with multiple scans on the same location. The laser bending of Al_2O_3 ceramic was highly sensitive to processing parameters; however, bend angles of more than 2° could be obtained.

Titanium alloys are extremely difficult to bend due to their brittleness. Gisario et al. (2017) studied laser-assisted bending of titanium Grade-2 sheets. They could obtain sharp bend angles (>140°) with small fillet radii. Gisario et al. (2016) improved springback effect by external force laser-assisted sheet bending of titanium alloys. Some researchers studied the laser bending of titanium (Walczyk et al. 2000; Bartkowiak et al. 2004 and Fan et al. 2005).

2.3.7 Magnesium and magnesium alloys

Chen and Xu (2001) analyzed the effect of scanning speed on the bend angle in magnesium alloy M1A. It was observed that the bend angle initially increases slightly and then decreases with increase in scan speed. At high scan speed, the available heat energy gets reduced. The reduction in heat energy reduces the peak temperature generated at the surface of sheet, which leads to the reduction in temperature gradient along the thickness and consequently the bend angle (Shichun and Jinsong 2001). Kant and Joshi (2016) carried out experimental and finite element method (FEM) simulation studies in the multi-pass laser bending of magnesium M1A alloy sheets.

2.3.8 Plastics

Okamoto et al. (2000) investigated precision laser forming of plastic with Nd:YAG laser by the experimental analysis. Bend angle increases rapidly during cooling process after laser irradiation. The largest bend angle is achieved under a certain energy density. Okamoto et al. (2004) studied deformation behaviour of a plastic (high density polyethylene) in Nd:YAG laser forming. A large amount of bend angle could be achieved due to viscoelastic nature of the plastic.

2.4 Curvilinear Laser Bending Process

In the case of curvilinear laser bending, the laser pass follows curved geometry. Chen et al. (2002) reported laser bending of titanium alloy sheets on the curvilinear profile numerically and experimentally. They found that the bending angle decreased with increasing scan path curvature. Zhang et al. (2009) studied the curved laser irradiation for the ring shaped sheet metal. The result showed a continuous variation of bending process due to the rigid ends-effect. It caused warping of sheet edge. When the spot diameter increased, the warped curvature also increased.

Kant and Joshi (2014) carried out experimentally and numerically the curvilinear laser forming of magnesium alloy M1A workpiece. They studied bend angle, deformation behaviour and edge displacement. The curvilinear and straight laser bending process displayed different deformation behaviours. In curvilinear laser bending process, the bend occurred outside the scanning path curvature. Effect of process parameters on bending offset was studied. It was observed that the bend offset decreases with the increases in laser power and decreases with the decrease in laser beam diameter. Beam diameter was the most effective parameter that influenced the bend offset. They observed less edge effect for the curvilinear laser bending process than that obtained in straight line bending process. However, the edge effect increased with the increase in arc height during curvilinear motion.

Safari and Farzin (2015) investigated experimentally the laser bending of a saddle shape with spiral laser irradiating pattern. The samples were made of mild steel having size of 100 mm × 100 mm × 0.85 mm. Laser bending experiments were studied with a continuous CO_2 laser with the maximum laser power of 150 W. Spiral

irradiating scheme was found to be a suitable method for the production of saddle shapes. It was obtained by different process parameters, *viz.*, pitch of spiral path, number of spiral paths, in-to-out spiral path and reversely out-to-in spiral path. The curvature of saddle shape increased with increasing number of spiral paths.

2.5 Process Parameters in Laser Bending

There are various factors and process parameters which control the laser bending process significantly. Many researchers carried out the result of process parameters on laser bending. These process parameters can be classified into four groups—

1. Laser process parameters: Laser bending process is strongly influenced by laser process parameters because this process is associated with heating by laser. The laser process parameters are laser power, scan speed, laser beam diameter and number of laser passes.
2. Workpiece geometry parameters: The size of the workpiece being formed also plays a key role in the forming process. The most important parameters are length, width and thickness.
3. Material properties parameters: The material properties of workpiece play a key role in the laser forming. The material properties are mechanical and thermal properties as well as absorptivity.
4. External constraint parameters: They include force cooling, external mechanical load and clamps.

The effects of these parameters on laser bending process are presented in the following subsections.

2.5.1 Effect of laser power

In general, laser power has direct relationship with heat flux density. To achieve the maximum laser bend angle, there is an optimum value of laser power. The bend angle is increased with increasing laser power (Chen and Xu, 2001; Shichun and Jinsong, 2001 and Hsieh and Lin, 2004b), but after attaining a certain value, the bend angle decreases when the laser power increases (Lawrence et al. 2001). This bend angle reduction happens due to two reasons. Firstly, the workpiece may melt instead

of plastically deforming due to the application of high laser power (Paunoiu et al. 2008). Secondly, the temperature variation between the top and bottom surfaces of the sheet may reduce due to high laser power (Kant et al. 2013b). Lawrence et al. (2002) suggested that laser bending is not possible at laser power below certain level. It is because of the reversible elastic effect that requires a threshold energy. Vasquez-Ojeda and Ramos-Grez (2009) generated larger bend angles at low laser power by using proper scanning patterns (*viz.*, zig-zag, squared and step) providing spatial modulation of energy.

2.5.2 Effect of scan speed

The scanning speed is one of the key energy controlling parameters in the laser line heating process. Vollertsen and Rodle (1994) reported that the heat input per unit length and the temperature variation between the top and bottom surfaces along the sheet are controlled by scan speed. The heat input per unit length is inversely related to the scan speed. The increase in scanning speed reduces the time of contact between laser beam and sheet surface. This leads to the reduction in peak temperature as well as plastic deformation in the heated region. Due to reduced heat input, the bend angle also gets reduced (Ji and Wu, 1998 and Kyrsanidi et al. 1999). Li and Yao (2000) studied different combinations of laser power and scan speed by keeping peak temperature constant at the top surface of the workpiece. They found 30% decrease in the bend angle when the scanning speed doubled. Hu et al. (2001) studied various combinations of laser scan speed and power with constant energy input. They found larger bend angle due to high temperature gradient and power in fast laser scan.

Chen and Xu (2001) analyzed the effect of scan speed on the bend angle in magnesium alloy M1A and found that the bend angle initially increased slightly and then decreased with increase in scan speed. Bend angle reduction was attributed to decrease of energy per unit time transferred to the metallic worksheet. Barletta et al. (2006) observed increase in bend angle with the increasing scan speed at high laser power due to high temperature gradient. The scan speed has a direct relation with temperature gradient. The temperature gradient increases with scan speed that led to an increased bend angle. The plastic deformation at bottom surface reduced with an increase in the scan speed (Kant and Joshi, 2015).

2.5.3 Effect of laser beam diameter and geometry

The laser beam geometry is one of the important heat flux density controlling parameters. Laser beam geometry represents total spot area and laser beam shape. Circular shaped laser beam is very common. However, other beam shapes like line, circular, rectangular, triangular, star, donut, D-shape, cross, etc. can be used. The heat flux density has been controlled by beam geometry (the ratio of the power to laser beam cross section). The flux density and laser beam diameter have inverse relation. The flux density increases when the laser beam diameter decreases.

Safdar et al. (2007b) analyzed the effect of various beam shapes on continuous wave (CW) laser tube bending by experiments and finite element model. They studied circular, rectangular, triangular, and donut beam geometries. Based on the results, the donut beam seems to provide the least lateral bending but circular laser beam provided higher bending as compared to other laser beam geometries. Mazhukin et al. (2007) studied the effect of variation of the laser pulse shape on temperature distribution for different laser applications. Sheikh and Li (2010) observed that the laser beam shape was beneficial for controlling the temperature distribution, temperature gradients, heating and cooling rates. The geometry of the beam on temperature gradient mechanism dominated process significantly controlled the bend angle, radius of bending edge (radius of curvature) and edge effect (Jamil et al. 2011b). The laser beam diameter is one of the key energy controlling parameters. The temperature variation between top and bottom surface of the workpiece increases with the decrease in the laser beam diameter. The bend angle decreased with increasing laser beam diameter; however, based on buckling mechanism, the laser beam diameter may yield different result (Chen and Xu, 2001 and Kant and Joshi, 2015).

2.5.4 Effects of number of laser passes

Single laser pass line heating produces a bend angle in the order of 0.1°–3°. Thus, repeated laser passes are required to produce large bend angles. Laser bending obtained by applying more than a single-scan is known as multi-scan laser bending process. It used to achieve large bend angle, in the order of 10°. Lawrence et al. (2001) and Edwardson et al. (2010a) observed that the bend angle increases with increasing number of laser of passes. However, there was a reduction in the increment

in bend angle per pass. Similar observation was reported by Wu et al. (2010a) by taking three different thicknesses of 0.1 mm, 0.2 mm and 0.3 mm silicon sheets. The main factors to reduce the increment in bend angle per pass are change in absorptivity, change in sheet thickness, change in laser beam (spot) geometry due to bending and strain hardening. Surface coatings like graphite get damaged and burnt off by repeated irradiations and decrease the bend angle per pass. During multi-pass laser bending process, right choice of process parameters and cooling condition is required for good quality bending result. Otherwise, the workpiece may melt due to the rise in temperature after every laser pass (Edwardson et al. 2010b). Griffiths et al. (2010) reported that absorption and geometrical effects become dominant during more number of passes. On the other hand, Kant and Joshi (2016) carried out experimental and FEM simulation studies in the multi-pass laser bending of magnesium M1A alloy sheets. They investigated that the peak temperature increases but the temperature difference between top and bottom surface decreases with increasing number of laser passes due to insufficient cooling time between two consecutive laser passes.

2.5.5 Effect of workpiece geometry

The geometrical parameters, *viz.*, length, width and thickness of sheet influence the bend angle. The thickness of workpiece is the key geometry parameter as it directly controls the variation of the temperature between top and bottom surface along with thickness. For example, the bending angle is approximately varying inversely to the square of the workpiece thickness (Geiger and Vollertsen, 1993 and Lee and Lin, 2002). The three most relevant process mechanisms are dependent on thickness. The transition of bending mechanism from BM to TGM was observed with varying thickness. The increase in the thickness of the workpiece results in change of buckling mechanism to temperature gradient mechanism. The workpiece thickness also affects the edge effects. Zahrani and Marasi (2013a) reported that the edge effect increase with the increase in the thickness of the workpiece. The sheet length (perpendicular to the scanned path) does not have much effect on the laser bend angle (Shichun and Jinsong, 2001 and Chen et al. 2004a). The predominant factors having large effect on deformation angle of laser bending process were identified by a number of researchers (Hu et al. 2001; Cheng et al. 2006 and Dixit et al. 2015).

Cheng et al. (2005b) studied the size effect on laser forming of low-carbon steel sheet experimentally, numerically and analytically. They observed that the bending angle increased with increasing sheet width (the dimension along the scanning direction) at a constant sheet length (perpendicular to the scanning direction). Shichun and Jinsong (2001), Chen et al. (2004a) and Shi et al. (2011) also reported similar observations.

Chakraborty et al. (2015b) used experiments and finite element (FE) simulations to develop a process that modifies bend angle of mechanically formed stainless steel blanks by using laser. Laser forming was carried out on both concave and convex sides of the mechanically bent specimens. They found that the bending angle is prominently bigger while scanning the laser on the convex side than on the concave side. Furthermore, they observed that the change in bend angle was increased during laser scanning on convex side. In case of concave side, opposite trend was observed. However, with increasing die-punch radius (from 4.5 to 9 mm), change in bend angle increased on the concave side. They explained these effects based on a kinematic hardening model.

2.5.6 The effect of absorptivity on laser bending

The absorptivity of the material plays a vital role in the laser bending process. If absorptivity is increased, energy input into the workpiece surface also gets increased. The high reflective materials result in significant power loss and affect the beam generation mechanism as well as the optical elements due to backscattering. A number of different surface conditions are used to enhance the absorptivity of sheet metal with the surface coating. It is a simple and low-cost method. Table 2.1 summarizes the literature on absorptivity of laser beam.

Table 2.1 Effect of absorptivity on laser bending process.

Reference	Main findings
Chen et al. (1999)	The absorptivity is affected by wavelength of the laser beam. Absorptivity increases with the decrease in the wavelength of the beam.
Lawrence (2002)	The absorptivity of diode laser was more efficient than CO_2 laser due to small wavelength.
Barletta et al, 2006	The bend angle improved by applying suitable coating in the scanning line of the workpiece
Edwardson et al. 2006; Carey et al. 2007	The graphite coating was preferred due to its high absorptivity (60%–80%), high melting point, low cost and simple coating technique.
Edwardson et al. 2007	Absorptivity reduced with number of laser passes.
Chehrghani et al. 2012	Graphite coating under pulsed laser irradiation enhanced absorptivity.
Singh et al. (2013b)	The hydrated lime coating was superior to graphite coating in CO_2 laser bending.
Dutta et al. (2013)	Higher bend angle was obtained for workpiece coated with blank enamel paint. The coating damaged due to heating. Applying coating after each scan produced larger bend angle.
Gautam et al. (2015)	The cement coating was superior to hydrated lime coating.
Dutta et al. (2017)	Graphite black spray paint increased the absorptivity of the sheet in CO_2 laser bending.

2.5.7 Effect of thermal properties

The thermal properties affect the temperature distribution in the workpiece. Both peak temperature and temperature gradient of the material increase with the decrease thermal conductivity. This is due to less heat dissipation in small conductive material (Li and Yao, 2001a and Hu et al. 2002). The thermal conductivity controls

the heat flow in the neighbouring materials. The peak temperature and temperature gradient vary with the thermal conductivity (Bejan and Kraus, 2003). Yanjin et al. (2003) studied the effect of the material properties on laser bend angle. The bend angle is inversely proportional to specific heat capacity, density and thermal conductivity of the material. While it is directly proportional to the coefficient of thermal expansion. Guan et al. (2005) found that the peak temperature increases when thermal conductivity, specific heat capacity and density are reduced. Due to this the plastic deformation and bend angle are increased.

2.5.8 Effect of mechanical properties

The mechanical properties that influence the laser forming process are yield strength, coefficient of thermal expansion, Poisson's ratio and modules of elasticity. The bend angle decreases with the increase in the temperature dependent yield strength because of less plastic deformation (Yanjin et al. 2003 and Guan et al. 2005). The Poisson's ratio and strain hardening do not affect the bending process significantly. With the increase in thermal expansion coefficient, bending angle increases (Vásquez-Ojeda and Ramos-Grez, 2009). The Poisson's ratio governs the thickening of the heated region. With increasing Poisson's ratio thickening increases. Generally, the bend angle decreases with increasing elastic modulus.

2.5.9 Effect of forced cooling

Multi-pass laser irradiation is necessary to achieve the desired value of deformation. Forced cooling is the main condition for an effective and high quality multi-pass laser bending process. In the process, significant reduction in waiting time between successive passes has been achieved (Cheng and Yao, 2001). Forced cooling reduced undesirable effects on microstructure change and other mechanical behaviour.

Lambiase et al. (2013) reported an experimental study on passive water-cooling with partial immersing of a workpiece into the stationary water during laser forming process. They observed that passive water cooling allowed a drastic reduction of the cooling time between consecutive passes and rapidly reduced the temperature, preventing from excessive oxidation and melting of the scanned surface. Kant and

Joshi (2013a) reported that on application of forced cooling there was an increase in the bend angle by using FEM simulations,

Shen et al. (2014) studied experimentally underwater pulsed fibre laser forming of stainless steel 304. The size of the workpiece was 100 mm × 50 mm × 1 mm. The effects of water and air cooling on bending angle were studied. The highest bend angle was achieved when the top surface was kept open keeping the bottom surface immersed in water. In the fully immersed case, the depth of immersion had a profound effect on the heat affected zone (HAZ). There is an optimum depth for minimizing HAZ. In the fully immersed case, the job is protected against surface oxidation and thus a better quality is obtained.

2.5.10 Effect of external load

Laser bending is a non-contact process of bending, in which the heating by a laser beam generates thermal stresses that in turn govern the deformation of the material. The other way is to carry out mechanical bending along with laser heating for localized softening of the material. To distinguish it from laser bending, this method is called laser-assisted bending (Kratky, 2007). It helps to get larger bend angles with a single laser scan, even in the hard materials with a very less amount of ductility (Dearden and Edwardson, 2003 and Roohi et al. 2012). It has many applications in ship building (naval), automobile, aerospace, medical, and microelectronics industries. Bammer et al. (2011) carried out laser-assisted bending of Mg alloys (AZ31, ZE10), Al alloys (7075, Titanal), Ti alloys (Titan grade 2, WL 3.7164), and steels (M85, St 52, Hardox). Up to 12.7-mm-thick sheets of Ti alloy could be successfully bent. There are a number of variants of laser-assisted bending, some of which have been reviewed by Dixit et al. (2015).

In the method adopted by Samm et al. (2009), a transparent sapphire tool was used through which the laser beam was passed, and material was heated just at the contact point of the tool (Fig. 2.3). Kant et al. (2013b) proposed a method by using a mechanical load that moves in a path parallel and synchronous to that of the laser beam (Fig. 2.4). Another way is to preload a cantilever sheet by applying a mechanical load at the free end having the tendency to bend the sheet toward laser beam as shown in Fig. 2.5 (Yanjin et al. 2003). The bend angle is enhanced when the direction of the

load is consistent with the deformation direction in laser bending. The preloading increased the bend angle significantly. Gisario et al. (2011) carried out mechanical V-bending followed by the laser heating post-treatment.

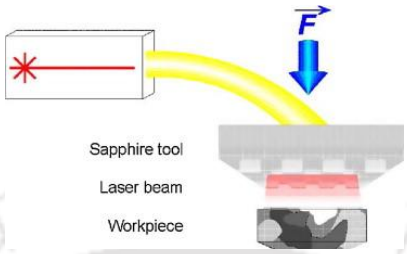

Figure 2.3 A laser assisted bending using transparent sapphire tool. With permission from Shamm et al. (2009). Copyright (2009) Elsevier.

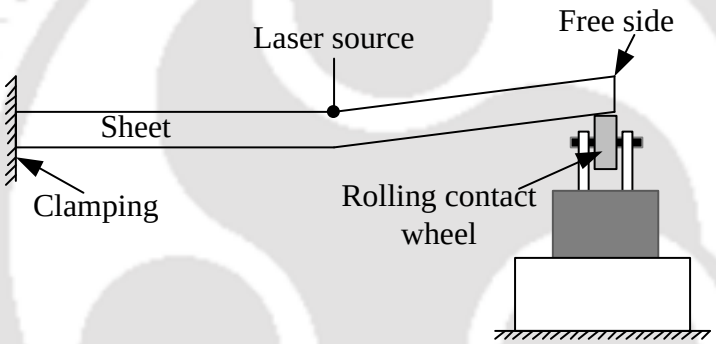

Figure 2.4 A laser assisted bending by moving mechanical load

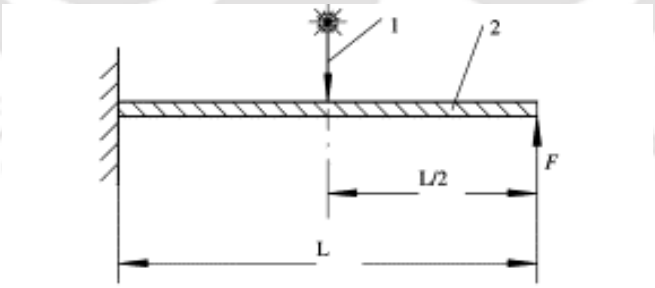

Figure 2.5 Laser assisted bending by applying a load at the free end of a cantilevered sheet. With Permission from Yanjin et al. 2003. Copyright (2003) Elsevier.

Laser assisted bending has been successfully employed to bend brittle materials (Bammer et al. 2011). Laser Origami technique was invented by Mueller et al. (2013) to rapidly form three-dimensional objects by folding a sheet by softening it

at bend lines with the help of a defocused laser beam (Mueller et al. 2013). In the original proposal of LO technique, the bending was accomplished by gravity, but any external force can be applied to accomplish it. Gisario et al. (2016) applied an external-force (pneumatic tool) and local and selective heating by irradiation with a high power diode laser to bend Grade 2 CP titanium and AA 7075 T6 aluminium sheets. They improved the springback effect by using external force laser-assisted sheet bending.

2.5.11 Effects of clamp

The workpiece clamp (fixture) is one of the significant factors to improve the laser bending. The clamping provides a mechanical constraint that can hold the workpiece during laser pass. The clamping reduces the edge effect along scanning direction due to the distribution of stress into the sheet. Clamping technique affect bend angle and edge effect.

Birnbaum et al. (2007) studied the clamping effect on the laser forming process. They carried out experiments in two conditions on a squared sheet with side of 80 mm and 0.89 mm thickness. In one condition, the sheet was clamped in a cantilevered manner as shown in Fig. 2.6 (a) and in other condition, the sheet was simply put on a platform as shown in Fig. 2.6 (b). Both the clamped and free specimens were scanned at distances of 40 mm, 25 mm, and 10 mm from the left edge. For both (clamped and unclamped) cases, the greatest bend angle was achieved when scanning was carried out at 25 mm distance from the left edge and the lowest bend angle was achieved when the scanning was carried out at a distance of 10 mm from the left edge. Except for 10 mm distance case, the bend angles for the clamped sheet were greater than those for the unclamped sheet.

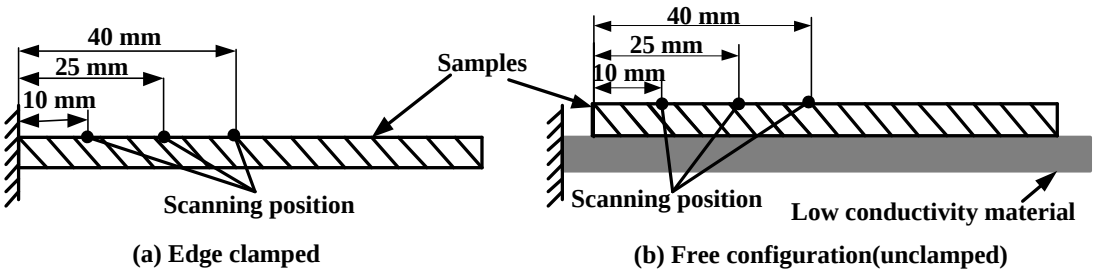

Figure 2.6 Schematic of clamped and unclamped configurations

Kant and Joshi (2012b) carried out numerical simulations to investigate the effect of clamping in laser bending process. They used four different ways to clamp workpiece– sheet clamped at one side completely, sheet clamped at mid-point of the side, sheet clamped at two corners of the side and unclamped sheet. The maximum edge effect was observed for the unclamped case and it was the minimum for clamping the sheet completely at one side. Hu et al. (2013) conducted simulations and experiments for two types of clamping conditions– (1) conventional method in which the sheet was clamped at one edge of the workpiece and (2) clamps where put at the start and end points of laser scan. The edge effect was the minimum for the latter case.

2.6 Edge Effect in Laser Bending Process

Shi et al. (2013) carried out various heating methods for reducing the edge effect using multiple scans. Shi et al. (2016) proposed to reduce edge effect under the action of two unequal concentrated forces. In their method, one force is applied at the right side of the free end and the other force is applied in the left side as shown in Fig. 2.7. With F_1= 10 N and F_2= 2 N, the relative variation in bend angle decreased by about 80% as compared to conventional laser bending. Zahrani and Marasi, (2013b) reported that the edge effect decreased with the increase in the number of laser passes.

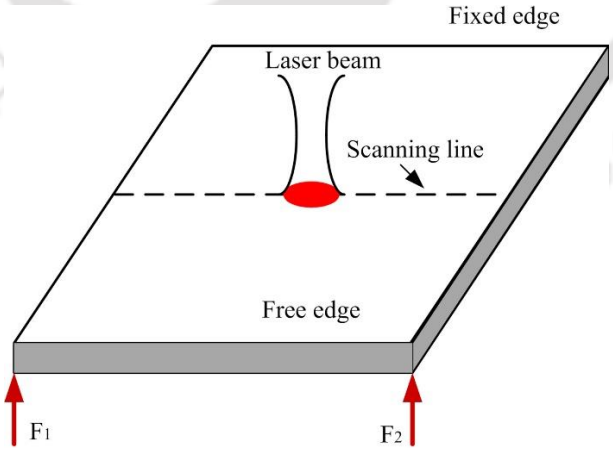

Figure 2.7 A proposed scheme of reducing edge effect by applying two unequal forces at the free end. With permission from Shi et al. (2016). Copyright (2016) Elsevier.

As discussed in Section 2.5.11, Hu et al. (2013) suggested the reduction in the edge effect by proper clamping. The first method was to clamp one edge completely. The second one was clamping both the ends of the scanning line. The maximum temperature distribution along the heating line was calculated by the analytical model. It showed good agreement with the simulation results with reduced edge effects. Numerical simulations and experiments were carried out to validate the model and the strategy.

Zahrani and Marasi (2013a) experimentally studied the relative variation of the bending angle (RBAV) and concave depth of longitudinal distortion (CDLD) in the laser bending process. They investigated the effect of process parameters, *viz.*, laser power, scan speed, laser beam diameter, thickness of workpiece and scan path position from the free edge of the workpiece on RBAV and CDLD. The results showed that increasing laser power, scan speed and thickness of the workpiece led to the reduction of RBAV and CDLD. As the laser beam diameter decreases, both responses reduce. With the increase in number of passes, the RBAV decreased drastically but CDLD increased. As the heating-position from the free edge of the workpiece decreased, the CDLD decreased but there was no effect on RBAV. It was observed that with the increase in scan speed the edge effect decreases.

2.7 Process Modelling of Laser Forming Process

Modelling of laser forming process provides information related to laser forming, which has been investigated for about two decades. The literature review for the modelling of laser forming process is classified into three categories analytical modelling, numerical simulation and soft computing. The literature review of modelling of laser forming are described in the following subsections.

2.7.1 Analytical models on laser bending

Laser forming is used to deform sheets by means of thermal heating by a laser beam. The process is suitable for rapid prototyping and deforming the metal, non-metal, brittle material, etc. The researchers developed various analytical models for better understanding the mechanism of the process for predicting the bend angle,

stress and temperature distribution in the sheet. A brief review of an analytical model of the linear laser bending process is presented in this section.

One of the earliest and simplest models of laser bending was provided by Vollertsen (1994). According to this model, the bend angle varies directly with laser power. It also varies inversely with the scan speed of the laser beam and square of the sheet thickness. This model does not consider the yield strength and elastic modulus of the work material. The analytical expression is given by

$$\alpha_b = \frac{3\alpha_{th} P\eta}{\rho c_p v t^2}, \tag{2.1}$$

where α_b is the bending angle, α_{th} is the coefficient of thermal expansion of the workpiece, P is the laser power, η is the absorptivity, ρ is the density, c_p is the specific heat capacity, v is the scan speed and t is the sheet thickness.

The Vollertsen's model does not include the effect of yield strength of material and Young's modules of material. Yau et al. (1998) included this effect in their model. The bending angle is giving by

$$\alpha_b = \frac{21\alpha_{th} P\eta}{2\rho c_p v t^2} - \frac{36 l_h \sigma_y}{tE}, \tag{2.2}$$

where E is the Young's modulus, σ_y is the yield stress and l_h is the half length of heated zone.

The model of Yau et al. (1998) considers the effect of yield strength and elastic modulus, but it is not suitable for high laser power when the bend angle is nonlinearly related to laser power. Kyrsanidi et al. (2000) considered non-uniform temperature distribution throughout the thickness of the plate, the development of plastic deformation on a certain area of the material and the subsequent distortion at the end of the process due to the developed plastic strains. Their model, although computationally efficient, requires programming and includes iterative steps.

Cheng et al. (2006) have provided a model to predict the bend angle for a plate with varying thickness. They considered that the variation of the bend angle is primarily due to the variation of the heat sink and the variable bending rigidity. The bending angle of the plate at the location with $t(x)$ thickness is

$$\alpha_b = b(1-\mu^2)\varepsilon_{\max}\left(\frac{3f(x)\pi}{2t^2(x)} - \frac{4f^2(x)}{t^3(x)}\right), \tag{2.3}$$

where

$$b = c_1\sqrt{P/v}, \tag{2.4}$$

and

$$f = c_2 P/(vt), \tag{2.5}$$

where c_1 and c_2 are constants dependent on materials properties, t is the thickness of the sheet and μ is the Poisson's ratio. In Eq. (2.3), $\varepsilon_{\max}$ is the maximum plastic strain at the heated surface. It is given by

$$\varepsilon_{\max} = \alpha_{th} T_{\max} - \sigma_y / E, \tag{2.6}$$

where T_{max} is the maximum temperature increase and σ_y is the yield stress.

Shen et al. (2006) developed an analytical model based on the assumption that the plastic deformation occurs only during heating. The plate undergoes only elastic deformation during cooling. The model is valid for both BM and TGM.

Lambiase (2012) developed an equation for the bending angle, by assuming elastic-bending theory. Plastic deformation during heating and cooling phases was not considered. Lambiase used a two-layer model where the heated layer thickness depends on the effective temperature distribution along the sheet thickness. The main process parameters, i.e., scanning speed, laser power and sheet thickness were varied among several levels to evaluate the accuracy of the model. The bend angle is given by

$$\alpha_b = \frac{3\eta P(t-t_h)\alpha_{th}}{\rho v c_p t(t^2 - 3tt_h + 3t_h)}, \tag{2.7}$$

where t and t_h represent sheet thickness and thickness of heated volume, respectively, which is invariably estimated empirically. Lambiase and Ilio (2013) proposed a complex analytical model for predicting the thin sheets deformation.

Shi et al. (2007a) proposed a model to estimate the bend angle in plane axis perpendicular to the laser irradiation path. The material along scanning direction produces thermal expansion during the heating, and the expansion of the top surface is greater than that of the bottom surface. At the cooling phase, the material in the top layer contracts, and then a local shortening of this layer causes bending about the perpendicular axis to the scan direction. The bending angle is given by

$$\alpha_b = \frac{6.92\eta P \alpha_{th} w r^{1/2}}{\pi^{3/2} l^2 t (\rho c_p k v)^{1/2}}, \tag{2.8}$$

where w is width of workpiece, l is length of workpiece and k is thermal conductivity.

Vollertsen et al. (1995) provided an analytical model to estimate bend angle of thin sheets as a function of sheet thickness, laser power, laser scan speed, modulus of elasticity and flow stress. This model estimate the bend angle during BM. The strain near the center of the laser beam is plastic and the strain away from the center of the beam is considered elastic. The model provides bend angle

$$\alpha_b = \left[36 \frac{\alpha_{th} \sigma_y}{c_p \rho E} \frac{\eta P}{v} \frac{1}{t^2} \right]. \tag{2.9}$$

Kraus (1997) proposed a closed–form expression for estimating the bend angle during upsetting mechanism. Kyrsanidi et al. (2000) developed a mathematical model to predict the bend angle in laser forming. Ueda et al. (2005) developed an empirical expression to obtain bend angle based on the measurement of surface temperature. Gollo et al. (2011) proposed a formula based on the relation of laser process parameters including number of laser passes, material properties and thickness of the workpiece to predict bend angle. Lambiase (2012) developed a model on basis of the elastic-bending theory. In general, these models predict high amount of error in the estimation of bend angles. Lambiase and Ilio (2013) proposed a model for predicting the laser bending of thin sheets by incorporating a relatively accurate thermal model. Recently, Eideh et al. (2015) proposed a model of laser bending which works on elastic-plastic bending theory. These recent models provide reasonable prediction in some cases, but contain more than 25% error in some other cases. A detailed review of laser forming systems has been carried out by Dixit et al. (2015).

The review indicates that a large amount of experimental and theoretical research has been performed in the laser bending. The accuracy of the prediction of the bend angles from analytical expressions ranges from about 10 to 50%.

Temperature distribution has great importance for laser bending. Hence, various researchers developed several analytical models to estimate the temperature distribution during laser bending. Woo and Cho (1999) introduced an analytical model to predict transient temperature distribution in a finite thickness plate during laser surface hardening with convection boundary condition at the surfaces of the workpiece. Cheng and Lin (2000a) proposed an analytical model in laser forming to describe the three dimensional temperature field for the finite thickness. The laser beam is considered as a Gaussian profile moving at a constant velocity along the *x*-axis. Shen et al. (2001) proposed an analytical model for laser heating and melting by suggesting a simple temperature profile. The temperature profile before melting as well as after melting is described. Cheng et al. (2005a) proposed an analytical model in laser forming to obtain the temperature distribution over a finite size sheet. The size effect, including variation along length and width of workpiece, on laser-induced deformation was investigated experimentally, numerically, and analytically. Shi et al. (2007b) developed an analytical model for estimating the temperature field during laser forming using convection and radiation boundary conditions. They considered variation of temperature only in thickness direction and used a one-dimensional heat conduction model for estimating the temperature during laser forming. Van Elsen et al. (2007) introduced an analytical model for a uniform moving heat source of any type for use in laser materials processing from the solution of an instantaneous point heat source. In this study, the heat source is considered as the semi-ellipsoidal. Belghazi et al. (2010) proposed an analytical model of transient heat conduction in two-layered material of finite depth, subjected to Gaussian laser beam. Chen et al. (2010) developed an analytical model to estimate the temperature distribution. It works on temperature similarity at different thickness.

Recently, Kumar and Dixit (2017) developed an empirical model to predict the maximum temperature generated during laser bending process. The developed empirical model is given as

$$T_{\text{pred}} = 0.954 \frac{\eta P}{D_t^{0.72} c_p^{1.0372} v^{0.4} D^{1.15} t^{0.1}} + T_a, \quad (2.10)$$

where η is absorptivity, P is laser power , D_t is thermal diffusivity, c_p is specific heat capacity, v is scan speed, D is laser beam diameter, t is thickness and T_a is ambient temperature. Also, they optimized the process parameters, *viz.*, power, scan speed and laser beam diameter for getting prescribed laser bend angle so that production rate is high, energy consumption is less and tensile residual stress is small in magnitude.

2.7.2 Numerical models on laser bending

The numerical simulation is executed in order to enhance the basic knowledge of the laser forming process. Numerical models were developed starting from early 1990s. Notable among them are finite difference method (FDM) and finite element method (FEM) based model to achieve the temperature variation and bend angle (Vollertsen et al. 1993). Ji and Wu (1998) performed FEM simulation of transient temperature field formed in laser bending process. Chen et al. (1999) compared the bending angle predicted by finite element method with experiment. Kyrsanidi et al. (1999) developed a 3D finite element algorithm. The algorithm includes a non-linear transient coupled thermal–structural analysis, the temperature dependency of the thermal and mechanical properties of the material being accounted. This model made the process simulation to produce a sine shape from a flat workpiece. Hu et al. (2001) developed a 3D-FEM simulation system that includes a nonlinear transient indirect coupled thermal-structural analysis accounting for the temperature-dependent thermal and mechanical properties of the materials. The distribution of stress–strain, residual stress, temperature and bending angle were obtained from simulation. Hsieh and Lin (2004a) examined the vibration phenomenon for pulsed laser bending of thin metal sheet. Zhang and Xu (2005b) proposed a finite element model for simulating pulsed laser bending involving melting and solidification using the uncoupled thermal and thermo-mechanical theory. It is assumed that the pulsed laser beam is uniform across the width of the specimen (the *x*-direction). Thus, a 2D thermal-stress model can be applied, which greatly reduces the computational time. Safdar et al. (2007a) applied FEM to investigate the effects of scanning schemes on laser bending process.

Several researchers modelled the laser bending problem using commercially available FEM packages, *viz.*, ABAQUS®, ANSYS®, COMSOL® etc. For example, Holzer et al. (1994) performed the FEM simulation using ABAQUS® for analysing BM. Chen and Xu (2001) applied a 3D-FEM model to simulate the continuous wave laser bending process induced by the temperature gradient mechanism. The nonlinear finite element solver, ABAQUS® has been employed to investigate both the thermal and the mechanical properties of the workpiece. Labeas (2008) developed an ANSYS® based model for simulating the laser bending of aluminium workpiece. The experimental validation of this model in single and multi-pass laser forming has been also performed. Venkadeshwaran et al. (2012) used ANSYS® package to model the laser bending of stainless steel sheets. The experimental validation of this model was not carried out. Edwardson et al. (2010a) studied empirical data and numerical simulation by use of COMSOL® MultiPhysics of the multi-pass laser bending of sheet mild steel, Ti-6Al-4V and AA5251 by CO_2 laser. Pitz et al. (2010) carried out simulation of the laser forming with moving mesh in COMSOL package. The laser irradiated portion was fine meshed and the outer parts were coarse meshed. The fine mesh moved synchronously with the laser beam.

Yilbas and Akhtar (2014) used commercially available ABAQUS® FEM package for predicting temperature and residual stress. Also, the morphological and metallurgical changes in the heated regions were examined. It was found that the ferritic–pearlitic microstructures were transformed to martensite because of the high cooling rates.

FEM models give good predictions; however, the computational time is large for every simulation. To resolve this problem, various efforts have been employed for reducing the computational time. Proper mesh refinement and time-increment is crucial for obtaining the accurate results within reasonable computational time. Yu et al. (2001) proposed a finite element model and adopted rezoning technique to reduce the simulation time significantly. The effects of the mesh size refinement on temperature distribution and final distortion are studied. Zhang et al. (2002) developed 3D finite element thermo-mechanical model to validate pulsed laser bending. They developed an efficient method for reducing the total computational time significantly.

In their method, initially the transverse strains are calculated based on a few pulses. These are imposed on the whole plate as an initial condition. Zhang et al. (2004) developed FEA models to establish minimum spatial and temporal requirements for discretization and mesh density on angular distortion to reduce the computational time for modeling the laser forming. They suggested that the temporal discretization required at least four time-increments while moving a distance equal to laser beam radius and the spatial discretization required at least two elements in a beam radius and 3 elements in the thickness direction.

Pitz et al. (2010) developed a new efficient method for large workpiece. They introduced a concept of moving mesh that saved the computational time significantly. The mesh nearer to the laser position was fine meshed and the remaining part was coarse meshed. The mesh kept on moving with the laser beam.

Hu et al. (2012) proposed a simple, robust and accurate modeling method of laser bending by using multi-layered shell elements. In their model, the workpiece was divided into three zones, heating zone, diffusion zone and cooling constraint zone. The temperature gradient of heating zone was steep but the other two zones were nearly equal to zero under temperature gradient mechanism. It used different element sizes in various zones. Three different models, *viz.*, solid, solid-shell and multilayered shell were used. The simulation efficiency of the solid-shell and multi-layered shell models improved greatly as a result of the reduced nodes and elements. For solid-shell the total number of the nodes decreased by 26.34% and elements by 20%. For multilayered shell model the total number of the nodes decreased by 70.24% and elements by 66.67%.

A method to enhance computational speed with accelerated cooling strategy was proposed by Eideh (2014). The convective heat transfer coefficient was taken as 10 $W/m^2.K$ during heating phase, and it was taken as 1,000 $W/m^2.K$ during cooling phase. The maximum temperatures of the workpiece are same during conventional and forced cooling cases. Both the cases (force cooling and natural cooling) predicted almost the same bend angle, but the computational time drastically reduced for accelerated cooling case. This model was able to predict with good accuracy and was appropriate for the simulation of large workpiece.

2.7.3 Soft computing models

Soft computing refers to the use of self-learning methods such as neural network, approximate reasoning methods such as fuzzy set theory and evolutionary optimization techniques such as genetic algorithms. There have been numerous efforts related to using artificial neural networks (ANN) for laser bending. Dragos et al. (2000) proposed the use of ANN for predicting bend angles in laser bending using experimental data. Cheng et al. (2000b) also presented three supervised learning methods using neural network for the prediction of bend angle in laser bending. A feed-forward back-propagation multilayer perceptron (MLP) neural network was used in two ways—one using hyperbolic tangent activation function and one using logistic transfer function, and the third was a radial basis function (RBF) neural network. The best performance was obtained using an RBF neural network. A feed-forward MLP ANN model with back propagation for laser bending was presented by Casalino et al. (2002). The number of hidden layer neurons varied from 6 to 20 in an iterative process. Barletta et al. (2009) carried out a comparative study of various neural network models of a hybrid forming (mechanical bending along with laser scanning to reduce springback) using RBF, generalized feed forward (GFF), and MLP. Out of these, MLP provided the best performance. Maji et al. (2013) used neural network to predict the bend angles and carried out inverse analysis for laser forming. Similar work was carried out for pulsed laser forming by Maji et al. (2014a) and laser forming on a dome-shaped surface by Maji et al. (2014b). Palani et al. (2015) proposed the use of ANN for parametric investigation in laser forming and predicted bend angles by using experiment data. Experiments were conducted for the laser bending of FE-410 steel sheets of 100 × 50 × 8 mm^3 size using CO_2 laser. During parametric study, laser power varied from 2–3 kW in step size of 250 W, scan speed varied from 0.6–1.2 m/min in step size of 0.3 m/min, laser beam diameter varied from 9–13 mm in step size of 2 mm and laser passes varied from 1–210. The measurements were taken after every 10 passes. The proposed artificial neural network model provided good prediction accuracy. Kant et al. (2015) used an integrated FEM-ANN method for predicting bend angles as a function of beam diameter, power, and scanning speed that was verified using experimental data. Optimization of multi-pass laser bending

by means of soft computing techniques was carried out by Lambiase et al. (2015). A set of experimental tests were performed on thin AISI 304 stainless steel sheet. An ANN model was fitted that was used in the optimization.

In all the aforementioned works, the training and testing data were divided on a random basis. In the work presented by Dragos et al. (2000), the bulk of the experimental data were divided into two halves each for training and testing. Barletta et al. (2009) divided the whole data into 60 % training, 15% cross-validation, and 25% testing data. In all the works presented by Maji et al. (2013, 2014a, 2014b), 1000 data were divided into two subsets of equal size at random. One subset was used for training and testing the ANN, whereas the other subset was used for validation. The training and testing data were interchanged to ensure the participation of both data in the training. Out of 1000 data, some data were experimental and the remaining data were generated by a regression model. The number of experimental data was 129 in Maji et al. (2013); 45 in Maji et al. (2014a), and 75 in Maji et al. (2014b).

Pérez et al. (2010) used an adaptive neuro-fuzzy inference system(ANFIS) model for laser surface heat treatment to predict the maximum surface temperature of the workpiece at a particular sampling time from the input parameters— laser beam power and the temperature from the previous sampling time. MATLAB was used to develop the model. Jovic et al. (2017) used an adaptive neuro-fuzzy inference system (ANFIS) model in order to select the most dominant factors for the bending and thickening prediction of the shaped surface.

Cheng and Yao (2004) determined the optimal values of diverse process parameters for laser forming process based on genetic algorithm (GA) to generate a desired shape. The control parameters, *viz.*, laser power, laser scan speed and width (along scan line) and type of fitness function have significant effects on GA results. The number of decision variables was close to 30; however, it took a large number of generations to achieve convergence. It showed that the algorithm control parameters and the fitness function type have significant effects on the GA synthesis results. The proper selection of fitness function is important for balancing among competing objectives, such as forming time, geometric accuracy and energy consumption. Du et al. (2010) improved the accuracy of bend angle prediction by improving back-

propagation network (BPN) based on the Double Chains Quantum Genetic Algorithm (DCQGA). The BPN-DCQGA network was trained and verified through the sample experimental data. This proposed network enhanced the rate of convergence and obtained higher training efficiency. Maji et al. (2013a) conducted laser bending process by use of both genetic-neural network (GA-NN) and genetic adaptive neuro-fuzzy inference system (GA-ANFIS) based on experimental data. During the analysis, laser power, scan speed, spot diameter, scan position and number of scans were taken as inputs and bend angle as the output. They concluded that GA-NN approach was better than the GA-ANFIS approach in predicting the bend angle, while the predictions using inverse analysis were comparable in both the approaches.

2.7.4 Inverse modelling

The inverse modelling is useful for finding out certain properties of laser beam, workpiece materials and laser-workpiece interaction parameters. Specific attempts have been reported in inverse modelling. Recently, several researchers have used inverse heat conduction analysis for the estimation of mechanical and thermal properties, heat flux and boundary condition.

Romer and Maijer (2000) calculated the power density profile of the laser beam by inverse analysis. Kim and Oh (2001) used an inverse heat transfer formulation using a 2D finite element model to evaluate the heat transfer coefficient during heat treatment. Rouquett et al. (2007) estimated the parameter of Gaussian heat source by the Levenberg-Marquardt method in an electron beam welding. Yang et al. (2007) applied a conjugate gradient method for inverse analysis in laser machining. They estimated the time dependent laser heat flux and melted depth during laser processing based on the temperature measurement by inverse methodology. Woodfield et al. (2007) developed a method to determine the thermal diffusivity of a solid using analytical inverse solution for unsteady one-dimensional heat conduction based on temperature measurements at two points and the semi-infinite boundary condition.

Shidfar et al. (2012) estimated the pulse parameter of a time-exponentially varying laser pulse to obtain temperature at the material surface by using conjugate gradient method (CGM). Mishra and Dixit (2013) determined absorptivity, thermal

diffusivity and laser beam diameter by inverse heat conduction method. They measured the temperature at one location at the centre of the workpiece from bottom side at different time interval and thermal properties were estimated using this measured temperature. Eideh and Dixit (2013) used an inverse estimation by measuring the temperature at two locations based on heuristic methods. The objective was to minimize the combined error between predicted and measured temperatures at two locations. Xu et al. (2013) estimated absorptivity of the workpiece based on a combine approach of experimental and simulation results. Maji et al. (2013) used the response surface methodology to model and optimize the pulse laser bending process.

2.8 Process Optimization of Laser Forming Process

A number of researchers have studied the effect of process parameters on bend angle and acquired optimum process parameter combinations. Design of experiment is a well-known method to determine the relationship between factors affecting a process and the output of that process. Cheng et al. (2000b) used neural network for prediction of bend angle of sheet metal. They developed regression model for bend angle in terms of line energy and volume energy. Liu and Yao (2002) used response surface method as an optimization tool for determining a set of parameters for a prescribed shape of sheet metal. Gollo et al. (2011) and Maji et al. (2013) used Taguchi experimental design method to pin point the parameters, which significantly affect the laser bending process. The factors in descending order of influence on bending angle are number of laser pass, sheet thickness, scan velocity, beam diameter and material parameter. The other less influential factors are laser power and pulse duration in the chosen range. A regression equation for bend angle was derived. Akinlabi et al. (2015) used L27 orthogonal array design to study the parametric effect on laser bending. The percentage contribution of parameters was as follows— number of laser pass: 32%, scan speed: 27%, laser power: 21%, beam diameter: 18% and cooling effect: 2%. Das and Biswas (2015) reported the effect of operating parameters on mild steel plate bending by laser line heating. They developed the design of experiment by using L-16 orthogonal array. The percentage contribution of parameters on bending angle revealed that the number of passes is the most

influencing parameter in achieving good results followed by sheet thickness, laser power and scan speed. Roohi et al. (2015) studied the effects of foam sheets geometrical parameters on bending angle by fixing laser parameter (power P=210 W, scan speed v= 800 mm/min and laser beam (spot) diameter d= 5 mm). The foam sheets' geometrical parameters are relative density, mean cell size and sheet thickness. They carried out a set of 27 numerical simulations based on the full factorial design of experiments. The bending angle decreased with increase of relative density, mean cell size and sheet thickness. The bend angle decreased by 70.9%, 61.7% and 12.3%, when relative density increased by 40%, sheet thickness by 100% and mean cell size by 66.6%, respectively. Recently, Kumar and Dixit (2017) have carried out a multi-objective optimization of single pass laser bending. A fuzzy set based methodology was used to tackle multi-objectivity.

2.9 Effect of Laser Forming on Mechanical and Microstructural Properties

The effect of laser forming on the mechanical and microstructural properties of a material must be understood to manufacture serviceable components. During laser scanning, high surface temperature and localized deformation occurs in the heated region. The material in the vicinity of laser scan line undergoes strain hardening, dynamic recrystallization and phase transformation. This changes mechanical and microstructural properties of the heated region. Researchers studied mechanical and microstructural changes on workpiece due to laser process parameters.

2.9.1 Effect of laser forming on microstructural properties

Many studies about the microstructure of the workpiece during laser forming have been published. Cheng and Yao (2002) analysed microstructure integrated modelling of multi-scan laser forming of low carbon steel. The effect of microstructure changes on the flow stress was studied. Fan et al. (2007) investigated the effect of phase transformations on mechanical behaviour of AISI 1010 steel in laser bending. The boundary of the HAZ is clearly observed. They observed that the

refined grains in the HAZ are much smaller than in the base material due to high cooling rate.

Cheng et al. (2007) investigated feasibility of a hybrid forming technique based on laser dynamic forming (LDF). It is a new hybrid forming process that combines the advantages of laser shock peening and metal forming process, with an ultra-high strain rate forming utilizing laser shock waves. After the forming process, the microstructure of the formed copper foils was characterized. The microstructure changes were characterized quantitatively with electron backscatter diffraction (EBSD) techniques. The effects of initial grain size and the assisted heating on the microstructure changes after LDF were investigated.

Liu et al. (2011) studied the effect of laser scanning path on microstructures of laser solid formed nickel-base super-alloy Inconel 718. They used two different laser beam scanning paths, i.e. single direction raster scanning (SDRS) and cross direction raster scanning (CDRS) respectively, by using same laser solid forming (LSF) processing parameters. The grain size of the recrystallized SDRS sample was not as uniform as that of the recrystallized CDRS sample. After heat treatment, recrystallization occurred and grains of both samples refined. The grains of the CDRS sample were finer than the SDRS sample.

Singh et al. (2013a) carried out the microstructure study for multi-scan laser bending of mild steel. After laser bending, the average grain size gradually increased from the top to the bottom surface along the thickness direction. Fine grains were observed on and near the scanning surface due to higher temperature at the top surface of the workpiece. Palani et al. (2015) studied microstructure for CO_2 laser formed steel sheets. Microstructure analysis of the deformed region and the heat affected zone of FE-410 plate was done. It showed the bainite formation in the irradiated region and grain coarsening in the heat affected region in comparison to unaffected region. The microhardness reduced in the irradiated part as well as in the heat affected region.

2.9.2 Effect of laser forming on mechanical properties

Literature reveals various attempts on the study of mechanical properties after laser forming. Laser bending process generates compressive and tensile strains, residual stresses and hardening in the scanning region, which affect the mechanical

properties like tensile strength, fatigue strength, hardness and ductility of material. Laser irradiation induces hardness changes in the workpiece, i.e., it creates the difference between the hardness values of the base material and the laser bent workpiece. Merklein et al. (2001) observed that the hardness of AA1050 increased with the number of laser pass. The work hardening was not uniform due to dislocation density, temperature and relevant stress or strain material. Thomson and Pridham (2001) reported material property changes associated with laser forming of mild steel components. Laser forming increased the yield strength of the material locally in the formed sections.

Majumdar et al. (2004) reported laser bending of AISI 304 stainless steel with 2 kW continuous wave CO_2 laser. The microhardness of the laser-irradiated zone (bend zone) was increased by 1.5 to 2 times as compared to the base material due to grain refinement associated with rapid quenching during laser bending. McGrath and Hughes (2007) studied fatigue performance of laser-formed high-strength low-alloy (HSLA) steel plate after laser scanning by using a 5 kW continuous wave CO_2 laser. The endurance limit of the laser formed workpiece was increased.

Shen and Yao (2009) investigated mechanical properties after laser forming of low carbon steel workpiece. The tensile strength and yield strength were enhanced after laser forming, while the percentage elongation was reduced. The fatigue life of low carbon steel improved after laser forming. Singh et al. (2013a) carried out laser forming of mild steel workpiece and found that the hardness of laser formed workpiece increased with laser power because of higher peak temperature.

2.10 Major Gaps in the Literature

The information gathered from the review of the published literature reveals a few research gaps and possibilities remain for further investigation. The gaps found from the literature are summarized as follows:

- Although the effect of workpiece geometry on bend angle was investigated, no work has been reported till date for laser bending of small sized workpiece by using stationery and movable laser heat source.

- For accurate numerical simulation temperature-dependant material properties are required. For a particular material, it is difficult to get temperature dependant material properties from literatures. Hence, there is a need to develop a method for inversely obtaining the material properties.
- There is no research paper on laser bending of welded sheets.
- Only a few researchers have developed artificial neural network (ANN) model of laser assisted bending for predicting bend angle, parameter study and inverse estimation of laser bending.
- Only a limited number of studies are available on microstructure and grain size refinement after laser pass.
- The absorptivity of the material plays a vital role in the laser bending process. The high reflective materials result in significant power loss and affect the beam generation mechanism as well as the optical elements due to backscattering. The absorptivity of sheet metal can be enhanced by using surface coating (black colour, graphite, cement coated, etc.) and surface roughening. Each method has its own pros and cons. On one hand, the surface coating is a simple and low cost method. On the other hand, there are problems of coating getting removed during laser scanning, impregnation of coating along grain boundaries of the base material and environmental hazard due to vaporization of the paint. No researcher has studied the effect of surface roughening on absorptivity during laser forming.
- The single laser scan produces a small bend angle (less than 3°). However, in many life applications, large bend angles (>10°) are needed with reduced cost and hence in less number of laser passes. It was also reported that the bend angle was not uniform along the scanning path along the width of the workpiece during laser assisted bending. This is undesirable in most of the applications.
- Laser assisted bending has successfully used a sapphire die transparent to solid-state, movable (roller) mechanical load that moves synchronously with a scanning laser beam and applied load at the free end of cantilever. All these methods use the contacts of mechanical load with the sheet. There is hardly any research on non-contact laser assisted bending.

2.11 Scope and Objectives of the Present Thesis

Based on the literature survey, the following objectives are decided:

1. **Experimental and numerical investigation on small size workpiece**

   The first objective of the present thesis is to investigate the effect of workpiece size on bending angle by using stationery and moving laser heat sources of different laser powers and laser beam diameters. The stationary heat source supplies the continuous heat for a fixed period. For both stationary and moving heat source, same heating duration needs to be considered for proper comparison.

2. **Experimental and numerical investigation on single and multi-pass laser bending of strips**

   Experimental and numerical study on single and multi-pass laser bending of strips are carried out to evaluate the bending angle. The motivation is to produce large and uniform bend angle along the scanning line using multi-pass laser irradiation. The emphasis is on studying mechanical and microstructural properties apart from the bend angle.

3. **Experimental study and FEM simulation on laser bending of friction stir welded sheet**

   Both laser bending and friction stir welding have many applications in aerospace, automotive, shipbuilding and material processing industries. Experimental study and FEM simulation investigation are planned for laser bending of friction stir welded sheet. FEM simulation requires temperature-dependent mechanical and thermal properties. Hence, an inverse method for the estimation of properties is also the need of the hour.

4. **Experimental investigation on laser bending of friction stir processed and cement coated sheets**

   To enhance the absorptivity of sheet metal, another objective of this work is to study the performance of laser bending with surface roughening.

5. **Experimental and numerical investigation on laser assisted bending by mechanical and magnetic loads**

   In order to get enhanced bend angle, the last objective is to study the laser assisted bending. Two methods are planned— (1) direct mechanical load and (2) magnetic load.

The flow chart showing the research plan is presented in Fig. 2.8.

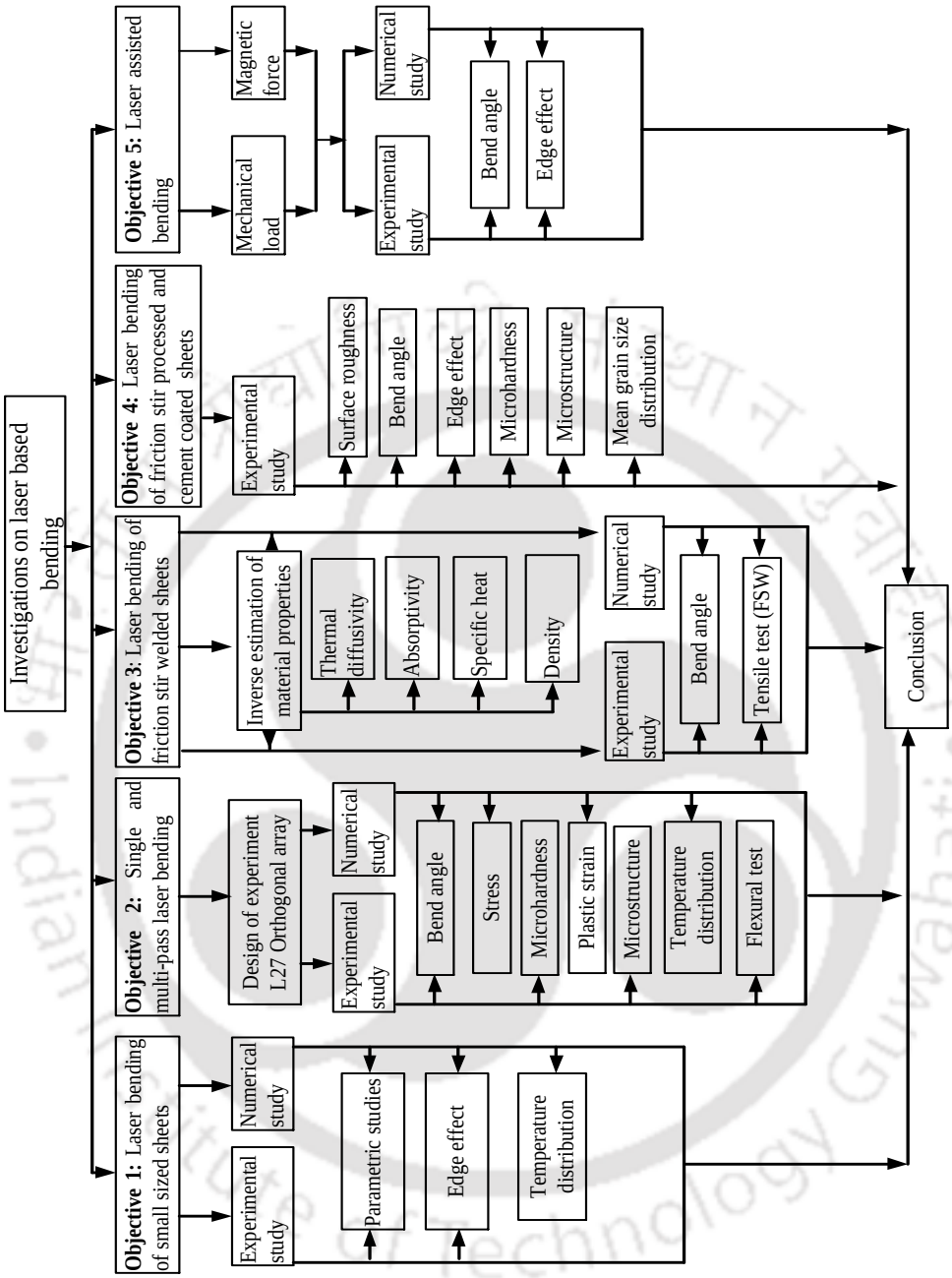

Figure 2.8 Flow chart of research plan

Chapter 3

Details of Experimental and Simulation Procedures

3.1 Introduction

This chapter discusses the experimental setup and equipment used for experimental work (laser bending) as well as its modelling by finite element method (FEM). Details of the experimental setup, working procedure and methods, workpiece geometries, laser parameters, type of working material and heating condition (stationary and moving heat source) are discussed. The experimental work is validated by using FEM model. This chapter discusses the methodology of FEM simulations. It also discusses how the mesh sensitivity analysis was carried out and how an optimum mesh was selected in the models of various types of experiments. The chapter only focuses on methodology; the research findings are reported in the subsequent chapters.

3.2 Chemical Compositions of the Materials

In this work, three work materials were studied— aluminum alloy 5052-H32, ship building mild steel AH36 and stainless SUS304. Tool material for friction stir welding (FSW) and friction stir processing (FSP) was H13 high speed steel. The chemical compositions of aluminum alloy (5052-H32), mild steel (AH36) and tool material (H13) were obtained by energy dispersive X-Ray spectroscopy (EDS). After tensile test of a few friction stir welded (FSW) samples, fracture test was performed by field emission scanning electron microscopy (FESEM). The properties of stainless steel were taken from the literature.

3.2.1 Field Emission Scanning Electron Microscopy (FESEM) and Energy Dispersive X-Ray Spectroscopy (EDS)

Scanning electron microscopy (SEM) is used for high-resolution imaging of surfaces to get higher magnification and greater depth of field than that obtainable by

optical microscopy. The electrons interact with atoms of the specimens to produce various signals that contain information about the surface topography, morphology and compositions. For high resolution and high magnification imaging a cold field emission (FE) gun provides the best results. Field emission scanning electron microscopy (FESEM) gun emits the electron from a much smaller area than SEM, helping to get better magnification, resolution and image quality. In FESEM (Make: Zeiss, Model: Sigma), high resolution imaging can be performed with cold emission in contrast to thermionic emission in SEM. After tensile testing of a few friction stir welded (FSW) samples, fractural tests were performed by using FESEM. Figure 3.1 shows the photograph of FESEM machine. The detailed results are discussed in Section 6.4.1 of Chapter 6.

FESEM machine is equipped with EDS to detect the presence of various phase at different positions by using elemental mapping and line scanning methods. In FESEM, samples of size 10 mm × 10 mm × 2 mm were prepared. In case of electrically conducting sample, FESEM measurements have to be carried out without any coating. The important specifications of the FESEM are given in Appendix A.

Figure 3.1 Field emission scanning electron microscope

The chemical compositions of aluminum alloy (5052-H32), mild steel (AH36), HSS and stainless steel (SUS304) in weight percentage were obtained from the EDS as shown in Fig. 3.2. The composition of aluminum alloy in weight percentage was Al-97.0%, Mg-2.5%, Cr-0.2%, Mn-0.1% and Cu-0.2% and that of mild steel was Fe-98.2%, Mn-1%, Si-0.3%, Cu-0.3% and C-0.2%. EDS of tool material HSS (H13) was also carried out. Its chemical composition, in weight percentage, was Fe-76%, W-18%, Cr-4%, V-1%, C-0.8% and Co-0.2%. The chemical composition of stainless steel (SUS304) was Fe-70.8%, C-0.07%, Si-1%, Mn-2%, P-0.045%, S-0.03%, Ni-8.15%, Cr-18.7%.

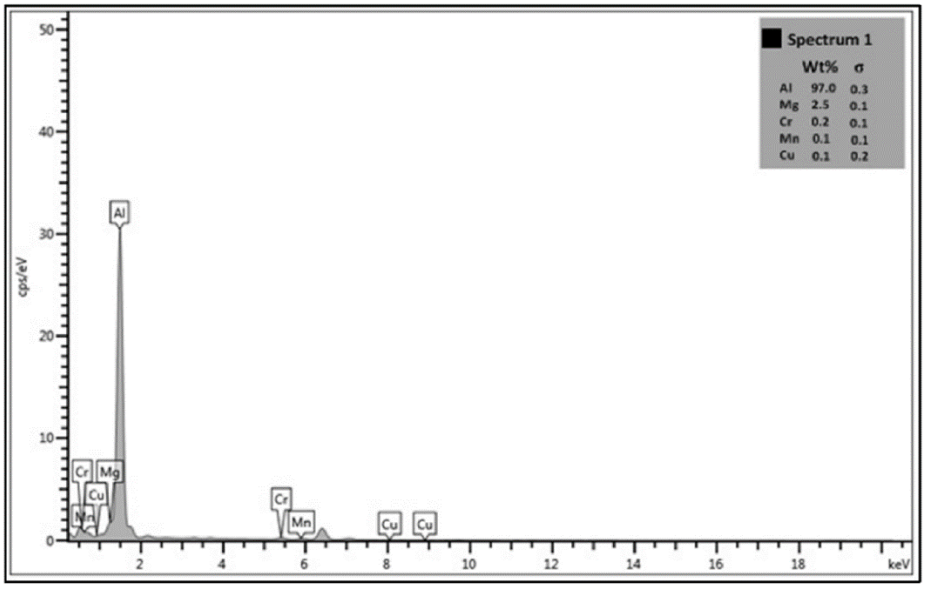

(a)

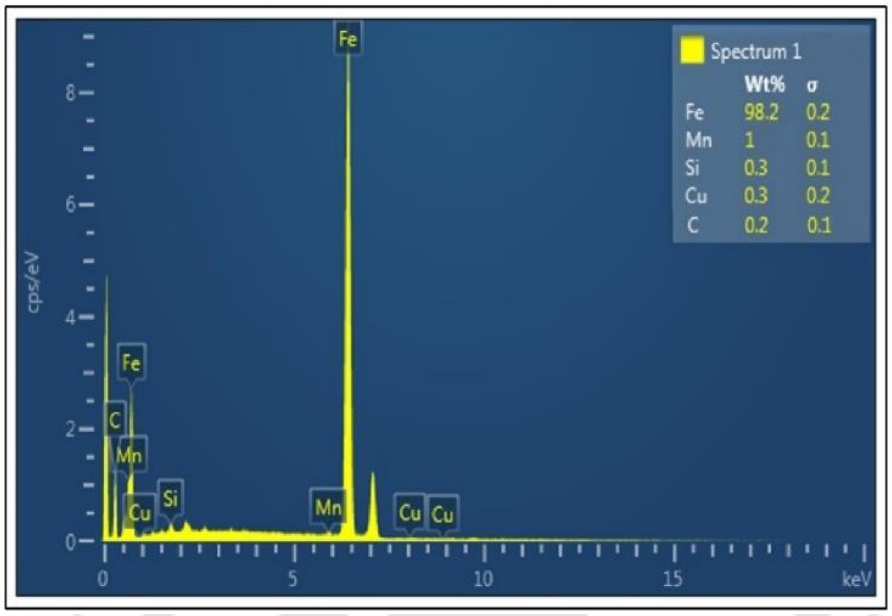

(b)

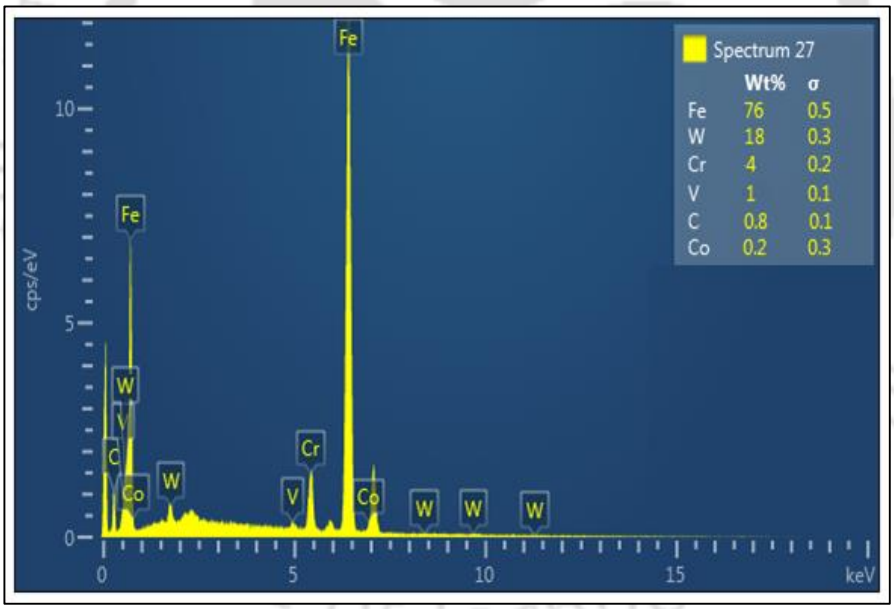

(c)

Figure 3.2 Energy dispersive X-ray spectrum of (a) aluminum alloy 5052-H32 (b) mild steel (AH36) and (c) HSS (H13)

3.3 Experimental Study on Laser Machine and other Instruments

For laser bending, CO_2 laser machine was used for experimental work. During experimental work, the temperature of laser irradiated workpiece was recorded by using thermocouples and pyrometers at the bottom side of the workpiece. The bend

angle was measured by a Coordinate Measuring Machine (CMM). Some details are provided in the following subsections.

3.3.1 CO_2 laser machine

A CNC controlled 2.5 kW continuous wave (CW) mode CO_2 laser (Make: LVD, Model: Orion 3015) was used to perform laser-based bending of different samples. The cutting head moves along Y-axis and work table moves along X-axis to define irradiation path. The laser beam travels along Z-direction. The gases used for laser beam generation are helium (He), nitrogen (N_2) and carbon dioxide (CO_2) with a composition of 60%, 35% and 5%, respectively. Nitrogen is used as exciting medium that transfers energy to carbon dioxide, helium is used for cooling the gases and carbon dioxide gas is used for laser production by lasing action. Figure 3.3 shows the photograph of the laser machine. The important specifications of the laser machine are given in Appendix B.

Figure 3.3 Orion 3015 2.5 kW CO_2 laser machine

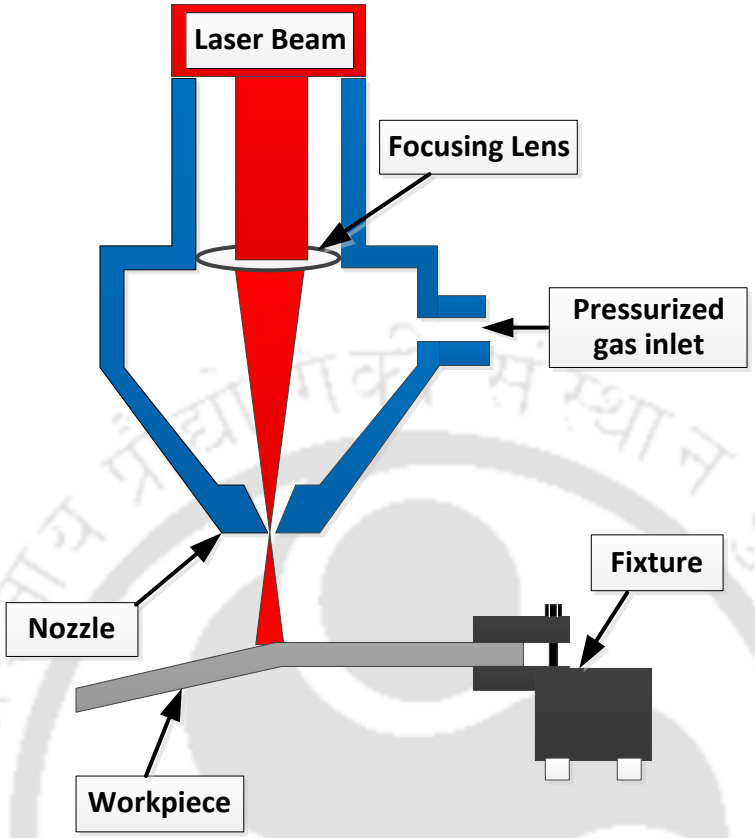

(b)

Figure 3.3 Orion 3015 2.5 kW CO_2 laser machine: (a) Photograph and (b) Schematic diagram of CO_2 laser bending process

3.3.2. Sample preparation

To carry out the laser bending operations, samples were mechanically straightened before lasers bending. This was accomplished by placing the samples between two flat platens and applying the pressure. Sample sizes were different for different experiments. The workpiece surfaces were polished by emery paper and cleaned by acetone to remove wax, oil or dusts. In order to enhance absorption of laser irradiation, three types of coatings were used, *viz.*, lime, cement and graphite. After coating the samples were dried for one day. Some preliminary experiments were conducted in order to determine the process parameters and their ranges that caused bending without melting. Laser parameters (laser power, scan speed and laser spot beam diameter) and geometric parameters (length, width and thickness) used for different experiments are listed in Table 3.1.

Table 3.1 Laser and material parameters for different experiments

Operation	Material	Sample size			Laser parameters		
		Length (mm)	Width (mm)	Thickness (mm)	Laser power (W)	Scan speed (mm/min)	Laser spot diameter (mm)
Lase bending of small sized plates	Mild steel (AH36)	15, 25	10, 20	2	100, 150, 200, 225, 250	1200	4, 8
Laser assisted bending by mechanical load	Aluminum alloy (5052-H32)	100	50	2	500, 600, 700, 800, 900	400, 500, 600	7.76
Laser bending of friction stir welded sheets	Aluminum alloy (5052-H32)	60	60	2	800	800	7.76
Laser bending of strips	Mild steel (AH36)	200	20, 30, 40	1, 1.5, 2	500, 600, 700	800, 900, 1000	7.76, 9.4, 11.4
Laser bending of friction stir processed sheets	Aluminum alloy (5052-H32), Mild steel (AH36)	200	120	2	1000	1000	9.4
Laser assisted bending by magnetic force	Stainless steel (SUS304), Mild steel (AH36)	200	120	2	1000	700, 800, 900, 1000, 1100	7.6

3.3.3 Temperature measuring instrument

Thermocouple and pyrometers were used to measure experimental temperature from the bottom side of the workpiece at different laser process parameters. K-type thermocouple was used to measure the temperature from mild steel (AH36) and stainless steel sample at the bottom side. Figure 3.4 shows that the thermocouple was fixed at the bottom of the workpiece by the thermocouple attachment unit (Dina-Weld TAU 100). The thermocouple wire end was connected to the Agilent Data Acquisition System (Model: 349701A LXI Data Acquisition System). The data Acquisition System was connected to computer where the data were stored in Agilent Bench Link Data Logger Software.

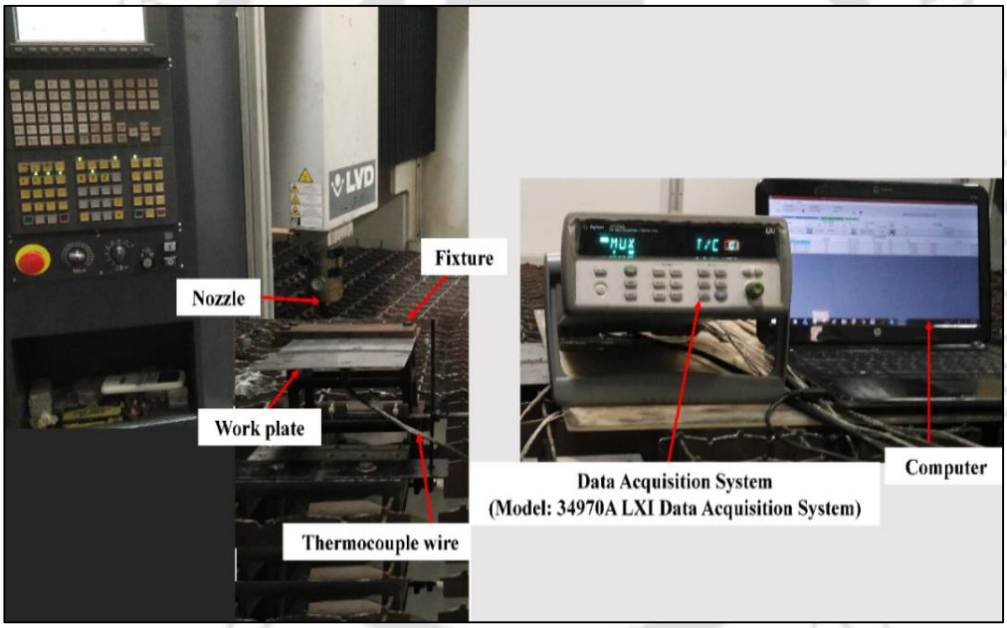

Figure 3.4 Experimental setup for measuring temperature from bottom side of the workpiece by using thermocouple

Similarly, pyrometers were used to measure temperature of aluminum alloy (5052-H32) at the bottom side of the workpiece. The experimental set up was fitted on the laser bed that was designed to hold two sensors (pyrometers) as shown in Fig. 3.5. This setup could hold two pyrometers at a time to measure the temperature at various positions at the back of the workpiece. The temperature of the workpiece was recorded continuously for each millisecond using the Datatemp@multidrop rev.4.6.2 software.

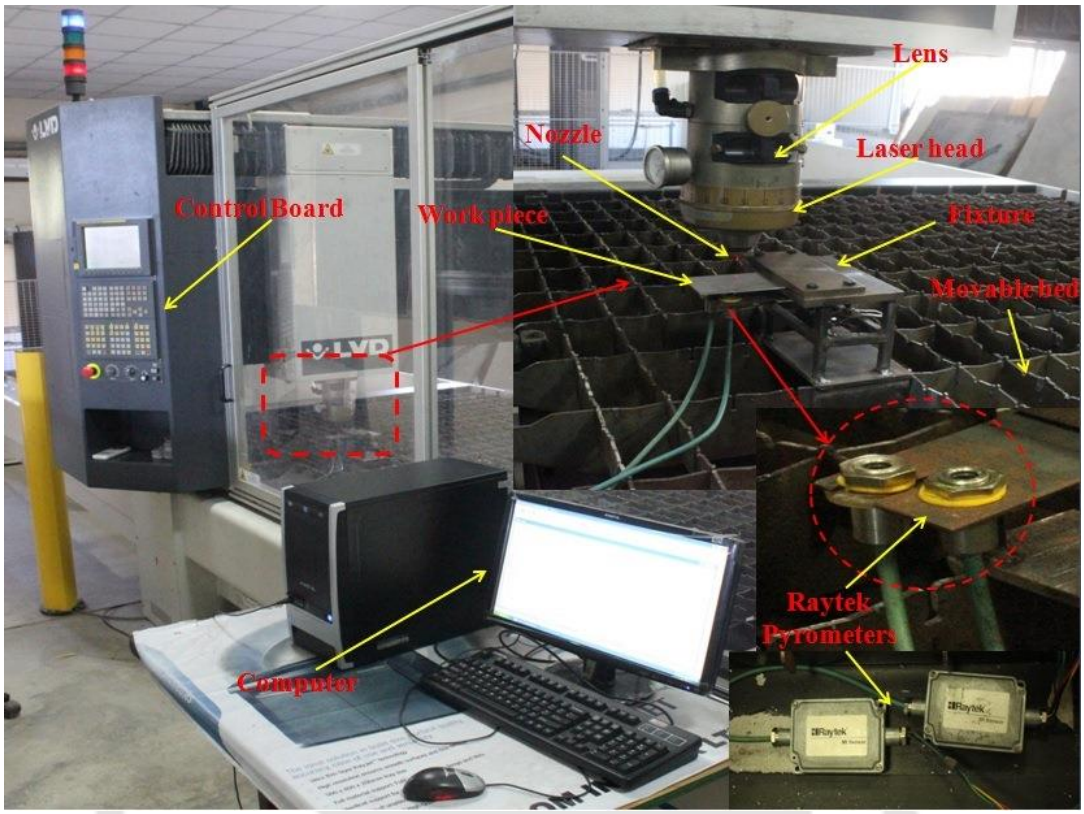

Figure 3.5 Experimental setup for measuring temperature from bottom side of the workpiece by using pyrometers

3.3.4 Coordinate measuring machine (CMM)

Bend angles were measured at five different locations including the edges along the width (laser scan) direction by using coordinate measuring machine (Make: Zeiss^{TM}; Model: Vista). The average bend angle results were reported. The touch probe was moved along *x*, *y*, and *z*-axis to collect the data points on either side of scan line. Figure 3.6 shows a photograph of the CMM and its specifications are listed in Appendix C. Figure 3.7 shows a schematic of data points located on the workpiece to obtain the bend angle. The bend angle was computed between these two lines as

$$\theta = \tan^{-1}\left(\frac{h_a - h_b}{L_{ab}}\right) + \tan^{-1}\left(\frac{h_d - h_c}{L_{dc}}\right), \tag{3.1}$$

Figure 3.6 CMM machine (Make: Zeiss^{TM}; model: Vista)

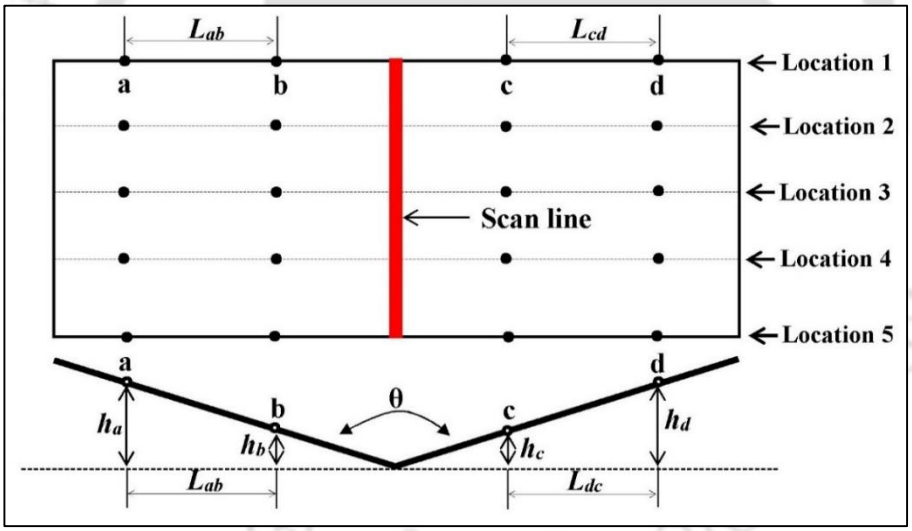

Figure 3.7 A schematic of bend angle measurement

3.4 Study on Mechanical Properties of Workpiece

The mechanical properties like tensile strength and percentage elongation of raw samples, friction stir welded workpiece and friction stir processed workpiece were evaluated. From each tensile test, three samples were prepared and tested. For laser bent strip samples, the flexural tests were conducted. The tensile property and flexural tests were conducted according to American Society for Testing and Materials (ASTM) Standard on a universal testing machine.

3.4.1 Universal testing machine

In order to measure the mechanical properties of parent materials (aluminum alloy and mild steel), friction stir welded aluminum alloy and friction stir processed (aluminum alloy and mild steel), uniaxial tensile tests were carried out according to ASTM E8M standard. All the samples were tested in universal testing machine (UTM) (Make: INSTRON, Model: 8801J4051) of 100 kN capacity at room temperature with a constant cross-head speed of 1 mm/min as shown in Fig 3.8 (a). The gauge length and strain rate were 25 mm and of the order of 1×10^{-3} s^{-1}, respectively. Three replicates were used in each case. The average properties were taken for analysis. The load extension data from the machine was converted into engineering stress-strain behavior and the mechanical properties such as yield strength, ultimate tensile strength and total elongation were evaluated for each base material (aluminum alloy and mild steel), friction stir welded aluminum alloy and friction stir processed test samples of aluminum alloy and mild steel.

Flexural strength was measured to get the bending strength of laser applied workpiece, which is defined as the stress in the material just before yielding starts in the flexure test. This method measures behavior of materials subjected to simple beam loading. Flexure test applies tensile stress in the convex side of the specimen and compression stress in the concave side. The flexural test was conducted using the same machine (Universal Testing Machine) with a different fixture. Three-point bending test was performed to find out the flexural modulus and strength. The laser bent samples were placed on the test fixture as shown in Fig. 3.8 (b). After placing the sample in the fixture, its top surface was convex and the bottom surface was concave. The load was applied by the middle roller till the roller-sample contact point was at 60 mm below the supporting rollers. All the samples were tested at room temperature with a strain rate of less than 1×10^{-3} s^{-1}. The span length of the test samples was 100 mm, widths were 20, 30 and 40 mm and thicknesses were 1, 1.5 and 2 mm. The important specifications of the universal testing machine are given in Appendix D.

(a)

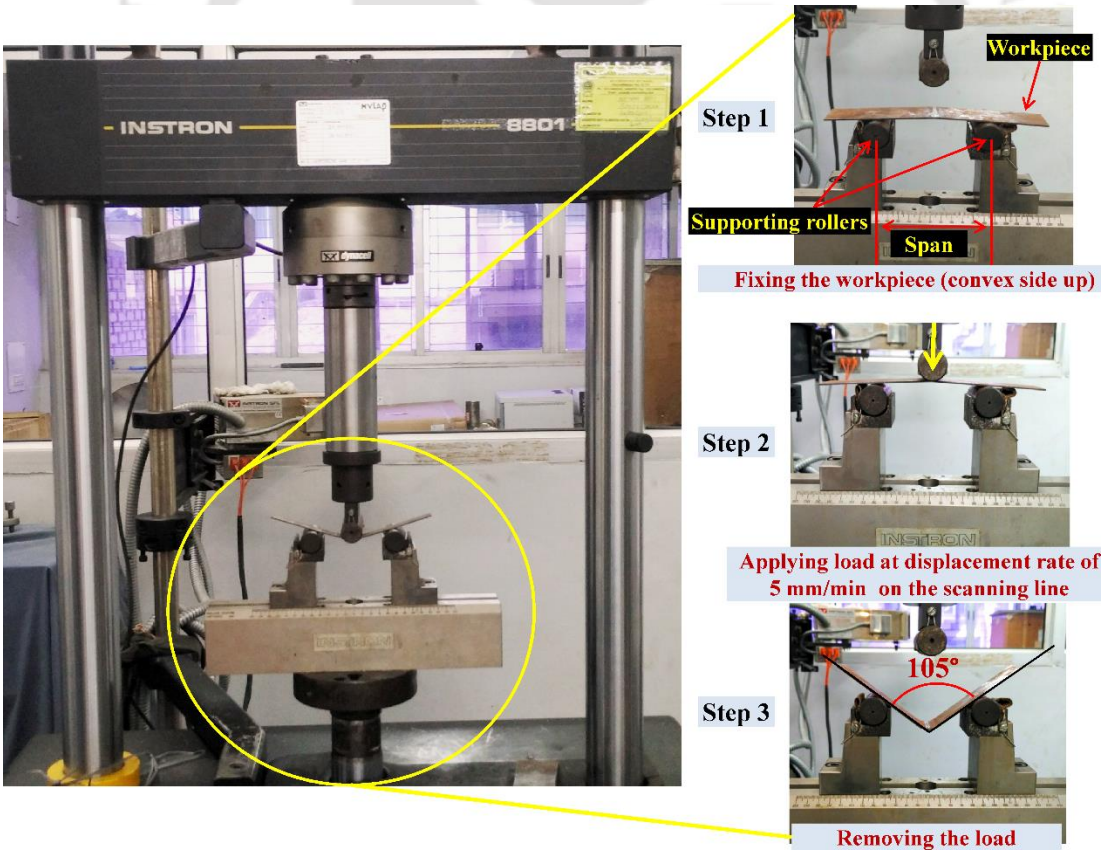

(b)

Figure 3.8 Universal testing machine for (a) tensile test and (b) flexural test

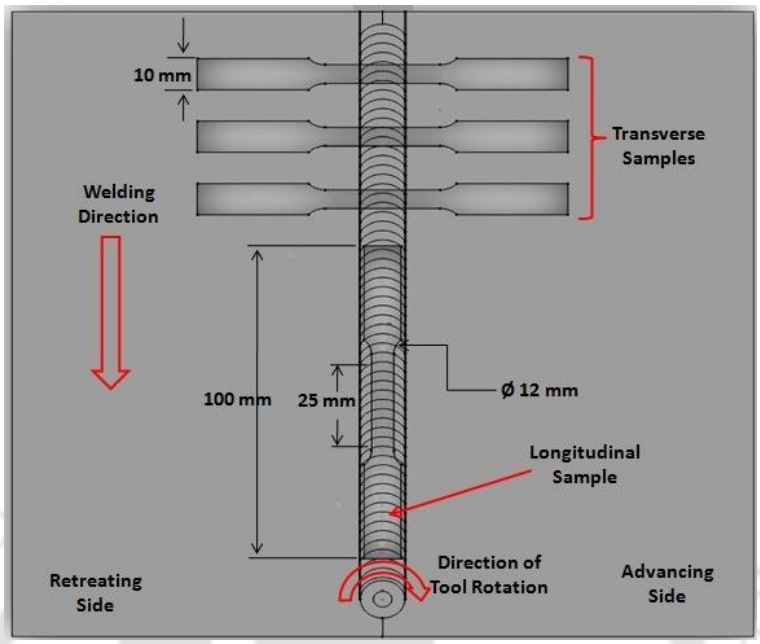

(a)

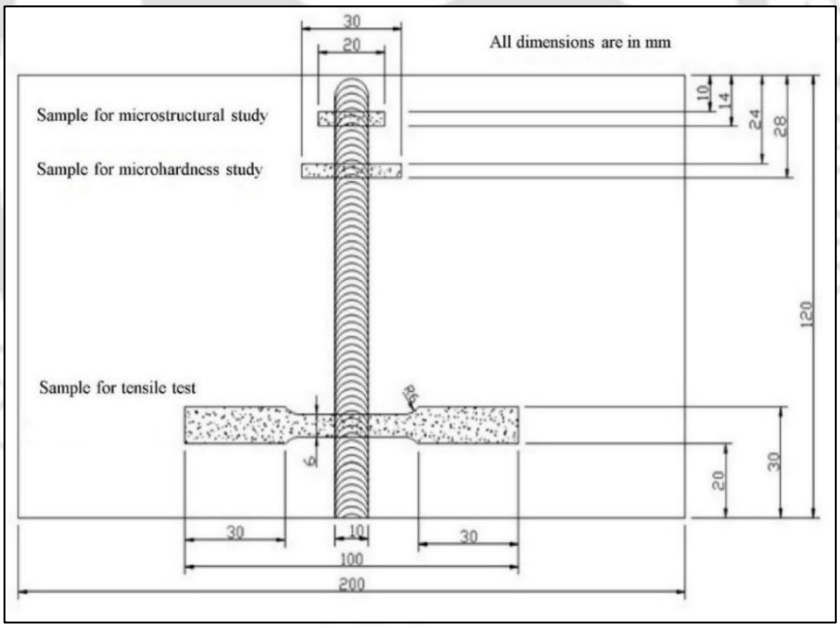

(b)

Figure 3.9 Uniaxial tensile test specimens for longitudinal and transverse directions: (a) FSW workpiece and (b) FSP workpiece

Test specimens were prepared for different cases. Figure 3.9 (a) and (b) shows the dimension of the tensile specimen for friction stir welded and processed cases. From each experiment condition three tensile test specimens and one sample each for

microhardness and microstructure analysis were extracted. The tensile tests were carried out for base plate and friction stir processed plate to determine mechanical properties. Figure 3.10 shows tensile test specimens after testing.

Figure 3.10 Tensile test samples after testing

3.5 Study on Metallographic Sample Preparation and Examination

Figure 3.11 shows the basic steps followed for the preparation of samples for finding microstructure and microhardness. Different instruments were used in the whole operation (metallographic sample preparation and examination). They are explained in the following subsections.

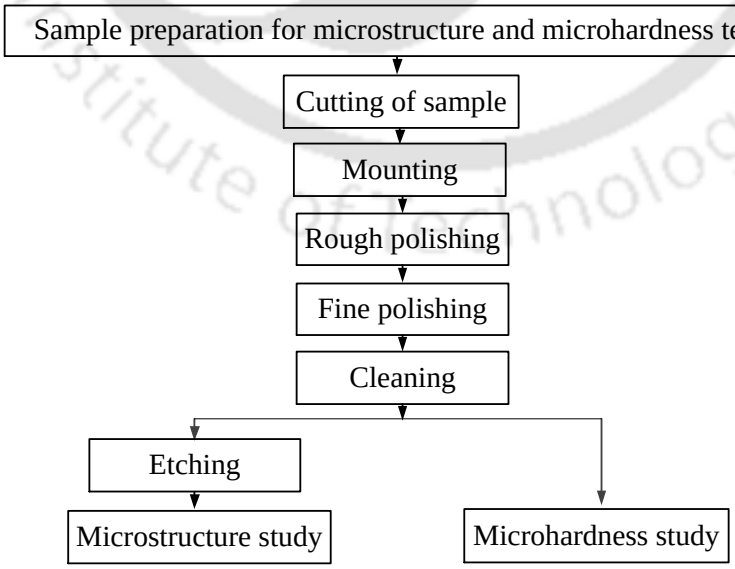

Figure 3.11 Basic steps for microstructure and microhardness sample preparation

3.5.1 Precision hack saw

Precision cutting saw was used for precise and deformation-free cutting. It produced samples that were in perfect condition for the next step. Figure 3.12 shows precision hacksaw that generates less heat with less cutting time due to integrated flood coolant delivery system from both sides of the blade. It produces very less depth of damage with minimum material loss. All the samples are cut in precision hacksaw (Make: BUEHLER; Model: Isomet® 4000) for microstructure and microhardness study.

Figure 3.12 Precision hack saw

3.5.2 Sample molding press machine

After cutting the specimen, the next step is mounting. The aim of mounting is to handle samples and to protect fragile materials, thin layers or coating during preparation as well as to provide good edge retention. Mounting produces specimens with uniform size so that it is easier to handle for further preparation steps. Figure 3.13 shows the molding machine where phenolic plastic was used for encapsulating the sample. The sample was mounted under heat and pressure with a hot mounting press. All samples holder for microstructure and microhardness were prepared by this molding press machine (Make: BUEHLER; Model: Simpliment® 2).

Figure 3.13 Molding machine

3.5.3 Polishing machine

All microhardness and microstructure samples were polished by using double disc polishing machine (Make: B.S. Pyrometic India (P) LTD.); Model: BSPIL–MET–01008A) (8A)) as shown in Fig. 3.14. It has smooth speed variation of the grinding wheel with soft start and stop. Polishing machine was used to avoid surface effect in microhardness and microstructure testing. The sample holder was held by operator and desired grinding depth was also manage by operator. All samples were polished by silicon carbide abrasive paper having 400–2000 grit size and finally polished on velvet cloth using MicroPolish alumina particles of size 1 μm (Fig. 3.15).

Figure 3.14 Double disc polishing machine

Figure 3.15 Silicon carbide abrasive paper in the range of 400-2000 grit size for specimen polishing, velvet cloth and polished samples

3.5.4 Optical microscope

The polished and etched samples were examined using an optical microscope (Make: Carl ZEISS; Model: Axiotech-100HD) as shown in Fig. 3.16. The polished and etched samples were examined at different magnifications, *viz.*, 5×, 10×, 20×, 50×, and 100×. For relevant metallographic observation, the samples were taken from laser irradiated and base regions. For finding the grain size, the image analysis method using AxioVision SE64 Rel.4.9.1 software and the line intercept methods were employed. The average results of grain size at laser irradiated and base material regions are reported. The specification of the microscope is given in Appendix E.

Figure 3.16 Optical microscope

3.5.5 Microhardness testing

Microhardness test is performed to measure hardness of laser irradiated sample (bent sample) and base material. Figure 3.17 shows the microhardness tester (Make: BUEHLER; Model: Micromet-2101) used for the study. In the microhardness testing machine, the loads of 1, 10, 50, 100, 300, 500 and 2000 g force can be applied smoothly (without impact), forcing the indenter into the test workpiece by using different indentation time. The proper indentation force (g force) varies from material to material. The microhardness is measured at three position along and across thickness direction by using 100 gf for aluminum alloy and 500 gf for mild steel and stainless steel. The microhardness tests were conducted as per ASTM E384 standard. Microhardness tester specifications are listed in Appendix F.

Figure 3.17 Microhardness tester

3.5.6 Non-contact profilometer

The surface roughness of base material and friction stir processed samples before laser irradiation was measured by using 3D optical non-contact surface profilometer (Make: Taylor Hobson®; Model: CCI-Lite). Twelve measurements were made per specimen along friction stir processed region along width (tool traverse) direction and unprocessed (raw) sheets for aluminum alloy and mild steel. The

average of 12 measurements was taken. Figure 3.18 shows the 3D non-contact optical profilometer. Its specifications are listed in Appendix G.

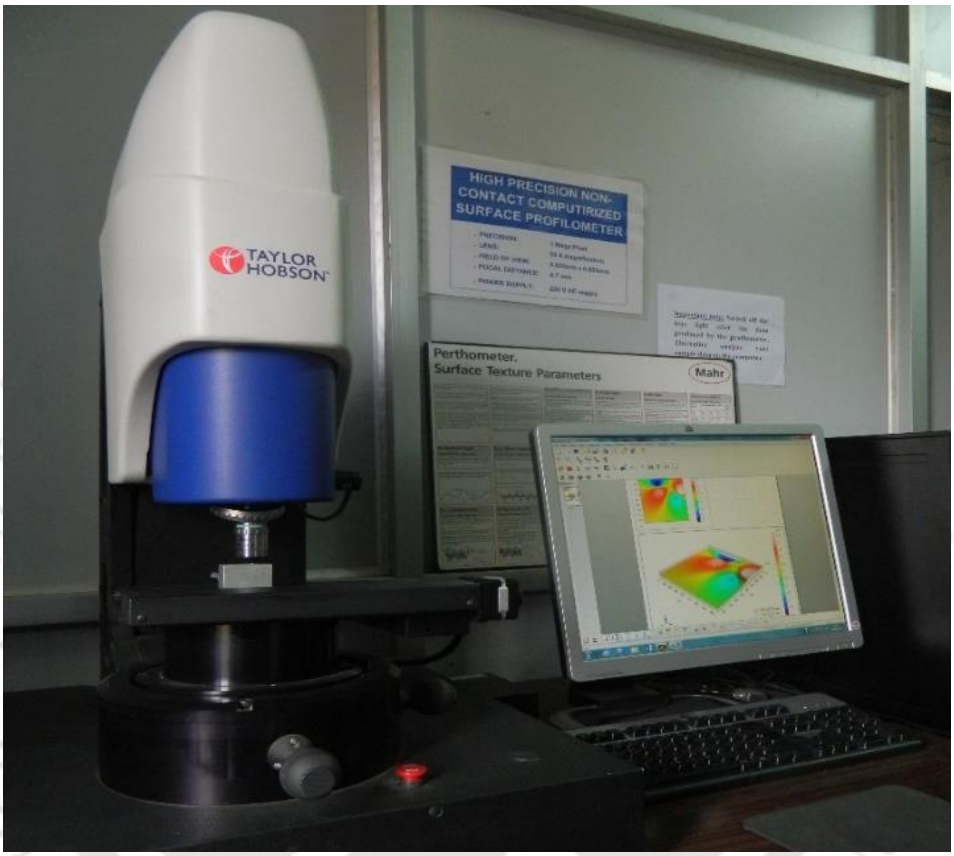

Figure 3.18 Non-contact profilometer

3.6 Experimental Setup of Friction Stir Welding (FSW) and Friction Stir Processing (FSP)

A vertical milling machine was converted to friction stir welding/processing machine as shown in Fig. 3.19. A large number of independent parameters control the friction stir welding and friction stir processing to produce welding or surface roughness of workpiece. The main purpose of FSP was to enhance the absorptivity of the sample. The machine was operated by varying tool rotational speed in the range 50–1500 rpm and traverse speed in the range 22–555 mm/min.

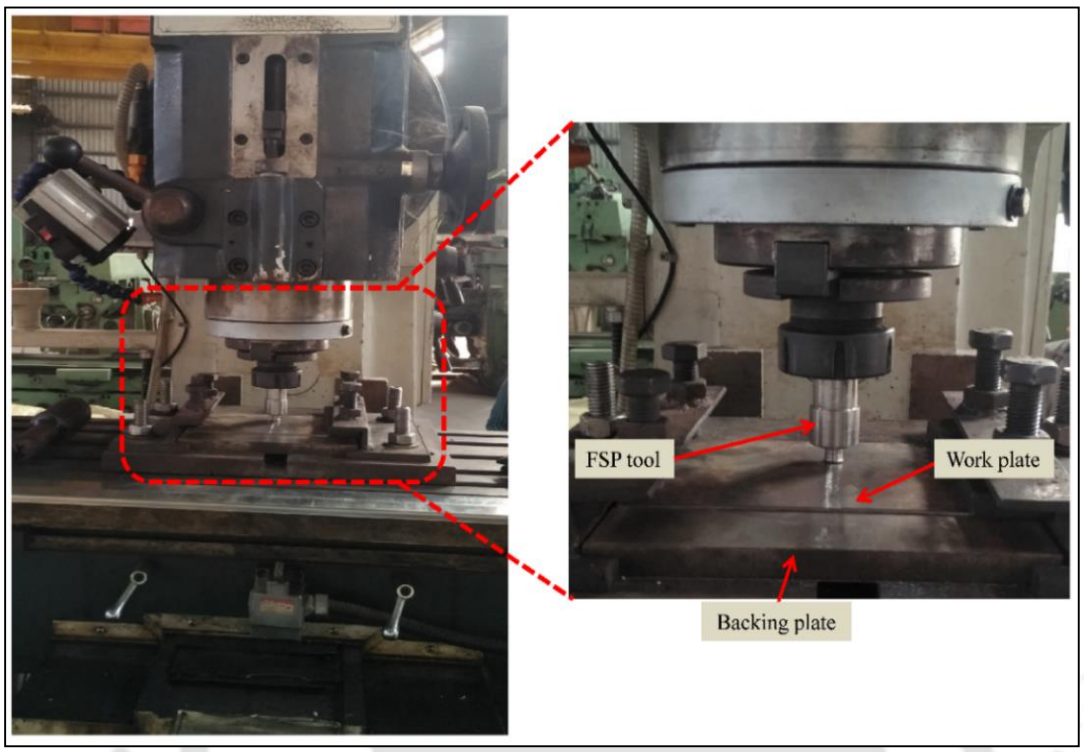

Figure 3.19 Photograph of friction stir welding (FSW) machine

3.6.1 Fabrication of friction stir welding and processing tools

Cylindrical shoulder was used for friction stir welding and processing tools. Cylindrical tool with pin were used for friction stir welding. Tool shoulder and pin diameter affect the weld quality. Vijayavel et al. (2014) observed that a shoulder to pin diameter ratio of 3 provided good welding. For friction stir welded plate preparation, the tool shoulder diameter was taken as 15 mm and pin diameter as 5 mm to make friction stir welded sheets. Three different tool pin lengths were chosen as 1.95, 1.85 and 1.75 mm to produce weld joints of different thicknesses. On the other hand, cylindrical tool without pin was used for friction stir processing (FSP). Both tools were made of H13 tool steel. The tool shoulder diameter was taken as 10 mm for FSP operation. The widths of the stirred and welded zones were dependent on the shoulder diameter of the tool. Figure 3.20 shows the FSW and FSP tools.

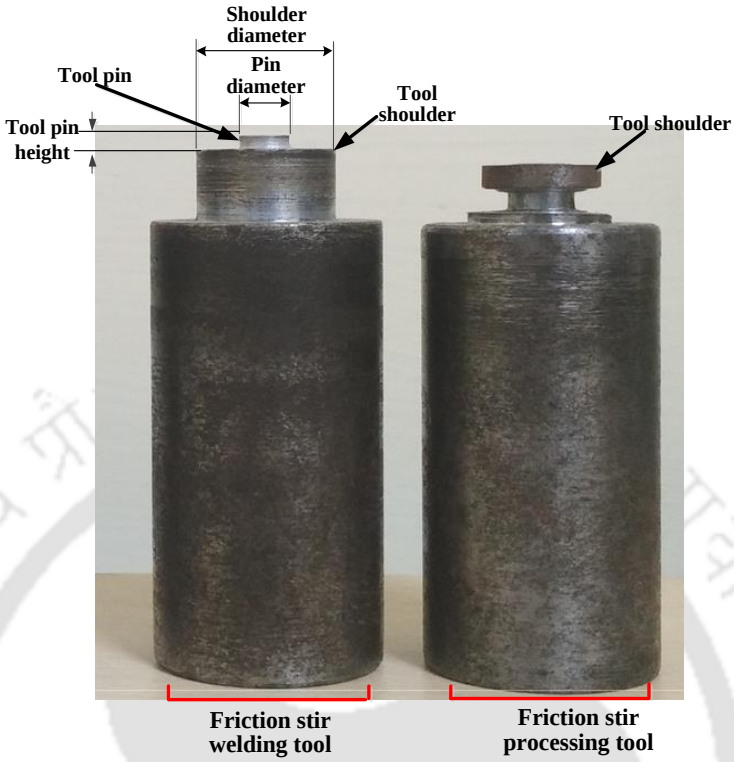

Figure 3.20 Friction stir welding and friction stir processing tools

3.6.2 Preparation of sheets by friction stir welding and friction stir processing

For friction stir welding, aluminum alloy sheets of 200 mm × 100 mm × 2 mm were used to get square butt joint in a single pass. Square butt joint configuration has been prepared to fabricate FSW joints. In the case of FSP, aluminum alloy and mild steel sheet metal were used as the base metals. The sheets were cut as rectangular samples of 200 mm × 120 mm × 2 mm size. They were properly positioned above a backing plate and clamped rigidly using a special fixture to eliminate any movement. In FSW, the tool pin penetrated the workpiece and the shoulder rubbed the top surface of the workpiece as depicted in Fig 3.21. Preliminary experiments were conducted in order to determine important parameter ranges.

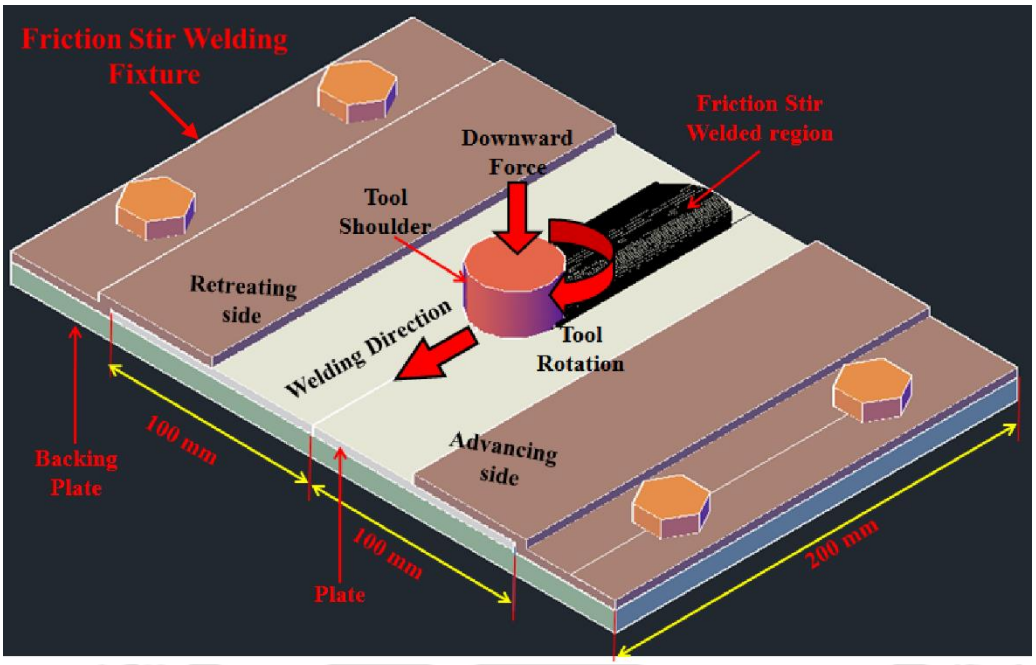

Figure 3.21 Schematic diagram of the friction stir welding process

In case of FSW, it was found that the surface defect free joints could be fabricated by choosing four levels of traverse speeds, *viz.*, 36, 63, 98 and 132 mm/min for 1500 rpm tool rotation speed. When these traverse speeds were used with 1100 rpm tool rotation speed, defects were produced. Hence, the traverse speed was reduced to 22 mm/min, which could get a defect free weld. Three tool pin lengths were used for friction stir welding— 1.95, 1.85 and 1.75 mm. For FSP, the basic aim was to produce high surface roughness without affecting the thickness of workpiece. For all experiments, the tool rotated at 240 rpm and traversed at 98 mm/min. For both FSW and FSP, tool tilt angle was zero. The traverse was along the rolling direction of the sheet. Single pass was used for both FSW and FSP.

3.7 FEM Model of Laser Bending

The commercial FEM package ABAQUS® was used to model the laser bending process using 3D coupled thermo-mechanical analysis. In ABAQUS/CAE modelling process, the following modules were used: part, property, assembly, step, interaction, load, mesh and job. They are briefly described.

- Part module: A part can be created using the part module tools. For laser bending process, 3D geometric parts were created.

- Property module: Temperature dependent material properties were assigned using this module.
- Assembly module: Assembly module placed the part in a global coordinate system.
- Step module: Fixed time step increments were chosen for coupled temperature-displacement analysis.
- Interaction module: For laser bending process, surface to surface contact interaction was selected. A film condition interaction property defined a film coefficient as a function of temperature and field variables.
- Load module: It uses the load, boundary condition, and predefined field managers to view and manipulate the stepwise history of prescribed conditions. It can also use the step list located in the context bar to specify the steps in which new loads, boundary conditions, and predefined fields become active by default. Amplitude toolset in the load module was used to specify time dependencies. For laser bending process, thermal load was applied in the form of heat flux. The laser beam was assumed to be circular with Gaussian distribution of heat flux.
- Mesh module: The mesh module generated the mesh. It has a variety of tools that allow to specify different mesh characteristics, such as mesh density, element shape and element type. The partition toolset was used to divide geometric regions into smaller regions that could be assigned different mesh sizes (fine and coarse). The workpiece was discretized with three-dimensional linear hexahedron eight-node elements (C3D8T). The part was discretized with fine mesh in the heated region and coarse mesh for outer region to minimize the simulation time. Various details of the mesh sensitivity analysis are given in Section 3.7.3.
- Job module: After finishing all of the tasks involved in defining a model (defining the geometry of the model, assigning section properties, assembling parts in a global coordinate system, assigning steps, applying load and meshing), it was submitted for analysis. After the analysis, temperature, stress-strain, bend angle, edge effect and springback were recorded.

A laser bending process involves nonlinear interaction between various laser parameter and workpiece geometry parameters. The following assumptions were considered in the simulation:

1. The material is isotropic.
2. The CO_2 laser has Gaussian distribution of heat flux inside the spot diameter.
3. The material yields as per von Mises criterion (suitable for ductile materials).
4. The workpiece is considered flat, weight-less and free of residual stresses.
5. Heat transfer is through conduction and convention. The radiation effect is very small and it can be clubbed with convection.

3.7.1 Thermal and mechanical properties of the materials

The thermo-mechanical analysis requires temperature-dependent mechanical and thermal properties of the materials. Many times, this data is not available in handbooks. Even if temperature-dependent material properties are available, some variation may occur from batch to batch. In this work, an inverse procedure was used for determining temperature dependent aluminium alloy (5052-H32) properties. Detailed procedure is discussed in Chapter 6. The temperature dependent material properties of mild steel and stainless steel were taken from Zhang et al. (2004) and Deng and Murakawa (2006), respectively.

3.7.2 Thermal and mechanical analysis

Thermal load is in the form of applied heat flux in the vicinity of scanning line. Heat flux model and boundary conditions are discussed in detail. The numerical simulation of the laser forming process was performed with three-dimensional thermo-mechanical analysis.

A) Heat flux model

The laser beam was assumed to be circular with the Gaussian distribution of heat flux. The beam diameter was controlled by varying the standoff distance between the tip of the nozzle and the top surface of the workpiece. The laser beam radius *r* was calculated as (Sun, 1998)

$$r = w_0 \left\{ 1 + \left(\frac{M^2 \lambda H}{\pi w_0^2} \right)^2 \right\}^{1/2}, \tag{3.2}$$

$$w_0 = \frac{2M^2 f \lambda}{\pi D_L}, \tag{3.3}$$

where w_o is the laser beam waist, M^2 is a beam quality factor. For perfect Gaussian beam, M^2 is 1, but in actual practice M^2 is more than 1; here M^2 = 1.4. H is standoff distance, λ is the wave length (10.6 μ m for CO_2 laser), f is the focal length (127 mm for the machine used), D_L is laser beam diameter before lens (24 mm for all experiments). During the simulation, thermal load was given in the form of heat flux that obeys the normal Gaussian distribution given by

$$q(x,y) = \frac{2\eta P}{\pi r^2} \exp\left(-2 \frac{\left(x^2 + y^2\right)}{r^2} \right), \tag{3.4}$$

where q is the thermal heat flux density of laser beam, η is the absorptivity of the sheet material, P is the power of the laser and r is the radius of the laser beam.

B) Boundary conditions

To avoid the rigid body movement, clamped side of the workpiece was fully constrained in mechanical analysis (zero displacement and rotation). All the other sides were free from mechanical boundary condition in the case of laser bending; however, for laser assisted bending the mechanical load was applied on the free side. After the laser beam irradiation, the sheet metal was cooled down in the air. Heat convection took place between the sheet metal and the surroundings. The convective boundary conditions can be expressed by Newton's law of cooling as

$$q = h\left(T_S - T_a\right), \tag{3.5}$$

where q is the heat flux, h is the convective heat transfer coefficient, T_s is the sheet surface temperature and T_a is the ambient temperature (25 °C).

To minimize the computational time, a force cooling strategy was adopted during simulation time as proposed by Eideh (2014). During heating phase, the convective heat transfer coefficient (h) was taken as 10 W/m^{2}K and during cooling

phase it was taken as 1000 W/m^2.K causing accelerated cooling. This strategy was applied for all simulations except small size bending simulation, where computational time is anyway much less. It was ascertained by a number of simulations that accelerated cooling approach does not hamper the accuracy.

3.7.3 Mesh sensitivity and time increment analysis

Numerical simulations of laser bending as well as laser assisted bending processes are performed to determine temperature distribution, stress-strain, edge effect, springback and bend angles. A coupled thermo-mechanical process is conducted to simulate the laser bending and laser assisted bending process. The numerical simulation of the laser forming process was performed with three-dimensional thermo-mechanical analysis.

Proper mesh refinement and time-increment is crucial for obtaining the accurate results within reasonable computational time. Zhang et al. (2004) used 20-node brick elements and suggested 4 elements in a beam diameter and 3 elements in thickness direction. In the present work, 8-node brick element has been used for different experiments for different laser beam diameters and workpiece geometries as listed in Table 3.1. Therefore, taking Zhang et al. (2004) as a guideline, the mesh sensitivity analysis was carried out. The mesh size depends upon the size of workpiece thickness and laser beam diameter. Mesh refinement was carried out for different widths of the workpiece based on the size of the laser beam diameter.

It was also observed that simulation time increased as the laser power increased. This was due to increase in temperature at high power case causing high thermal gradient. According to Zhang et al. (2004) temporal discretization requires at least four time increments per radius. For this research work, different laser beam radii are used as given in Table 3.1 and the duration of laser beam irradiation (t_1) is the ratio of laser beam diameter to scan speed. The scan speed was chosen during experimental work as per Table 3.1. Considering the guideline of Zhang et al. (2004), the time increment should be less than $t_1/4$. Here, the simulations were carried out with time-increments of 0.01 and 0.005 second and it was observed that at these two conditions, almost the same predictions were obtained. Hence, 0.01 second time-increment was

appropriate. The mesh sensitivity of laser bending and laser assisted bending is discussed below in detail.

A) Mesh sensitivity for laser bending

In the case of laser bending, three experiment were conducted: (1) bending of small sized plate/sheet, (2) bending of strip and (3) bending of friction stir welded sheet. The entire domain of the workpiece was divided into three regions in the case of laser bending of strip and bending of friction stir welded sheet. Laser irradiated line (Region I) was fine meshed but coarse mesh was used for far region (Region II and III). Figure 3.22 shows the meshing scheme. Region II and III are had same size of elements. In the case of laser bending of small sized plate, the mesh size was uniformly fine in the entire domain. Due to small size, simulation time was less for this experiment.

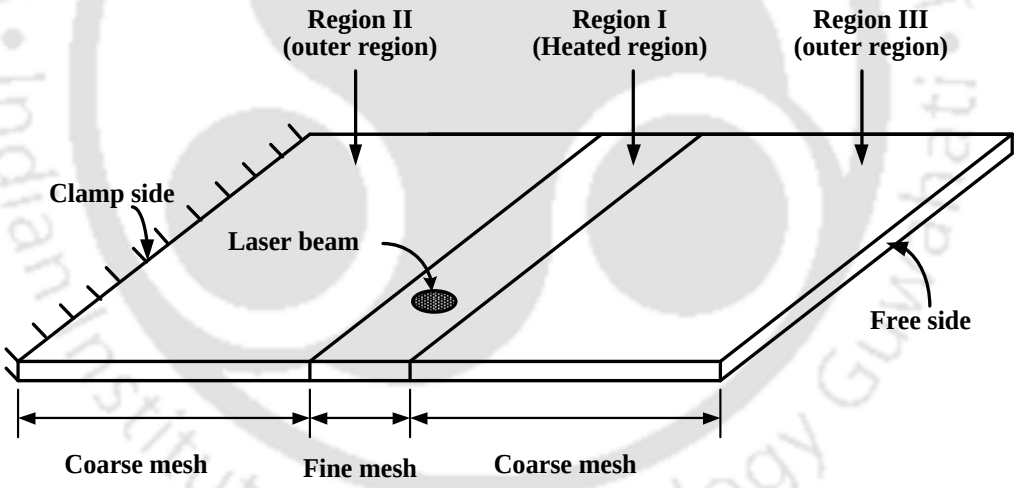

Figure 3.22 Schematic representation of workpiece meshing with region

Laser bending of small size sheet

For laser bending of small size sheets, stationary as well as moving heat source was used. The heating time for every single load step was 0.05 seconds for both the workpieces in case of moving heat source. For moving heat source model, the laser beam center was incremented by 1 mm in each discrete step. It was the same for both 4 mm and 8 mm laser beam (spot) diameters. The total heating time depends on the scanning speed and the width of the workpiece. The same scanning speed of 20 mm/s

was used for both the workpieces. For both heat sources (movable and stationery), the total heating time was taken to be the same. Figure 3.23 depicts a typical model of the meshed small sized workpiece.

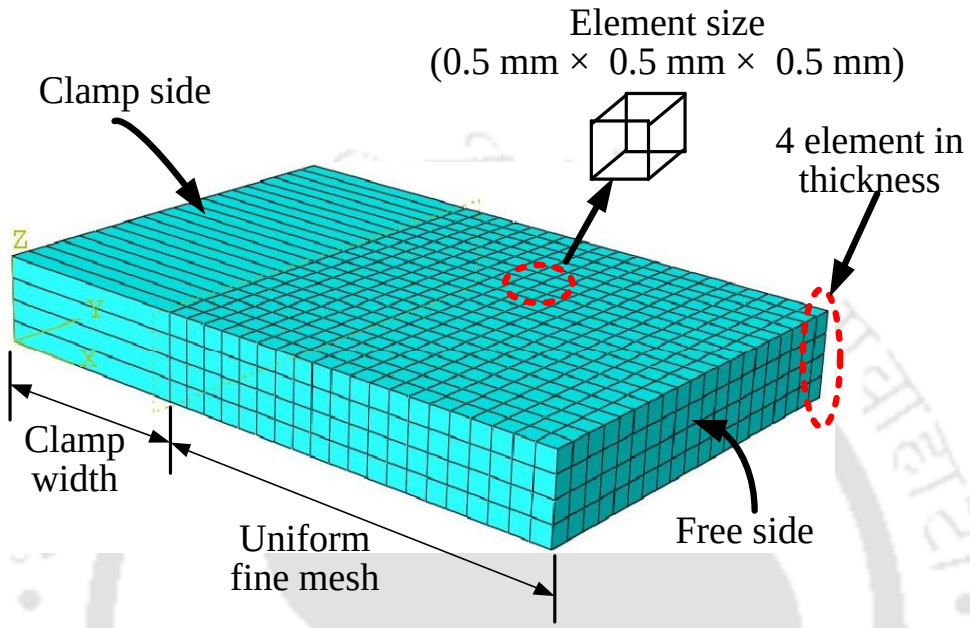

Figure 3.23 The small sized workpiece mesh model

As illustrated in Table 3.2, mesh sensitivity study was carried out by varying mesh size and comparing the simulation time with bend angle. After mesh sensitivity study, the element of size 0.5 mm × 0.5 mm × 0.5 mm was chosen throughout for both cases (stationary and movable heat source) for sample sizes of 25 mm × 20 mm × 2 mm and 15 mm × 10 mm × 2 mm as shown in Table 3.3. Clamp width is 5 mm in both the cases. Uniform mesh was used throughout the workpiece (except in clamped region, where the length of the element was taken as 5 mm) due to the small size workpiece.

Table 3.2 Mesh sensitivity study for fine mesh region for stationary heat source, workpiece size of 25 mm × 20 mm × 2 mm, laser power of 225 W and laser beam diameter of 8 mm

Element size (mm^3)	Screen time (min)	Bend angle (degree)
1 × 1 × 1	2	–0.016
0.5 × 0.5 × 1	10	–0.1
0.25 × 0.25 × 1	45	–0.108
0.15 × 0.15 × 1	120	–0.115
0.5 × 0.5 × 0.5	20	–0.2
0.5 × 0.5 × 0.25	60	–0.208

Table 3.3 FEM models for workpiece of different size

Case	Geometry of workpiece (mm^3)	Element size (mm^3)	Total number of elements
1	25 × 20 × 2	0.5 × 0.5 × 0.5	6560
2	15 × 10 × 2	0.5 × 0.5 × 0.5	1760

Laser bending of strips

In similar fashion, mesh sensitivity study was also conducted for strip bending. The length of the workpiece in all cases is the same 200 mm but 1 mm, 1.5 mm and 2 mm thicknesses and 20 mm, 30 mm and 40 mm widths were considered. Effect of element size on bend angle for laser power of 500 W, scan speed of 800 mm/min, laser beam diameter of 7.76 mm and single scan is shown in Table 3.4. Figure 3.24 shows a typical mesh model of the strip bending.

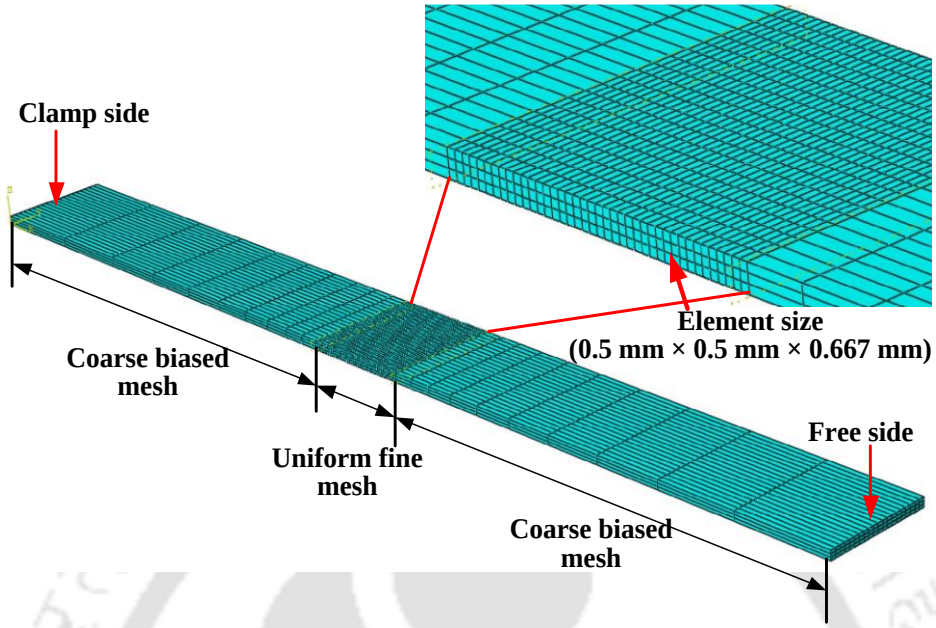

Figure 3.24 The mesh model for strip

Table 3.4 Effect of element size for refined zone on bend angle (20 mm width)

Thickness of workpiece (mm)	Element size (mm^3)	Bend angle (degree)	Screen time (s)
1	2 × 2 × 1	0.6	2560
	1 × 1 × 0.5	0.72	4000
	0.5 × 0.5 × 0.33	0.84	5280
	1 × 1 × 0.25	0.842	7850
1.5	2 × 2 × 1.5	0.27	2020
	1 × 1 × 0.75	0.35	3705
	0.5 × 0.5 × 0.5	0.44	4990
	0.5 × 0.5 × 0.25	0.44	7065
2	2 × 2 × 2	0.2	1865
	1 × 1 × 1	0.24	3525
	0.5 × 0.5 × 0.667	0.3	4830
	0.5 × 0.5 × 0.5	0.31	6915

In the present study, only 3 elemental divisions were taken in the thickness direction for 1 mm, 1.5 mm and 2 mm thickness and its appropriateness was confirmed by the mesh sensitivity analysis. Table 3.5 shows the element size and total numbers of elements generated for different widths.

Table 3.5 FEM mesh size for workpiece of different widths

Width (mm)	Element size (mm^3)	Total number of elements
20	0.5 × 0.5 × 0.667	5280
30	0.5 × 0.5 × 0.5	7920
40	0.5 × 0.5 × 0.33	10560

Laser bending of friction stir welded sheet

The mesh sensitivity result for friction stir welded bending is shown in Table 3.6. As a compromise between computational time and accuracy, an element size of 1 × 1 × 0.667 mm^3 in refined zone and 4.5 × 1 × 0.667 mm^3 in coarse zone was chosen. The total number of elements in the mesh was 3600. In each refined and coarse zone, the mesh size was uniform. Figure 3.25 is shown a typical mesh model of the friction stir welded plate.

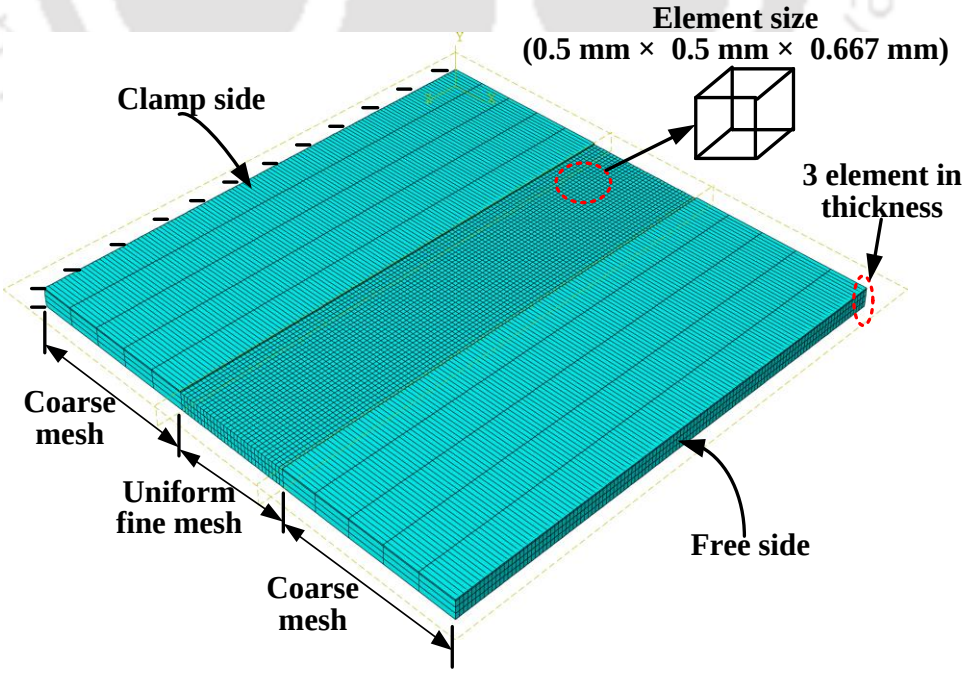

Figure 3.25 The friction stir welded plate mesh model

Table 3.6 Effect of element size in refine zone on bend angle for laser power of 800 W, scan speed of 400 mm/min and laser beam diameter of 7.76 mm

Element size in refined zone (mm^3)	Bend angle (degree)	Screen time (s)
2 × 2 × 0.667	0.77	1800
1 × 1 × 0.667	0.94	6000
0.5 × 0.5 × 0.667	0.955	10600
1 × 1 × 0.5	0.96	12000

B) Mesh sensitivity for laser assisted bending

In the case of laser assisted bending, the entire domain was divided into three regions. The mesh was the finest in Region I (containing the heating line), the coarsest in Region II (from fixed end to heating zone) and the coarse Region III (from heating zone to mechanical load side). During laser assisted bending, mostly the deformation takes place between the scan line and point of the application of the mechanical load or magnetic force. During simulation time, one interesting thing was observed in the Region II between the clamped side and laser irradiated zone; the mesh size was not having much effect during lase bending. A relatively finer mesh was used in the Region III between laser scan line and load side. Figure 3.26 depicts the mesh schemes during laser assisted bending.

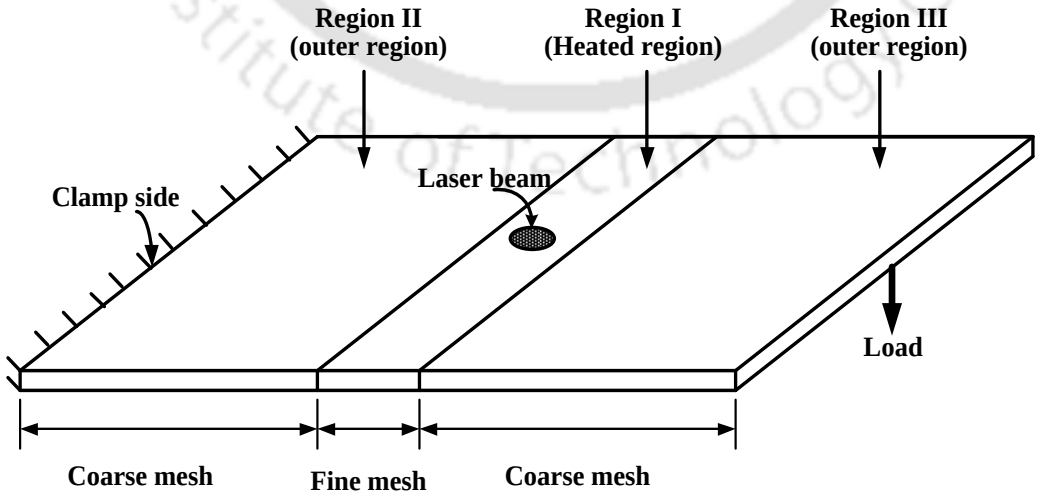

Figure 3.26 Schematic representation of workpiece meshing with region

Laser assisted bending by using mechanical load

For laser assisted bending by using mechanical load the mesh size was uniform for each region. The mesh sensitivity results for laser power of 700 W, mechanical load of 30 N, scan-line distance of 60 mm and scan speed of 400 mm/min for Region I, Region III, and Region II are shown in Table 3.7, Table 3.8 and Table 3.9, respectively.

Table 3.7 Effect of element size in Region I (refined zone)

Element size (mm^3)	Bend angle (degree)	Screen time (s)
2 × 2 × 0.667	1.78	7800
1 × 1 × 0.667	1.9	10000
0.5 × 0.5 × 0.667	2.11	14400
1 × 1 × 0.5	1.95	15600

Table 3.8 Effect of element size in Region III

Element size (mm^3)	Bend angle (degree)	Screen time (s)
7 × 0.5 × 0.667	2.11	14400
5 × 0.5 × 0.667	2.16	15000
2.5 × 0.5 × 0.667	2.28	16000
1 × 0.5 × 0.667	2.283	17000

Table 3.9 Effect of element size in Region II

Element size (mm^3)	Bend angle (degree)	Screen time (s)
17.5 × 0.5 × 0.667	2.28	16000
7 × 0.5 × 0.667	2.29	16200
5 × 0.5 × 0.667	2.3	16500
1 × 0.5 × 0.667	2.3	17210

An element size of 0.5 mm × 0.5 mm × 0.667 mm was considered appropriate for Region I. The appropriate size of the element for Region III was 2.5 mm × 0.5 mm × 0.667 mm. The appropriate element size for region II was 5 mm× 0.5 mm × 0.667 mm. The total number of elements generated in the mesh was 15000.

Laser assisted bending by using magnetic force

The results of laser assisted bending by using magnetic force for fine mesh are shown in Table 3.10. As a compromise between computational time and accuracy, an element size 0.5 mm × 0.5 mm × 0.33 mm was found to be appropriate in the laser irradiated zone. In the zone between the clamped side and laser irradiated Region II, it was sufficient to have 5 divisions along the length. A relatively finer mesh was used in the Region III between laser scan line and free edge. Table 3.11 shows the results of mesh sensitivity analysis for this zone. Based on this table, 20 divisions along the length were taken in Region III (from heating zone to mechanical load side). In both the coarse mesh zones, the ratio of the division length of larger element to smaller element was 5:1.

Table 3.10 Effect of element size in Region I on bend angle for laser power of 1000 W and scan speed 1000 mm/min (number of divisions along length in each Region II and III fixed at 5)

Element size in refined zone (mm^3)	Bend angle (degree)	Screen time (s)
2 × 2 × 0.333	0.67	12,400
1 × 1 × 0.333	0.72	18,000
0.5 × 1 × 0.333	0.78	21,350
0.5 × 0.5 × 0.333	0.8	25,350
0.5 × 0.5 × 0.25	0.81	36,000

Table 3.11 Mesh sensitivity analysis for coarse bias mesh in region between refined zone and free end for laser power of 1000 W and scan speed of 1000 mm/min (element size in refined zone: 0.5 × 0.5 × 0.333 mm^3, number of elements in region between refined zone and fixed end fixed at 5)

Number of element in coarse biased mesh Region III	Bend angle (degree)	Screen time (s)
5	0.8	25,350
10	0.83	27,120
15	0.85	29,235
20	0.87	34,330
25	0.87	39,115

For all workpiece thicknesses (1 mm, 1.5 mm and 2 mm), 3 elements were taken in the thickness direction. As per this meshing scheme, the total number of element generated in the model was 32,400. The maximum time increment was taken as 0.01 second.

3.8 Measurement of Edge Effect and Springback Effect

Laser bending quality is one of the major expectations in laser bending processes. Different process parameters in laser bending play crucial role in providing better quality results. Many researchers have studied the edge effect and springback effect by using numerical simulations and compare them with experiment result.

3.8.1 The edge effect

The bend angle variation from one end to the other end is called the edge effect. The edge effect is attributed to the distribution of the temperature along the scan line and the geometric constraint of the workpiece. The edge effect is defined as a relative variation in bend angle (*RVBA*) along the laser scan line:

$$RVBA = \frac{\alpha_{\max} - \alpha_{\min}}{\alpha_{ave}} \times 100, \tag{3.6}$$

where α_{max}, α_{min}, and α_{ave} are the maximum, minimum and average bend angles along laser pass direction, respectively. The edge effect is more when the value of *RVBA* is higher and vice versa. The edge effect was measured using CMM.

3.8.2 Springback effect

After a bending operation, residual stresses will cause the sheet metal to springback slightly due to elastic recovery. In the case of laser bending process, the springback does not have separate existence as the process itself involves achieving the final bend after cooling (with heat load removed). However, it does exist in laser assisted bending. When external pre-displacement is removed, the elastically deformed material tries to return to the original position, but it is partially restricted by plastically deformed surrounding material. This elastic recovery is called springback. The limitation of laser assisted bending is springback effect. The springback is calculated as a difference of maximum bend angle observed with mechanical load applied and final bend angle obtained after removal of the load. This can be easily estimated from simulations. The percentage springback angle is calculated as

$$\%\text{Spring-back} = \left[\frac{\text{Springback angle}}{\text{Final bend angle}}\right] \times 100. \tag{3.7}$$

3.9 Conclusion

This chapter explained the details of planning regarding experiments and simulations. In the case of experiment work, experimental setup, use of different machines and instruments, types of work material and sizes of workpiece are explained. Different machines are used for evaluating different test results. A summary is presented in Fig. 3.27

The commercial FEM package ABAQUS® was used to model the laser bending process. The numerical simulation of the laser bending process was performed using the 3D non-linear coupled thermo-mechanical analysis. Gaussian distribution heat flux was applied on the workpiece surface. The temperature-dependent material properties were used for the forming of aluminum alloy, mild steel and stainless steel.

Mesh sensitivity analysis was carried out for accurate prediction in a reasonable time. The screen time is reported, which is also not much different from CPU time in this case.

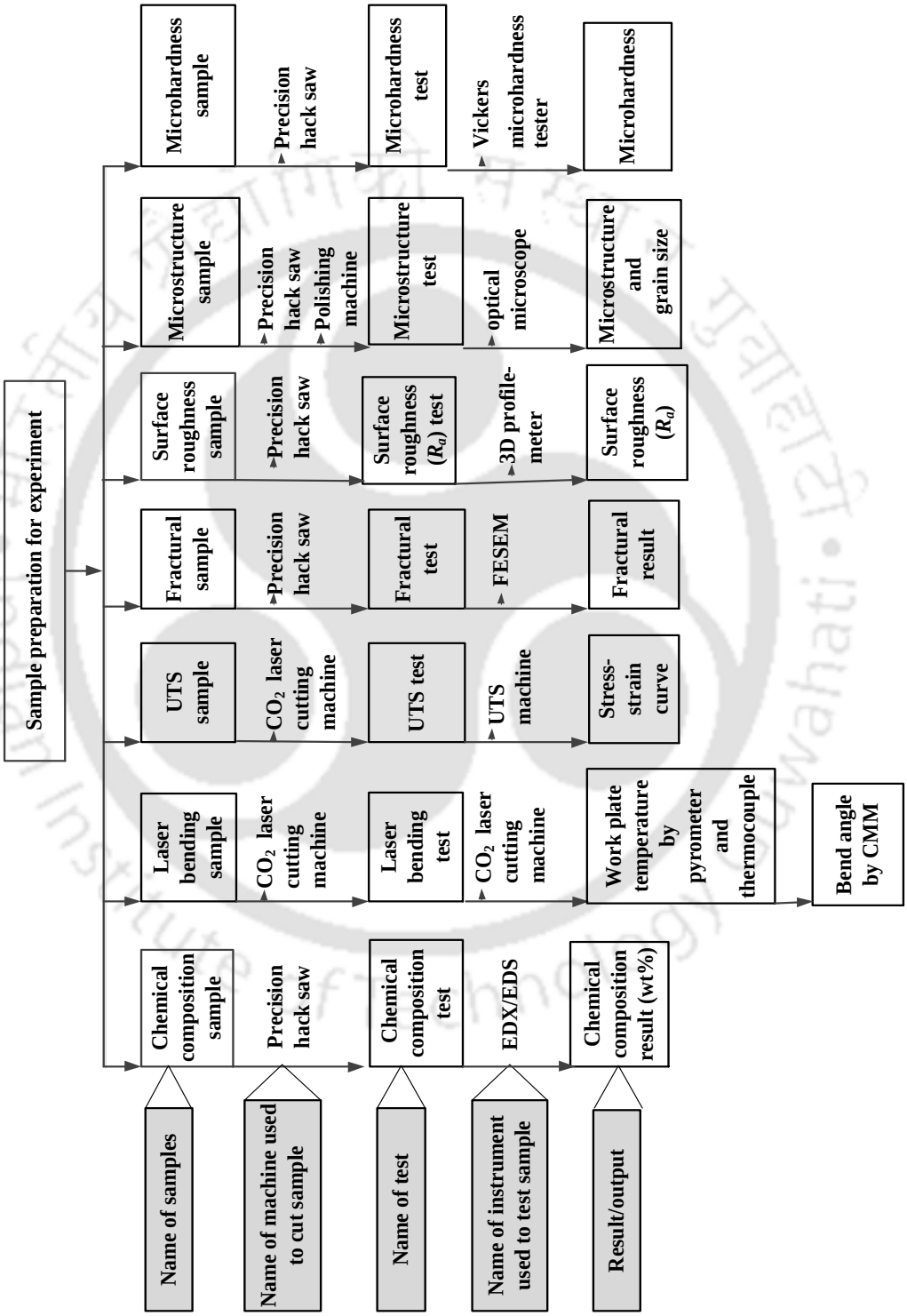

Figure 3.27 Overview of the experimental work

Chapter 4

Laser Bending of Small Sized Workpiece

4.1 Introduction

This chapter presents numerical and experimental studies on laser bending of small size workpieces. Initially the methodology for numerical simulations using finite element method is presented. Further, the detailed analysis of the effects of process parameters on bending mechanism and deformation behaviour for stationary and moving heat sources is discussed. The experiments were carried out to validate the results predicted by the numerical model. In this chapter, the effect of processes parameters *viz.*, laser power, laser beam diameter, length and widths of the workpiece and type of heat source (moving and stationary) on small size workpiece is discussed.

In literature, the laser bending process has been investigated for different materials. Most studies considered large sized sheets. The geometric parameters like length, width and thickness influence the bend angle. For example, the bend angle was observed to be approximately inversely proportional to the square of the workpiece thickness (Geiger et al. 1993 and Lee and Lin, 2002). The bend angle increased with increasing width (along scanning path) of the workpiece at a constant workpiece length (Cheng et al. 2005 and Shichun and Jinsong, 2001). The length of the workpiece had little influence on the bend angle (Chen et al. 2004b).

In the bending of small components, all geometrical dimensions have profound influence on the bend angle. The direction of bend is also influenced by a number of parameters. Li and Yao (2001a) suggested that direction of bending can be assessed by evaluating the Fourier number given by

$$F_0 = \frac{D_t D}{t^2 v}, \tag{4.1}$$

where D_t is the thermal diffusivity, D is the diameter of laser beam at the surface of the workpiece, t is the workpiece thickness and v is the scan speed. It was seen that

corresponding to small values of the Fourier number in the range 6.25–6.6, positive bending occurred (toward laser irradiation direction). In this case, temperature gradient along the thickness direction is high and temperature gradient mechanism (TGM) plays a dominant role. For the Fourier number in the range 6.6–6.8, the direction of bending was uncertain i.e., sometimes positive and sometimes negative due to dominance of buckling mechanism. In the range of Fourier number of 6.8–7.5, negative bending occurred. The objective of this work is to evaluate the effect of laser power, workpiece geometry (length and width), laser spot diameter and type of heat source (stationary and moving heat sources) on the bend angle of the small sized workpieces.

4.2 Experiment and FEM Simulation

Numerical simulations were carried out using ABAQUS® package in order to analyse the variations in the bend angle by applying stationary and moving heat sources with different laser parameters. In this work, a 3D nonlinear thermo-mechanical numerical model is developed by using finite element method. Details regarding the governing equations, boundary conditions and mesh sensitivity were discussed in Chapter 3, Section 3.7.3. Three-dimensional thermally coupled brick elements (C3D8T) with 8 nodes were used. The fixed increment time was used. The temperature-dependent thermal property and mechanical properties of the D36 shipbuilding steel are taken from Dixit et al. (2013). The absorptivity of the sheet is η = 0.8. Clamped surface of samples were considered to be insulated and convection heat transfer coefficients (h) equal to 10 $W \cdot m^{-2} \cdot K^{-1}$ was used for the exposed surfaces. As illustrated in Table 3.3, mesh sensitivity study was carried out by varying mesh elements size and chosen final element size is listed in Table 3.4. During the simulation, the thermal load is given in the form of heat flux that obeys a normal Gaussian distribution as discussed in Chapter 3. The numerical model was validated by comparing it with the experimental results. Simulations were carried out using full factorial design of experiments with levels presented in Table 4.1.

Table 4.1 Process parameters

Process parameter	Symbols	Unit	Level
Power	*P*	W	100, 150, 200, 225 and 250
Laser spot diameter	*D*	mm	4 and 8
Length × Width	*l* × *w*	mm	15 ×10 and 25 × 20
Heating source			Stationary and moving

Details of experiments, such as experimental machine, sample preparation, procedure measurement, bend angle and edge effect measurement methodology were presented in Chapter 3. Laser bending was performed by CO_2 laser machine. The bend angle was measured by a coordinate measuring machine (CMM).

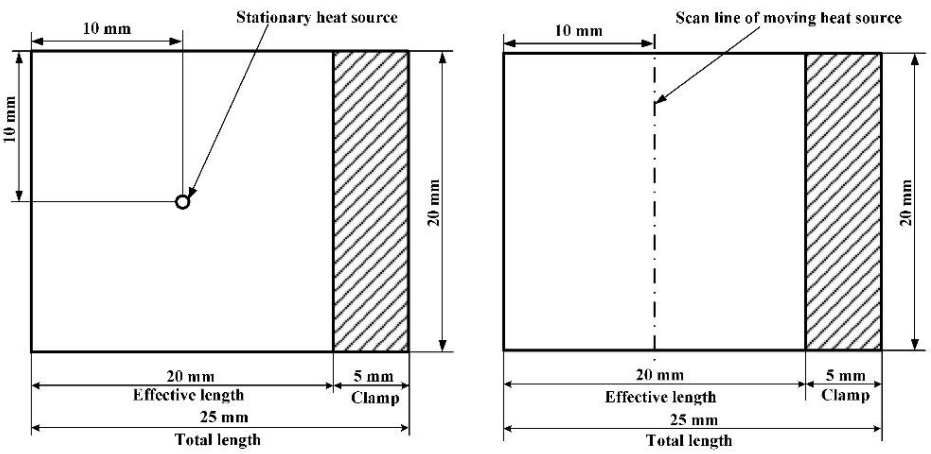

(a)

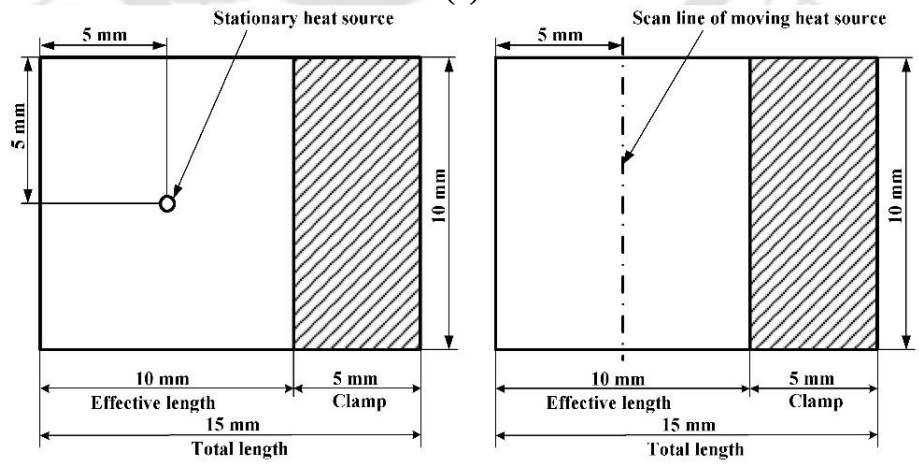

(b)

Figure 4.1 The workpieces for stationary and movable heat source with size of (a) 25 mm × 20 mm × 2 mm and (b) 15 mm × 10 mm × 2 mm

Figure 4.1 (a) and (b) show the top views of workpiece indicating the locations of moving and stationary heat sources. For each workpiece, 5 mm length was used for clamping at one side of the workpiece parallel to scanning direction. In case of stationary heat source, the laser heating was applied at points (15, 10) and (10, 5) for 25 mm × 20 mm and 15 mm × 10 mm, respectively from the right top corner of the clamped workpiece as shown in Fig. 4.1. In case of moving heat source, the laser heating line was 10 mm and 5 mm away from the free end of the workpiece along width direction, respectively, for 25 mm × 20 mm and 15 mm × 10 mm workpieces.

In case of moving heat source, the heating time for every single load step was 0.05 seconds for both the workpieces of sizes 25 mm × 20 mm × 2 mm and 15 mm × 10 mm × 2 mm. At each load step, the beam moved by 1 mm. To model a continuous laser beam heating, the time increment size of 0.01s was taken for both 4 and 8 mm laser beam diameter. The total heating time depends on the scanning speed and the width of the workpiece. The scanning speed was 20 mm/s. Therefore, the heating time for 25 mm × 20 mm × 2 mm and 15 mm × 10 mm × 2 mm workpieces were 1 s and 0.5 s, respectively. Details about mesh sensitivity have been discussed in Chapter 3.

4.3 Results of Experimental and Numerical Studies

The behaviour of material components under laser bending process were influenced by combinations of laser process parameters, geometry, material parameters and shape of heat source. In this work, the effect of process parameters, such as laser power, beam diameter, type of heat source and workpiece geometry on the bending mechanism, bend angle and edge effect are presented.

4.3.1 Effect of laser power

Laser power is an important parameter that directly controls the heat flux density of the laser beam and the energy input into the workpiece surface. The heat flux density and energy input both increase with the laser power. The effects of laser power on the bending of 25 mm × 20 mm × 2 mm workpiece size was observed for stationary and moving heat sources. The simulation and experimental results revealed that the bend angle was critically dependent on the laser power. It was observed that,

the numerical results were in good agreement with the experimental results. The trend of variation of bend angle predicted by the developed numerical model was similar to those obtained in the experiment.

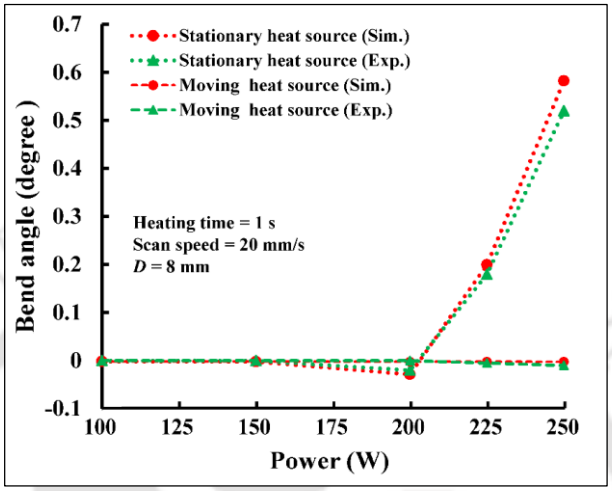

(a)

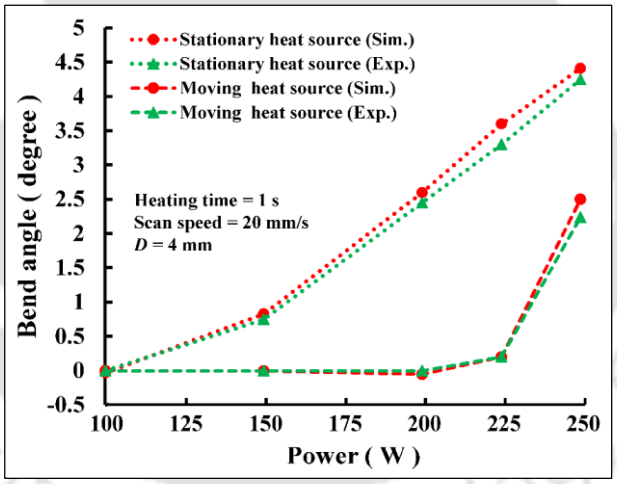

(b)

Figure 4.2 Effect of laser power on the bend angle for stationary and moving heat sources on 25 mm × 20 mm × 2 mm workpiece for (a) 8 mm beam diameter and (b) 4 mm beam diameter

It is observed that laser bending is not possible at laser power below certain level. It is because of the reversible elastic effect that requires a threshold energy. In present work, it is observed that for a typical case i.e., D = 4 mm and scan speed = 20 mm/s, there is no bending of the workpiece up to 200 W. With further increase in laser power, the bend angle of the workpiece increases.

In case of stationary heat source with 8 mm laser beam diameter, the bend direction was negative (away from laser source) for the range of laser power of 100–200 W. Beyond 200 W, the workpiece started to bend towards positive direction (towards laser source) as shown in Fig. 4.2 (a). However, for moving heat source, the bending direction was negative for the range of 100–250 W. The bend angle obtained in case of moving heat source was too small as compared to the stationary heat source. In case of stationary heat source with 4 mm beam diameter, the bending direction was positive for the range of laser power of 150–250 W, while it was negative for the laser power of 100 W as shown in Fig. 4.2 (b). In the case of moving heat source, the bend angle was negative for the range of 100–200 W. After 200 W, it started to bend toward positive direction.

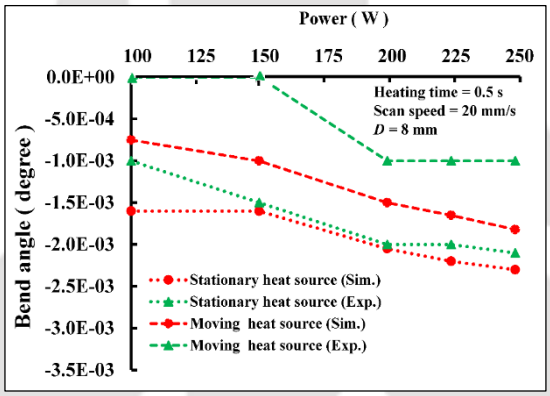

(a)

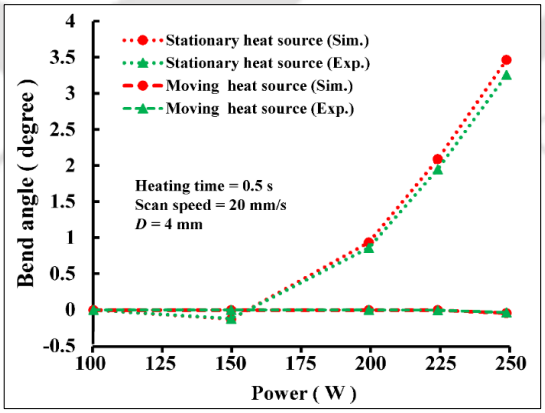

(b)

Figure 4.3 Effect of laser power on the bend angle for stationary and moving heat sources on 15 mm × 10 mm × 2 mm workpiece for (a) 8 mm laser diameter and (b) 4 mm laser diameter

The similar study was carried out for 15 mm × 10 mm × 2 mm workpieces. Here, for 8 mm laser beam diameter, the bend angle was very small and the bend was away from the heat source (negative) for both stationary and moving heat source as shown in Fig. 4.3 (a). The experimental results revealed that there was no bending of the workpiece from 100 W–150 W laser power. However, with further increase in laser power the workpiece bent towards negative direction (Fig. 4.3 a). The trend was different for 4 mm laser beam diameter as shown in Fig. 4.3 (b). The bend direction was negative in the range 100 W–150 W of laser power, but the sheet started to bend toward positive direction after 150 W for stationary heat source. In the case of moving heat source, the bend direction was negative for 100 W–250 W laser power.

4.3.2 Effect of laser beam diameter

Figure 4.2 and 4.3 show the effect of laser beam diameter on bend angle after applying moving and stationary heat sources, respectively. From Fig 4.2 (a) and (b), it can be seen that the bend angle increased with the decrease in laser beam diameter. This was due to increase in the heat flux density and temperature gradient along the thickness direction with the decrease in beam diameter. The same behaviour is seen in Fig 4.3.

4.3.3 Edge effect

In all the cases, the bend angle was greater in the case of stationary heat source. However, in the case of stationary heat source, the bend angle was not uniform across the width as shown in Fig. 4.4. At laser power of 100 W, the bend angle along scan direction was almost uniform. The variation in the bend angle along width direction increased with increase in the laser power. The bend angle was higher at the middle of the workpiece along the scan direction.

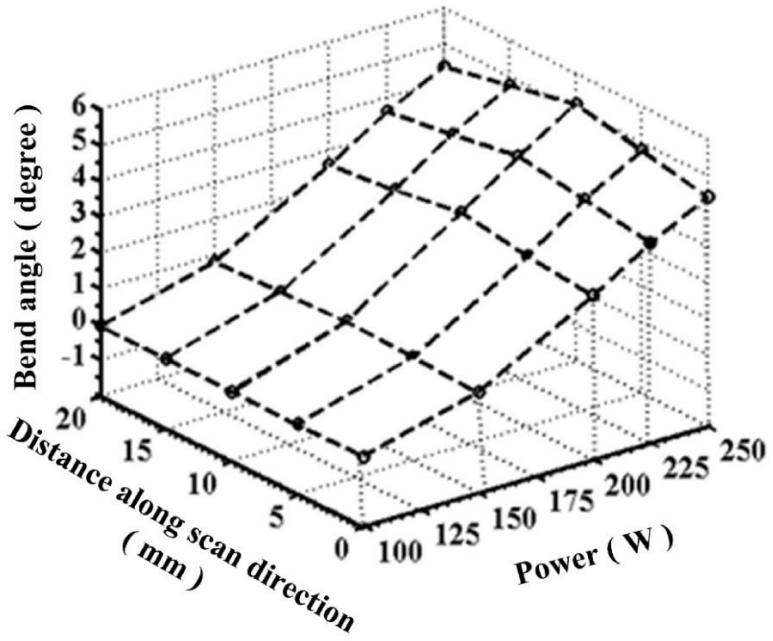

Figure 4.4 The effects of stationary heat source on bend angle along width direction by using 4 mm laser diameter on 25 mm × 20 mm × 2 mm workpiece

In the case of 25 mm × 20 mm × 2 mm, the edge effect for both type of heat sources was studied. For 250 W laser power, the bend angle deviation between stationary and moving heat source was approximately 2° and the bend angle was the maximum at the middle of the bent workpiece in both experimental and simulation results (Fig. 4.5 a). However, for 100 W moving heat source, the edge effect was very small (Fig. 4.5 b). For 100 W laser power, the bend angle was larger at the middle of the workpiece in both experimental and simulation results. However, the bend angle direction along scanning path was opposite to that for 250 W of laser power.

The edge effect in the workpiece occurs due to uneven temperature distribution along the scan length. In case of stationary heat source the temperature is the maximum at the heating point and reduces at the points away from it, whereby the bend angle is the maximum at the heating point. However, in moving heat source the temperature is the maximum at nearby end point of the scan line which reduced the temperature gradient along the thickness direction and therefore the bending was only slightly reduced at the end.

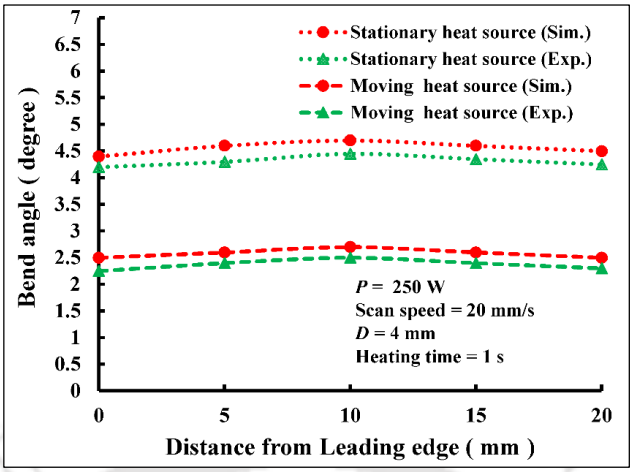

(a)

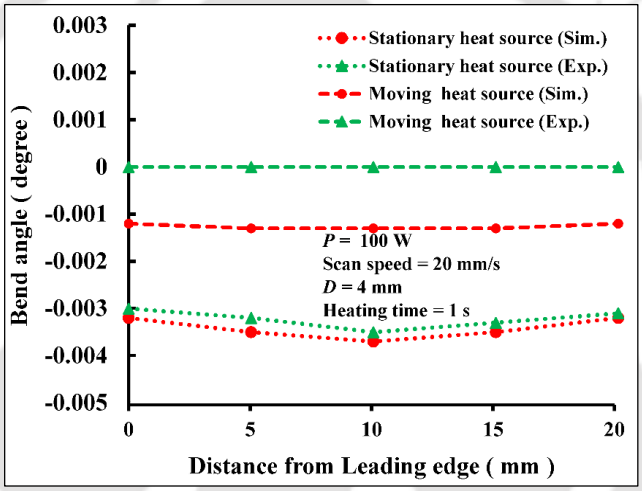

(b)

Figure 4.5 Effect of laser power on bend angle for 25 mm × 20 mm × 2 mm workpiece for (a) 250 W laser power and (b) 100 W laser power

4.4 Temperature Distribution by Simulation

Figure 4.6 shows the variation in temperatures with laser power in the top and bottom surface centre point for 4 mm laser beam diameter. Rate of increase of power was greater at the top surface than bottom surface. The maximum temperature at 250 W laser power was 1200 °C, which was below the melting point temperature of the workpiece. Figure 4.7 shows that the laser beam diameter has a profound effect on the maximum temperature at top and bottom surface centre points of the workpiece. The maximum temperature was obtained at the small laser beam diameter than the large one.

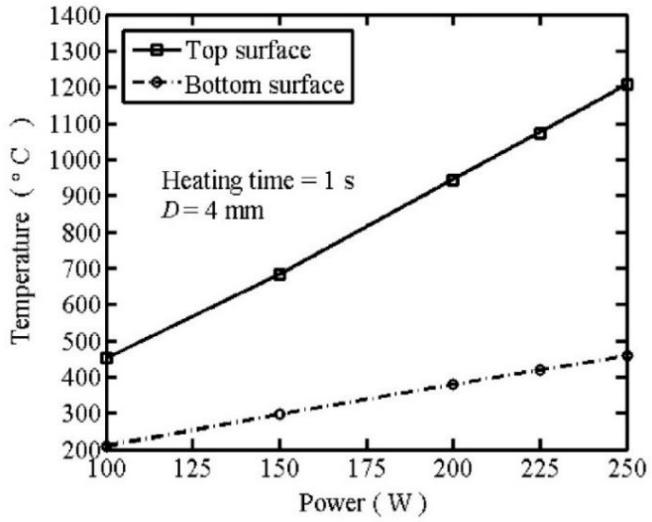

Figure 4.6 Variation of top and bottom surface centre point temperature with laser power for 25 mm × 20 mm × 2 mm workpiece

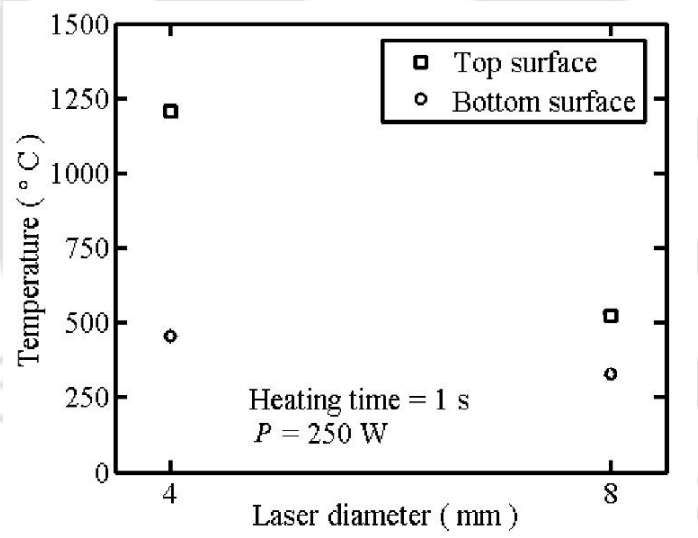

Figure 4.7 Variation of top and bottom surface centre point temperature with beam diameter for 25 mm × 20 mm × 2 mm workpiece

Figure 4.8 (a) and (b) show the variation in temperature and bend angle with time. It was observed that the bend angle was negative in the beginning and then the sheet started to bend along the positive direction. The bend angle became the maximum (in algebraic sense) when the temperatures of the top and bottom surfaces were equal. For moving heat source, the bend angle was negative (away from laser beam) however, it was positive (towards the laser beam) for stationary heat source.

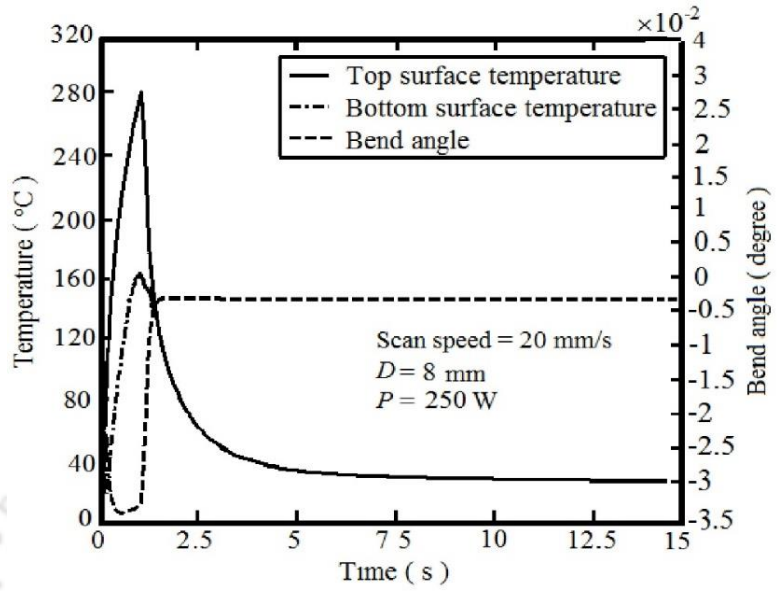

(a)

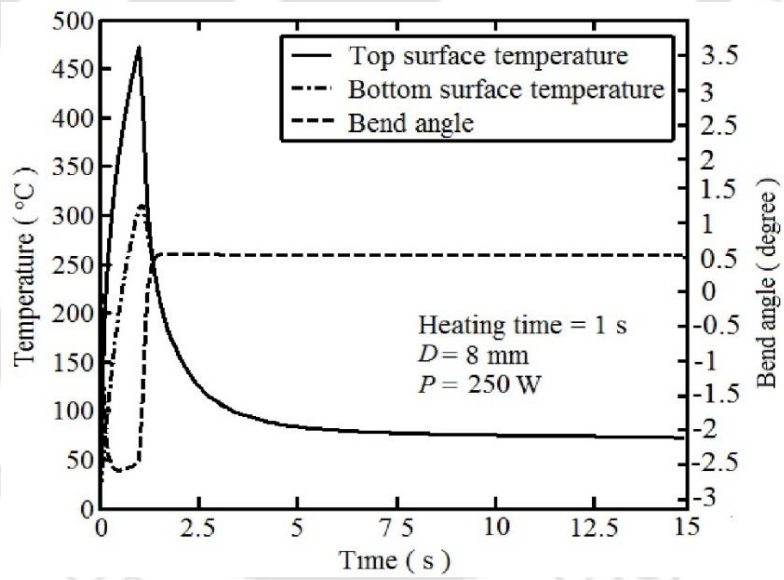

(b)

Figure 4.8 Temperature distributions at the top and bottom surface centre point and variation of bend angle with time for the workpiece of size (25 mm × 20 mm × 2 mm) for (a) moving heat source and (b) stationary heat source

The Fourier number was calculated at different laser powers, for the workpiece of size 25 mm × 20 mm × 2 mm, laser beam diameter at 4 mm and scanning speed of 20 mm/s. The temperature-dependent data (Dixit et al. 2013) for the thermal conductivity, density, and specific heat capacity was used to calculate the magnitude

of thermal diffusivity and Fourier number. It was observed that for lower power of 100–200 W, the magnitude of thermal diffusivity and Fourier number were 9.404×10^{-6} m^2/s and 0.9404 respectively. However, for 225–250 W laser power, the thermal diffusivity and Fourier number were 8.655×10^{-6} m^2/s and 0.8654, respectively. It was observed that, the bending direction was negative for the power range of 100–200 W. However, it was positive for 225–250 W.

In the case of 8 mm laser beam diameter, the Fourier number decreased with increase in laser power (100–250 W) as shown in Table 4.2. For laser power in the range of 100–250 W, the bend angle direction of the workpiece was away from laser source (negative bend). Lee and Yao (2001) obtained Fourier numbers in the range of 6.25 to 7.75, in which the smaller values provide positive (towards the laser beam) bend. Here also, the small Fourier numbers tend to provide positive bend.

Table 4.2 Fourier number for 25 mm × 20 mm × 2 mm for 8 mm laser diameter

Power (W)	Thermal diffusivity (m^2/s)	Fourier number	Bending direction
100	9.404×10^{-6}	0.4702	Negative bending
150	8.655×10^{-6}	0.4327	Negative bending
200	7.784×10^{-6}	0.3892	Negative bending
225	7.784×10^{-6}	0.3892	Negative bending
250	6.766×10^{-6}	0.3383	Negative bending

4.5 Conclusion

In this part of research work, numerical and experimental studies on the laser bending of small size workpiece were carried out. It was observed that the laser bending process was suitable for micro-bending applications by applying stationary and movable heat source. Following conclusions are drawn:

- The bending angle is highly dependent on laser power; as the power increases the bend angle also increases for both stationary and moving heat sources.
- The experimental and simulation result of small size plate bending depicted that the bending angle is highly dependent on type of heat sources; the

stationary heat source provides more bend. A bend angle of about 2.5° could be achieved by a moving heat source and 4.5° by a stationary heat source.

- Changing laser beam diameter from 4 mm to 8 mm changes the bend angle; it is greater for small diameter.
- The pattern of bend angle variation along width direction is different for laser powers of 100 W and 250 W.
- With stationary heat source, the bend angle is more non-uniform across the width (along scan direction) as compared to moving heat source.
- The temperature difference in the thickness direction is increased with the increase of the laser power from 100 W to 250 W.

Chapter 5

Single and Multi-Pass Laser Bending of Strips

5.1 Introduction

This chapter presents experimental and numerical studies on single and multi-pass laser bending of mild steel (AH36) strips. Researchers have studied the effects of different combination of process parameters related to the laser source, material and workpiece geometry on laser bending of metal sheets. The workpiece parameters like sheet thickness, length (perpendicular to scan direction) and width (parallel to scan direction) affect the bend angle.

The bending accuracy was different for different geometries, even when the laser parameters were kept constant. Therefore, the workpiece geometry must be considered to get an accurate estimation of bend angle. Lee and Lin (2002) studied the effect of workpiece thickness on bend angle. They observed that the bend angle increased with the decreases in thickness provided the peak temperature of the workpiece was below the melting point. Shichun and Jinsong (2001) suggested that the length (perpendicular to scanned path) of the workpiece had a little influence on the bend angle. However, Chen et al. (2004b) and Shichun and Jinsong (2001) reported that the bend angle increased with a decrease in the sheet thickness and increased with an increase in the sheet width. The predominant factors having large effect on deformation angle of laser bending process were identified by a number of researchers (Hu et al. 2001; Cheng et al. 1999 and Dixit et al. 2015).

In this work, the effects of workpiece geometry (width and thickness) and laser parameters (laser power, scan speed, laser spot diameters and number of passes) on laser bending of mild steel (AH36) strips were studied experimentally and numerically. Finite element model using ABAQUS® was developed to investigate the size effects on the prediction of the bend angle. Further detailed analysis of the effects of process parameters on bending mechanism and deformation behaviour for multi-

scan mode of operation is presented. Experimental and numerical studies are carried out to explore the insight of the process parameters in terms of bend angle, edge effect, temperature distribution, stress, plastic strain, flexural strength, microhardness and microstructure during single and multi-pass mode of operation.

5.2 Experiment and FEM Simulation

In the present work, the laser bending of mild steel strips was carried out with different sets of workpiece dimensions and laser parameters. Following a design of experiment method, 54 experiments were conducted. The effect of process parameters on bend angle and flexural strength was studied using design of experiments (DOE) technique. In the case of microhardness, DOE technique was not used. The entire procedure is described in the following subsections.

5.2.1 Experimental setup and procedure

In this chapter a parametric study on the effect of process parameters, *viz.*, laser power (P), scan speed (v), laser beam diameter (D), number of passes (N), thickness of strip (t) and width (w) is presented. The sample cutting and bending were performed on a 2.5 kW continues wave (CW) mode CO_2 laser of Make: LVD and Model: Orion 3015 as shown in Fig. 3.3. The laser beam was irradiated in a direction parallel to free edge (along width) of clamped specimens, which was perpendicular to the rolling direction of the strip. After the laser beam irradiation, the heated specimens were allowed to cool naturally. In case of multi pass bending, a gap of 5 s was kept in between two successive irradiations. Bend angles were measured along the width direction at 5 locations, using a coordinate measuring machine (CMM) of Make: Zeiss™ and Model: Vista (Fig. 3.6); the average bend angles are reported. Three-point bending test was performed on the specimens to find out the flexural strength of the specimens. The specimens were placed on the test fixture setup on a 100 kN Universal Testing Machine of Make: INSTRON and Model: 8801J4051 shown in Fig. 3.8 (b). All the samples were tested at room temperature with a constant displacement rate of 5 mm/min. The load was applied on the opposite side of the laser irradiated surface of the specimen along the scan line. The span length was 100 mm. Microstructure of bent strips were examined using an optical microscope of Make: Carl Zeiss™ and

Model: Axiotech-100HD (Fig. 3.16). The microhardness tests were conducted on a microhardness tester (Make: Buehler; Model: Micromet-2101) in transvers direction (perpendicular to thickness and scan direction) and the middle of the bent workpiece thickness. All the measurements were taken in as-polished condition. The hardness was measured using microhardness tester of (Fig. 3.17) with indenting force of 500 gf and dwell period of 20 seconds. The indentations were taken at 1 mm intervals, along perpendicular to the scanned path.

5.2.2 Design of experiment

In the present study, six process parameters, *viz.*, power, scan speed, laser beam diameter, number of pass, thickness and width (scan length) were selected and their effect was studied for laser bending of mild steel. For each parameter three different levels were selected, which are listed in Table 5.1.

Table 5.1 Process parameters and corresponding levels

Process parameter	Symbols	Unit	Level 1	Level 2	Level 3
Power	*P*	W	500	600	700
Thickness	*t*	mm	1	1.5	2
Width	*w*	mm	20	30	40
Number of passes	*N*	-	1	3	5
Scan speed	*v*	mm/min	800	900	1000
Beam diameter	*D*	mm	7.6	9.4	11.4

To determine the effects of laser and geometrical parameters, a set of 27 experiments based on L_{27} orthogonal array (OA) design (Logothetis, 1992), were carried out. The OA consists of 13 columns (factors) and 27 rows (experimental runs). The process parameters i.e., power, thickness, width, number of passes, scanning speed and beam diameter were assigned to columns 1, 2, 5, 7, 9 and 10, respectively according to the standard three levels. Two replicates were carried out at each condition with a total number of 54 experiments.

5.2.3 FEM simulations

To model the strip laser bending, the commercial FEM package ABAQUS® was used. Three-dimensional thermo-mechanical 8-noded brick elements (C3D8T) are used. Details regarding the mesh of heated and nearby region of workpiece, mesh sensitivity and boundary condition have already been discussed in Chapter 3. As illustrated in Table 3.5, mesh sensitivity study was carried out by varying element's size and chosen final element sizes are listed in Table 3.6. The initial range of absorptivity was taken in between 0.1 to 0.9. Bisection method was used to determine the particular value of absorption coefficient by comparing simulation results with experimental results for four different parameter combinations, *viz.*, experiment (Exp.) number 1, 8, 22, and 27. It provided the absorption coefficient of material as 0.85. In the last pass, the cooling process was accelerated which is described in Eideh et al. (2014) and it was adopted to minimize the computational time in this work. Temperature-dependent thermal and mechanical properties of material are considered and taken from Zhang et al. (2004). The density of mild steel was taken constant as 7850 kg/m^3.

5.3 Results and Discussion

To know the effect of parameters on the bend angle, individual analyses of experimental and simulation results were carried out and then comparison was made in between these two results. Also the effects of process parameters on mechanical properties of material were studied.

5.3.1 Experimental and FEM results

The numerical simulation results for bend angle were compared with experimental results to verify the validity of the numerical simulation. Table 5.2 shows the percentage deviation between experimental and numerical simulation results. It can be seen that the maximum deviation is 11.1% for experiment (Exp.) number 26.

Table 5.2 Experimental and simulated bend angle

Exp. number	Parameters						Response				Dev. (%)
							Bend angle (degree)				
	P (W)	*t* (mm)	*w* (mm)	*N*	*v* (mm/min)	*D* (mm)	Replicate 1	Replicate 2	Avg.	Sim.	
1	500	1	20	1	800	7.6	0.83	0.87	0.85	0.84	1.2
2	500	1	30	3	900	9.4	2.1	2.3	2.2	2	9.1
3	500	1	40	5	1000	11.4	2.8	2.95	2.88	2.6	9.7
4	500	1.5	20	3	900	7.6	2.4	2.6	2.5	2.64	5.6
5	500	1.5	30	5	1000	9.4	1.15	1.25	1.2	1.12	6.7
6	500	1.5	40	1	800	11.4	0.33	0.31	0.32	0.34	6.3
7	500	2	20	5	1000	7.6	2.35	2.25	2.3	2.1	8.7
8	500	2	30	1	800	9.4	0.24	0.26	0.25	0.25	0.0
9	500	2	40	3	900	11.4	0.33	0.31	0.32	0.35	9.4
10	600	1	20	3	1000	11.4	2	1.9	1.95	1.82	6.7
11	600	1	30	5	800	7.6	4.1	4.3	4.2	4.6	9.5
12	600	1	40	1	900	9.4	0.72	0.75	0.735	0.66	10.2
13	600	1.5	20	5	800	11.4	2.5	2.3	2.4	2.6	8.3
14	600	1.5	30	1	900	7.6	1	1.08	1.04	1.1	5.8
15	600	1.5	40	3	1000	9.4	2.2	2.1	2.15	2.3	7.0
16	600	2	20	1	900	11.4	0.48	0.52	0.5	0.55	10.0
17	600	2	30	3	1000	7.6	2.34	2.46	2.4	2.5	4.2
18	600	2	40	5	800	9.4	3.9	4	3.85	4.26	10.6
19	700	1	20	5	900	9.4	3.6	3.7	3.65	3.35	8.2
20	700	1	30	1	1000	11.4	0.64	0.68	0.66	0.6	9.1
21	700	1	40	3	800	7.6	2.7	2.74	2.72	2.75	1.1
22	700	1.5	20	1	1000	9.4	0.7	0.71	0.7	0.72	2.9
23	700	1.5	30	3	800	11.4	1.75	1.85	1.8	1.93	7.2
24	700	1.5	40	5	900	7.6	3.95	3.75	3.85	4.2	9.1
25	700	2	20	3	800	9.4	2.23	2.37	2.3	2.55	10.9
26	700	2	30	5	900	11.4	2.8	2.6	2.7	3	11.1
27	700	2	40	1	1000	7.6	1.14	1.22	1.18	1.15	2.5

Avg. – Average, Exp. – Experiment, Sim. – Simulation, Dev. – Deviation

Figure 5.1 shows the bend angle deviation of experimental and simulation results along scanning direction for the strip. For 500 W laser power, the bend angle

is almost uniform along width direction after the first pass (Fig. 5.1 (a)). In Fig. 5.1 (b) and (c), the bend angle is increasing along width and it is the maximum at the end of the scanning line; however, the percentage variations are very small. It observed that the experimental results have a good agreement with the simulated ones.

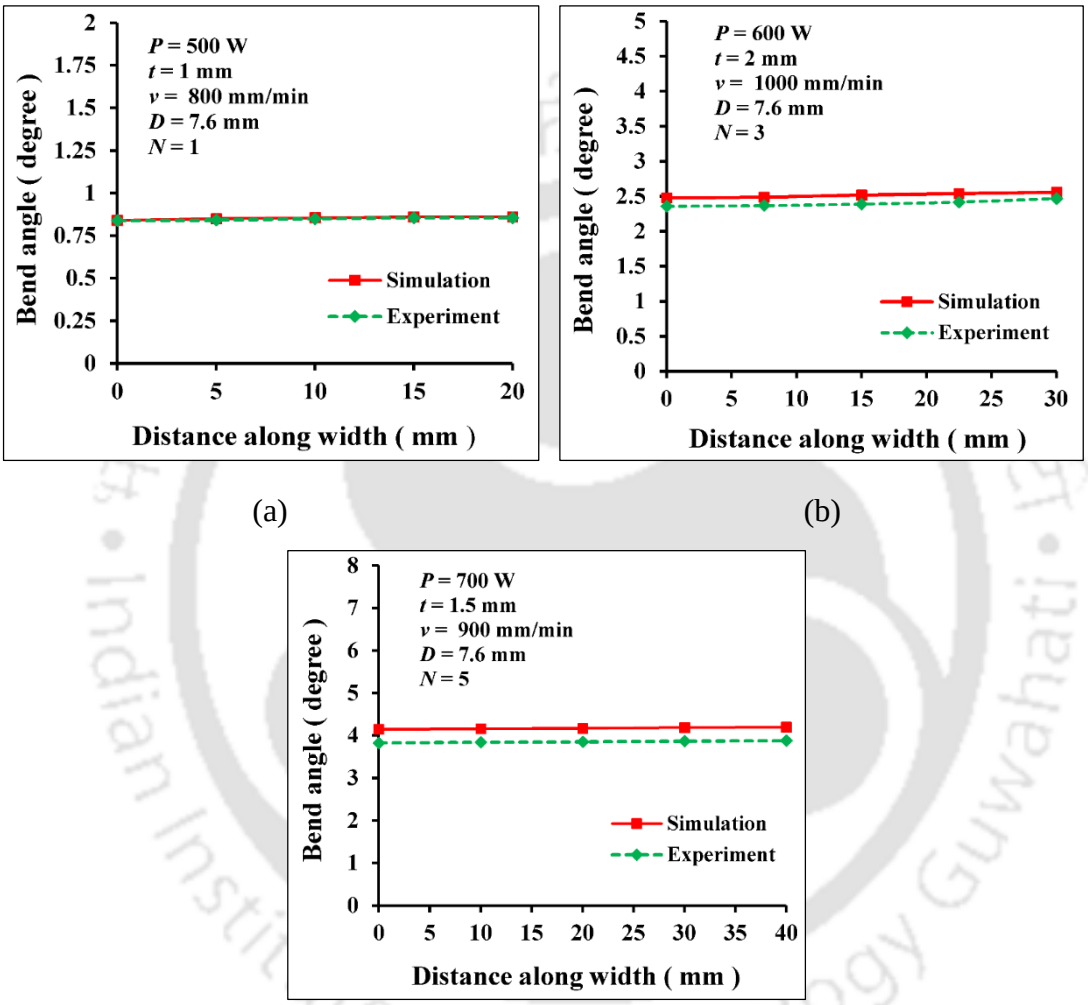

Figure 5.1 Comparison between experimental and simulation results for bend angle variation at different process parameters for (a) 20 mm width (b) 30 mm width and (c) 40 mm width

Fig. 5.1 (a) pertains to first pass of laser bending and depicts almost zero error between the experiments and the simulation. As the number of pass increases, the absorptivity decreases due to the deterioration of the graphite coating. However, in this work, only a constant value of 0.85 is used in the simulations. Hence, it is expected that the

accuracy of the simulation will reduce with the number of passes. That is why some deviation is observed between experiments and simulation in Fig. 5.1 (b), which pertains to third pass. The amount of deviation is even more in Fig. 3(c) representing the bend angle after fifth pass; however, it is still below 9%.

Figure 5.2 shows the temperature and bend angle history in FEM simulation. Across the strip thickness, the local irradiation of laser beam produces a steep temperature gradient, which is the main reason that causes the bending of metal strip. In each successive pass, the peak temperatures at both top and bottom surfaces were higher than those in previous laser pass, as the workpiece was preheated.

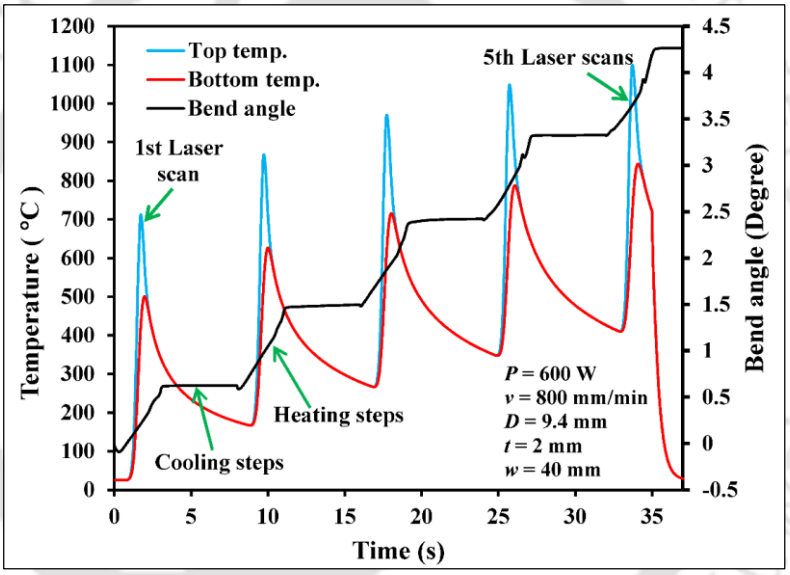

Figure 5.2 Variation of temperature and bend angle with time

The bend angle increased with the increase in the number of passes due to preheating of the workpiece in the previous pass. Also it can be seen that the bend angle increased during the laser heating phase and it was almost constant during the cooling phase. The temperature difference between top and bottom surfaces, in a sequence of first pass to fifth pass, were 212 °C, 241 °C, 255 °C, 261 °C and 256 °C, respectively, and corresponding bend angles were 0.62°, 1.492°, 2.42°, 3.35° and 4.26°. The results show that the temperature difference gets increased with the number of passes resulting in an increase of bend angle after each pass.

Table 5.3 shows the relation between the temperature gradient and bend angle increment after each pass. It is observed that the increment in bend angle is positively

correlated with temperature gradient. The temperature gradient increased up to 4th laser pass and then decreased. Similar trend is observed in the bend angle increment.

Table 5.3 relation between temperature gradient and bend angle for P = 600 W, v = 800 mm/min, D = 9.4 mm, w = 40 mm and t = 2 mm

Laser pass	Total bend angle (degree)	Incremental bend angle (degree)	Temperature gradient (°C)
1	0.62	0.62	212
2	1.492	0.872	241
3	2.42	0.928	255
4	3.35	0.93	261
5	4.26	0.91	256

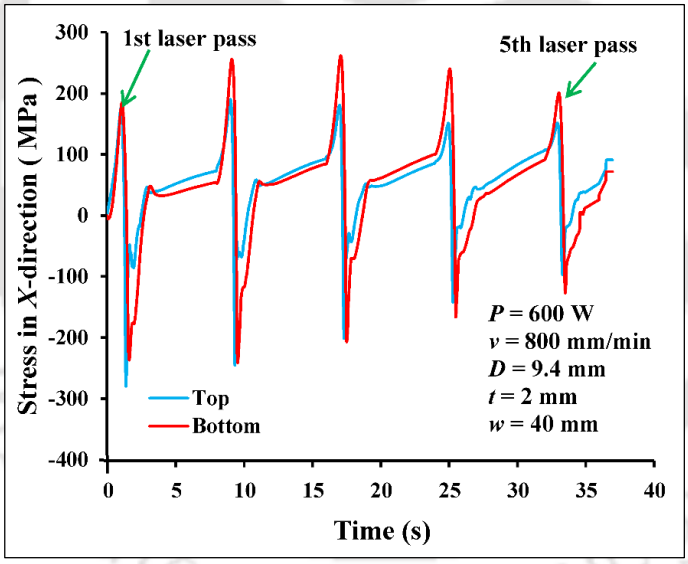

Figure 5.3 X-direction (along length) stress at top and bottom surfaces of the workpiece

The X-direction (along length, perpendicular to scan direction) stress history was studied at the centre point of the workpiece, at the top and the bottom surface, as shown in Fig. 5.3. It is observed that during each pass both tensile and compressive stresses were induced at top and bottom surfaces. The magnitude of the stress decreased with successive laser beam irradiations due to the increase in workpiece temperature. At the end of the pass tensile residual stresses remained at both surfaces.

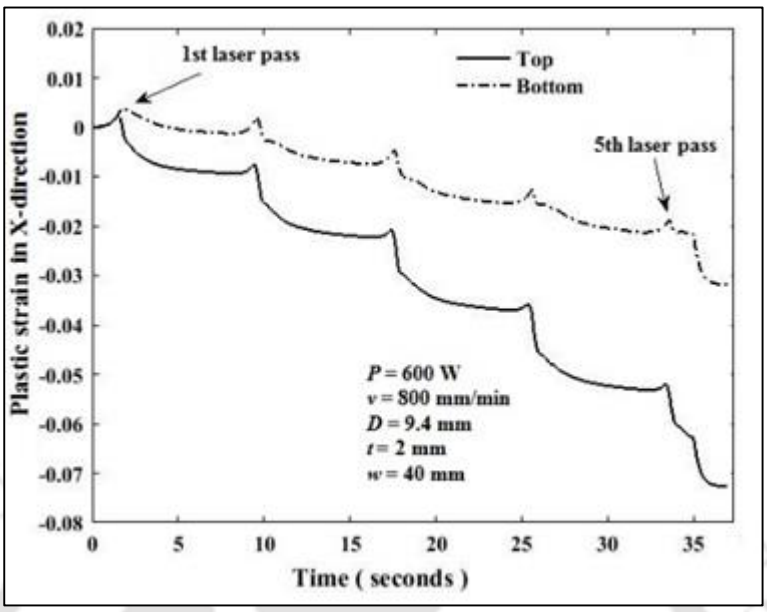

Figure 5.4 Plastic stain in *X*-direction at top and bottom surface centre points of the workpiece

Figure 5.4 shows plastic strain in *X*-direction at the top and the bottom side of the workpiece. It is seen that the plastic strain is compressive at both top and bottom surface centre points. The difference between plastic strain at top and bottom surface centre points increases with increasing number of passes that leads to increase in bend angle after each pass.

5.3.2 Microhardness

To illustrate the effect of thickness and number of passes on microhardness value of mild steel strip, four additional laser bending experiments, as per parameters indicated in Fig. 5.5 (a) and (b), were conducted. The influence of workpiece thickness and number of passes on microhardness value are illustrated in Fig. 5.5 (a) and (b), respectively. It is seen that the microhardness profile exhibited a symmetric characteristic with a higher hardness at the centre of scanned zone. The microhardness increased with decrease in thickness (Fig. 5.5 a) and with increase in number of passes (Fig 5.5 b).

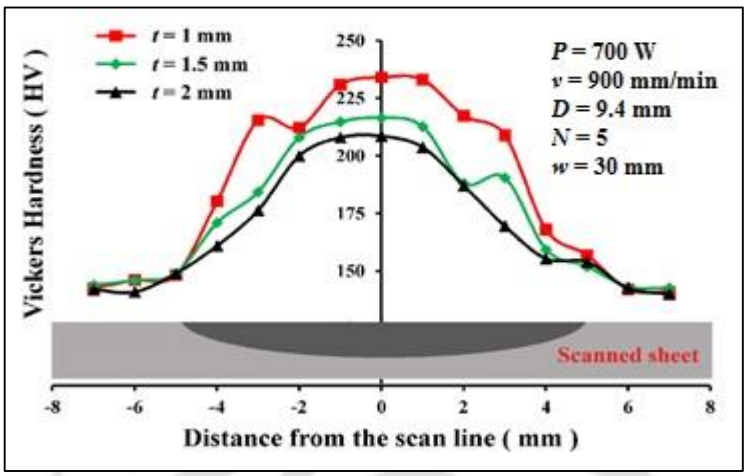

(a)

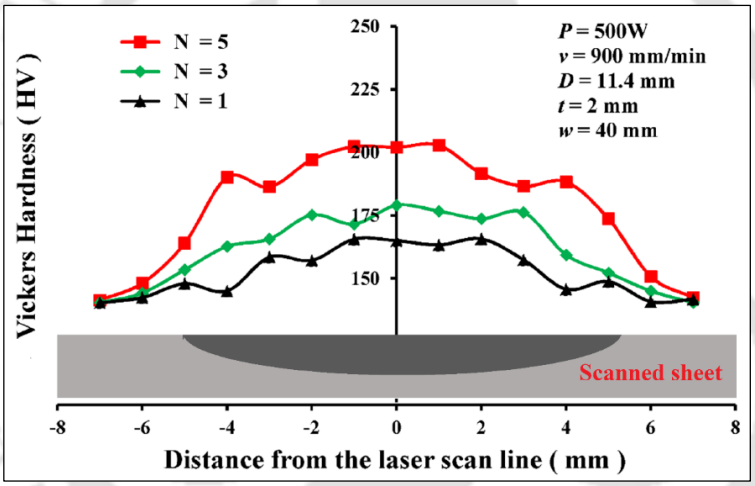

(b)

Figure 5.5 Microhardness profile across thickness of the laser bending process for (a) different thickness and (b) number of passes

The microhardness of the laser scanned region was higher than the base material due to the grain size becoming smaller and closer compared to base material under the action of temperature gradient (Yang et al. 2010). Upon heating the steel surface above the upper critical temperature, ferrite structure changes to austenite, which dissolves the sufficient amount of carbon. Due to rapid cooling during laser forming, carbon is not able to precipitate and austenite structure is transformed to martensite, providing high microhardness (Kennedy et al. 2004).

As the thickness of the strip decreases, the maximum temperature increases, which also implies high rate of cooling, high plastic strain and sufficient interaction time at high temperature. This produces finer structure with more martensite having retained carbon that increases the microhardness. Cheng and Yao (2001) observed that the forming of the sheets at higher laser power results a finer grain size and higher hardness. Reducing the thickness has a similar effect on the temperature and plastic strain. Hence, it is not surprising that microhardness of the laser bent strip increases with reducing thickness, if all other parameters are kept the same. Microhardness also increases with increase in the number of passes. As shown in Fig. 5.2, with increasing number of passes, the maximum temperature increases. Similarly, Fig. 5.4 shows that the plastic strain increases with the number of passes. The combined effect of large cooling rate, high plastic strain and more interaction time increases the microhardness with the number of passes. It is worth mentioning here that at certain conditions, Cheng and Yao (2001) observed an increase in the hardness of AISI 1010 steel up to two laser passes and subsequently some softening with increasing number of passes due to recovery/recrystallization. In this work, softening was not observed for the chosen processing conditions.

5.3.3 Flexural test

The flexural test for straightening of laser bent specimens were carried out for all samples (two replicates). Details of experimental flexural test measurement was discussed in chapter 3 in Fig. 3.8 (b). Figure 5.6 shows that the flexural stresses for the laser scanned specimens increased as compared to parent metal. Table 5.4 shows all the experimental results of flexural strength of laser scanned specimens. Results show that flexural strength was influenced by laser specific energy. Flexural strength increases with the increase in laser specific energy. The laser specific energy is defined as the ratio of power to the product of scan speed and laser beam diameter i.e., ($P/(vD)$). The value of the flexural strength is 985 MPa, 730 MPa, and 679 MPa at a specific energy of 6.9 J/mm^2, 4.74 J/mm^2, 4.38 J/mm^2, respectively while the flexural strength of parent material is 582 MPa.

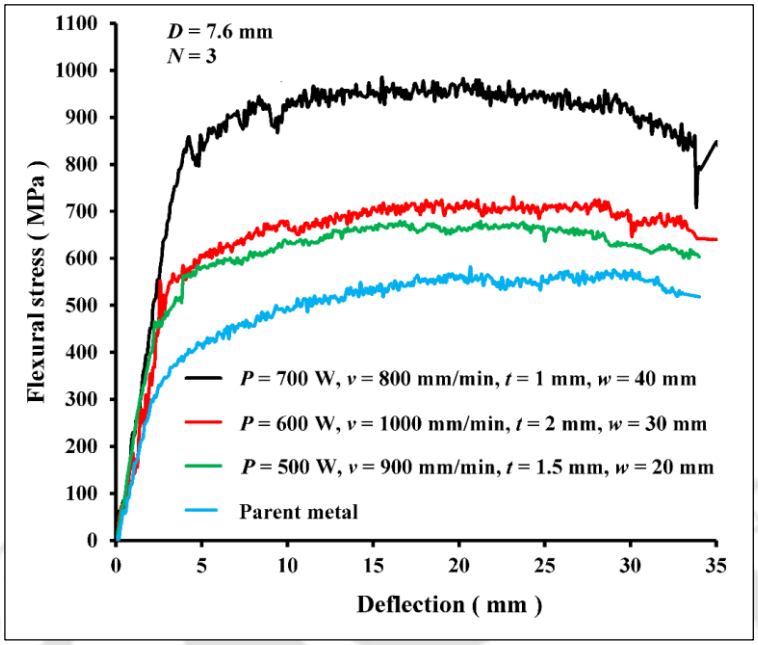

Figure 5.6 Flexural stress variation with deflection for three different parameters and base material

Table 5.4 The flexural strength of laser scanned specimens

Exp. number	Flexural strength (MPa)	Exp. Number	Flexural strength (MPa)	Exp. Number	Flexural strength (MPa)
1	603.6	10	697.7	19	952.8
2	631.4	11	1056	20	608.3
3	709.4	12	603	21	985
4	679	13	898	22	611.8
5	739.7	14	623	23	831.4
6	594	15	723.8	24	995.2
7	793.2	16	613.7	25	868.2
8	588.6	17	730	26	923
9	611.4	18	1020.7	27	689.7

5.3.4 Main effects of factors on bend angle and flexural strength

The average values of experimental bend angle and flexural strength for each factor, *viz.*, *P*, *t*, *w*, *N*, *v* and *D* at three levels, *viz.*, level 1, level 2 and level 3 were obtained from Table 5.2. Figure 5.7 and 5.8 show the main effect plots of factors for bend angle and flexure strength. It is observed from Fig. 5.7 (b), (d) and (e) that the bending angle decreased with increasing beam diameter, strip thickness and scan speed. It is due to decreased heat input that produced low energy density and plastic deformation in the heated region of the workpiece. From Fig. 5.7 (a), (c) and (f), it is found that with increase in the number of passes, laser power and width, the bend angle increases. This is due to the higher plastic deformation produced in the heated region of the workpiece.

The main effects of parameters on flexural strength is similar as the effects of parameters on bend angle. The only difference is in the effect of thickness of the workpiece on the flexural strength. It can be concluded that flexural strength increases when the number of passes, laser power, thickness and width are increased as shown in Fig. 5.8 (a), (c), (d) and (f), respectively. Figure 5.8 (b) and (e) show that the flexural strength decreased with increasing beam diameter and scan speed.

The main effect plots of factors are shown in Fig. 5.7 and Fig. 5.8. Figure 5.7 shows that $P_3t_1w_3N_3v_1D_1$ combination of parameters provides the highest bend angle; here subscripts denote the level of a particular variable. Similarly, $P_3t_3w_3N_3v_1D_1$ combination of parameters provides the maximum flexural strength. Analysis of variance (ANOVA) tables are shown in Table 5.5 and Table 5.6. The F-ratios were obtained at 95% level of significance. The percentage contributions of factors for bend angle in descending order are number of passes (66.21%), power (8.83%), beam diameter (8.51%), thickness (3.07%), scan speed (1.74%) and width (0.41%). For flexural strength, the percentage contributions of factors in descending order are number of passes (59.18%), power (21.65%), scan speed (12.55%), beam diameter (4.13%), width (0.52%) and thickness (0.26%).

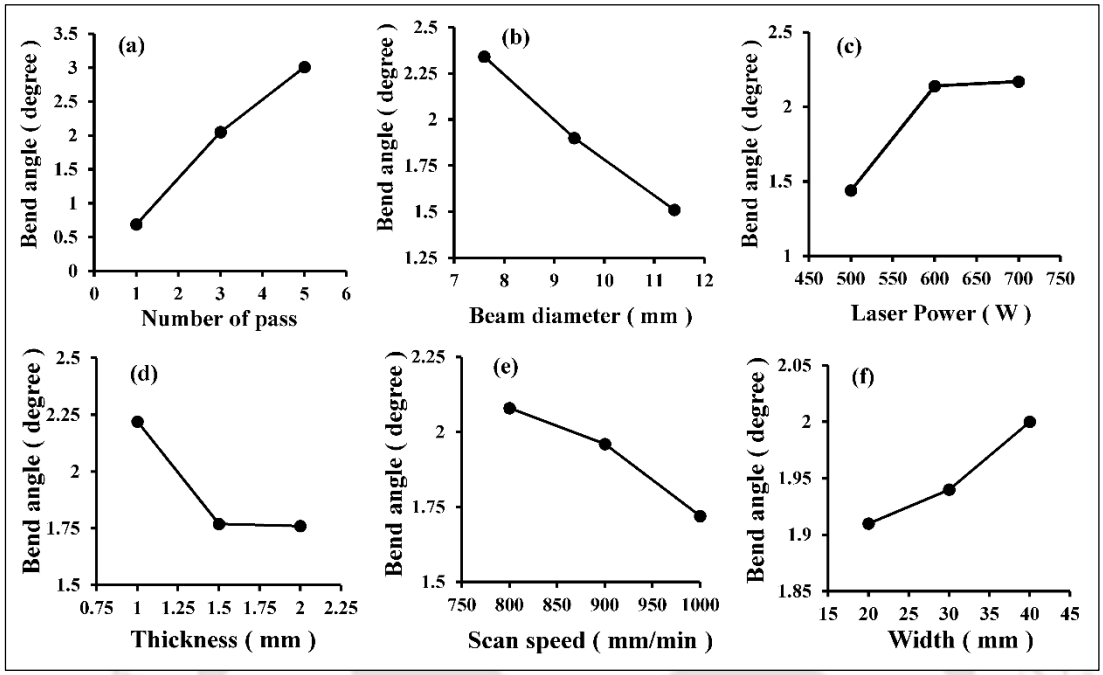

Figure 5.7 Plot of main effects for bend angle

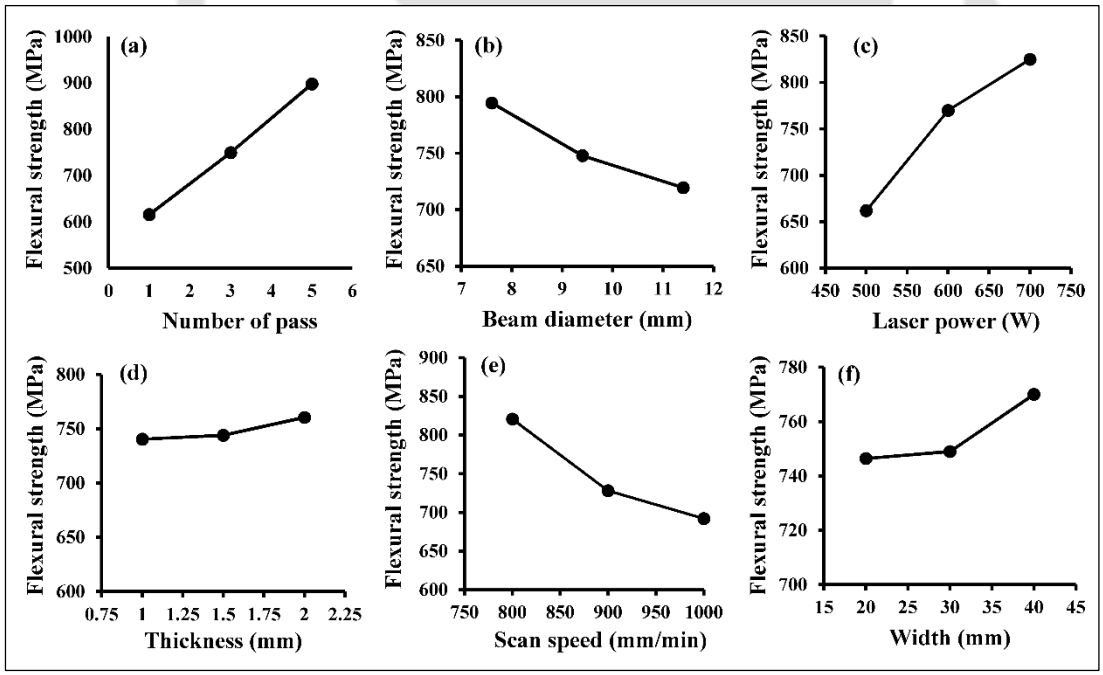

Figure 5.8 Plot of main effects for flexural strength

Table 5.5 ANOVA table for bending test

Factors	DOF	SS	MSS	F-ratio	p-value	Contribution (%)
P	2	6.5185	3.26	46.81	0.000	8.83
t	2	2.2625	1.13	16.25	0.000	3.07
w	2	0.3046	0.15	2.19	0.130	0.41
N	2	48.872	24.44	350.93	0.000	66.21
v	2	1.2844	0.64	9.22	0.001	1.74
D	2	6.278	3.14	45.08	0.000	8.51
$P \times t$	4	1.9062	0.477	6.84	0.001	2.58
$N \times t$	4	2.6086	0.65	9.37	0.000	3.53
$t \times w$	4	1.7561	0.44	6.3	0.001	2.38
Error	29	2.0193	0.07			2.74
Total	53	73.810				100.00

DOF – Degree of Freedom, SS – Sum of Squares, MSS – Mean Sum of Squares

Table 5.6 ANOVA table for flexural strength

Factors	DOF	SS	MSS	F-ratio	p-value	Contribution (%)
P	2	132462	66231	88.60	0	21.65
t	2	1604	802	1.07	0.37	0.26
w	2	3199	1600	2.14	0.16	0.52
N	2	362118	181059	242.22	0	59.18
v	2	76781	38390	51.36	0	12.55
D	2	25259	12629	16.9	0	4.13
Error	14	10465	748			1.71
Total	26	611887				100

DOF – Degree of Freedom, SS – Sum of Squares, MSS – Mean Sum of Squares

To determine the relationship between factors for bending angle and flexural strength, regression analysis was performed. A second-degree polynomial was fitted for laser bending and flexural strength. The coefficient of determination (R^2) indicates how well the model fits the data. A value closer to 1 indicates a good fitting. The

regression equation in terms of factors was obtained and Eq. 5.1 for the bend angle (in degree) and Eq. 5.2 for the flexural strength (in MPa) are expressed as

$$\begin{aligned}\alpha_b &= -25.4757 + 0.0481691P + 1.93963t - 0.138753w + 0.833N \\ &+ 0.031939v - 0.245225D - 0.0000469031P^2 + 0.0042649Pt \\ &+ 0.000462805PD + 0.0113541wN + 0.0120697wD \\ &+ 0.0007375NP - 0.219947Nt - 0.0460417N^2 \\ &- 0.0454027ND - 0.0000195455v^2 - 0.451744Dt \\ &+ 0.0105019D^2\end{aligned} \tag{5.1}$$

$$\begin{aligned}S_F &= -298.273 + 4.66945P - 0.966667t + 133.214N - 0.678289v \\ &+ 0.938234w - 46.7792d - 0.00286722P^2 - 0.026975\,PD \\ &- 0.0439\,NP + 1.49861N^2 - 4.75015\,ND + 3.03622\,D^2\end{aligned} \tag{5.2}$$

The value of coefficient of determination R^2 is 0.948 and adjusted R^2 is 0.921. For flexural strength, the coefficient of determination R^2 is 0.978 and Adjusted R^2 is 0.965. From Table 5.7, it can be seen that the deviation (percentage errors) in between estimated and experimental bend angle results is very small. Also the model simulation result shows small deviation (5.4%) from experimental and estimated results.

Table 5.7 Additional test for confirmation

	Optimal condition			**Deviation**
	Estimation (regression)	**Experiment (Exp.)**	**Simulation (Sim.)**	**[(Exp. – regression)/ Exp.]×100 (%)**
Level	$P_3t_1w_3N_3v_1D_1$	$P_3t_1w_3N_3v_1D_1$	$P_3t_1w_3N_3v_1D_1$	-
α_b	4.16	4.4	4.5	5.45

5.3.5 Microstructure

The microstructures of laser irradiated workpiece were studied using optical microscope to determine the effect of the process parameters on the structure of the materials. The specimens were ground with silicon carbide papers of several grades

(400–2000 grit size) followed by velvet polishing with 1 µm alumina particles size. It removed 0.1 mm thickness from the top of laser irradiated surface. All polished specimens were etched with 95% ethanol and 5% nitric acid for 20 seconds. Figure 5.8 shows the micrographs for the laser irradiated mild steel strip. It reveals that the grain size in laser irradiated region is significantly smaller than in the outer-region (Fig. 5.8).

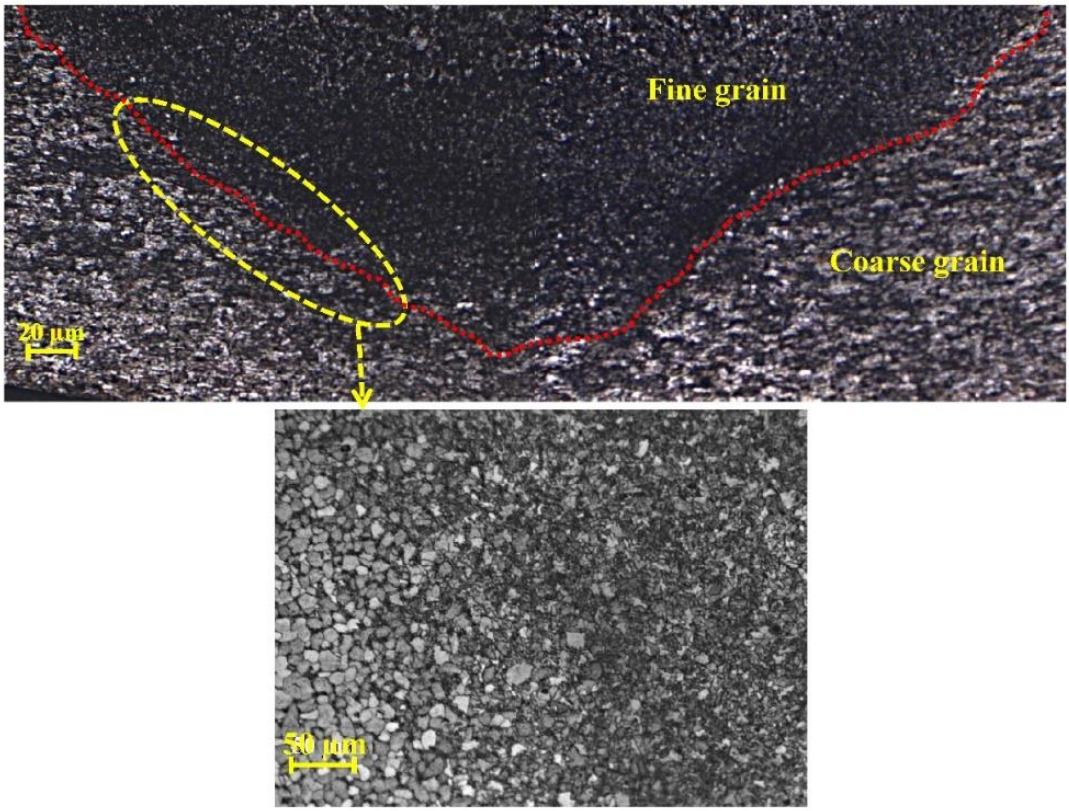

Figure 5.8 Optical microstructures at the cross section perpendicular to the scanning (along thickness direction) (×10 magnification)

The laser irradiated zone in mild steel strip has different grain size along thickness due to temperature variation. Grain size measurement was carried out by using the line intercept method as the grains were not equiaxed. The change in the number of laser pass on workpiece caused grain refinement in the laser irradiated zone. Figure 5.9 (a)–(d) shows microstructures, at a particular set of laser parameters (P = 700 W, v = 800 mm/min, t = 1 mm, w = 40 mm and D = 7.6 mm), at the top surface of laser irradiated direction after 5, 3 and 1 laser passes as well as base metal strip without laser irradiation. The average grain sizes are 7.63 µm, 9.89 µm 11.5 µm

and 15 µm, respectively. As the number of laser pass increase, the grain size reduced due to plastic deformation of the material during the process.

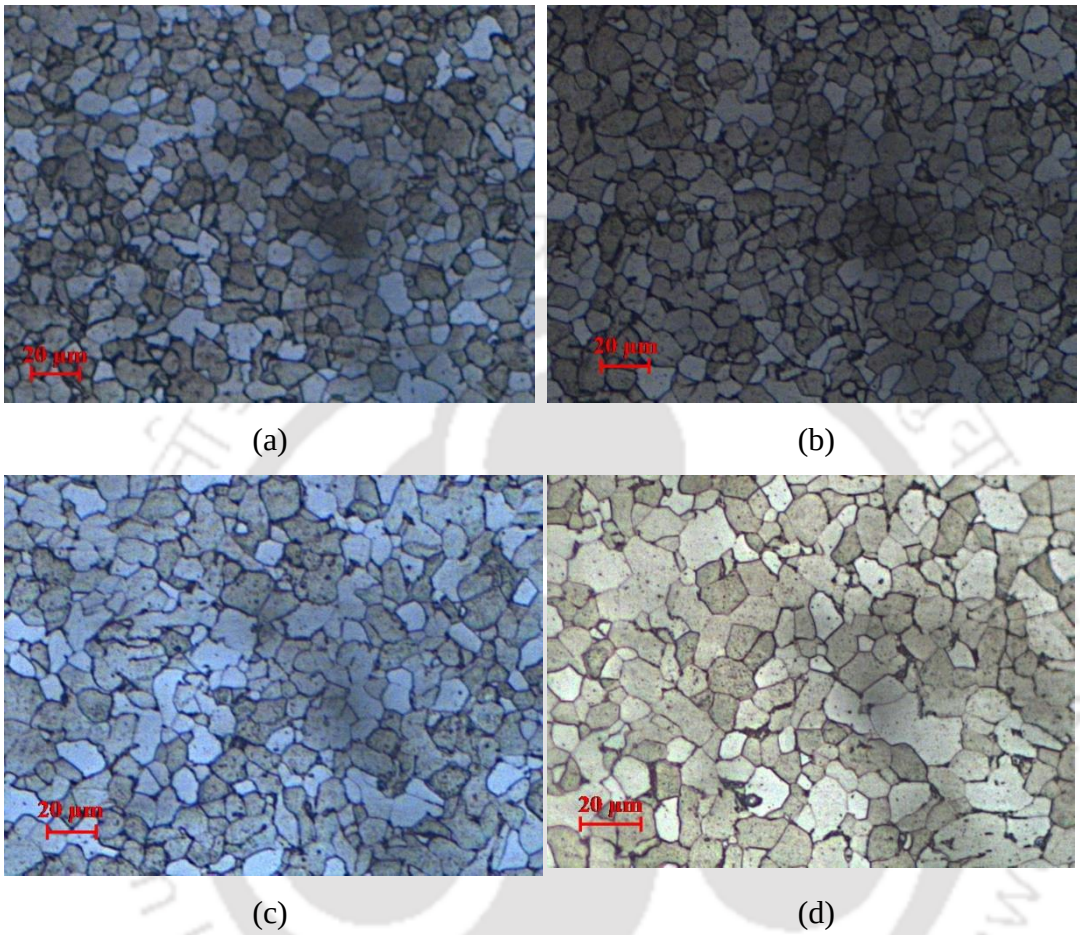

(a) (b)

(c) (d)

Figure 5.9 Optical microstructures at the centre of laser irradiated mild steel surface from top side (×40 magnification): (a) after fifth laser pass (b) after third laser pass (c) after first laser pass and (d) base plate (before laser bending)

Figure 5.10 (a)–(c) shows the microstructure after 5th laser pass on laser irradiated mild steel strips of three thicknesses. The process parameters are as follows: P = 700 W, v = 800 mm/min, w = 40 mm, D = 7.6 mm and N = 5 pass. The average grain sizes are 7.63 µm, 8.32 µm and 8.65 µm for 1 mm, 1.5 mm and 2 mm thickness strip, respectively. Smaller the thickness of the strip, higher was the temperature of the top surface. Therefore, the grain size was smaller for smaller strip thickness. This implies that thinner the strip, the harder becomes the laser irradiated surface.

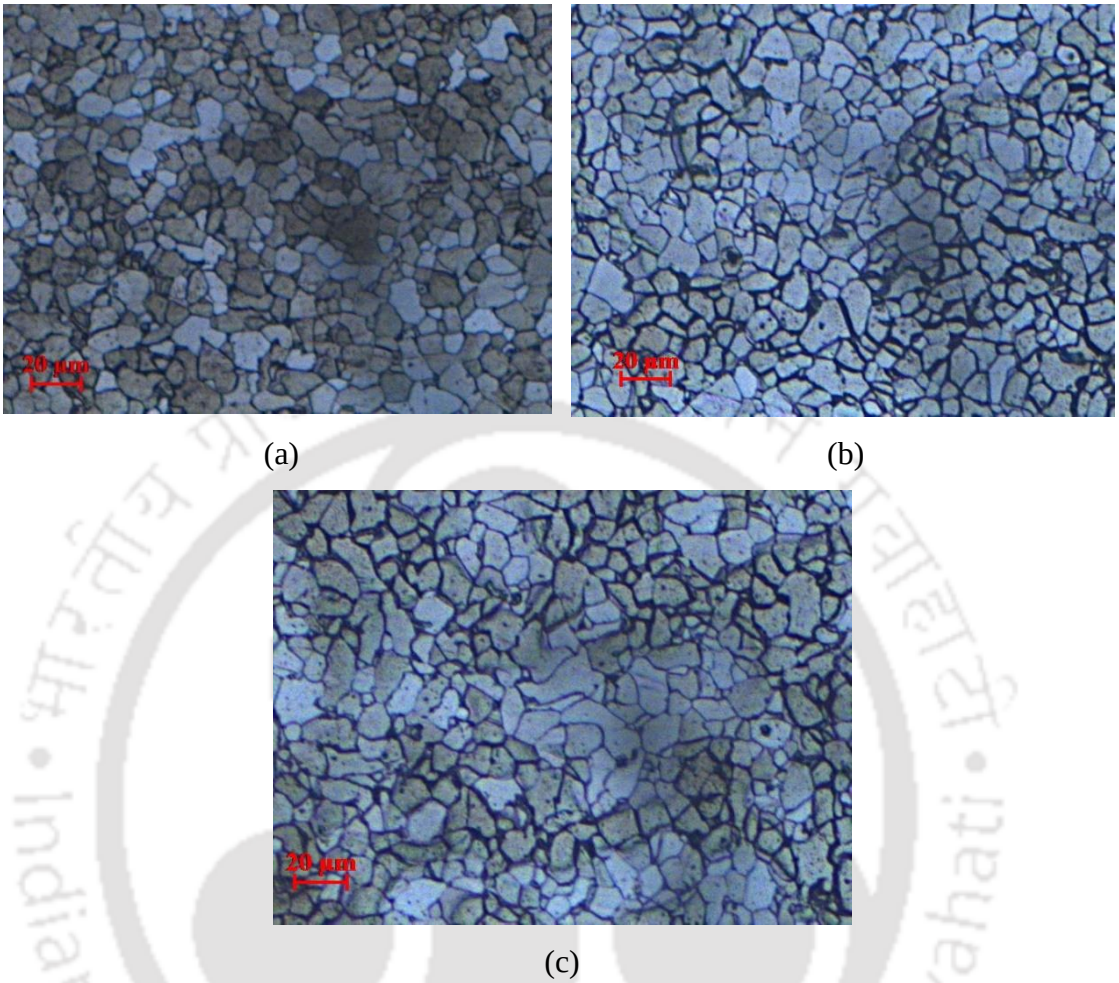

(a) (b)

(c)

Figure 5.10 Optical microstructures of laser irradiated surface after 5th laser pass of mild steel strip along laser scan line (×40 magnification) for strip thicknesses of (a) 1 mm, (b) 1.5 mm and (c) 2 mm

5.4 Conclusion

This chapter presented numerical and experimental study on the single and multi-pass laser bending of mild steel strips. On the basis of the obtained experimental and simulation results, the following conclusion are made:

- Experimental results have a good agreement with analytical results due to inverse estimation of absorption coefficient. The maximum deviation between experimental and numerical simulation results is 11.1%. This predictability provides the confidence in using the process in industry.

- The maximum bend angle was obtained at the following combination of the parameters: 700 W power, 1 mm thickness, 40 mm width, 5 number of passes, 800 mm/min scan speed and 7.6 mm beam diameter.
- The contributions of number of passes, power, beam diameter, thickness, scan speed and width were 66.21%, 8.83%, 8.51%, 3.07%, 1.74% and 0.41%, respectively. The corresponding values for flexural strength were 59.18%, 21.65%, 4.13%, 0.26%, 12.55% and 0.52%, respectively.
- The microhardness profile exhibited a symmetric characteristic with a higher hardness at the centre of scanned zone. The microhardness values get increased with decrease in sample thickness and an increase in number of passes.
- The flexural strength of laser scanned specimens was increased as compared to parent metal.
- The edge effect on strip bending is very small in both experimental as well as simulation result.
- As the number of laser passes was increased, the mean grain size of the laser irradiated strip reduced. The mean grain size increased with the thickness of laser irradiated strip for a particular set of laser parameters.

Chapter 6

Laser Bending of Friction Stir Welded Sheets

6.1 Introduction

Most of the researchers carried out FEM modelling of homogeneous sheets. It is not uncommon to encounter a situation where the material properties as well as thickness of sheets are not uniform. One such case is the bending of a sheet, which is prepared by joining two sheets by friction stir welding (FSW) process. FSW is a solid state joining process that uses a non-consumable rotating welding tool to generate frictional heat at the welding location. FSW has created a worldwide attraction in automobile, aerospace and shipbuilding sectors. The forming behaviour of FSW sheets has been studied by Ramulu et al. (2013) and Valvi et al. (2015). Safari and Farzin (2014) have evaluated various irradiating schemes for the laser bending of tailored machined blanks. In tailored machined blanks, thickness is non-uniform, but the properties are same.

In this study the laser bending of the friction stir welded aluminium alloy 5052-H32 sheets is accomplished experimentally and studied numerically. For proper control of the process, it is very important to develop a reliable mathematical model of the process. Here, a finite element model of the process was developed using ABAQUS® package. The temperature-dependent thermal and mechanical properties of the base material as well as friction stir welded zone are not readily available. Hence, there is a need to develop an efficient procedure for determining material properties (thermal and mechanical), beam radius and absorptivity by an inverse procedure.

Inverse heat conduction problems have been solved by a number of researchers. Several researchers have applied inverse heat conduction analytical models to manufacturing processes. Mishra and Dixit (2013) used inverse method to estimate thermal diffusivity, beam radius and absorptivity of sheet in laser forming. Sequential quadratic programming (SQP) method was used for minimizing the error

between the estimated (simulation) and experimentally measured temperature. Minimization of the objective function was carried out by a heuristic method by Chandrasekaran et al. (2012) in machining optimization and Eideh and Dixit (2013) for predicting the thermal diffusivity, thermal absorptivity and laser beam radius, in laser bending process.

In this work, instead of one pyrometer, two pyrometers were used to measure the temperature of the sheet at two locations in the experiment as was done by Eideh and Dixit (2013) for estimating thermal parameters. For minimizing the error, instead of a sequential quadratic programming method, a more efficient heuristic method was used. At different temperatures, thermal diffusivity, thermal absorptivity, specific heat, density and beam radius were determined by minimizing the error between measured (experiment) and simulated temperatures. The procedure of how to measure the temperature by using two pyrometers has been discussed in detail in Chapter 3, Section 3.3.3. Detailed inverse procedure has been described in this chapter. The temperature dependent flow stress of the material was inversely obtained by measuring the bend angle. After getting the temperature dependant material properties, simulation was conducted using these material properties for bending of friction stir welded aluminium alloy 5052-H32 plate by considering both thickness and property variations in the weld zone. The simulation results were validated with the experimental results.

6.2 Methodology for Inverse Estimation of Material Properties

In this section, the inverse estimation procedure is described in detail. Figure 6.1 shows top and bottom views of the sheet on which a laser beam scans along *y*-direction and locations of pyrometers. The sheets of size 100 mm × 50 mm × 2 mm were taken. The first pyrometer was located at middle of scan-line from the bottom side having coordinates as (35, 25, 2) mm. The offsets between two pyrometers are 10 mm along width and length directions (Fig. 6.1). The bottom surface temperature is measured at these two locations. Based on the temperature variations with time at these two locations, the unknown parameters, *viz*., thermal diffusivity, thermal absorptivity, specific heat, density and laser beam radius were determined by minimizing the error between measured (experimental) and simulated temperatures.

The details of numerical simulation, mesh refinement and time-increment of the laser forming process have been discussed in Chapter 3. During the simulation, thermal heat flux (q), and boundary conditions are as per Eq. 3.1–3.4.

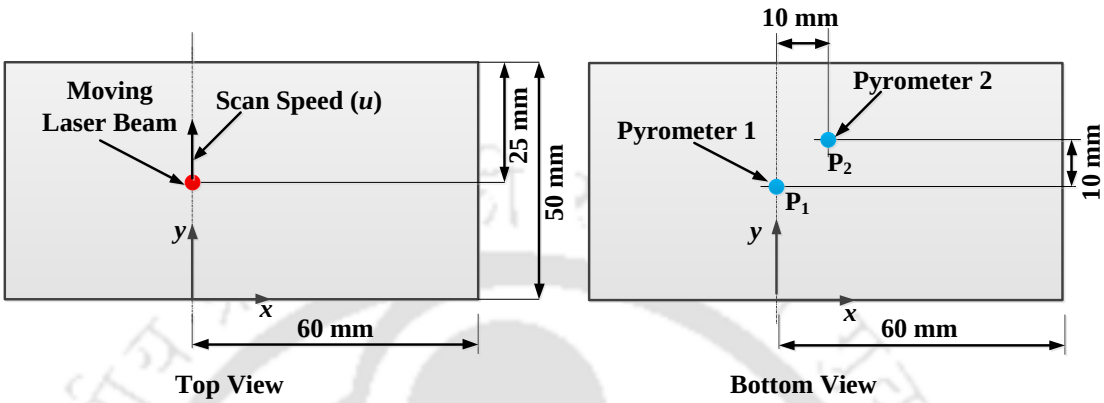

Figure 6.1 Top and bottom view of the workpiece showing the laser beam path and location of pyrometers

For experimental study, six different laser powers (500, 600, 700, 800, 900 and 1000 W) and a fixed scan speed of 300 mm/min were chosen as working parameters for recording temperature. Table 6.1 shows the experimental results of temperature at the bottom of the workpiece at points P_1 and P_2, where the two pyrometers are fixed. It recorded the temperature reading for a total of 15 seconds. Simulations are carried out by using ABAQUS® package.

Temperature dependent thermal diffusivity, thermal absorptivity, specific heat, density and laser beam radius were observed by heuristic optimization method based on minimizing the error between measured (experiment) and simulated temperatures. Temperature dependent flow stress of the material was inversely obtained by measuring the bend angle. Average temperature of top and bottom surface was considered to find out temperatures dependent mechanical and thermal properties. Detailed inverse procedure is described in the following subsections.

Table 6.1 Experimental results of temperature at the bottom of the aluminium alloy 5052-H32 workpiece at two locations, P_1 and P_2

Time (s)	Temperature readings for different laser powers (°C)											
	500 W		600 W		700 W		800 W		900 W		1000W	
	P_1	P_2	P_1	P_2	P_1	P_2	P_1	P_2	P_1	P_2	P_1	P_2
0	24.2	24.2	24.5	24.5	24.7	24.7	25	25	26	26	26	26
1	26	26	27.6	27	28	27.3	30	29	32	31	33	32
2	41.3	28.9	43.1	29	47.5	30	51.5	33.5	59	35.7	76	51
3	86	35	90.1	31	101.3	33.2	114.8	42	134.3	42	175	73
4	159	42	180	48	205.4	53.6	233.3	58	288.1	65.9	334	119
5	241.1	68	283.5	75	325.3	84.6	370	95	415	108	510	201.7
6	204	94	243	111	278	126	311.3	141.7	339.4	161	441.2	246.3
7	171.1	122	202.5	144	230.4	165	257.5	185.5	281.1	207.3	368.6	289.3
8	155.3	141	181.4	164.4	206.5	187.2	230.4	210.4	251.9	232.5	328.4	306.8
9	140.8	144	167.2	174.2	193.4	198.9	216	222.5	236.4	244.2	296.1	334.7
10	140.3	154.6	165.5	181.5	188.8	207.6	211	233.2	231	255.2	276.5	391.3
11	138	150.1	163	176.9	185.8	201.5	208.1	225.8	228	247.9	256.7	335
12	132.6	139	156.1	162.6	177.8	185.3	198.5	206.8	218	227.5	246.8	301.2
13	128	130	148	151	168.2	171.6	188	191	207.1	210.5	236.1	265
14	121.8	122.1	141.5	141.1	160.9	160.7	179.5	179	197.9	197	218.6	236.5
15	117	116.9	135.2	134.7	154.6	152.3	172.8	170	190.3	187.2	202.2	210.6

6.2.1 Heuristic algorithm for optimization

Heuristic optimization used for the inverse determination of thermal diffusivity (D_t) absorptivity (η), specific heat (C_p), density (ρ) and beam radius (r) was similar to that used by Eideh and Dixit (2013). Table 6.2 shows the initial ranges of parameters. For each parameter the range was divided into three linguistic zones, *viz*., low (L), medium (M) and high (H) as shown in Fig. 6.2 for five parameters. Thus, the entire domain was divided into $3^5 = 243$ cells. As an initial guess, the centre values of each parameter were chosen and simulation was carried out. Experimental temperatures at two locations were compared with the analytical results.

Table 6.2 Ranges of the initial parameters

Parameters	Symbol	Unit	Range
Thermal diffusivity	D_t	m^2/s	3×10^{-5}–9×10^{-5}
Thermal absorptivity	η		0.1–0.9
Specific heat	c_p	J/kg.°C	600–1500
Density	ρ	kg/m^3	1600–2800
Beam radius	r	m	0.001–0.01

The parameters D_t, η, c_p, ρ and r that minimize the error between experiment measured temperatures and temperatures estimated from simulation are considered as true parameters. The temperatures at two locations are measured experimentally by using two pyrometers. These temperatures are compared with the temperatures predicted from simulation. The root mean squared (RMS) errors of temperatures up to 15 s at two locations are indicated by E_1 (at pyrometer one) and E_2 (at pyrometer two).

$$E = \sqrt{\frac{1}{n} \times \sum_{i=1}^{n} \left(\frac{\text{Experimental temperature} - \text{Simulation temperature}}{\text{Experimental temperature}} \right)^2}, \tag{6.1}$$

where n is the number of experimental temperature data at each parameter. The objective was to minimize the combined error given by

$$E = \sqrt{\left(E_1^2 + E_2^2\right)/2}, \tag{6.2}$$

The numerical values of thermal conductivities indicate how fast heat flows in a given workpiece. During laser pass, the rate of laser heat flow through a workpiece is expressed as the amount of heat flows per unit time through a unit area, per unit temperature gradient. Thermal conductivity (k) of the sheet metal was calculated by

$$k = D_t \rho c_p, \tag{6.3}$$

where D_t is thermal diffusivity, ρ is density and c_p is specific heat

Minimization of the objective function is carried out by a heuristic method. Inverse modelling is carried out by using ABAQUS® package for determining the

material properties. Prediction errors in temperature are minimizing by using ABAQUS®. The methodology for finding out the material parameter, *viz*., thermal diffusivity (D_t) absorptivity (η), specific heat (C_p), density (ρ) and beam radius (r) during laser bending is as follows:

Step 1: Choose suitable ranges for material parameters D_t, η, C_p, ρ and r.

Step 2: For each parameter, the range is divided into three zones, *viz*., Low (L), Medium (M) and High (H) zones. Thus, the entire domain is divided into 3^5 = 243 cells.

Step 3: Choose the middle (M) values of all parameters as initial guess parameters of D_t, η, C_p, ρ and r and calculate RMS error, E using Eq. 6.1 and Eq. 6.2. The RMS errors at two experimental points, E_1 (at point P_1) and E_2 (at point P_2), are calculated by using 15 experimental data at each laser parameters.

Step 4: Fixing four parameters as constant, *viz*., η, C_p, ρ and r, carry out one-dimensional search for the optimum D_t. An effective way to do this is as follows:

- If the estimated temperatures at the current two locations (P_1 and P_2) are greater than the measured temperature, then increase the value of D_t by jumping to the centre of adjacent cell. If the new root mean error $(RMS)_{new}$ is greater than the old root mean square $(RMS)_{old}$, then keep the old point as the current point. If the new root mean error $(RMS)_{new}$ is less than the old root mean square $(RMS)_{old}$, then the current point is replaced by the centre of the new cell.
- If the estimated temperatures at the current two locations (P_1 and P_2) are less than the measured temperature, then decrease the value of D_t by jumping to the one cell behind. If the new root mean error $(RMS)_{new}$ is greater than the old root mean square $(RMS)_{old}$, then keep the old point as the current point. If the new root mean error $(RMS)_{new}$ is less than the old root mean square $(RMS)_{old}$, then the current point is accepted as the centre of current cell.

Step 5: Execute Step 4 for all variables. *i.e*., one parameter at a time is changed keeping other four parameters constant.

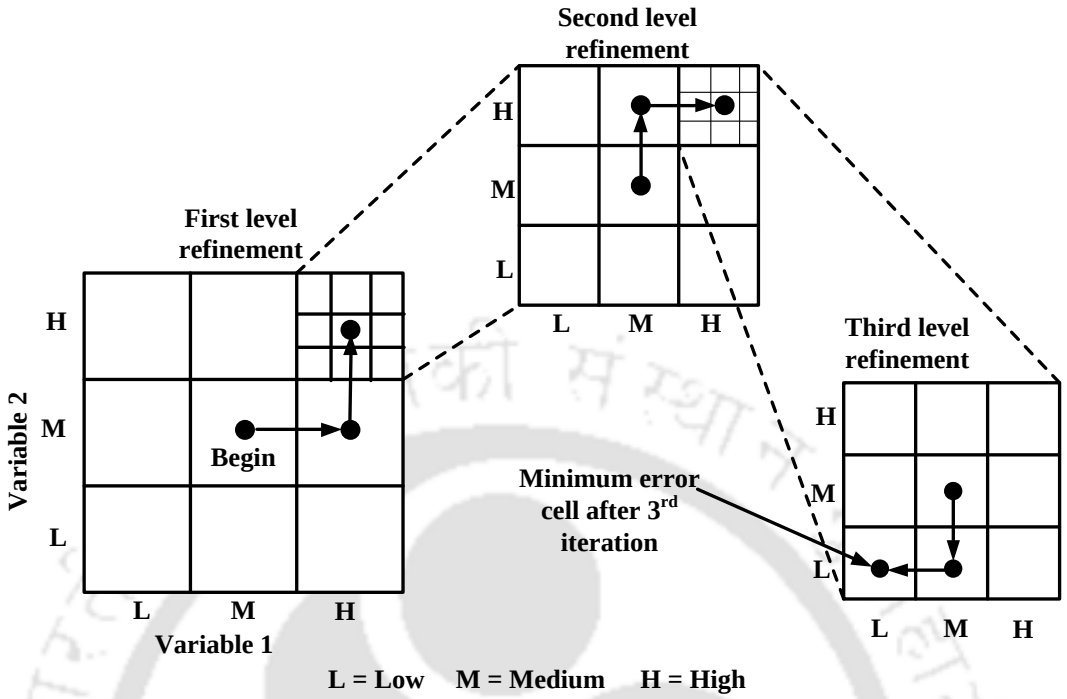

Figure 6.2 Two-dimensional graphical representation of search procedure

Step 6: For the further refinement, the optimum cell is further divided as in Step 2. Repeat the procedure of Step 3 to Step 5. After carrying out this procedure, if the *E* could not be reduced significantly, then the ranges of estimated and measured temperature need to be reduced. A graphical representation for reducing sizes of the search domain towards optimum is shown in Fig. 6.2. The basic steps of implementing heuristic optimization technique are summarized in Fig. 6.3.

In order to obtain temperature-dependent properties, this procedure can be followed for different laser powers at fixed scan speed. Different laser powers will produce different temperature distributions in the sheet. Hence, the inverse procedure can find out the thermal properties for different temperature distributions. As a simplification, these properties can be considered as the properties at some average temperature. In this work, the average is taken as the mean of bottom and top surface temperatures. Bottom surface temperature is directly measured by the pyrometer, whereas the top surface temperature is the estimated by FEM package. The key assumption is that it is the average temperature in the vicinity of laser irradiation zone

that is deciding the overall behaviour. Subsequent analysis shows that this assumption works reasonably well, but one should develop a more robust procedure in future.

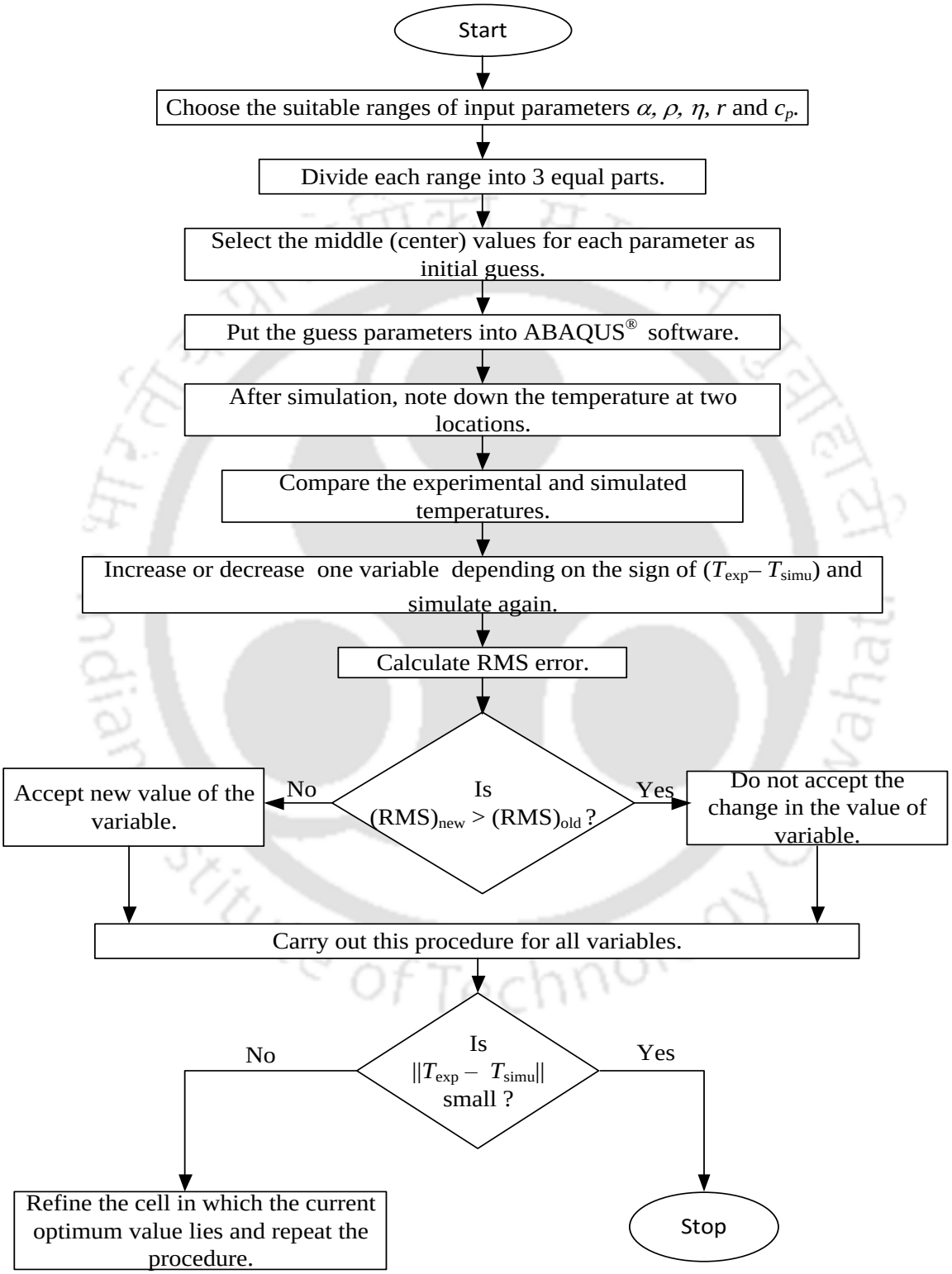

Figure 6.3 Flow chart of optimization techniques

6.2.2 Determination of mechanical properties

The value of yield stress and Young's modules at room temperature were taken from Toros et al. (2008). The following equation for the Young's modulus of elasticity was fitted based on the graph given in (https://law.resource.org/pub/eur/ibr/en.1999.1.2.2007.html).

$$E = \left(70 + 4.67\times10^{-3}T_s - 4.95\times10^{-4}T_s^{\,2} + 4.89\times10^{-7}T_s^{\,3}\right), \tag{6.4}$$

where T_s is in °C and E is in GPa. As the temperature varies across the thickness, the average of top and bottom surfaces is taken as T_s. The yield stress of the material is 190 MPa. The temperature-dependent yield stress for the sheet is expressed as follows:

$$Y = \begin{cases} Y = 190\ \text{MPa}, T_s \le T_a \\ 190 - 190\left(\dfrac{T_s - T_a}{T_m - T_a}\right)^m\ \text{MPa}, T_m \ge T_s > T_a \end{cases} \tag{6.5}$$

For the present material T_m and T_a are 607 °C and 25 °C, respectively. The proper value of m is obtained by minimizing the error between theoretical and experimental bend-angle using bisection method. It came as 0.7.

6.3 Results for Inverse Determination of Material Properties

As a result of inverse estimation, the values of material properties of aluminium alloy 5052-H32 samples, *viz*., thermal diffusivity (D_t) absorptivity (η), specific heat (C_p), density (ρ) and beam radius (r) were obtained at average temperature (of top and bottom temperatures). Figure 3.4, 3.5 and 3.6 show the variation thermal diffusivity, specific heat and density with temperature, respectively. It was observed that thermal diffusivity and specific heat capacity increase with temperature, whilst the density decreased with increase in temperature. The absorptivity value of the material and laser beam radius were 0.4 and 0.0039 m, respectively. The laser beam radius (r) was calculated based on Eq. 3.2. It is assumed that the absorptivity is not dependent on the temperature.

As a result of inverse estimation, the average values of parameters were obtained at different powers as shown in Table 6.3. These were considered as the values at different temperatures (corresponding to the average of bottom and top surface temperatures). It was observed that thermal diffusivity and specific heat slightly increase with temperature, whilst the density decreases with temperature.

Table 6.3 Variation of thermal properties, density and laser beam radius with temperature (absorptivity fixed at 0.4 based on earlier experiments, beam radius 0.0039 m)

Laser Power (W)	Maximum temperature of workpiece at bottom and top (°C)			Thermal diffusivity (m^2/s)	Density (kg/m^3)	Specific heat ($J/kg^{\circ}C$)
	T_B	T_T	T_{ave}			
500	241	276	258	6.45×10^{-5}	2634	995
600	283	332	308	6.54×10^{-5}	2595	1014
700	325	387	356	6.56×10^{-5}	2535	1030
800	370	440	405	6.57×10^{-5}	2250	1035
900	415	494	455	6.58×10^{-5}	2025	1045
1000	502	600	551	6.6×10^{-5}	2005	1052

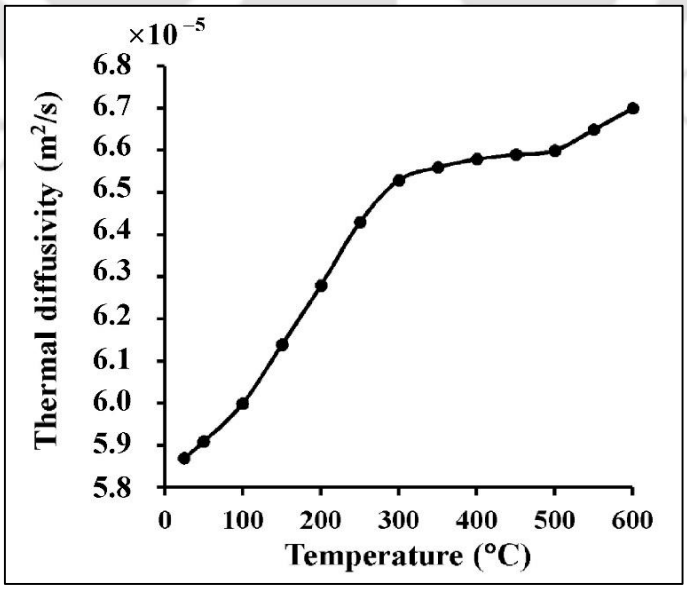

Figure 6.4 Temperature versus thermal diffusivity

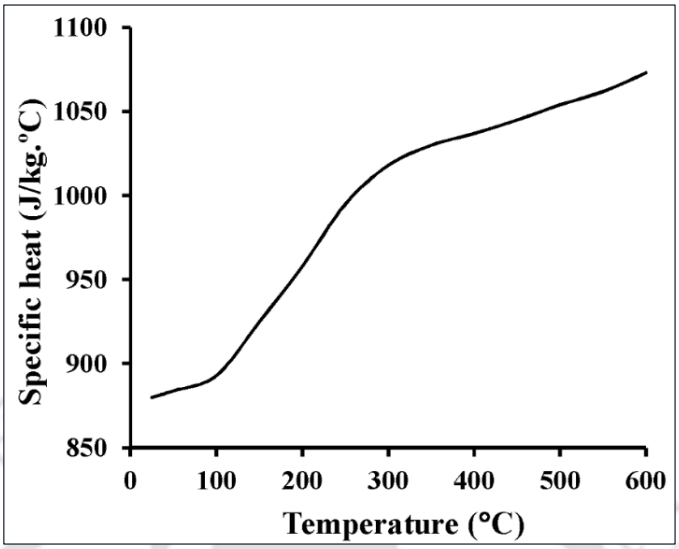

Figure 6.5 Temperature versus specific heat

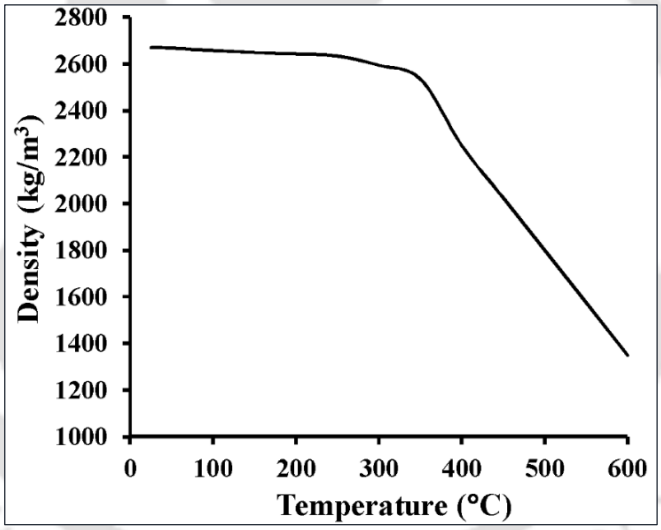

Figure 6.6 Temperature versus density

The temperature dependent mechanical properties of aluminium alloy 5052-H32 samples were calculated by using Eq. 6.4 and 6.5. Figure 6.7 (a) and (b) shows the variation of Young's modulus and yield stress with temperature. The values of Young's modulus and yield stress are inversely related with temperature.

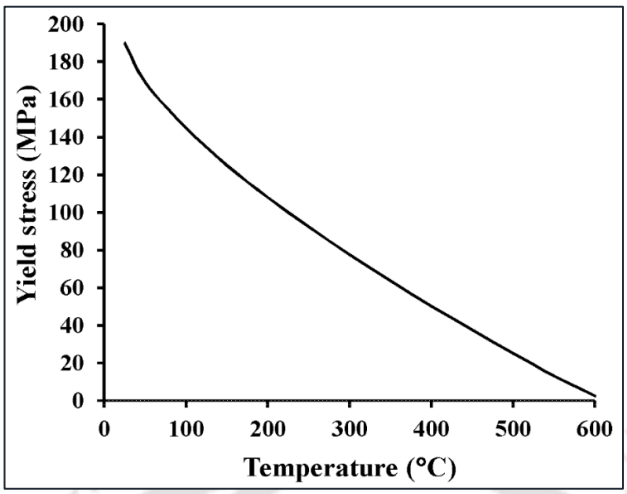

(a)

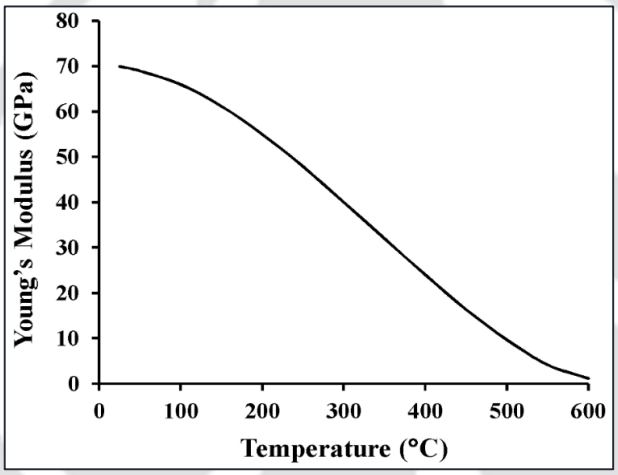

(b)

Figure 6.7 Mechanical properties of aluminium alloy (5052-H32) at various temperatures: (a) Yield stress and (b) Young's modulus

6.4 Results and discussion of laser bending in friction stir weld plate

After determining material properties by inverse method, the simulations were carried out for laser bending of friction stir welded aluminium 5052-H32 sheets. For this work, the friction stir welded sheets were made by different tool rotational and translational (welding) speed. In this investigation, fiction stir welded aluminium alloy 5052-H32 samples were prepared in the size of 60 mm × 60 mm × 2 mm. Hydrated lime coating was used to enhance absorptivity. Singh et al. (2013) observed that the hydrated lime coating was superior to graphite coating. The thickness of

friction stir welded zone was less than the base material thickness because of deformation due to plunge force. This was taken into account in numerical simulations. The chemical composition of the material with weight percentage was found from the EDS and the mechanical properties of the base material and friction stir welding were obtained by universal testing machine (UTM). Two replicates were conducted for each condition. Details of experiments, such as preparation of friction stir welding sheets, experimental equipment, bend angle, edge effect measurement methodology has been discussed in Chapter 3.

The four scanning direction were used for bending the friction stir welded sheets as shown in Fig. 6.8. Two replicates were conducted for each scanning direction and welding parameters. Experiment was carried out with full factorial design of experiments. The experiments were conducted with 800 W laser powers, 400 mm/min scan speed, single number of scan irradiation and fixed laser beam diameter (7.76 mm).

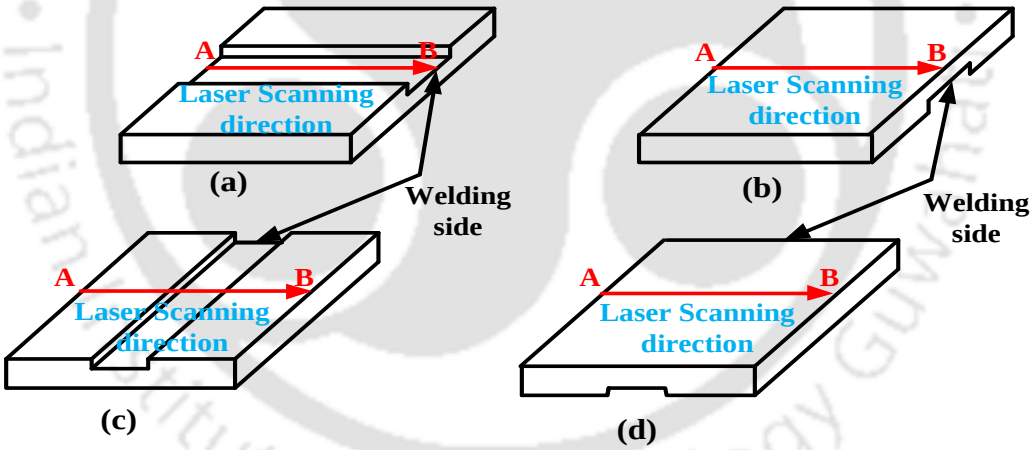

Figure 6.8 The scanning scheme on friction stir welded sheets: (a) along welding direction on the top surface, (b) along welding direction on the bottom surface, (c) across welding direction on the top surface and (d) across welding direction on the bottom surface

6.4.1 Tensile test results

Figure 6.9 shows stress-strain curve of aluminium alloy 5052-H32 sheets fabricated at four levels of welding speeds (WS) (36, 63, 98 and 132 mm/min) at tool rotation speed (TR) of 1500 RPM. The strength reduces with the welding speed. A

low tool rotation speed (1100 RPM) and welding speed (22 mm/min), both strength and the percentage elongation are the least. The weld zone thickness of 1.95 mm was used during tensile tests. Figure 6.10 shows the stress-strain curve of base metal as well as friction stir welded zone in the longitudinal direction. It was seen that the strengths did not vary much between longitudinal and transverse direction. Table 6.4 shows that the maximum yield stresses of the weld were 108.5, 107.7, 106.2, 105.8 and 105 MPa that are 66.6%, 66% , 65.2%, 64.9% and 64.4% of base material strength, respectively. The data used in simulation for weld zone provided in Table 6.4 is for room temperature. Temperature dependency was taken as explained in Section 6.2.2.

All tensile tests show that the failure occurs in the weld zone due to reduced strength and thinner cross-section of the welded zones. Park et al. (2008) also found that after surface friction stirring of aluminium alloy 5052-H32 sheets, its ductility improved in the stir zone but the strength reduced. Figure 6.11 shows that, fracture in the tensile tests occurred in this softened region, which happened to be the weakest point of the specimen at retreating side. Similar observations were also made by Scialpi et al. (2008).

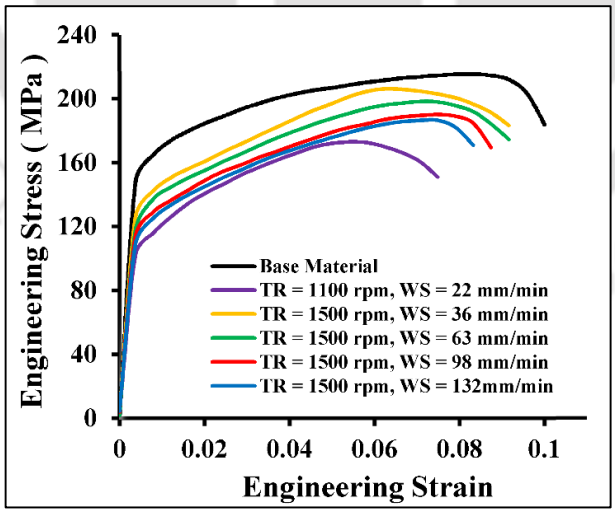

Figure 6.9 The engineering stress and strain of aluminium alloy 5052-H32 base metal sheet and the friction stir welded zone in transverse direction

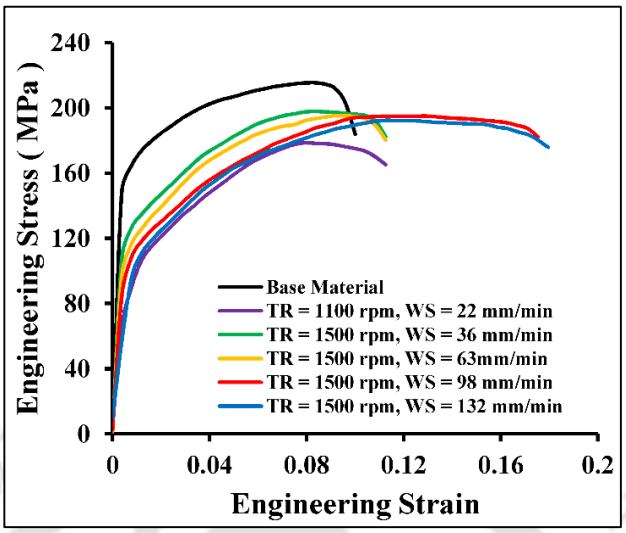

Figure 6.10 The engineering stress and strain of aluminium alloy 5052-H32 base metal sheet and the friction stir welded zones in longitudinal direction

Table 6.4 Yield stress and modules of elasticity for aluminium alloy 5052-H32 base material and friction stir welded zone based on longitudinal direction

Welding Parameters	Yield stress (MPa)	Modulus of elasticity (GPa)
TR=1100 RPM WS=22 mm/min	108.5	67
TR=1500 RPM WS=36 mm/min	107.7	73
TR=1500 RPM WS=63 mm/min	106.2	72
TR=1500 RPM WS=98 mm/min	105.8	69.6
TR=1500 RPM WS=132 mm/min	105	68
Base material	163	70

WS = welding speeds, TR = tool rotation speed

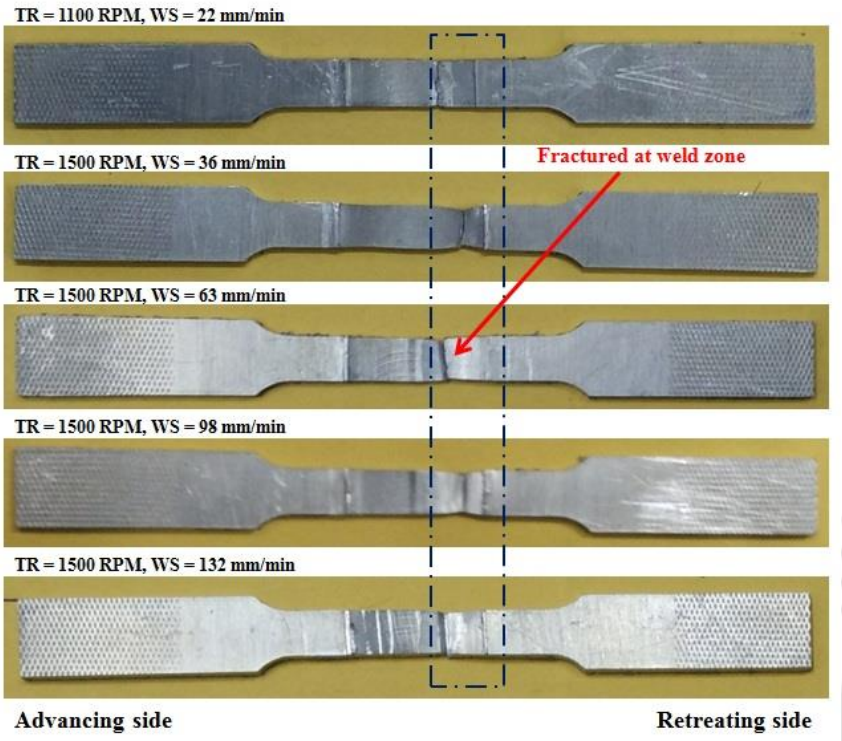

Figure 6.11 Fractured tensile specimen (friction stir welded aluminium alloy 5052-H32) at different tool rotations and welding speeds

6.4.2 Fracture test

The entire tensile test specimen failed at the thermo-mechanically affected zone (TMAZ) of retreating side as shown in Fig. 6.11. To confirm the type of fracture, fractography test was performed for some specimens. For representation purpose, only the fractograph images of highest modules of elasticity (tool rotation 1500 RPM and welding speed 36 mm/min) and the lowest modules of elasticity (tool rotation 1500 RPM and welding speed 132 mm/min) specimens are examined. The fracture surface exhibited voids and dimples. Dimples are formed due to coalescence of voids and are indicative of ductile fracture. Figure 6.12 (a) shows less dimples as compared to Fig. 6.12(b), which indicates the less ductility. From fractograph image (Fig. 6.12) and stress/strain diagram (Fig. 6.10), it can be concluded that the welding speed of 132 mm/min provides more ductility compared to welding speed of 36 mm/min. The behaviour is reverse for strength. Park et al. (2008) also found that surface friction stirred aluminium alloy 5052-H32 sheets improved their ductility in the stir zone but reduced the strength compared to base material.

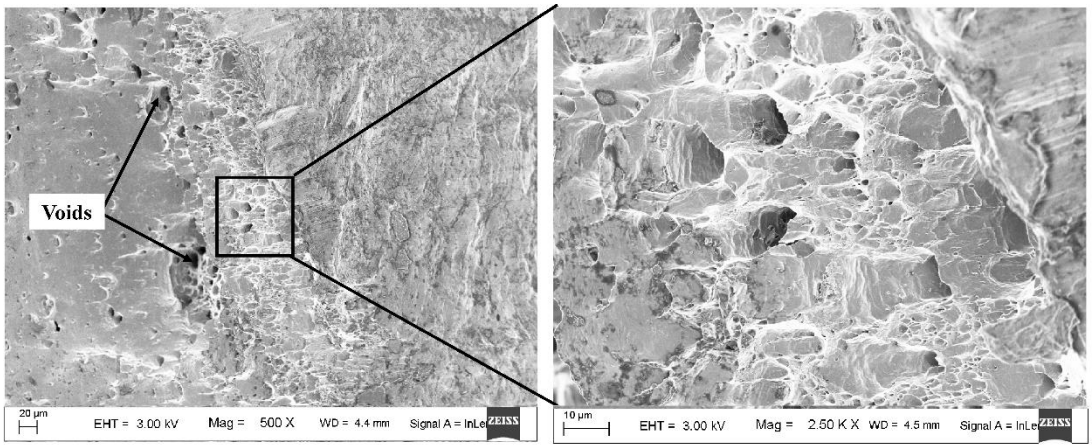

(a)

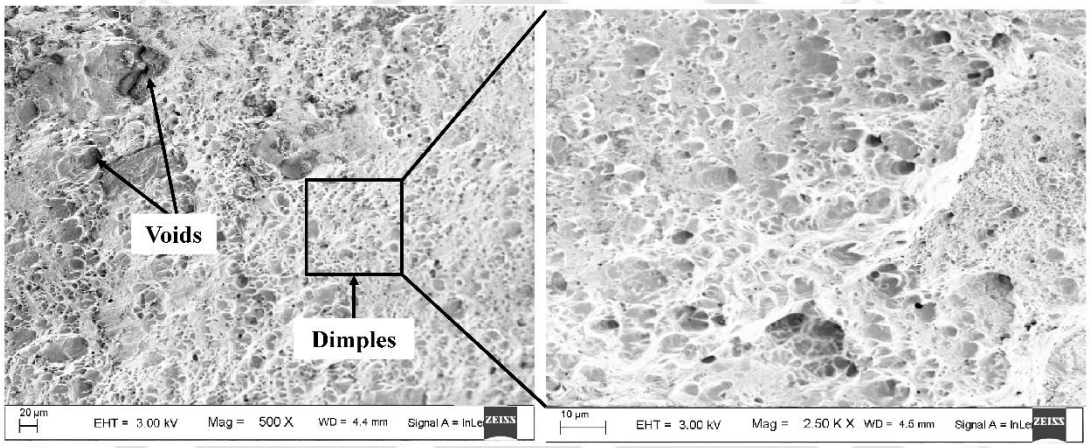

(b)

Figure 6.12 FESEM image of fracture test samples: (a) tool rotation 1500 RPM and welding speed 36 mm/min and (b) tool rotation 1500 RPM and welding speed 132 mm/min

6.5 Validation of FEM result

The four laser scanning schemes were studied. The simulation and experimental results are shown in Figs. 6.13–6.16. The observations from the figures are as follows:

1. The highest bend angle was achieved when the scanning was carried out at the top surface in the longitudinal direction. This was due to the reduced yield strength of the friction weld zone coupled with more heat entrapment in the slot. Due to the vertical slots at the top, the more surface area on the top side was at higher temperature.

2. Weld conditions used in friction stir welding process affect the bend angle during laser scanning. Scanning scheme also influences the bend angle.
3. When the scanning direction was transverse to the weld direction, the bend angle was reduced as the properties of base material dominate here. In this case, the scanning at the top surface produced slightly reduced bend angle compared to scanning at the bottom surface. This was due to the increased standoff distance at the weld zone in the former case.
4. The matching between experimental and simulation results were very good. In most of the cases, the error was less than 10%. The maximum error was 16% in one case. Inverse determination of material properties and absorptivity has a major role in providing better accuracy. The absorptivity may act as a fitting parameter. However, recently Kant et al. (2015) observed that inversely calculated absorptivity has a good qualitative agreement with absorbance obtained by the spectrometer.
5. The repeatability (based on 2 replicates) is very good as evident from figures.

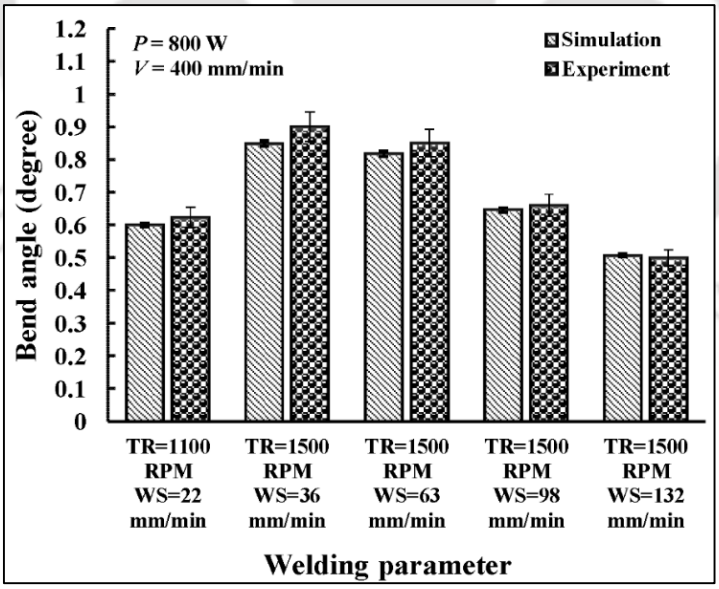

Figure 6.13 Simulation and experiment results of bend angles for friction stir welded sheet (weld zone thickness 1.75 mm and scanning along weld direction on the bottom surface)

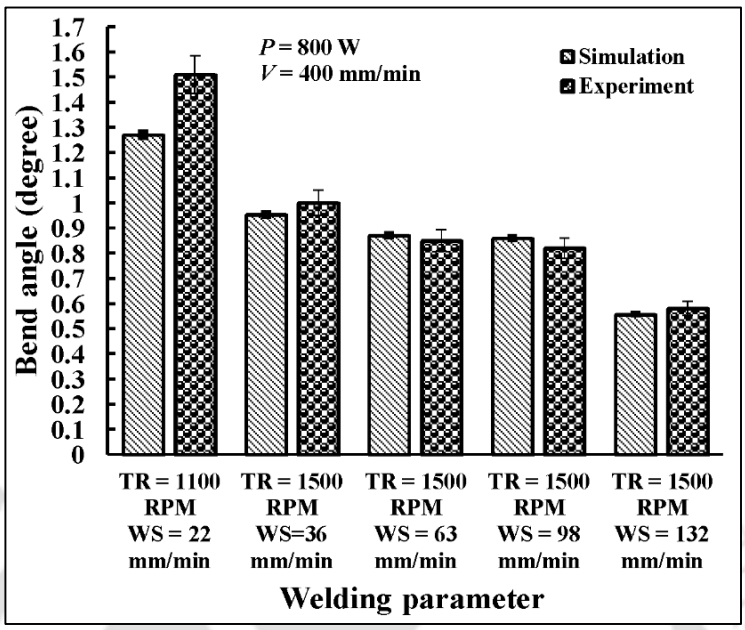

Figure 6.14 Simulation and experiment results of bend angles for friction stir welded sheet (weld zone thickness 1.75 mm and scanning along weld direction on the top surface)

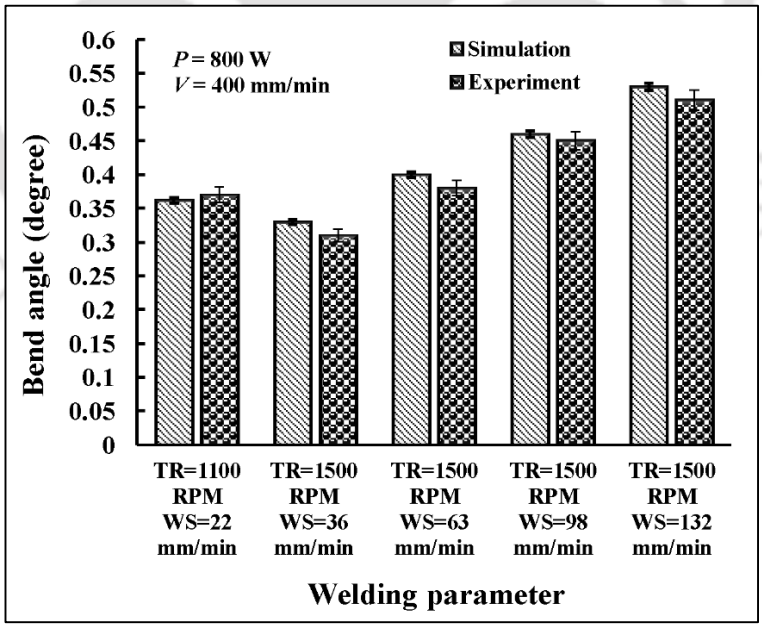

Figure 6.15 Simulation and experiment results of bend angles for friction stir welded sheet (weld zone thickness 1.75 mm and scanning across weld direction on the bottom surface)

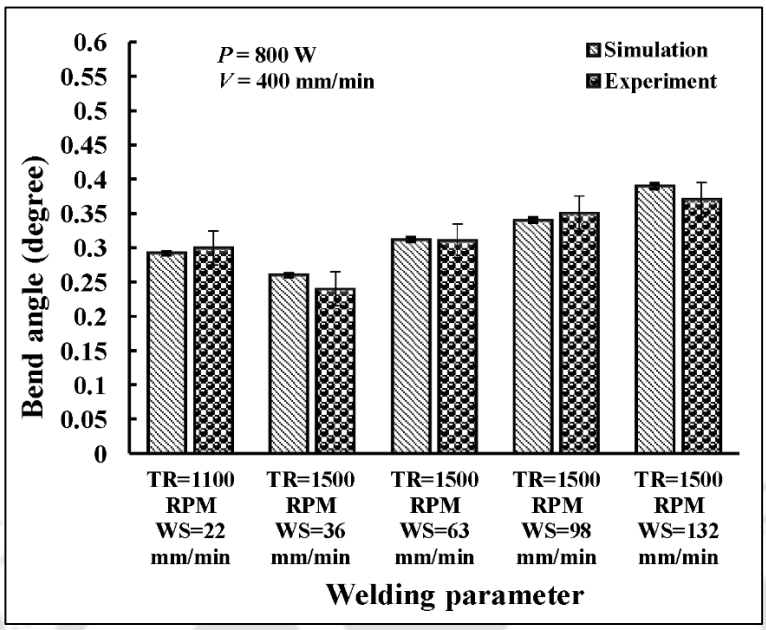

Figure 6.16 Simulation and experiment results of bend angles for friction stir welded sheet (weld zone thickness 1.75 mm and scanning across weld direction on the top surface)

The experiments were conducted for weld zone thickness of 1.85 and 1.95 mm also. It was observed that when the scanning was carried out along the weld direction, the bend angle reduced due to increase in local stiffness. When the scanning was carried out across the weld direction, in some cases, the bend angle increased with increase in the weld zone thickness. This was due to much lesser influence of the local stiffness and possibly due to increase in thermal gradient at some duration that contributed towards slightly more bend angle. The detailed results of 1.85 mm weld zone thickness case have been shown in Appendix H. The results of 1.95 mm weld zone thickness case are shown in Fig. 6.17–6.20.

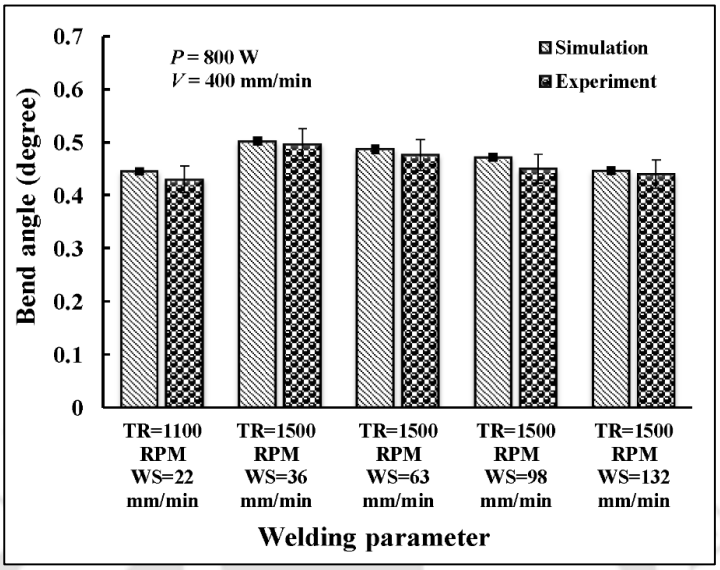

Figure 6.17 Simulation and experiment results of bend angles for friction stir welded sheet (weld zone thickness 1.95 mm and scanning along weld direction on the bottom surface)

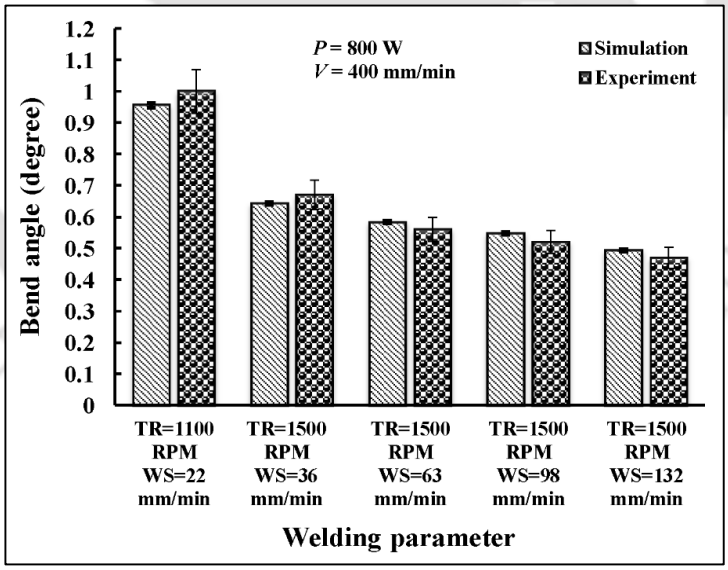

Figure 6.18 Simulation and experiment results of bend angles for friction stir welded sheet (weld zone thickness 1.95 mm and scanning along weld direction on the top surface)

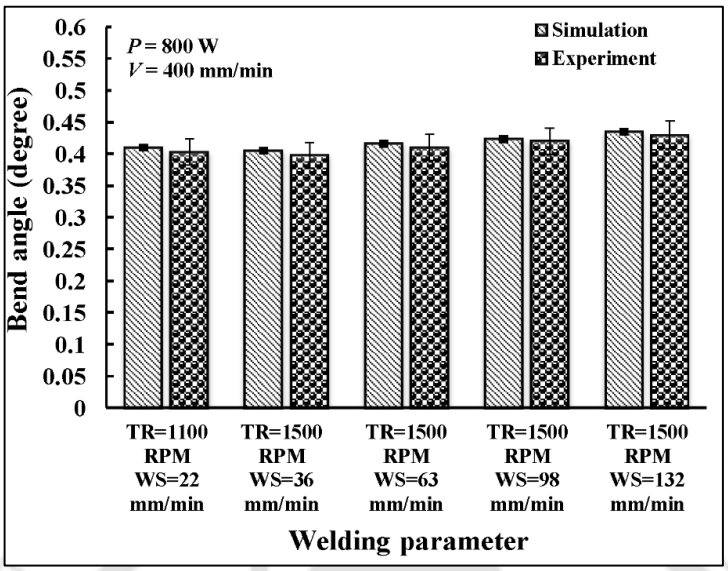

Figure 6.19 Simulation and experiment results of bend angles for friction stir welded sheet (weld zone thickness 1.95 mm and scanning across weld direction on the bottom surface)

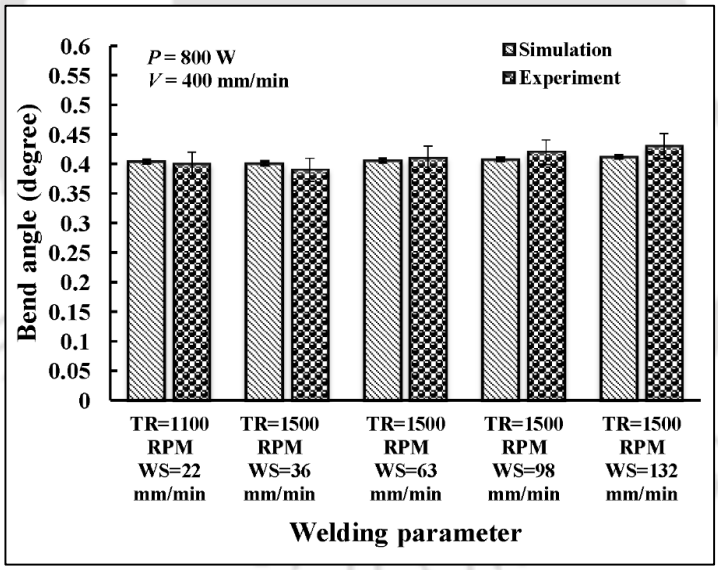

Figure 6.20 Simulation and experiment results of bend angles for friction stir welded sheet (weld zone thickness 1.95 mm and scanning across weld direction on the top surface)

Figure 6.21–6.23 show the simulated and experimental results of bend angle variation along the width direction (i.e, along the scan direction) for different weld zone thicknesses. In all the cases, the laser beam scanning was carried out at the top

surface along the weld direction. It was observed that the edge effect was small and more or less, same bend angle was observed throughout the width. The bend angle was slightly more at the end of scan than at the beginning of the scan in all the cases. This was due to slight increase in the temperature due to accumulated heat. Also, it was observed that the bend angle reduced with the increase of the thickness.

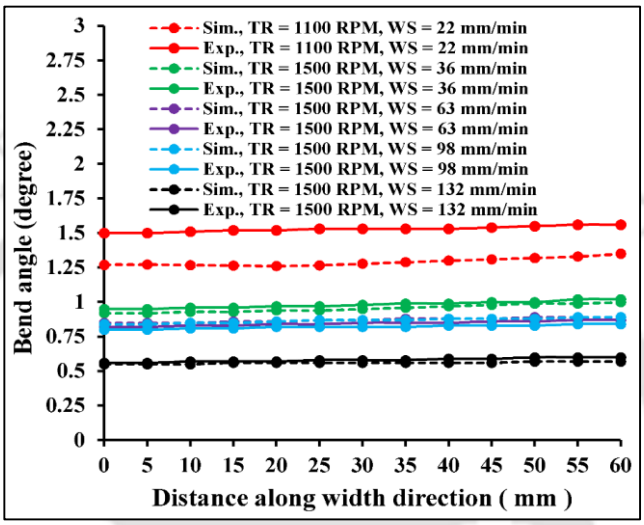

Figure 6.21 Variation of bend angle along width direction for weld zone thicknesses 1.75 mm (scanning on the top surface along the weld direction) for sheets produced by different FSW conditions

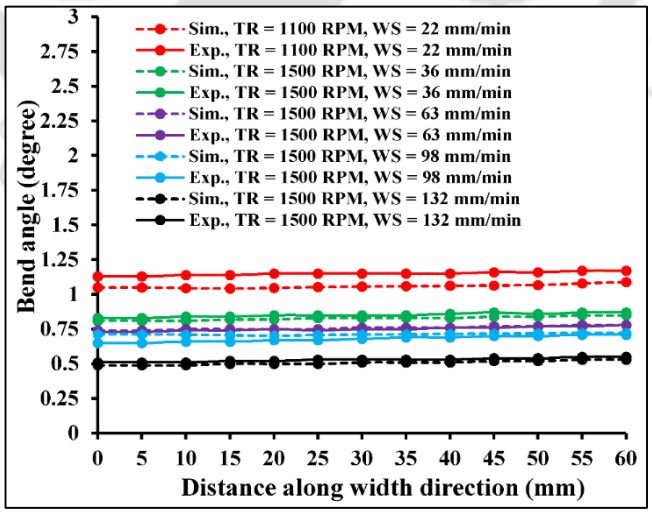

Figure 6.22 Variation of bend angle along width direction for weld zone thicknesses 1.85 mm (scanning on the top surface along the weld direction) for sheets produced by different FSW conditions

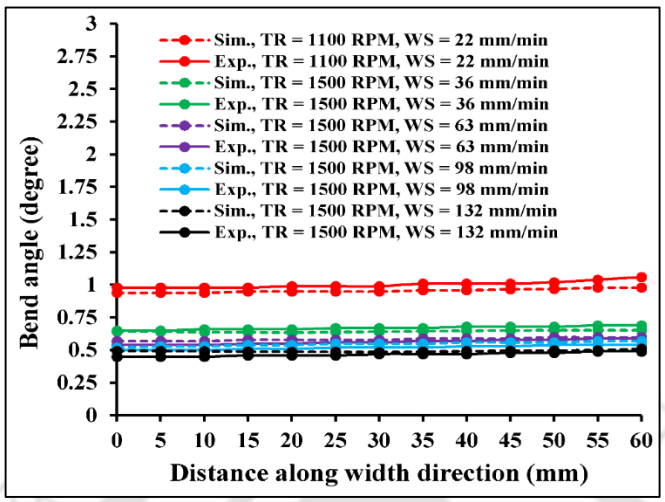

Figure 6.23 Variation of bend angle along width direction for weld zone thicknesses 1.95 mm (scanning on the top surface along the weld direction) for sheets produced by different FSW conditions

6.6. Conclusion

In this work, the effect of process parameters like welding parameters and scan schemes on laser bending of friction stir welded plate were studied. The following conclusions are drawn:

1. The temperature dependent thermal diffusivity, specific heat, absorptivity and density were obtained inversely based on temperature of the workpiece by using heuristic optimization method. The temperature dependent mechanical properties were also estimated inversely based on bend angle. Although the procedure is approximate and may not give unique results, it is able to predict the bend angle with reasonable accuracy.
2. In this work, laser bending of the friction stir welded aluminium alloy sheet of 5052-H32 developed using commercial package ABAQUS®. The error between experiments and simulated bend angles was minimized. In all the experiments, two replicates were carried out. Friction stir welding was carried out at different weld conditions. In most of the cases, the error was less than 10%. The maximum error was 16% in one case.

3. The effect of the thickness and mechanical properties of weld zone were investigated. It was observed that the welding conditions (tool rotation and welding speed) in friction stir welding have profound effect on bending behaviour. The bend angle reduced with increase in weld thickness when the scanning was carried out along the weld direction. However, its effect was less when the scanning was across the welding direction. The less variability in the results as well as closeness with the simulation provided confidence in the viability of laser bending process for bending friction stir welded sheets.

Chapter 7

Laser Bending of Friction Stir Processed and Cement Coated Sheet

7.1 Introduction

Laser bending is a non-contact process, which is highly suitable for obtaining miniature bend angles. The various kinds of process parameters related to workpiece material, workpiece geometry and external constraints control the laser bending process. The absorptivity of the material plays a vital role in the laser bending process. The high reflective materials result in significant power loss and affect the beam generation mechanism as well as the optical elements due to backscattering. A number of different surface conditions are used to enhance the absorptivity of sheet metal such as surface coating and surface roughening. Each method has its own pros and cons. On one hand, the surface coating is a simple and low cost method. On the other hand, there are problems of coating getting removed during laser scanning, impregnation of coating along grain boundaries of the base material and environmental hazard due to vaporization of the paint (Kannatey-Asibu Jr. 2009). Considering the pros and cons, it is better to opt for the surface roughening.

Friction Stir Processing (FSP) is an evolving technique for the modification of the surface and bulk properties. There are two classes of FSP— the Volume FSP (VFSP) that affects the full thickness and the Surface FSP (SFSP) that affects the material up to about 2 mm depth from the surface (Nascimento et al. 2009). SFSP has developed as a material processing technique, which follows the basic principles of Friction Stir Welding (FSW), (Mishra and Ma, 2005). In SFSP, a non-consumable rotating tool is plunged into the workpiece to rotate while traversing. The rubbing of the tool creates roughness in the stirred zone.

The SFSP is used to improve surface properties without affecting the bulk properties of the material (Ma, 2008 and Lathabai et al. 2009). Many researchers have

performed experimental (Mishra et al. 1999), analytical (Ma et al. 2009) and computational (Liechty and Webb, 2008 and Wang and Mishra, 2007) studies on FSP. Especially, the effect of the process parameters on microstructure evolution (Morisada et al. 2007), deformation behaviour and improvement in mechanical properties (Tewari et al. 2006; Cui et al. 2009 and Feng and Ma, 2007) were investigated. FSP has been applied for different materials like aluminium (Surekha et al. 2009; Karthikeyan et al. 2013 and Behnagh et al. 2012), mild steel (Langlade et al. 2016), stainless steel (Sato et al. 2005), magnesium (Cavaliere and De Marco, 2007 and Chang et al. 2007), copper (Dehghani and Mazinani, 2011) and composite material (Sharma et al. 2016).

The forming behaviour of FSP sheets has been studied (Venkateswarlu et al. 2012 and Sekban et al. 2015). The earlier research established that the cement coating provides much better absorptivity compared to graphite grease and lime coating (Singh et al. 2013 and Gautam et al. 2015). Hence, the laser bending of friction stir processed plates is compared with that of cement-coated plates for aluminium alloy (5052-H32) and mild steel (AH36).

7.2 Experimental Procedure

For this work, aluminium alloy (5052-H32) and mild steel (AH36) sheets of 2 mm thickness were used as study materials. These represent two classes of materials. Aluminium alloy (5052-H32) has high reflectively and conductivity, therefore it is difficult to bend it using laser scanning. The mild steel (AH36) has relatively low reflectivity and conductivity and gets easily bent while laser scanning.

The chemical compositions of aluminium alloy (5052-H32), mild steel (AH36) and HSS (friction stir processed tool) in weight percentage were obtained from the energy dispersive X-ray spectroscopy (EDS) as shown in Fig. 3.2 (a)–(c). Friction stir processing was done by vertical milling machine as shown in Fig. 3.19. For this work, friction stir processed tool had only a cylindrical shoulder of 10 mm diameter without a pin (Fig. 3.20). The width of the friction stirred zone is dependent on the shoulder of the tool. The tensile properties of base material and friction stir processed samples were measured by a universal testing machine (Make: INSTRON;

Model: 8801J4051) as shown in Fig. 3.8 (a). For each material, three samples were prepared from raw and friction stir processed sheets. Each tensile test reported the average values of three samples.

Laser bending was performed on raw, cement coated and friction stir processed aluminium alloy (5052-H32) and mild steel (AH36) sheets shown in Fig. 7.1. The laser power was 1000 W, scan speed 1000 mm/min, beam diameter 9.4 mm and number of passes varied from 1 to 6. After the laser beam irradiation, the heated specimens were allowed to cool naturally. The bend angles were measured at 5 different locations including the edges along the width (laser scan) direction by using coordinate measuring machine as shown in Fig. 3.6 and Fig. 3.7. The average bend angle results are reported. For calculating the edge effect along the laser scan path, Eq. 3.6 is used as per Zahrani, and Marasi (2013).

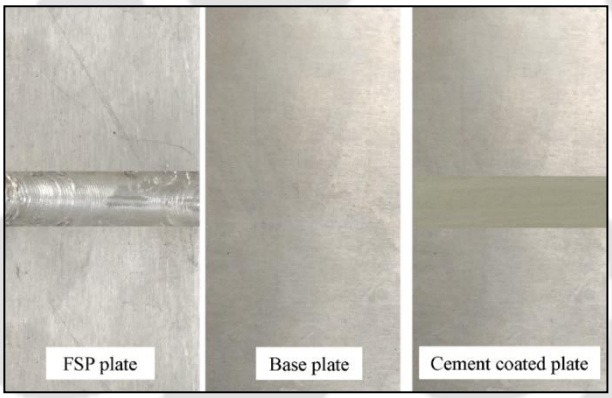

(a)

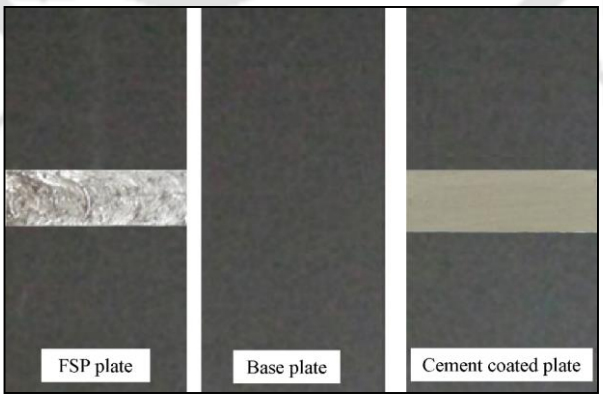

(b)

Figure 7.1 Photographs of sheets ready for bending: (a) aluminium alloys (5052-H32) and (b) mild steel (AH36)

For hardness test, all laser irradiated base (raw) and friction stir processed sheets were polished by silicon carbide abrasive paper in the range 400–2000 grit size. Afterwards, the specimen was polished by a velvet cloth using MicroPolish alumina particles of size 1 μm (Fig. 3.15). Microhardness was examined using microhardness tester (Make: BUEHLER; Model: Micromet-2101) shown in Fig. 3.17. The Vickers hardness tests were conducted in transverse (perpendicular to thickness and scan direction) and along the thickness directions at the middle of the sheet using a 500 gf load for 20 s dwell time for mild steel (AH36) and 300 gf load for 20 s dwell time for aluminium alloy (5052-H32). For microhardness reading in the transverse direction, the distance between the two indentations in the same line was 1 mm. For checking the microhardness variation along thickness direction, three indentations were taken in the thickness directions at 0.5 mm, 1 mm and 1.5 mm from top surface. At each height in thickness direction, three indentations were carried out and the average result was reported. A schematic of the indented sheet is shown in Fig. 7.2.

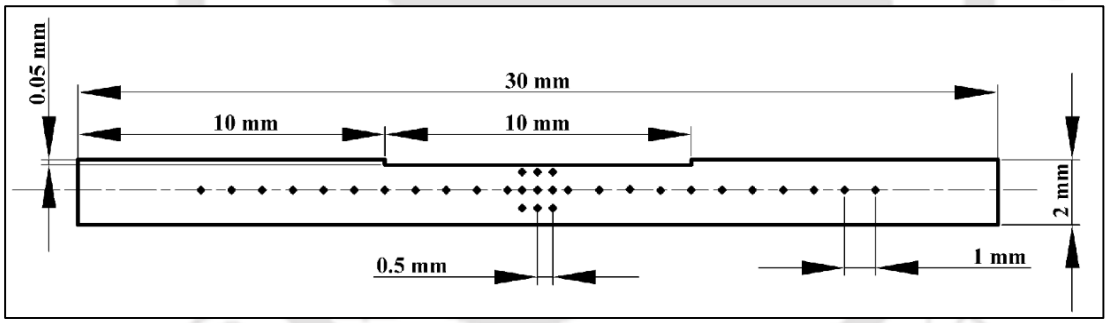

Figure 7.2 A schematic of the indented friction stir processed sheet after microhardness test

Microstructure of friction stir processed mild steel (AH36) specimen was examined. (The microstructure of aluminium alloy (5052-H32) could not be studied due to lack of clarity.) All samples were cut perpendicular to the laser scan direction to expose the surface containing the thickness and transverse direction. The samples were polished and etched using 95% ethanol and 5% nitric acid for 20 seconds. The polished and etched samples were examined using an optical microscope (Make: Carl Zeiss; Model: Axiotech-100HD) as shown in Fig. 3.16. The surface roughness of the friction stir processed sheets was measured by a noncontact optical profilometer

(Make: Taylor Hobsen; Model: CCI-Lite) (Fig. 3.18). The centreline average, Ra, value is reported.

7.3 Results and Discussion

The salient results of this study are presented in this section. The results have been presented for aluminium alloy (5052-H32) and mild steel (AH36) sheets of 2 mm thickness. Raw, cement coated and friction stir processed sheets are bent using a CO_2 laser and the properties of the bent sheet are studied.

7.3.1 Tensile strength

To obtain true stress-true strain data, tensile tests were conducted using tensile test specimens based on ASTM-E8. The true stress-strain curves of raw sheet and friction stir processed sheets are shown in Fig. 7.3. There is no appreciable effect of friction stir processing on the yield strength and Young's modulus of elasticity for both aluminium alloy (5052-H32) and mild steel (AH36). The yield stress decreases slightly in the case of aluminium alloy (5052-H32) and increases slightly in the case of mild steel (AH36). The ultimate tensile strength (UTS) of aluminium alloy (5052-H32) reduced by 10.3% and that of mild steel (AH36) increased by 1% as shown in Table 7.1.

Table 7.1 Mechanical properties for aluminium alloy (5052-H32) and mild steel (AH36) before and after FSP

Material	Yield stress (MPa)	UTS (MPa)	Modulus of elasticity (GPa)
Aluminium alloy (before FSP)	163	223	70
Aluminium alloy (after FSP)	155	200	70
Mild steel (before FSP)	260	382	230
Mild steel (after FSP)	263	386	230

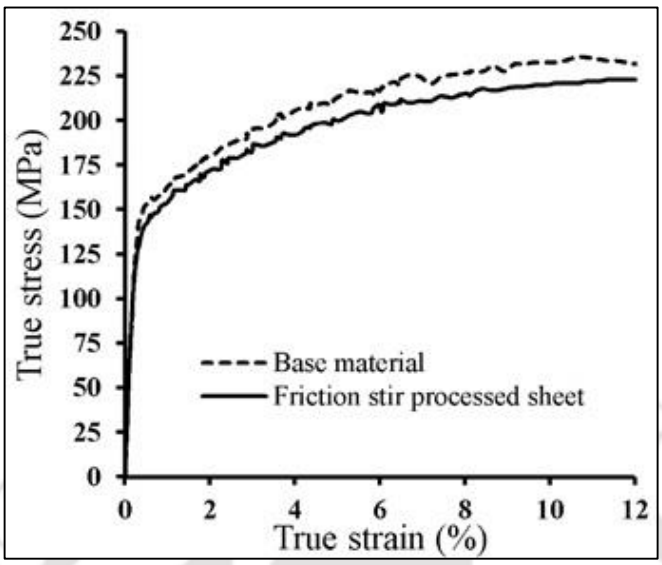

(a)

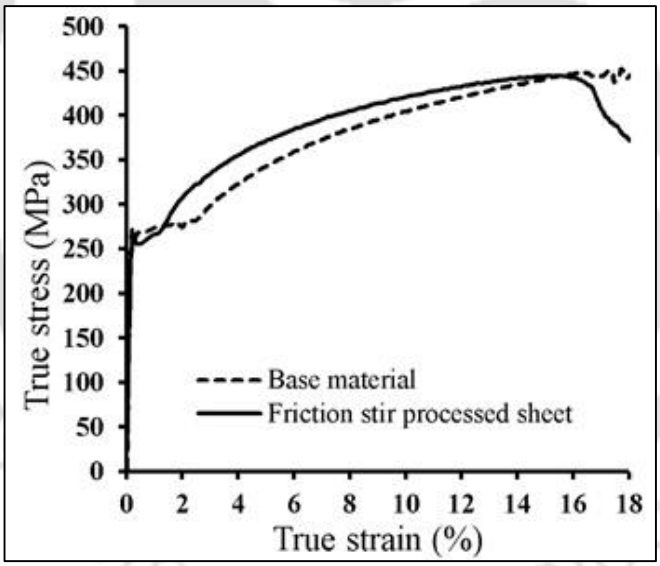

(b)

Figure 7.3 Experimental result of true stress verses true strain (a) aluminium alloy (5052-H32) and (b) mild steel (AH36)

7.3.2 Surface roughness

The surface roughness was tested by using an optical non-contact surface profilometer. Twelve measurements were made per specimen on friction stir processed region along the width (tool traverse) direction. The Ra values are shown

in Fig. 7.4. The centreline average, Ra, value of twelve measurements for each specimen along friction stir processed region in the case of aluminium alloy (5052-H32) and shipbuilding steel (AH36) sheet are 3.85 µm and 4.33 µm, respectively. The Ra values of the base material were 0.43 µm and 0.79 µm for aluminium alloy and shipbuilding steel (AH36), respectively.

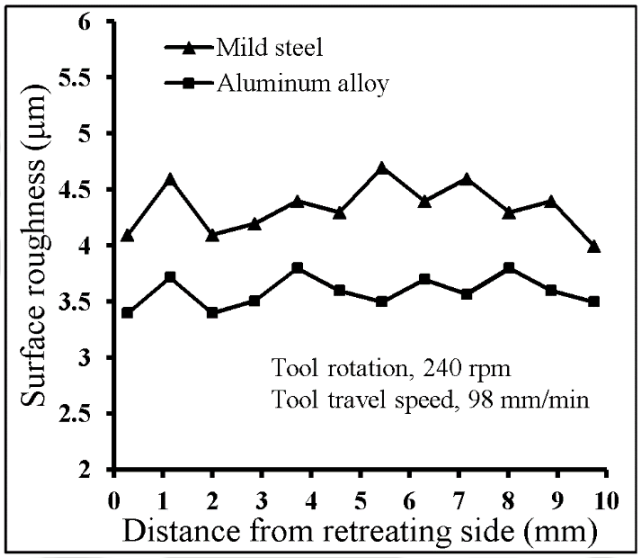

Figure 7.4 The centreline average surface roughness values of friction stir processed sheet at different sections

The 3D non-contact optical profilometer image of friction stir processed sheet is shown in Figs. 7.5 and 7.6 (a) and (b). For aluminium, the distance between the grooves is 430.41µm and the average peak to valley height was 21.93 µm. The corresponding values for mild steel (AH36) was 428.78 µm and 17.3 µm, respectively.

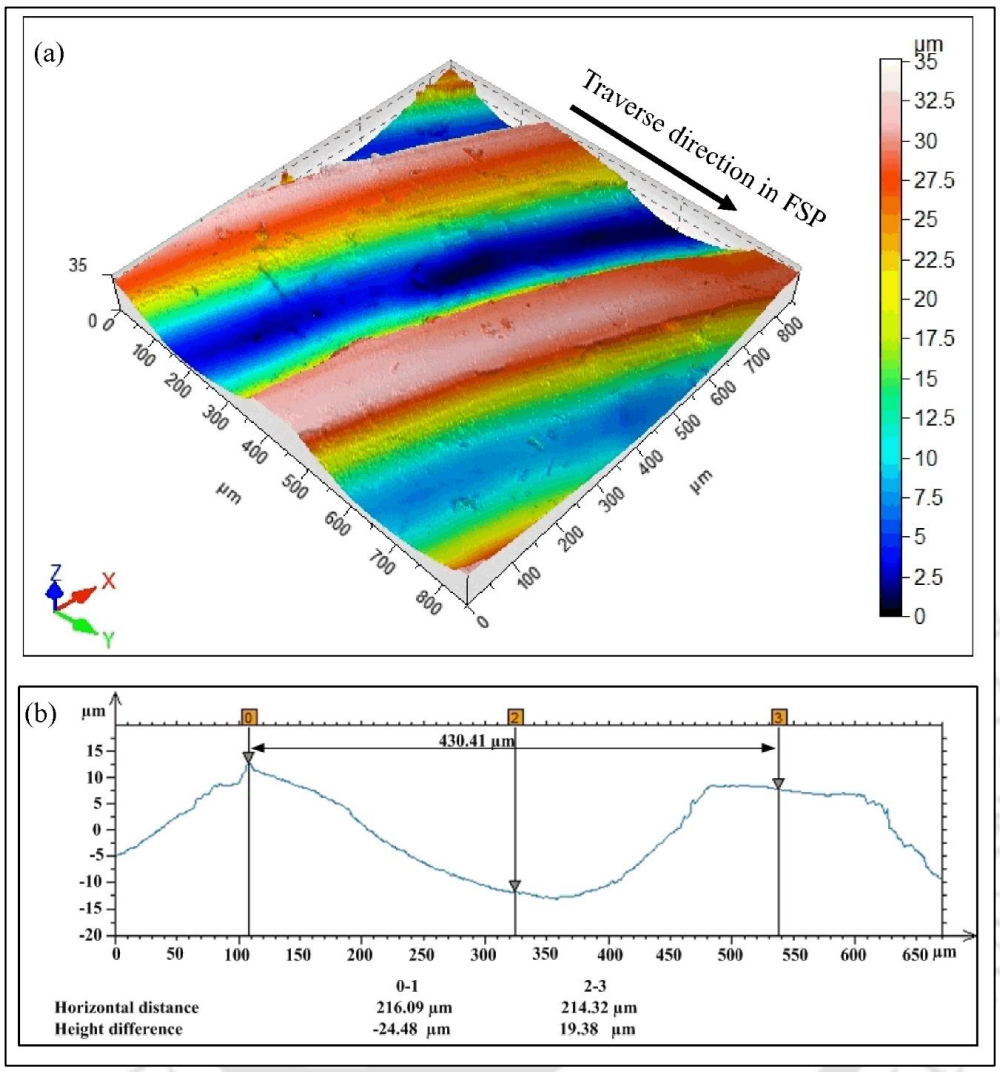

Figure 7.5 Results of 3D non-contact surface profilometer for friction stir processed aluminium: (a) surface topography and (b) scan profile showing the width and the height of the groove

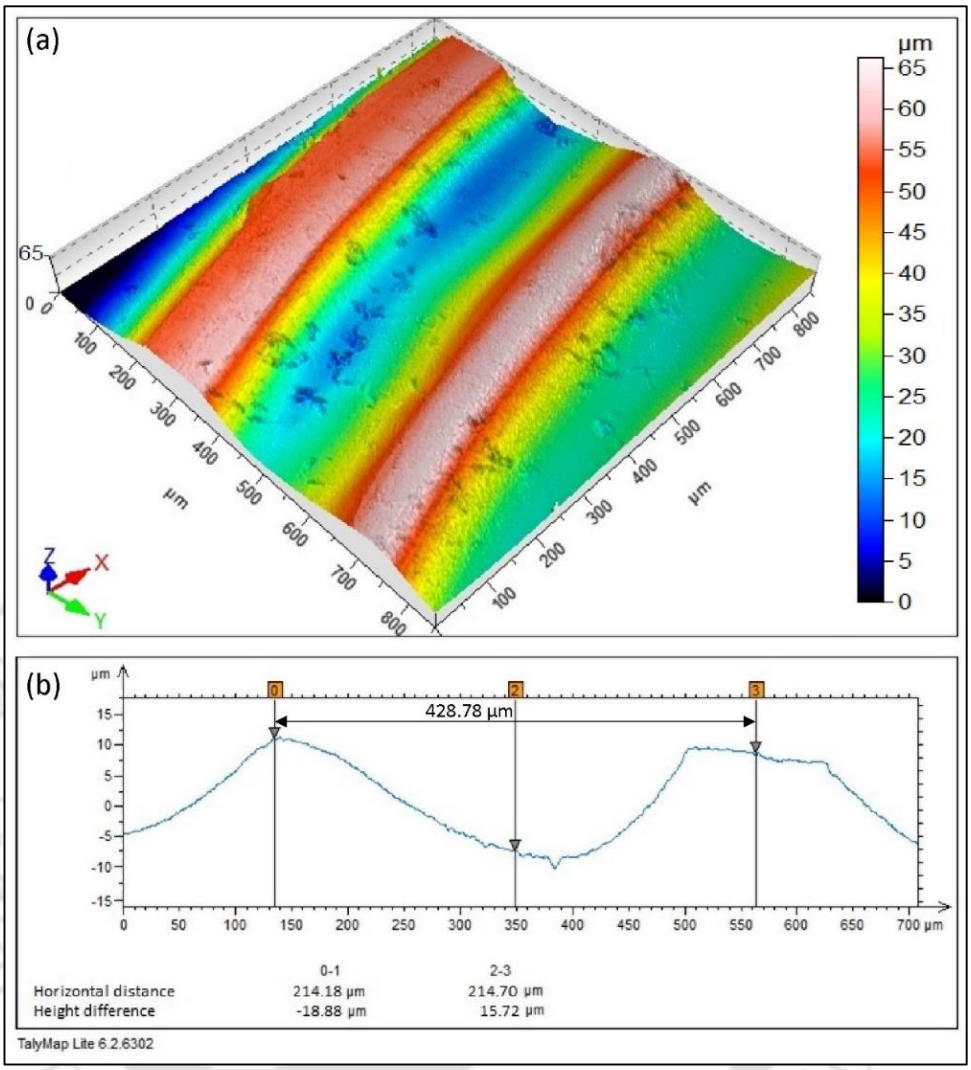

Figure 7.6 Results of 3D non-contact surface profilometer for friction stir processed mild steel (AH36): (a) surface topography and (b) scan profile showing the width and the height of the groove

7.3.3 Bend angle

The experimental bend angles were recorded at the following parameters: scanning speeds: 1000 mm/min, laser power: 1000 W, laser diameter: 9.4 mm and laser pass: 1 to 6. As shown in Fig. 7.7(a) and (b), for both aluminium alloy (5052-H32) and mild steel (AH36), the bend angle is greater in the case of cement coated sheet. However, for mild steel (AH36), the difference in bend angles between the cement coated and the friction stir processed sheets keeps on reducing with increasing number of passes. This is due to increase in absorptivity of friction stir processed sheets, thanks to further

roughening of the surface after heating. After the 6th pass, both cement coated and friction stir processed sheets bend to almost same degree. In the case of aluminium alloys sheet, the cement coated sheets bend more than friction stir processed and uncoated sheets even after sixth laser pass. This is due to high reflection even on friction stir processed sheet. Nevertheless, friction stir processed aluminium alloy (5052-H32) sheet bend more than uncoated sheet. After 6th pass, the bend angle for uncoated sheet was 0.5°, whilst it was 3° for friction stir processed sheet, which is an increase by a factor of 6.

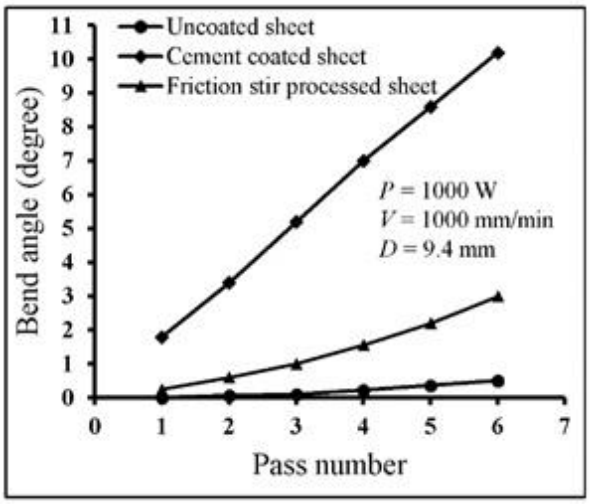

(a)

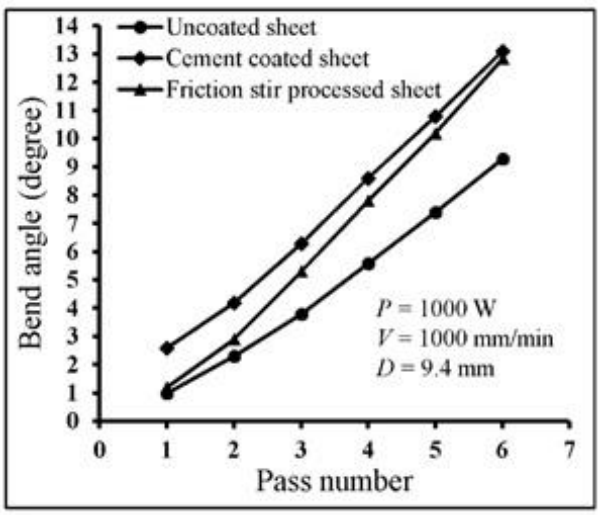

(b)

Figure 7.7 Effect of number of laser pass on bend angle for (a) aluminium alloy (5052-H32) and (b) mild steel (AH36)

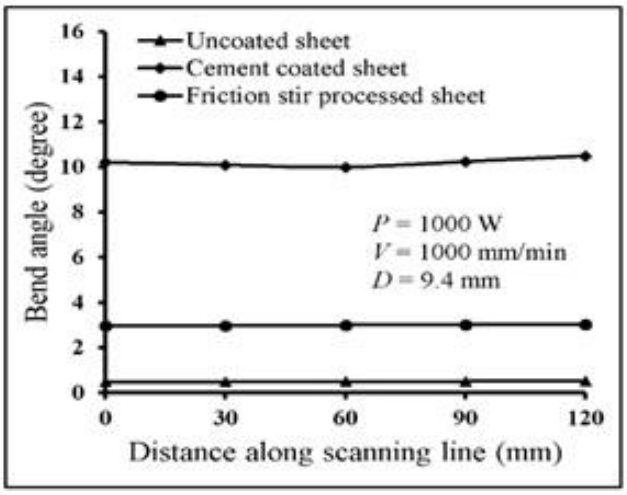

(a)

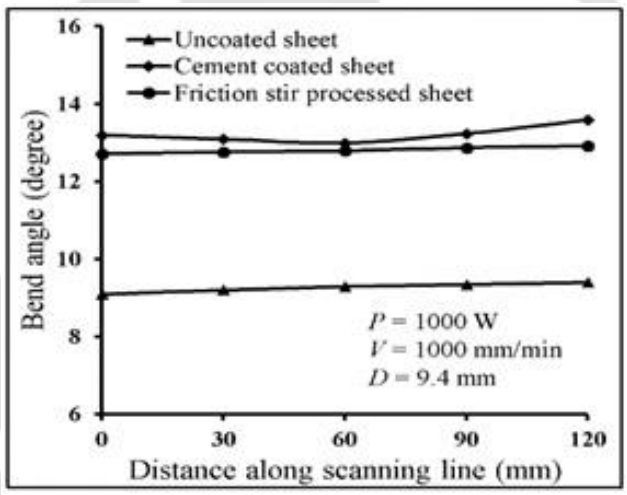

(b)

Figure 7.8 Variation in bend angle along the laser path after 6th laser pass for (a) aluminium alloy (5052-H32) and (b) mild steel (AH36)

After 6th laser pass, the bend angle variation along the width (scan direction) is studied. For all the sheets, the bend angle is the highest at the end of scanning as seen in Fig. 7.8 (a) and (b). In the case of friction stir processed sheets, the variations are small. The variations are more in the case of cement-coated sheets. The edge effect was evaluated using Eq. (1). Relative variation in bend angle (RVBA) is 8%, 4% and 2.3% for uncoated, cement coated and friction stir processed sheet, respectively. The corresponding values for aluminium alloy (5052-H32) are 3.23%, 4.57% and 1.72%, respectively.

7.3.4 Microhardness

Figure 7.9 represents the variation of microhardness of laser irradiated aluminium alloy (5052-H32) and mild steel (AH36) friction stir processed sheets as a function of laser pass number. For aluminium alloy (5052-H32), the microhardness of raw material was 68 HV. As a result of FSP, the microhardness at the middle of thickness increased to 74.5 HV. It was 77.4, 79, 81.2, 83.3, 86.8 and 90.6 HV for laser pass number 1, 2, 3, 4, 5 and 6, respectively as depicted in Fig. 7.9(a).

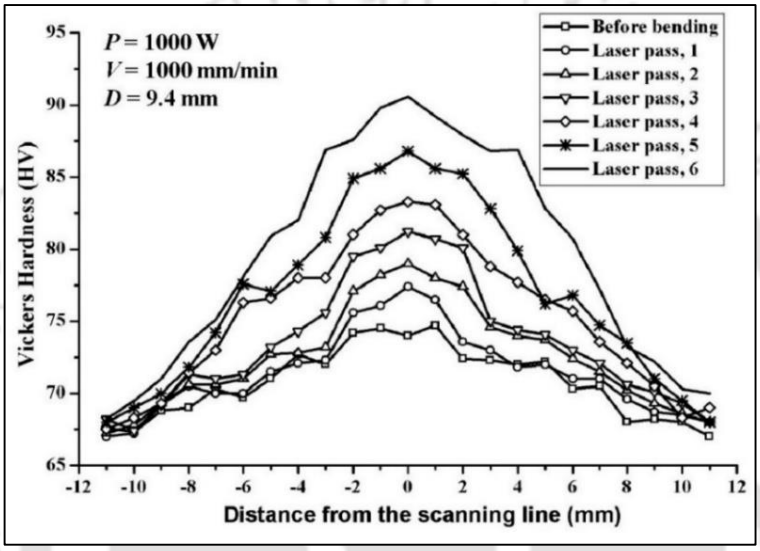

(a)

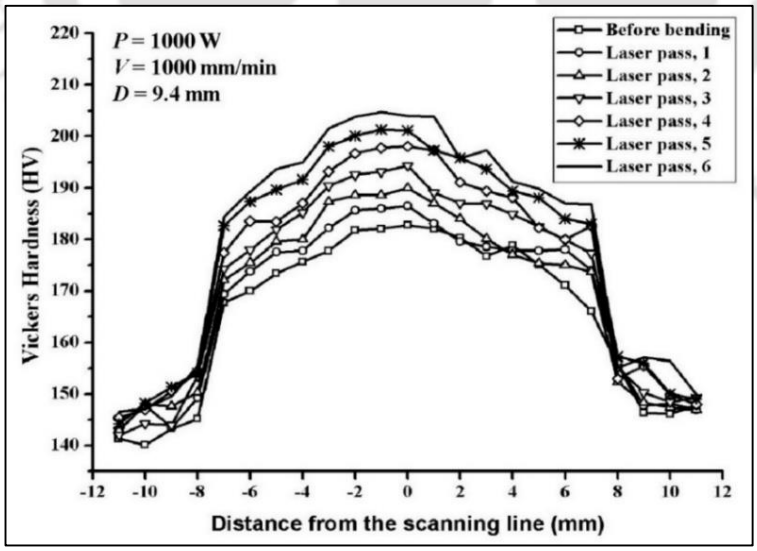

(b)

Figure 7.9 Microhardness profile of laser applied FSP sheet at the middle of the thickness (a) aluminium alloy (5052-H32) and (b) mild steel (AH36)

The hardness of mild steel (AH36) raw material was 130 HV. As a result of FSP of mild steel (AH36), the hardness at the middle of thickness reached to 182 HV. It increased to 186.5, 190, 194, 198, 201 and 204 HV for laser pass number 1, 2, 3, 4, 5 and 6, respectively as shown in Fig. 7.9 (b). Both FSP and laser bending produce heat and plastic deformation in the sheet followed by the natural cooling. The combined effect increases the microhardness of the material.

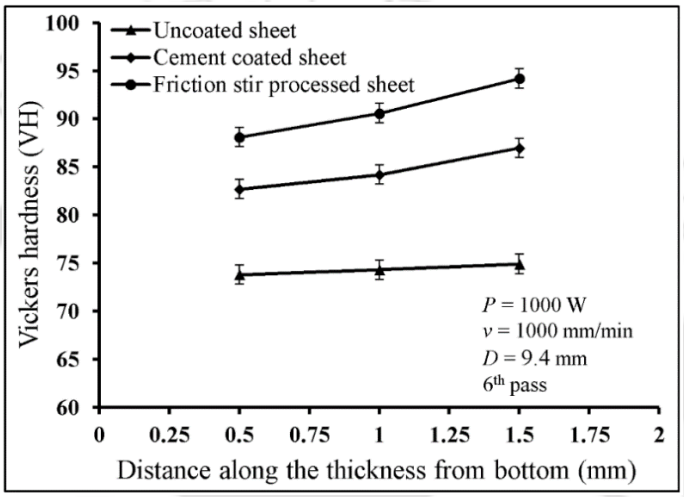

(a)

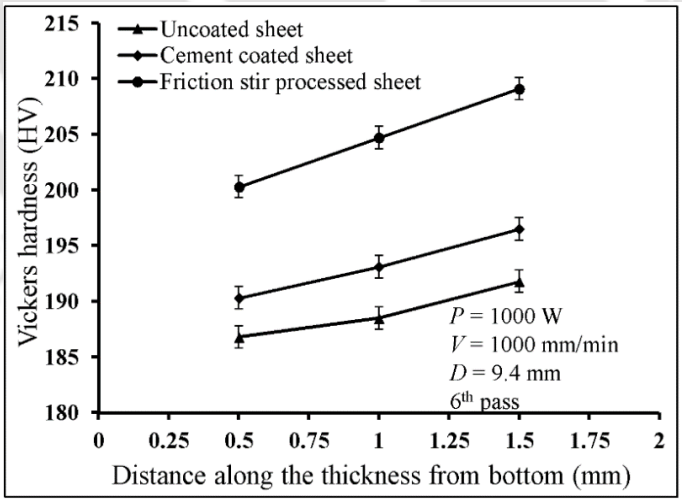

(b)

Figure 7.10 Microhardness profile after 6th laser pass on FSP, cement coated and raw sheets along thickness direction for (a) aluminium alloy (5052-H32) and (b) mild steel (AH36)

Figure 7.10 shows the microhardness variation along thickness direction after the 6th laser pass on friction stir processed, cement coated and raw sheet. Microhardness near the top surface of the workpiece was greater than the near bottom surface for both mild steel (AH36) and aluminium alloy (5052-H32) sheets. This happened because of high temperature and large plastic deformation at the top surface. For aluminium alloy (5052-H32) friction stir processed bent sheet, the microhardness at 0.5 mm from the top surface was 6.9% greater than that at 0.5 mm from the bottom surface. For the cement coated and uncoated bent sheets, the corresponding increases in the microhardness values were 5.2% and 1.5%, respectively. For mild steel (AH36), these values were 4.4%, 3.2% and 2.9% for friction stir processed, cement coated and uncoated sheets, respectively. This brings out the increased tendency of hardening of aluminium alloy (5052-H32) due to thermo-mechanical processing compared to mild steel (AH36).

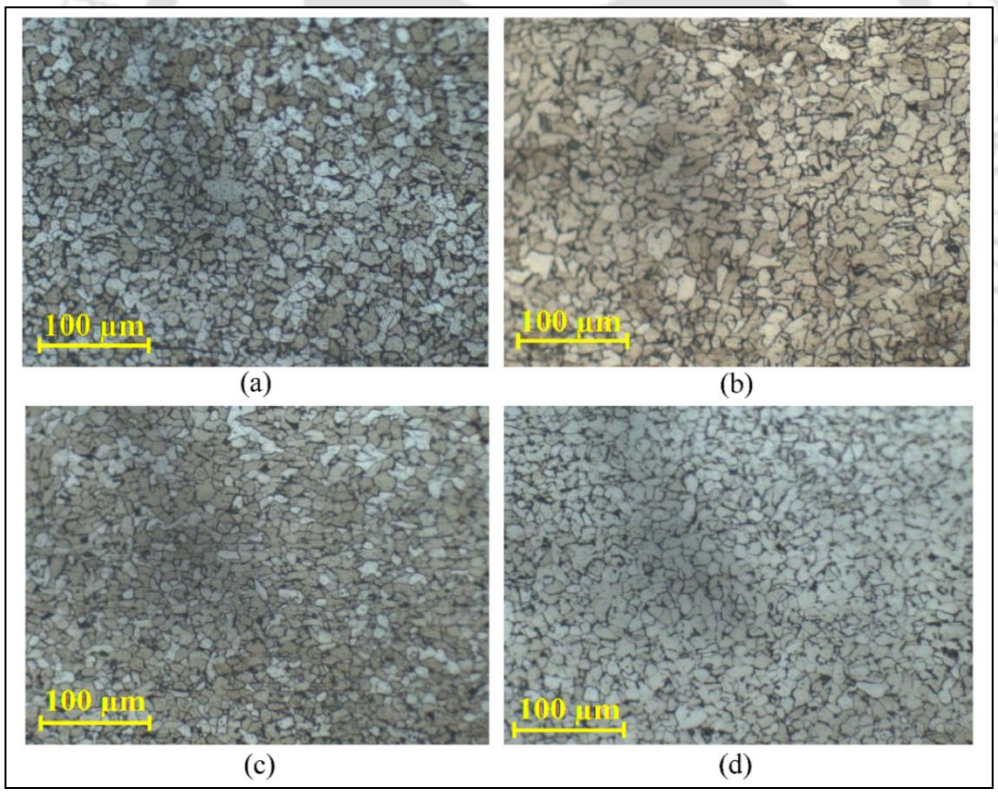

Figure 7.11 Optical microstructures at the centre of friction stir processed steel sheet (×20 magnification): (a) before laser bending, (b) after first laser pass, (c) after third laser pass and (d) after sixth laser pass

7.3.5 Microstructure

The mechanical stirring as well as the heat produced due to it breaks the coarser particles (Hassan et al. 2003 and Surekha et al. 2009). The optical microscope was used to study the microstructure of the friction stir processed and laser bent mild steel (AH36) sheets. Figure 7.11 (a)–(d) shows microstructures at the middle of the thickness on a plane normal to the scan direction for friction stir processed sheet without bending as well as after first, third and sixth laser pass.

The study focuses on the stir zone. It was observed that the grain size reduces due to FSP as also observed by Surekha et al. (2009). As the number of laser pass increase, the grain size reduces due to plastic deformation of the metal during the process. At each laser pass, the mean grain size reduces by 2–3%.

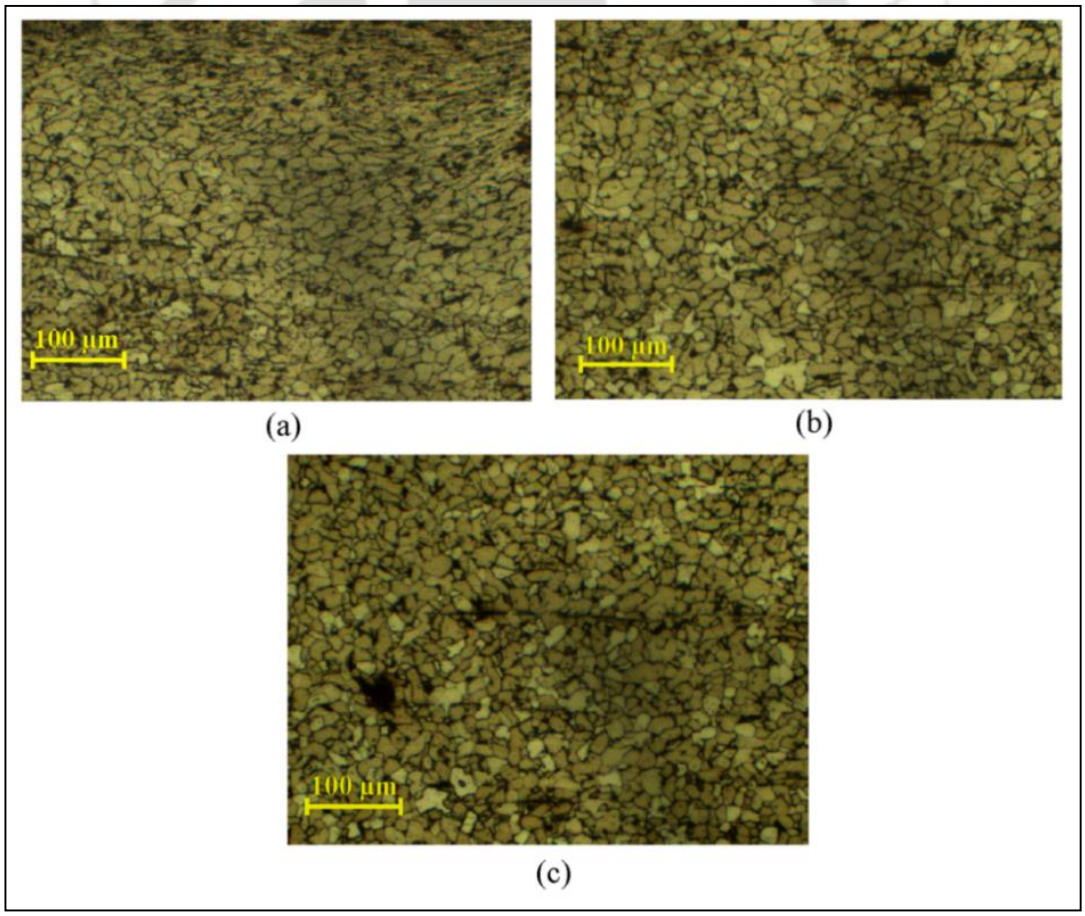

Figure 7.12 Optical microstructures after 4th laser pass of friction stir processed mild steel (AH36) sheet along thickness direction (×20 magnification): (a) near top, (b) middle and (c) near bottom

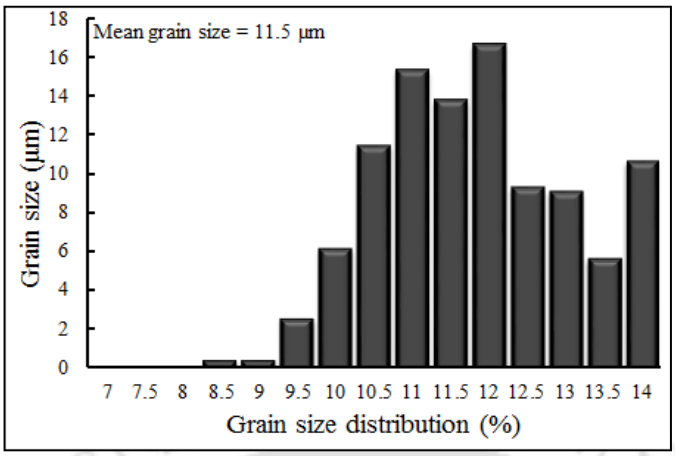

(a)

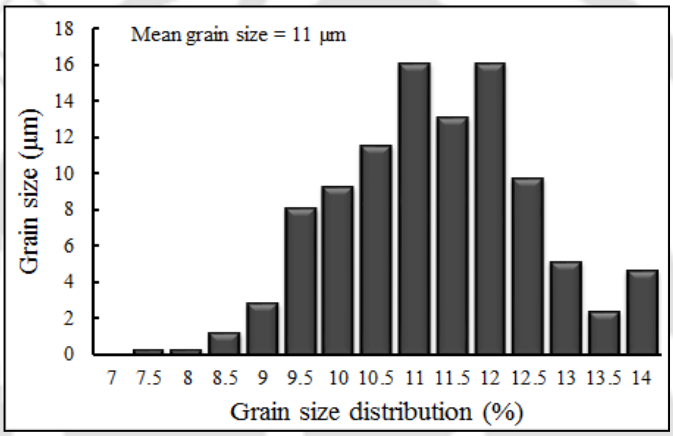

(b)

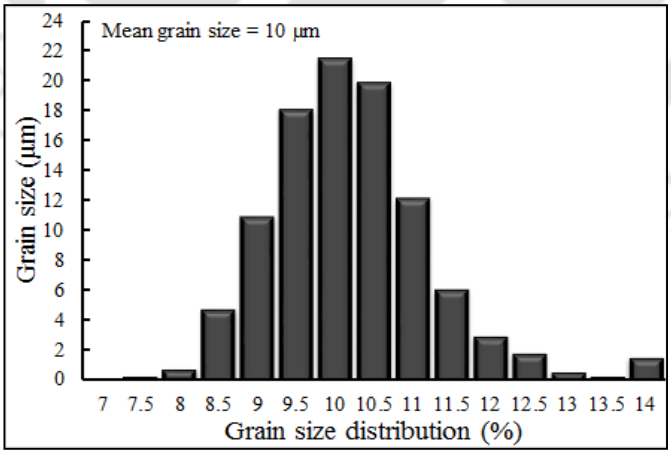

(c)

Figure 7.13 The mean grain size distribution for friction stir processed steel sheet after (a) first laser pass, (b) third laser pass and (c) sixth laser pass

Figure 7.12 (a)–(c) shows the microstructure after 4th laser pass on friction stir processed sheet. The microstructure study at the top, middle and bottom along thickness direction was carried out. The grain size reduced from bottom to top of the sheet as shown in Fig. 7.12 (a)–(c). The image analysis method using AxioVision SE64 Rel.4.9.1 software was employed for finding the grain size. The histograms of mean grain sizes after first, third and sixth laser passes on friction stir processed sheets at the middle of the thickness are shown in Fig. 7.13(a)–(c). The average grain size is 11.5 μm, 11μm and 10 μm for first, third and sixth laser pass, respectively.

7.4 Conclusion

In this work, laser bending of friction stirred processed and cement coated aluminium alloy (5052-H32) and mild steel (AH36) sheets was carried out and compared with the laser bending of unprocessed and uncoated sheets. From the experimental study the following conclusions are drawn:

- Friction stir processed sheets produce larger bend angles for the same set of processing parameters in comparison to uncoated sheets of mild steel (AH36) and aluminium alloy. This implies that FSP improves the laser absorptivity of both the materials. However, it could not match the absorptivity of cement coated sheets. For aluminium alloy, after six laser passes, the bend angle for cement coated sheet was 3.4 times more than for friction stir processed sheet. However, for mild steel (AH36), after six laser passes, the bend angle for cement coated sheet was only 1.02 times more than for friction stir processed sheet.
- Cement coated sheet provided the largest bend angles for both materials. For mild steel (AH36), as the number of passes increased, the difference in the bend angles of cement coated and friction stir processed sheets kept on reducing. This was due to increase in absorptivity of friction stir processed sheets due to heating.
- As the number of laser pass was increased, the mean grain size of the friction stir processed sheet reduced and the microhardness increased. The increase in

the microhardness at the scan-line and mid-thickness is 22% for aluminium alloy and 12% for mild steel (AH36).

- Friction stir processed sheets had higher microhardness than uncoated and coated sample. After laser bending, the microhardness of the irradiated surface was greater than that of the opposite surface. The microhardness varied almost linearly along thickness.
- For friction stir processed sheet, the bend angle variation along the width (scan path) was smaller as compared to coated as well as uncoated (raw) aluminium and mild steel (AH36) sheets.

Overall, friction stir processing is helpful for laser bending of the sheets. It increases the absorptivity and thereby the bend angle. It also helps to increases the microhardness of the sheet.

Chapter 8

Laser Assisted Bending by Using Mechanical Load

8.1 Introduction

There are predominantly two ways to bend sheets with the application of laser heat source (Dixit et al. 2012). One way is to carry out laser line heating of the sheet to induce thermal stresses in it. This process is called laser bending. It is a non-contact bending process, suitable for obtaining small bend angles. For obtaining large bend angles, multi-pass laser scanning is carried out. However, this leads to excessive processing time and increases the production cost. The bend angle per pass keeps on reducing with increasing pass number (Lambiase et al. 2015). This is due to the changes in absorptivity, thermal heating effect, strain hardening and section thickening of the workpiece (Edwardson et al. 2007). The other way is to carry out mechanical bending along with laser heating for localised softening of the material. To distinguish it from laser bending, this method may be called laser assisted bending (Kratky, 2007).

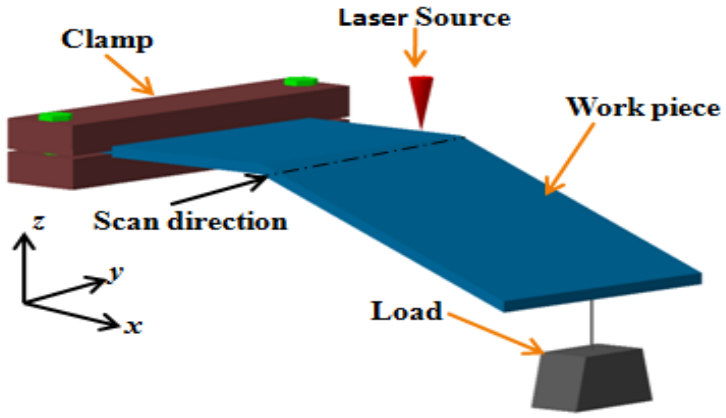

Figure 8.1 A schematic diagram of laser assisted mechanical bending

It helps to get larger bend angles with a single laser scan, even in the hard materials with a very less amount of ductility (Dearden and Edwardson, 2003; Roohi

et al. 2012). As the yield strength keeps on reducing at the line of heating, sheet will keep undergoing plastic deformation. The preloading increases the bend angle significantly. A simpler way is to hang a weight from the end of cantilever beam as shown in Fig. 8.1.

In this work, laser assisted bending of aluminium alloy 5052-H32 sheets was carried out by hanging a weight at the free end of the cantilevered sheet, whilst the laser scanning was carried out at the bend line. A finite element model (FEM) of the process was developed using ABAQUS® package. This model is rigorously validated in the present work. An ANN model was developed to predict the most likely, lower and upper estimates of the bend angles. The procedure makes use of Multi-Layer Perceptron (MLP) as well as Radial Basis Function (RBF) networks. Estimation of the upper and lower bound values of surface roughness in turning have been carried out by Kohli and Dixit (2005) using MLP and Sonar et al. (2006) using RBF neural networks, but not many researchers have followed this procedure to model other engineering systems perhaps due to perceived difficulty of the procedure.

In this work, an MLP was first trained using an optimum number of experimental data. After obtaining a desired fit model of the MLP, the model was used to generate additional levels of data to provide the testing data for the training of an RBF. Experimental data was used for testing the RBF. A similar approach was also used by Garg et al. (2007) in which only one MLP network was used for generating testing data for an RBF network.

8.2 Details of Experiment

Aluminium alloy 5052-H32 samples were prepared with dimensions 100 mm × 50 mm × 2 mm. The surface of the sheet was cleaned with oil and grease using acetone. Then hydrated lime coating was used to enhance absorptivity as Singh et al. (2013) has observed that the hydrated lime coating is superior to graphite coating. The experiments were performed on CO_2 laser cutting machine (Make: LVD; Model: Orion 3015) (Fig. 3.3). A simpler way is to apply a concentrated load at the free end of the cantilevered workpiece as shown in Fig. 8.2. The experiments were conducted with full factorial method by using different laser bending parameters as listed in

Table 8.1. In each case, two replicates of experiments were carried out. Bend angles were measured by using coordinate measuring machine (CMM) of Zeiss™ Make, Model: Vista (Fig. 3.6). The average bend angle results are reported.

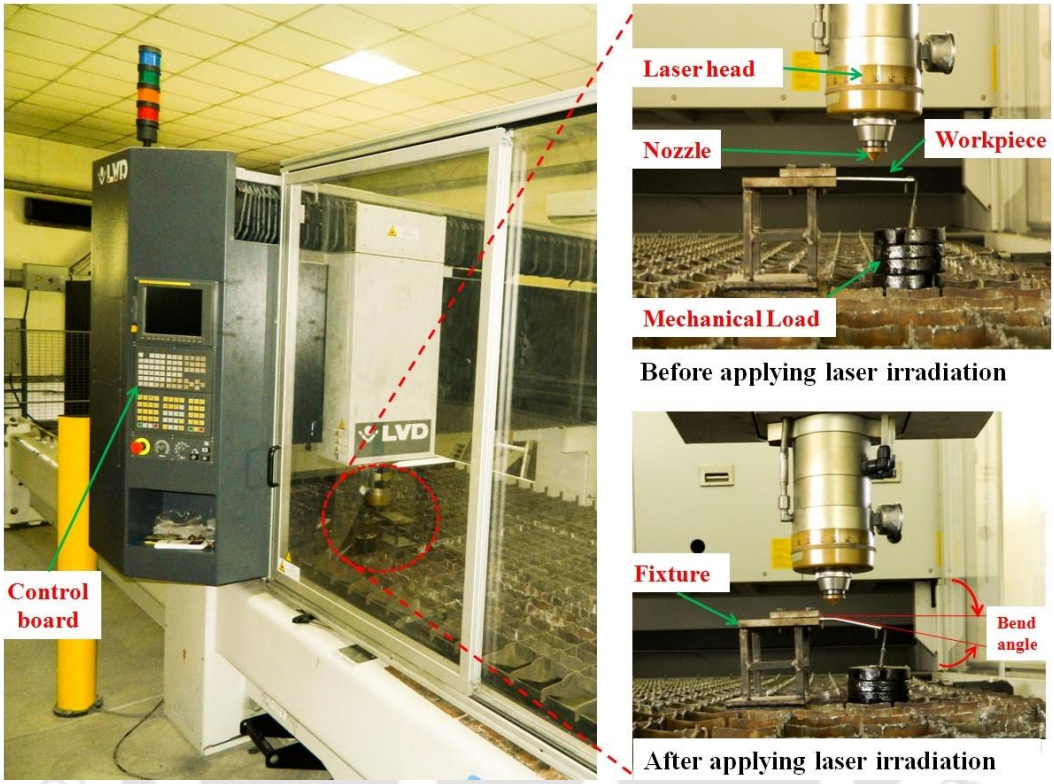

Figure 8.2 Experimental setup in the laser machine

Table 8.1 Process parameters and their levels in the experiment

Parameters	Unit	Levels
Laser power	W	500, 600, 700, 800 and 900
Mechanical load	N	20, 30 and 40
Scan-line distance	mm	30 and 60
Scan speed	mm/min	300, 400 and 500
Laser beam diameter	mm	7.74

The commercial FEM package ABAQUS® was used to model laser assisted bending. As the mechanical and thermal properties are temperature dependent, their estimation is carried out for different laser powers following an inverse procedure as discussed in Chapter 6. These properties were used for carrying out the corresponding

simulations in the presence of mechanical load. For the thermo-mechanical FEM formulation, three-dimensional linear elements were used, each with eight-node thermally coupled brick elements (C3D8T). The mesh sensitivity was discussed in Chapter 3. The entire domain was divided into three regions as shown in Fig. 3.26.

8.3 Neural Network Modelling

The FEM model of laser assisted bending can provide good results of bend angle for various process inputs and can be reliably used as a substitute to experiments when the cost of experimentation is expensive. However, FEM model also has a drawback of requiring a large amount of computational time. To overcome this difficulty, a well-trained neural network model can be used to predict good and accurate estimates of the bend angles for a particular set of inputs. In the present work, a neural network was modelled to predict the bend angle as a function of four input parameters— laser power (P), mechanical load (L), scan-line distance (d_s) from free end and scan speed (v).

An attempt was also made to reduce the number of input parameters to three by taking the product of mechanical load and scan-line distance and use bending moment as a single input parameter. However, it was noted that for the same bending moment, different combinations of scan-line distance and mechanical load provided different results. This was due to significant effect of shear deformation.

Two neural network models— one MLP and one RBF were used in MATLAB®. An MLP network was first trained based on the results obtained from the FEM model. After deciding the best model of the MLP, it was used to generate additional data for training an RBF neural network. All the experimental data was used for testing and validation of the RBF network. The RBF can be easily used to predict the upper and lower bound estimates of the bend angles. The details of network architecture, data selection and implementation using MATLAB® are discussed in the following subsections.

8.3.1 Selection of training and testing data set for MLP neural network

The criterion for choosing the training data set is identical to the one used by Kohli and Dixit (2005). For the four input parameters and the levels as shown in Table

8.1, a total of 90 data is available for the MLP modelling. The first initial basis of the training data set is formed by taking all the corner points in the input space. For the four inputs, the input space is a hypercube in a 4-dimensional space. Considering two levels (maximum and minimum) of each of the four parameters, a total of 2^4 corner points were obtained. Based on these 16 corner points, the effect of each parameter was calculated. The parameters with large effects were assigned more levels in the training data set whereas the parameter with the least effect was assigned only two levels. The effect of a parameter is given by (Dieter, 1991)

$$\text{Effect of a parameter} = \frac{\sum \text{responses at high levels} - \sum \text{responses at low levels}}{\text{half the number of runs in the experiment}}. \tag{8.1}$$

The effects of laser power, mechanical load, scan-line distance and scan speed were calculated as to be 4.378, 2.93, 1.168 and –0.655, respectively. Accordingly, 5 more levels of laser power and 3 more levels of mechanical load were generated. For each parameter, FEM simulations were carried out for the new levels taking random values of the other input parameters. The FEM simulation results based on the new levels were added to the training data set. For scan-line distance and scanning speed, only two levels from the corner points were retained. By adding the 16 corner points and the data from new 5 levels for laser power and 3 levels of mechanical load, 24 data were used for training the MLP.

The size of the testing data set is decided using the probability method proposed by Kohli and Dixit (2005). According to this, the probability P_0 that a network will be passed by n testing data even if it provides wrong prediction in p% cases is given by

$$P_o = \left(1 - \frac{p}{100}\right)^n \tag{8.2}$$

For the present study, the value of p is taken as 15 (implying that in 85% of the instances, the network should predict correctly with errors less than that of the prescribed limit) and P_0 as 0.1. This provides the value of n as 14.16. Hence, it was decided to take 15 testing data.

8.3.2 Implementation of MLP neural network

A MLP neural network with one hidden layer was designed using the neural network toolbox features in MATLAB®. The network architecture is shown in Fig. 8.3. The following criterion is used for deciding the range of number of hidden layer neurons (Lawrence and Petterson, 2002):

Minimum number of training data= 2 × (input + hidden + output) neurons,

Maximum number of training data=10 × (input + hidden + output) neurons. (8.3)

There are 4 input neurons and 1 output neuron. The starting number of training data is 24 and the maximum number of training data based on the full factorial design is 90. This limits the number of hidden layer neuron from 4 to 7.

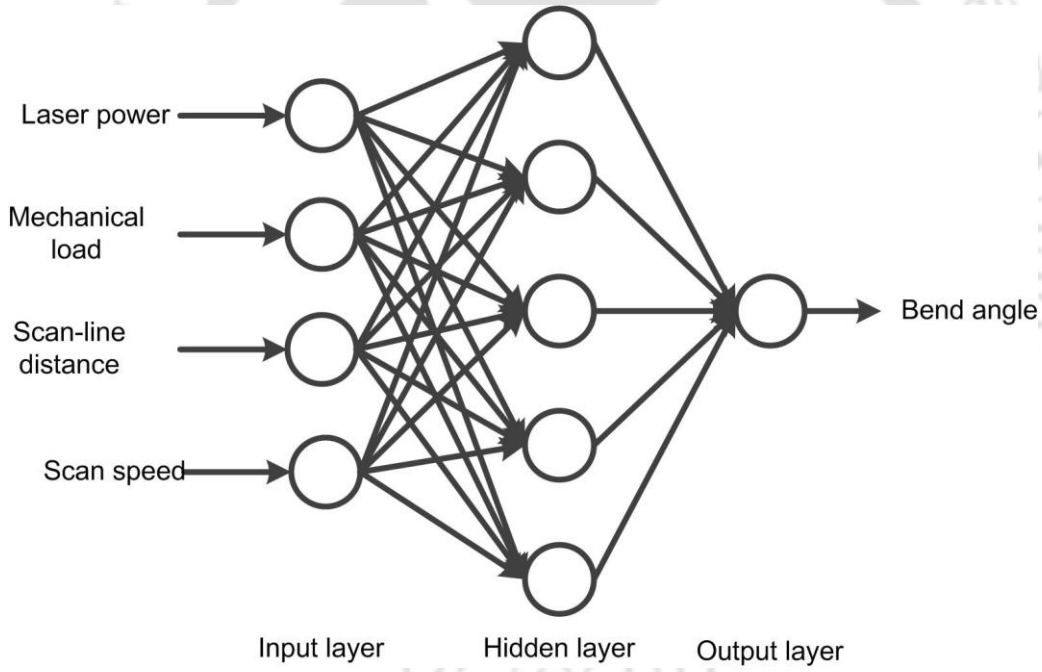

Figure 8.3 MLP neural network architecture

Before the introduction of the training data into the network, the target bend angles were normalized by taking their natural logarithm. This helped in ensuring a uniform distribution of percentage errors (Risbood et al. 2003). After this, the entire training data was normalized between –1 to 1. The network was trained using the TRAINLM function of MATLAB®. When a network model was achieved with a good

fit on the training data, the testing data set was provided to the network model as a completely foreign data to check its generalization. The training and testing errors of the network are expressed as root mean squared percentage error (RMS%), which is defined as follows:

$$\text{Root mean squared percentage (RMS\%) error } = \sqrt{\sum_{i=1}^{n} \frac{(\alpha_{bti} - \alpha_{bpi})^2}{n\alpha_{bti}^{\ 2}}} \times 100, \tag{8.4}$$

where α_{bti} is the target bend angle, α_{bpi} is the predicted bend angle and n is the number of data. The performance of the network is decided on the basis of effective error, which is the maximum of training and testing error.

The number of hidden neurons is varied from 4 to 7 and for a particular network topology the error goal is varied from 5×10^{-4} to 30×10^{-4} using an increment of 5×10^{-4}. By starting from a network topology with 4 hidden layer neurons and MSE goal 5×10^{-4}, the network training is allowed to run for 1000 times in a loop. For each pass in course of the loop run, the effective error in the current network model is monitored. If the effective error is less than or equal to a desired effective error, the model is saved and the desired effective error is updated to a new one which is set equal to the latest acquired effective error and the loop is restarted again. If the network topology using the set MSE goal fails to give any satisfactory result, then the MSE error goal is relaxed by incrementing with 5×10^{-4} and the training loop is started again. If the network topology still fails to give a good network model after trying all the MSE goals, a new topology is selected by incrementing the number of hidden neurons with 1. A training procedure proposed by Kohli and Dixit (2005) has also been applied in the present study. When the best network model was obtained for a selected topology, the individual percentage errors (between FEM bend angle and predicted bend angle) were computed in the testing set. If all the individual testing errors are less than 12%, then the training process is concluded. If there are one or more testing data with individual errors more than 12%, then these data are transferred to the training set and twice the number of fresh random data is added into the testing set. Based on this new data set, the training loop is started again. The whole procedure

took about 34 minutes of screen time. The training algorithm has been illustrated with a flowchart in Fig. 8.4 for a fixed number of hidden neuron. The similar procedure is carried out 4 times (from 4 to 7 hidden neurons).

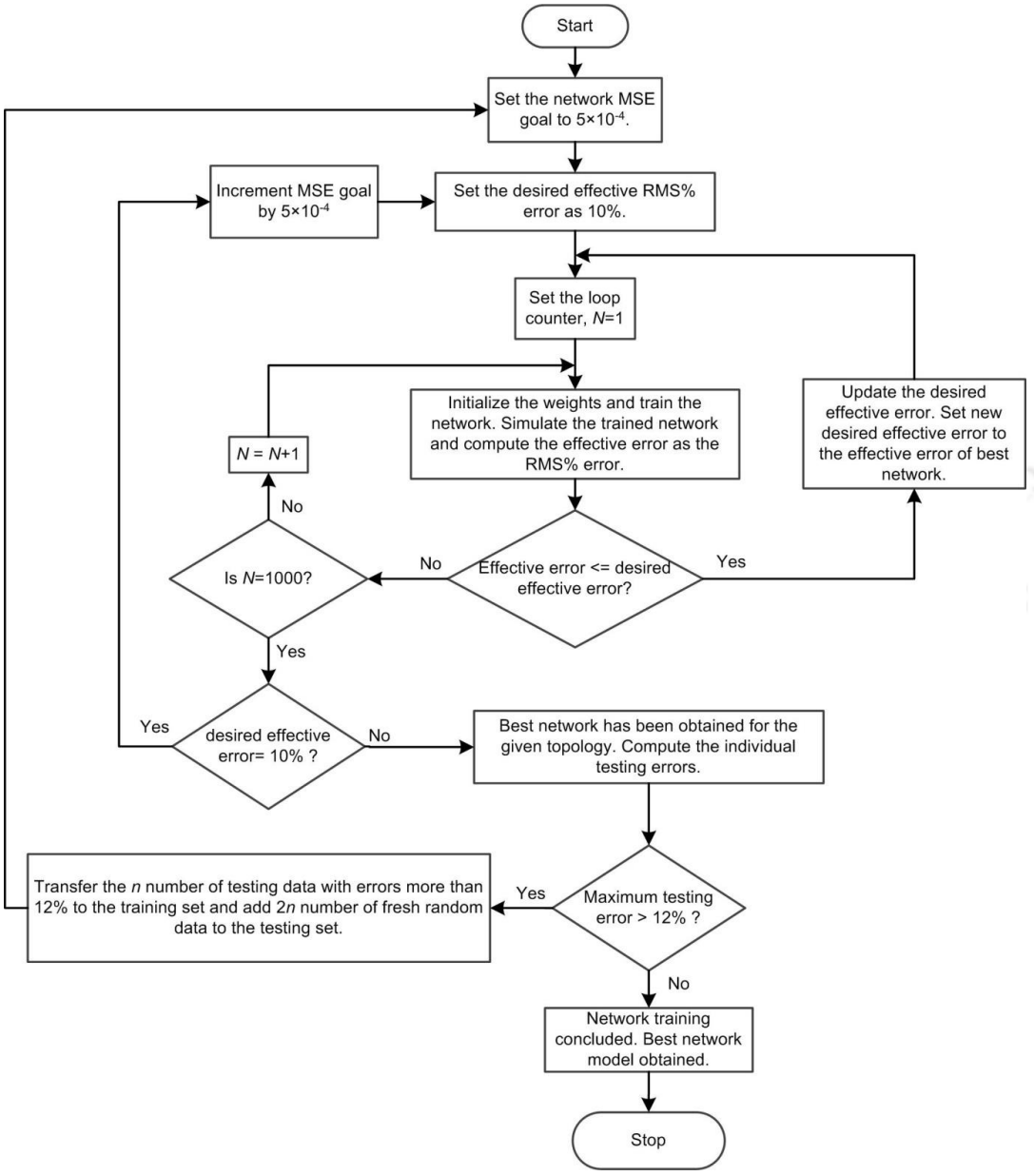

Figure 8.4 Flowchart for the training process

8.3.3 Selection of training and testing data set for RBF neural network

The best fit model of the MLP network which has been trained based on actual FEM data can be used to generate additional levels of data. A neural network is a good tool for interpolation. The trained MLP which incorporated all the 16 corner points of the input space, can be used to predict intermediate levels of data which suffices to the data size requirements for training an RBF neural network. Following this, 6 levels of laser power, 5 levels of mechanical load and 3 levels for each of scan-line distance and scan speed were generated using geometric progression and output angles were predicted for the combination of these new levels. Thus a total of 270 data was prepared for training the RBF.

The procedure for selecting the number of testing data is identical to that used for the MLP network. Only experimental data is used for testing the RBF. Since experimental data is employed, a more reliable prediction is expected. Out of 90 experimental data, 60 data used for testing. Eq. 8.2 provides P_o as 0.05 for p=5%. This ensures high reliability of the network.

8.3.4 Implementation of RBF neural network

An RBF neural network having one hidden layer was designed in MATLAB®. The network architecture is shown in Fig. 8.5. The output in the RBF neural is given by the following expression:

$$\alpha = \sum_{k=1}^{K} w_k \phi_k(\| \boldsymbol{x} - \boldsymbol{c_k} \|_2) + b,\ k=1, 2, 3, 4..... ,K, \tag{8.5}$$

where K is the number of the center and b is the bias. Each k^{th} hidden neuron accepts input vector $\boldsymbol{x}$ defined as $\{P, L, d, v\}^T$ and computes its Euclidean distance $\| . \|_2$ from the center c_k. The function ϕ is the Gaussian radial basis transfer function defined as follows:

$$\phi(x) = \exp(-x^2 / \sigma^2) \tag{8.6}$$

where σ controls the spread of the network. The target bend angles for RBF neural network are also initially normalized by taking their natural logarithms. After this, the whole training data set is normalized between 0.1 and 0.9.The network is trained using

the NEWRB function by varying the function parameters SPREAD and the number of centers. The SPREAD was varied from 1 to 5 by using an increment of 0.5 and the number of centers was varied from 100 to 270 (number of training data) by using an increment of 1. The criterion for the best network was set for an effective error less than 10%. Because of the large size of the testing data set, the prescribed limit of the maximum individual deviation in the testing data was set as 15%.

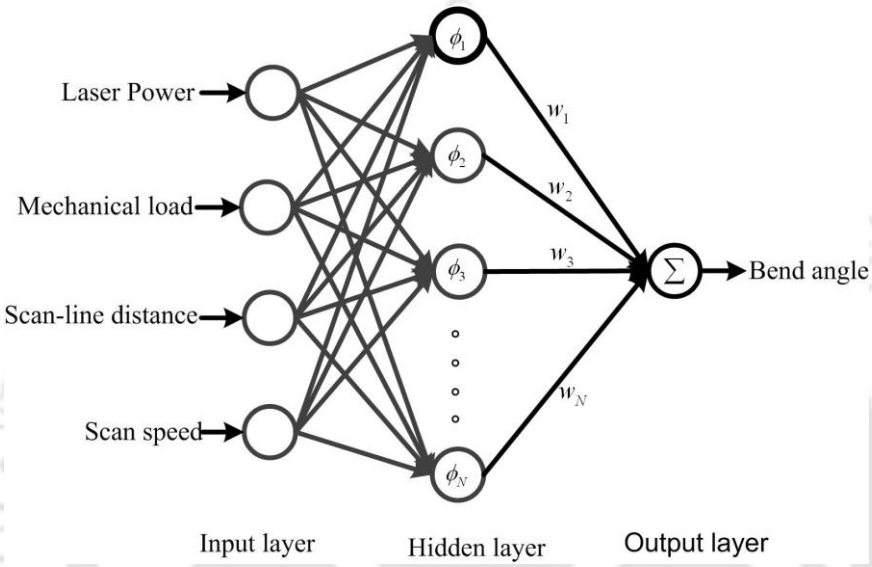

Figure 8.5 RBF neural network architecture

8.3.5 Upper and lower bound estimation

A method similar to the one used by Sonar et al. (2006) for predicting the upper and lower bound estimates of surface roughness in machining has been used. The coefficients w_k and b of Eq. 8.5 corresponding to lower and upper estimates are obtained by solving the following linear programming problem:

$$\text{Minimize} \qquad Z = \sum_{n=1}^{N} (b^u - b^l) + (w_1^u - w_1^l)\phi_{n1} + \ldots + (w_K^u - w_K^l)\phi_{nK} \qquad (8.7)$$

subject to

$$\left.\begin{aligned} b^l + w_1^l\phi_{n1} + \ldots + w_K^l\phi_{nK} &\le (1-\beta)\alpha_n, \\ b^u + w_1^u\phi_{n1} + \ldots + w_K^u\phi_{nK} &\ge (1+\beta)\alpha_n, \end{aligned}\right\}, n = 1, 2, \ldots, N, \qquad (8.8)$$

where β is the tolerance parameter. Sonar et al. (2006) did not use this parameter, which means it was 0 in their case. However, with β=0, in many of the testing data, the solution resulted in upper and lower limit predictions where the most of the estimations did not lie between the limits. By starting from a small value of 0.01 corresponding to 1% tolerance, the solutions were obtained for different values of β in increments of 0.01. The solutions obtained at β values of 0.01 and 0.02 also predicted incorrect limits which failed to locate the most likely estimates within the range of the upper and lower limits. At β=0.03, a satisfactory solution was obtained. Some incorrect predictions pertaining to very small bend angles were still there. Upon further increasing the value of β to 0.04, the range predictions became non-uniform in the sense that some ranges were much wider. Thus, the 3% tolerance was considered to be optimum.

8.4. Results and Discussion

In this section the experimental validation of FEM simulation and the results of the neural network model have been discussed. The lower and upper limits predictions have been shown for the testing and validating the data of the RBF neural network. Based on the RBF, a parametric study was carried out. Finally, the results of inverse analysis have been discussed.

8.4.1 Validation of FEM model

The experimental and FEM simulated bend angles were compared at various scanning speeds (300, 400 and 500 mm/min) and laser powers (500, 600, 700, 800 and 900 W) when mechanical loads 20, 30 and 40 N were applied at the free end at distances 30 mm and 60 mm from the scan-line with a constant stand-off distance of 50 mm. A good qualitative and quantitative agreement was obtained. Figure 8.6 shows the simulation versus experimental bend angles obtained at the same input parameters. There are a majority of 56 data within ±5 % and 87 data between ±10 % deviations. Deviation in all data is within ±15 %.

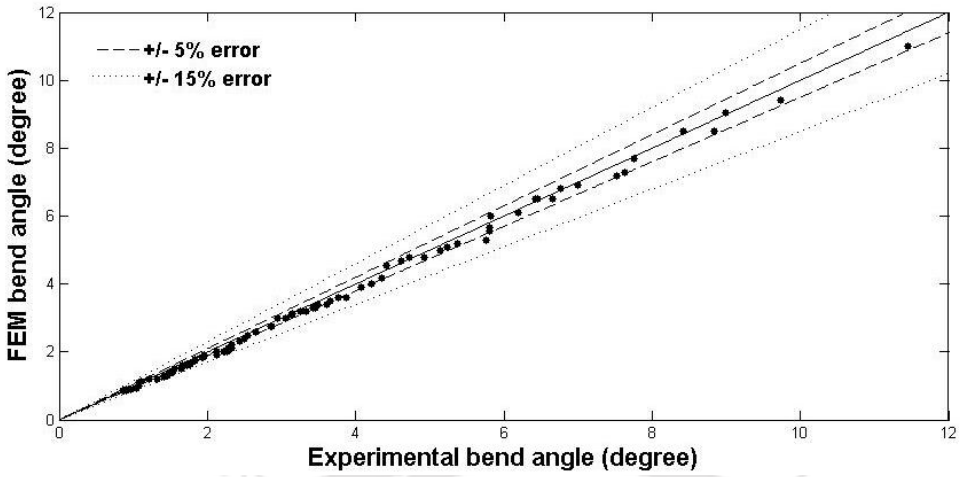

Figure 8.6 Experimental versus FEM result

8.4.2. Results of neural network model

The results of the overall neural network model have been discussed separately in two different subsections for MLP and RBF neural networks respectively.

A) MLP network results

The MLP training was concluded when there was a 3.92% error on 29 training data and 6.45 % error on 20 testing data. It was achieved by using 7 hidden neurons and an MSE goal of 0.0025 on the normalized target. The training was achieved in 9 epochs. It was observed that out of the 20 testing data, 17 data were within ±10% deviations and all data were within ±15%. This is shown in Fig. 8.7.

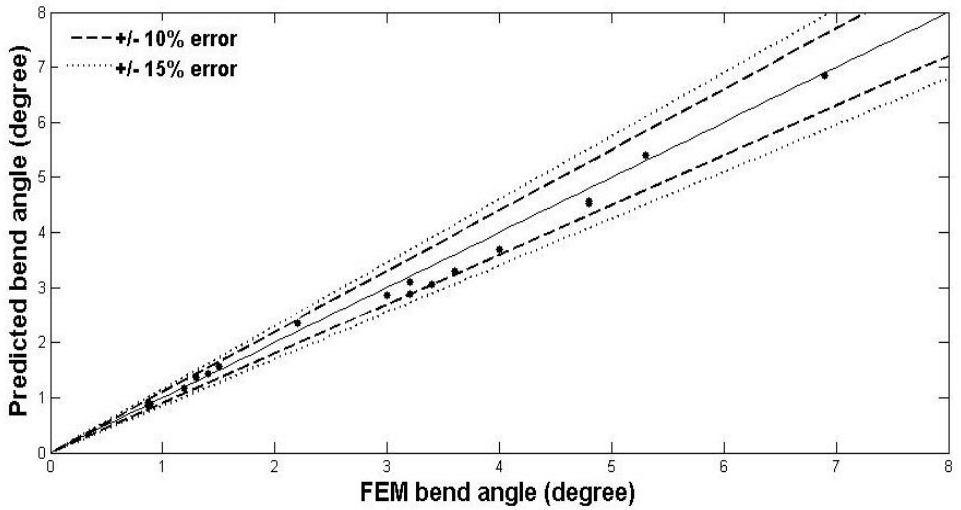

Figure 8.7 Testing results for MLP neural network

B) Testing and validation results from RBF

The best RBF network model was decided for a training error of 2.24% and testing error of 7.96%. It was achieved by using a SPREAD parameter of 4.5 and 129 hidden neuron centers. The maximum individual deviation in the testing data was 14.92%. It was observed that out of the 60 testing data, 46 data were within ±10% deviations and all data were within ±15%. This is shown in Fig. 8.8.

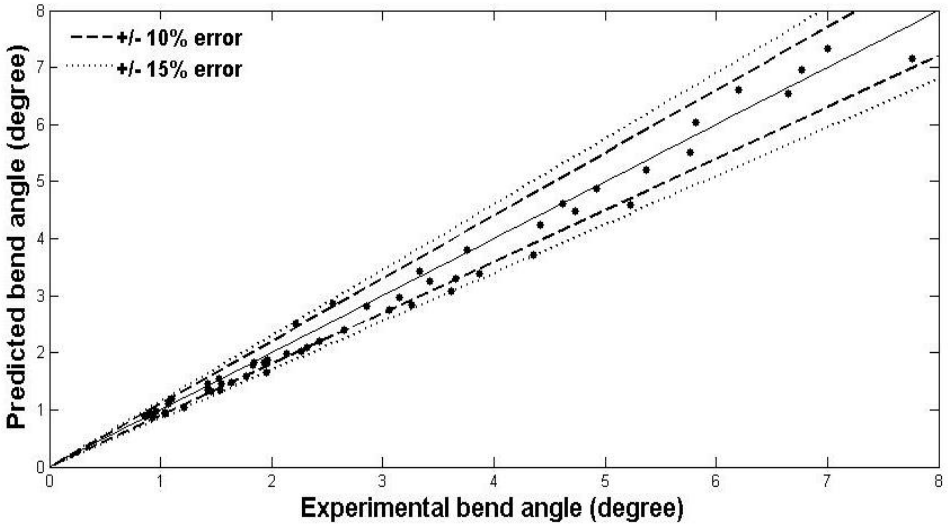

Figure 8.8 Testing results for RBF neural network

The RBF network was also validated using inputs from the remaining 30 experimental data. The network predictions were compared with the experimental and FEM results of the validation inputs. The RMS% error of the validation based on experimental and FEM data is obtained as 11.61% and 8.21% respectively. For the experimental data, there were only 2 predictions with deviations (between the prediction and the target) more than 20% with deviations of 23.91% and 20.34%. With FEM data, the maximum deviation was 18%. The results of validation are shown in Fig. 8.9 and Fig. 8.10.

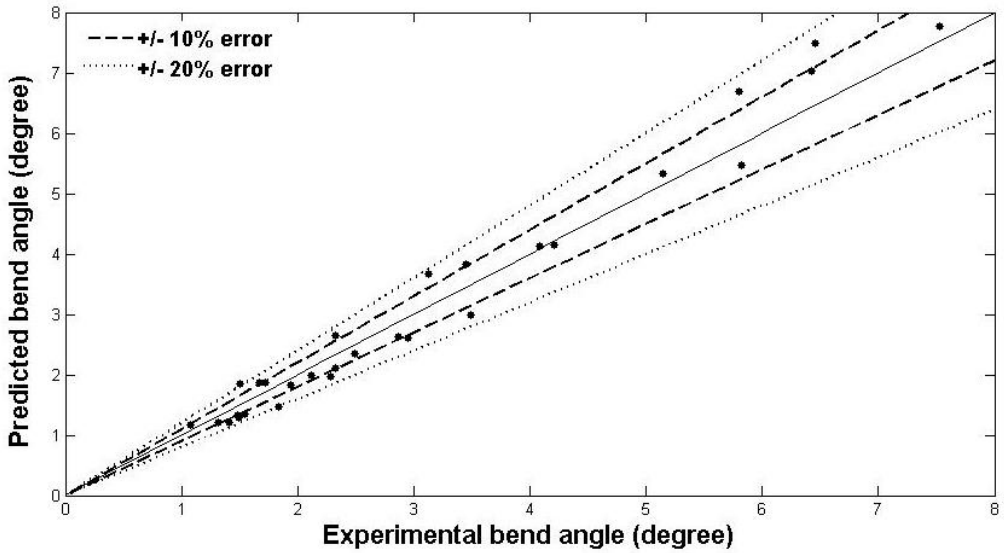

Figure 8.9 Experimental versus RBF predicted bend angles for validation inputs

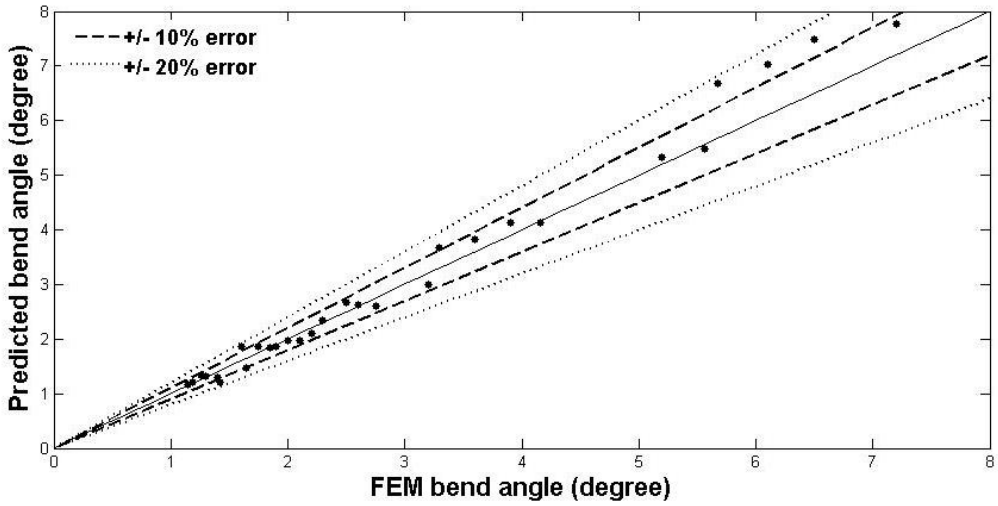

Figure 8.10 FEM versus RBF predicted bend angles for validation inputs

C) Results of the upper and lower bound estimation on testing and validation data

The linear programming problem formulation in Eq. 8.7 and Eq. 8.8 was optimized using the LINPROG function of MATLAB®. From the resulting solution, the predictions of the upper and lower bound limits of the testing and validation data of the RBF neural network are shown in Fig. 8.11 and Fig. 8.12 respectively.

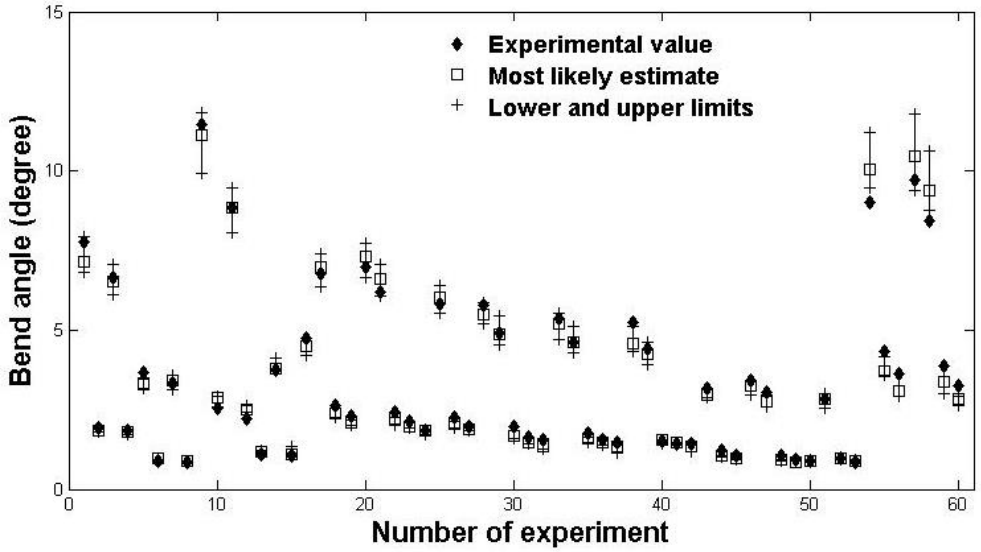

Figure 8.11 Upper and lower bound predictions of the testing data

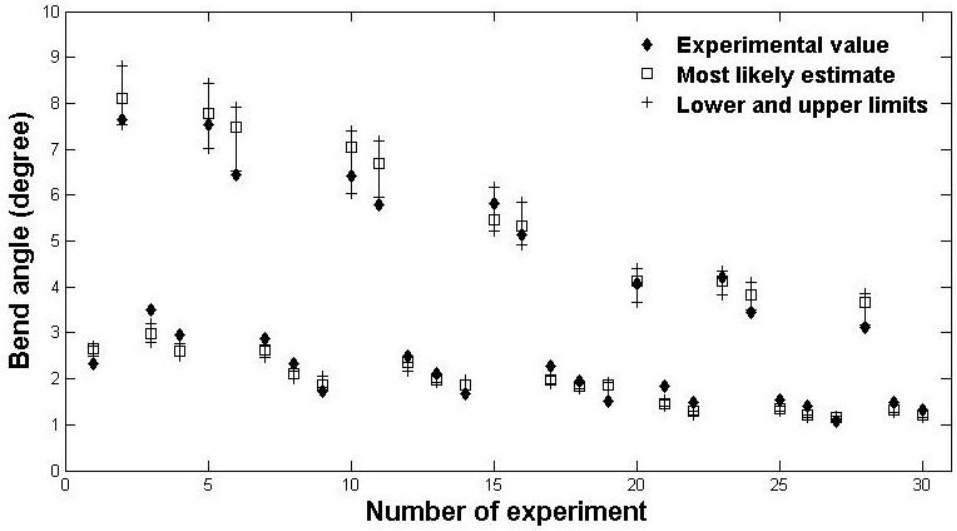

Figure 8.12 Upper and lower bound predictions of the validation data

There are a few cases of incorrect predictions where the most likely estimates were not lying in-between the lower and upper estimates. All of these cases were observed in very small bend angles. These small angle cases have been listed in Table 8.2.

Table 8.2 Errors in upper and lower limit predictions of small angle cases in testing data

Bend angles(degree)		
Lower bound	**Most likely estimates**	**Upper bound**
0.89	0.96	0.91
0.86	0.89	0.88
0.86	0.90	0.88
1.13	1.11	1.36
0.89	0.87	0.92
0.91	0.89	0.94

8.4.3 Parametric study

Based on the RBF neural network, a parametric study was carried out to study the variation of the bend angles according to the input parameters. For a particular input parameter, its value was independently varied taking typical constant values of the other three parameters and the variations of the bend angles are shown in Figs. 8.13−8.16.

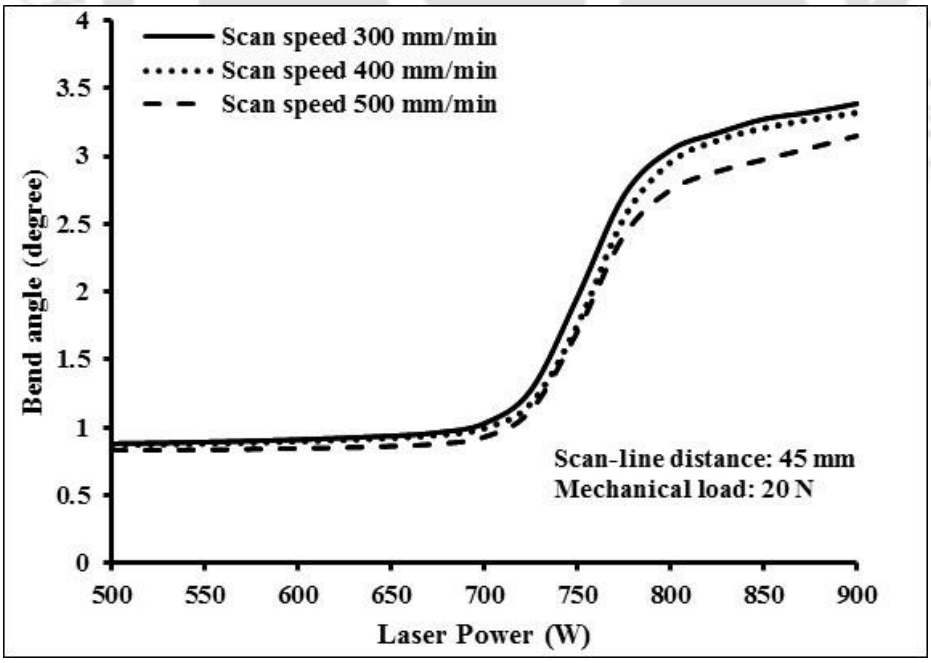

Figure 8.13 Power versus bend angle

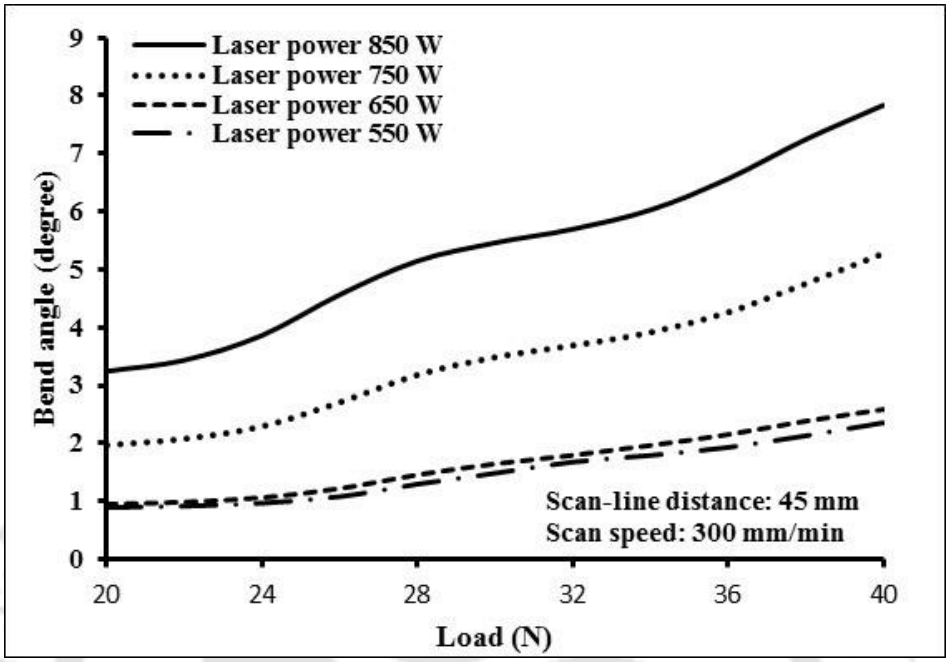

Figure 8.14 Mechanical load versus bend angle

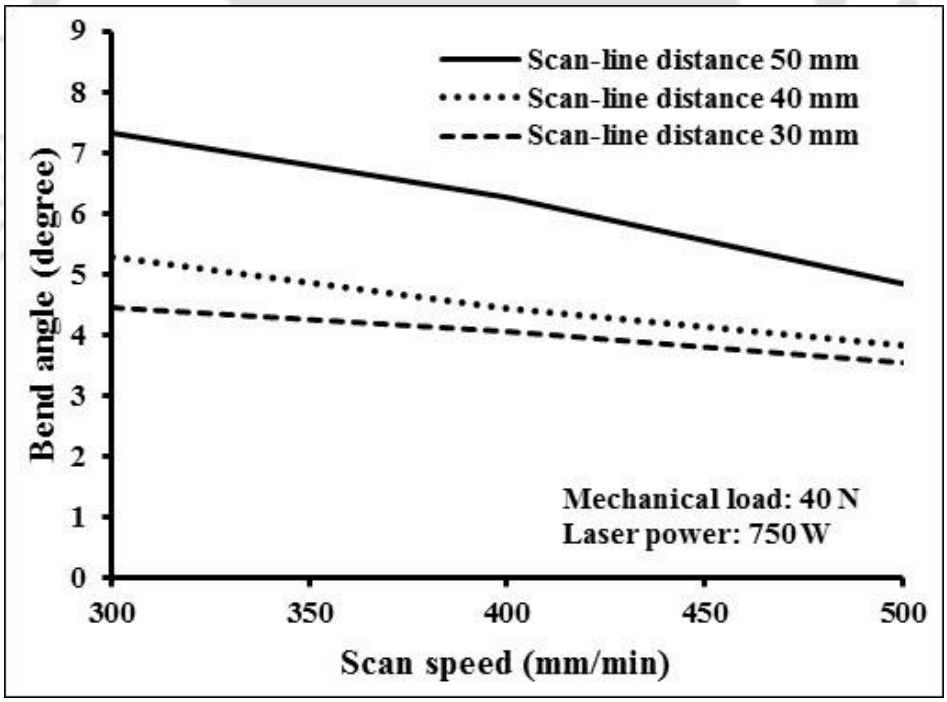

Figure 8.15 Scan speed versus bend angle

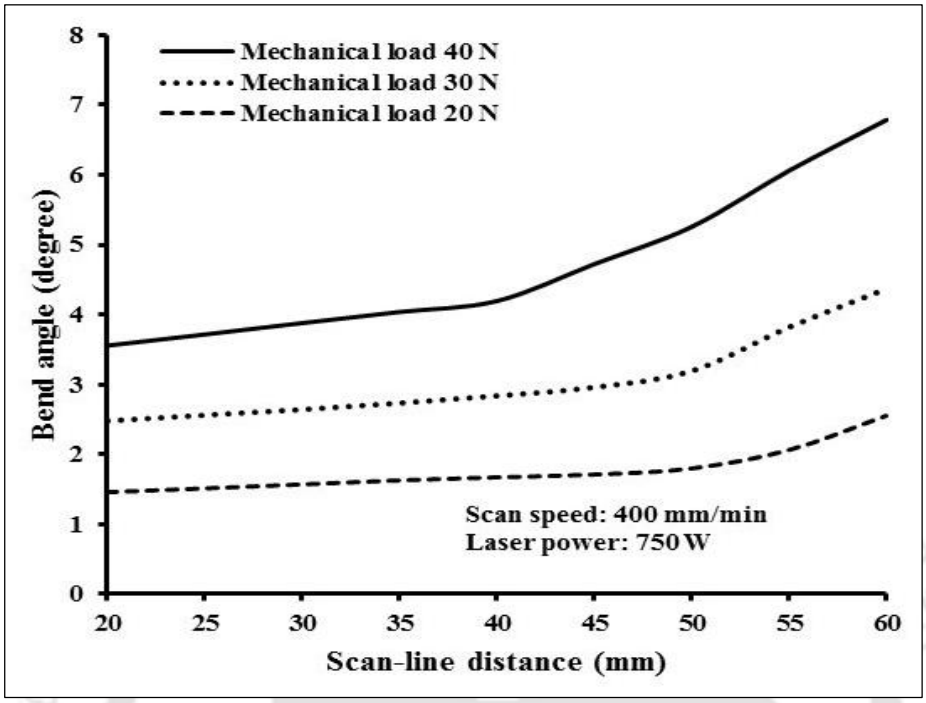

Figure 8.16 Scan-line distance versus bend angle

It can be seen in Fig. 8.13 that the bend angle changes suddenly at two points when the laser power is in the region of 700 W and 800 W. This behaviour can be attributed to the fact that yield stress of the material decreses as the working temperature increases. The FEM model used to find yield stress variation according to the working temperature by using Eq. 6.5. the yield stress variation has been plotted in Fig. 6.7(a).

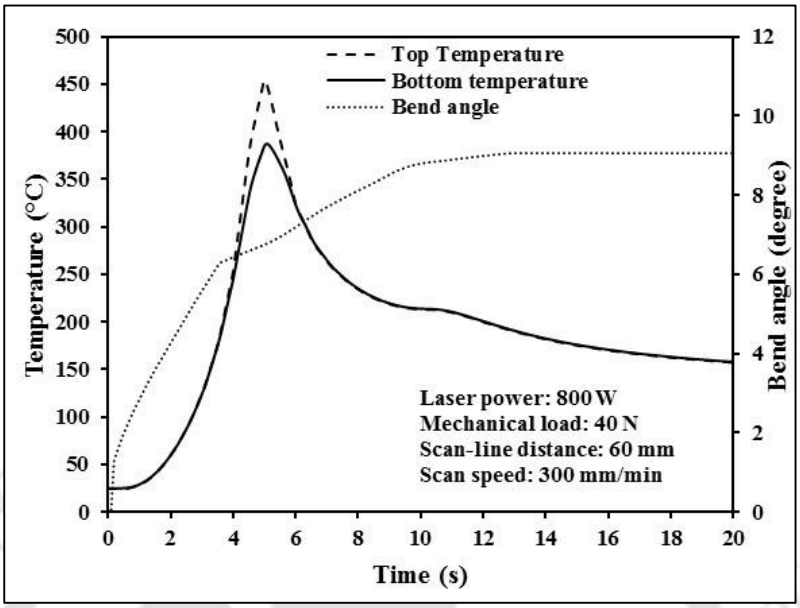

(a)

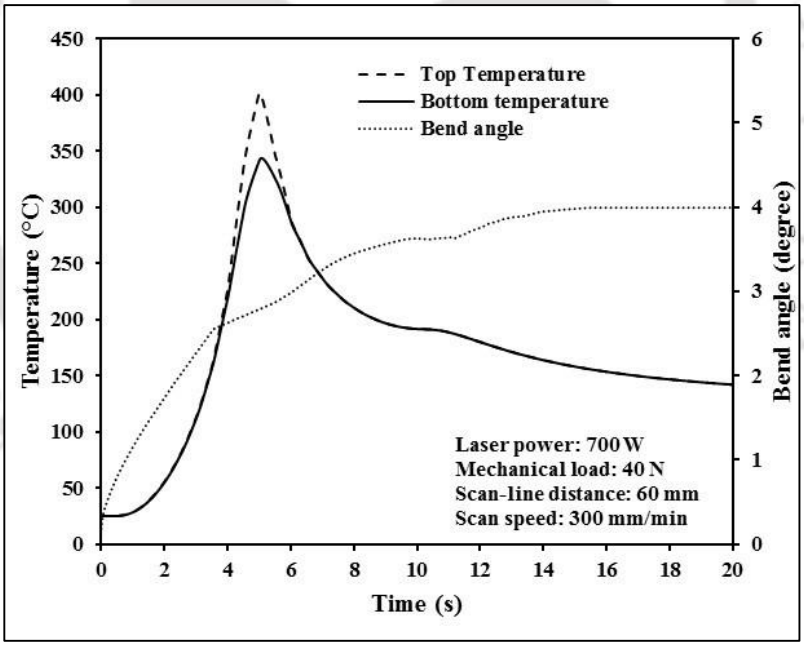

(b)

Figure 8.17 Time variation of bend anglewith the top and bottom surface temperatures of workpiece for (a) 800 W and (b) 700 W

Using the results of the FEM model, the time variation of the bend angle was plotted against the top and bottom surface temperatures of the workpiece at the two laser powers— 700 W and 800 W (Fig. 8.17a and b). From the trends of the bend

angle curve, it can be observed that, at these power levels, the bend angle starts increasing right from the instant the workpiece is exposed to the laser irradiation. When the temperature difference tends to be maximum, the slope of the bend angle curve starts changing. This continues until a steady state is reached where the temperature difference starts receding.

8.4.4 Inverse analysis

By using the best RBF network model, the inverse prediction of the two most influential parameters, laser power and mechanical load, were carried out using the bisection method. For laser power (P), the high and low level combinations of mechanical load (L), scan-line distance (d_s) and scan speed (v) were first taken. By keeping L, d_s and v constant in each of the combinations, the laser power was predicted in an inverse for the desired bend angle by simulating the RBF network model in a bisection method. A similar method was also used for the inverse prediction of mechanical load. By using the inverse predicted parameters, FEM simulations were carried out to check the correctness of the inverse predictions for the desired bend angle. The results of the inverse predictions and FEM simulations for laser power and mechanical load have been shown in Table 8.3 and 8.4, respectively.

Table 8.3 Inverse prediction of laser power using RBF

Desired bend angle (degree)	Fixed parameters			Inverse predicted parameter	Bend angle (degree)		Deviation between FEM and RBF (%)
	Mechanical load (N)	Scan-line distance (mm)	Scan speed (mm/min)	Laser power (W)	RBF predicted	FEM simulated	
3.06	20	30	300	802	3.064	3.3	–7.7%
	20	30	500	806	3.070	3.03	1.3%
	20	60	300	779	3.058	3.4	–11.2%
	20	60	500	787	3.054	3.26	–6.8%
	40	30	300	736	3.066	2.96	3.5%
	40	30	500	751	3.070	3.14	–2.3%
	40	60	300	599	3.063	3.4	–11.0%
	40	60	500	705	3.062	3.2	–4.5%

Table 8.4 Inverse prediction of mechanical load using RBF

Desired bend angle (degree)	Fixed parameters			Inverse predicted parameter	Bend angle (degree)		Deviation between FEM and RBF (%)
	Laser power (W)	Scan-line distance (mm)	Scan speed (mm/min)	Mechanical load (N)	RBF predicted	FEM simulated	
1.54	600	30	300	33	1.538	1.64	–6.7%
	600	30	500	37	1.544	1.7	–10.1%
	600	60	300	26	1.544	1.55	–0.4%
	600	60	500	23	1.540	1.48	3.9%
	700	30	300	28	1.538	1.48	3.8%
	700	30	500	30	1.536	1.42	7.6%
	700	60	300	22	1.538	1.65	–7.3%
	700	60	500	22	1.540	1.4	9.1%

8.5. Conclusions

An Artificial Neural Network (ANN) was modelled for laser assisted bending to predict bend angles using four input parameters— laser power, mechanical load, scan line distance and scan speed. A systematic method for selecting the training data is used by incorporating all the corner points of the hyper-cubic input space formed by the four considered inputs. The ANN was developed based on an FEM model. The FEM model was first validated using experimental data. Based on the FEM simulated data, a multilayer perceptron (MLP) neural network model was developed. This MLP model was then simulated to generate data for training a radial basis function (RBF) neural network. The RBF model was tested and validated only by the use of experimental data. The performance of the RBF on the experimental testing data was found to be better than that of the MLP. Thus, the RBF model was chosen as the preferred model for predicting the most likely estimates of the bend angles. The RBF neural network was subsequently used to propose a methodology to predict the upper and lower limits of the bend angles. It was found that the proposed methodology was able to predict the feasible ranges in most of the bend angles. The range predictions were also tested and validated using the testing and validation data used for the RBF neural network. However, there were a few cases of incorrect range predictions

pertaining to cases of very small bend angles in which the most likely estimates did not lie within the predicted ranges.

A parametric study was also carried out based on the RBF neural network. Finally, the RBF neural network was used to carry out an inverse analysis using a bisection method. The result of inverse analysis was also validated by using FEM simulations. The maximum deviation of the inverse predicted bend angles from the FEM simulations was found to be 11.2%. The results derived from this particular study support that a well-trained neural network can predict the bend angle in the laser assisted bending with a very good accuracy.

The main reason behind using RBF neural network was its ease of calculating upper and lower bound. However, RBF networks provides stable results only with a huge amount of testing data. Hence, in this work, first an MLP network was trained that provided data for RBF. As the testing data of RBF was experimental and training was done afresh, the errors of MLP network did not get transferred to RBF network.

Chapter 9

Laser Assisted Bending by Magnetic Force

9.1 Introduction

In the last three decades, there has been a lot of research on the use of a laser heat source for the forming of materials particularly for the bending of sheets, strips and tubes (Dixit et al. 2015; Safdar et al. 2007 and Folkersma et al. 2016). The use of laser for bending can be classified into laser bending and laser assisted bending. Laser bending is a non-contact process of bending, in which heating by a laser beam produces thermal stresses that in turn governs the deformation of the material. On the other hand, in laser assisted bending, the bending is carried out by the application of a load; the role of laser is to heat the material for reducing its flow stress and increasing the ductility. Laser assisted bending has been successfully employed to bend brittle materials (Bammer et al. 2011 and Xu et al. 2013). There are a number of ways to carry out laser assisted bending. Samm et al. (2009) used a sapphire die transparent to solid-state and excimer laser beams to carry out the forming of the sheet metals. Kant and Joshi (2013) used a roller to apply mechanical load that moves synchronously with a scanning laser beam. Yanjin et al. (2003) simulated a laser assisted bending, in which a load was applied at the free-end of a cantilever sheet. The bend angle was enhanced when the direction of the load was consistent with the deformation direction in laser bending. In their experiments, the role of laser beam was mainly to reduce the flow stress of the material.

So far, only mechanical loads have been applied in laser assisted bending through physical contact. In this work, a magnetic force was applied along with laser heating. The magnetic force does not require physical contact and can reach to inaccessible areas. Moreover, it can be easily controlled. Magnetic force has been already used in metal forming processes. For example, Vivek et al. (2011) carried out electromagnetic compression of steel tubes and also demonstrated that this process can be simulated with a fair degree of confidence. In the age of competitive

manufacturing, a process that can be simulated properly has better chances of adaptation by the industry. Laser forming has been simulated numerically as well as analytically by a number of researchers. However, a review of literatures indicate that simulation of the process needs more maturity in terms of accuracy and computational efficiency (Eideh et al. 2015 and Kant et al. 2015). Respecting this requirement, apart from experimental investigation, finite element simulations of laser assisted bending by magnetic force was also carried out.

9.2 Procedure of Experiments

The magnetically assisted laser bending of mild steel and stainless steel workpieces was carried out. The magnetic force was measured experimentally for using the appropriate value of force in finite element (FEM) simulations. Afterwards, a number of experiments were carried out on a CO_2 laser machine. This section describes the experimental procedure.

9.2.1 Preparation of magnetic and nonmagnetic workpiece

The samples were cut using CO_2 Laser Cutting Machine into the required size of 200 mm × 120 mm for both magnetic and nonmagnetic material to carry out experiments. The rust and dust particles were removed from the surfaces by dissolving them in acetone. Graphite coating was used to enhance the absorptivity. For this work, mild steel was used as a representative magnetic material and stainless steel as a representative nonmagnetic material. Samples were mounted as cantilever beams of 195 mm length (5 mm length was used for clamping). Laser scanning was carried out along 120 mm width.

9.2.2 Measurement of magnetic force

Six neodymium permanent magnets, each of size 20 mm × 10 mm × 10 mm, were used in the experimental work. Magnet pulling force strength was affected by material properties, air gap (distance between magnet and workpiece) and workpiece thickness. Magnetic saturation in the workpiece limits the effective attractive force between the workpiece and magnet. Figure 9.1 shows a setup for measuring the magnetic force. One side of the workpiece was fixed by a hinge and the other side

hanged from a digital load scale. The permanent magnet was attached below the workpiece. For magnetic work material, the position of the magnet was set at the bottom of workpiece without any contact between the workpiece and magnet. In case of nonmagnetic work material, three magnets were positioned at left, middle and right on the top surface of the work place along width direction and the other three were fixed on the magnet holder below the workpiece. The opposite poles were facing each other such that there was attractive force between them. In both the cases, the net magnetic force measured at the following gaps between the bottom surface of the workpiece and the top surface of lower magnets: 20, 17.5, 15, 12.5, 10, 7.5, 5, 2.5 and 1 mm.

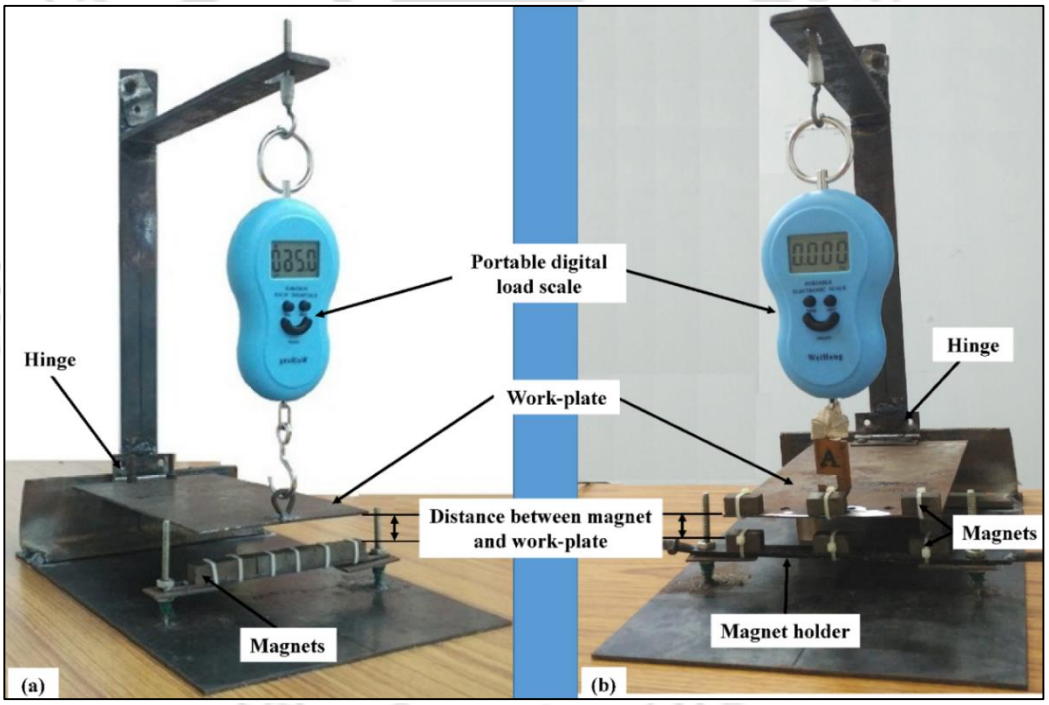

Figure 9.1 Experimental setup to measure the magnetic force on workpieces which are made of (a) mild steel and (b) stainless steel

9.2.3. Measurement of the temperature during laser heating of workpiece

Temperature at the bottom of the workpiece was measured for laser power of 1 kW, laser spot diameter of 7.6 mm and scan speeds of 700 mm/min and 1100 mm/min. The K-type thermocouples (Nickel chromium–nickel silicon) with an operative range between −40 °C and +1260 °C and ±1% accuracy was used for

measuring temperature. The thermocouples were fixed at the bottom of the workpiece through the thermocouple attachment unit (Dina-Weld TAU 100), 60 mm away from the start point of the scan line, *i.e.* at mid-width. The experiment setup for measuring the temperature is shown in Fig. 9.2. The thermocouple wire end was connected to the Agilent Data Acquisition System (Model: 349701A LXI Data Acquisition System). The data Acquisition System was connected to the computer where the data was stored using Agilent bench link data logger software.

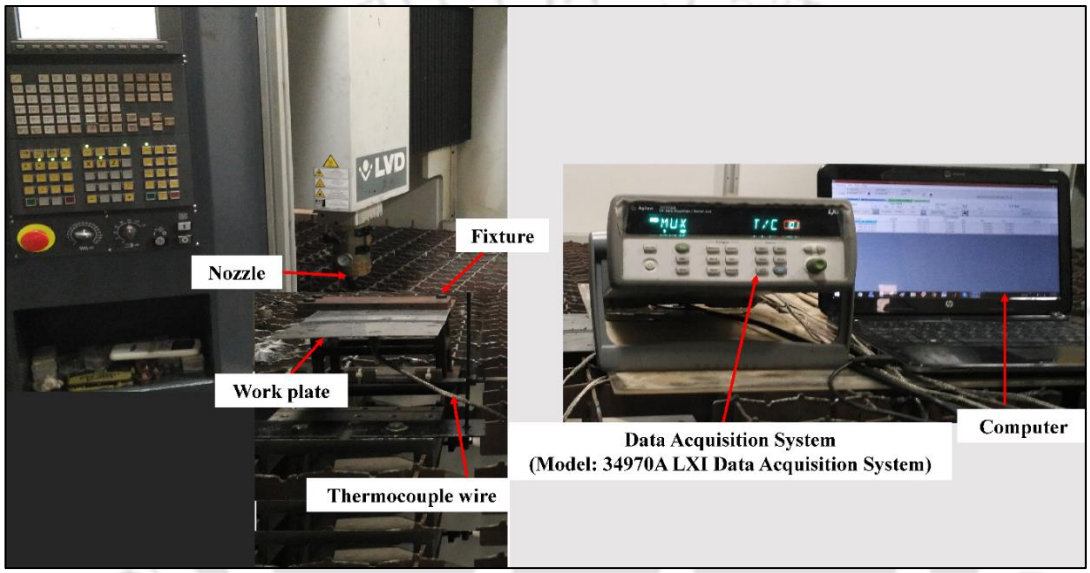

Figure 9.2 Experimental setup for measuring the temperature from bottom side of the workpiece

9.2.4. Experiments on laser assisted bending

For laser assisted bending, the workpiece was properly clamped on one side. The magnet holder was fixed either at the bottom or at the top side of the workpiece as shown in Fig. 9.3 and Fig. 9.4, in the case of magnetic material (mild steel) and nonmagnetic material (stainless steel), respectively. The magnet holder could easily move up and down though the slot for varying the distance between magnets and workpiece. The scale fixed at the side of the setup was used to measure the distance between the workpiece and magnet. Before laser irradiation, the distance between workpiece and magnet or between opposing magnets were kept constant and there was no bending just due to the magnetic force. The gap between the lower surface of the workpiece and the top surface of the lower magnets was 15 mm for nonmagnetic

material and 10 mm for magnetic material due to attractive force between magnets or between workpiece and magnet, respectively.

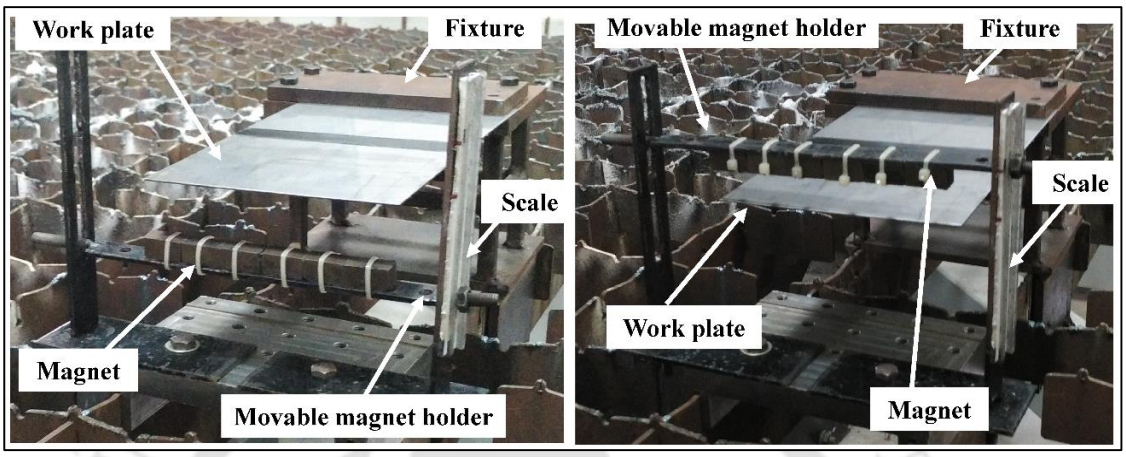

(a) (b)

Figure 9.3 Photograph of the experimental setup for magnetic material (mild steel): (a) magnet holder fixed at the bottom and (b) magnet holder fixed at the top

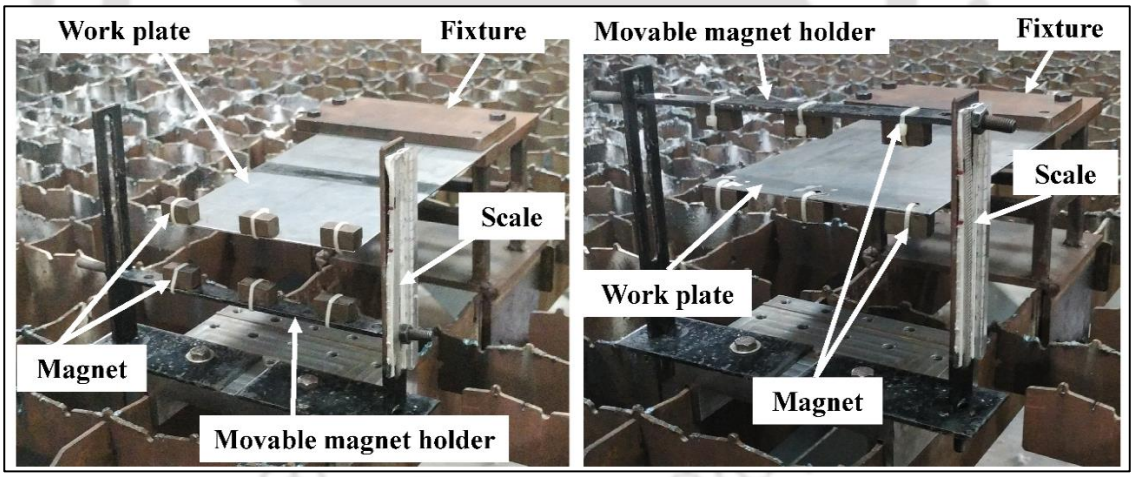

(a) (b)

Figure 9.4 Photograph of the experimental setup for nonmagnetic material (stainless steel): (a) magnet holder fixed at the bottom and (b) magnet holder fixed at the top

The experiments were performed by using 2.5 kW continuous wave mode CO_2 laser (Make: LVD, Model: Orion 3015). The laser beam was irradiated in a direction parallel to free edge (along width) of clamped specimens at a distance of 100 mm away from free end. After the laser beam irradiation, the heated specimens were allowed to cool naturally.

The CO_2 laser was utilized at different laser parameters. To validate the experiments of laser assisted bending by applied permanent magnet force, the experiments were carried out at different process parameters as listed in Table 9.1. Process parameters are as follows: laser power (P), beam diameter (D) and scan speed (v). The deformations of the laser irradiated workpiece samples were measured using a Coordinate Measuring Machine (CMM) and the bend angles were estimated. The details for FEM model of laser assisted bending process is discussed in chapter 3.

Table 9.1 Experimental process parameters

Parameters	Symbol	Unit	Values
Laser power	P	W	1000
Laser beam diameter	D	mm	7.76
Scan speed	v	mm/min	700, 800, 900, 1000 and 1100
Magnet holder position	–	–	Top, bottom and without magnet
Material	–	–	Mild steel and stainless steel
Thickness	t	mm	1, 1.5 and 2

9.3 Results and Discussion

In this section experimental as well as simulation results are discussed. A comparison between the two results are made. The results clearly demonstrate the efficacy of the proposed process.

9.3.1 Measurement of magnetic force

Figure 9.5 (a) and (b) shows the variation of magnetic attraction force with distance between the top surface of the magnet and bottom surface of the workpiece for magnetic as well as nonmagnetic material. The results are presented for three workpiece thicknesses: 1 mm, 1.5 mm and 2 mm. It was observed that the magnetic attraction force increased slightly with the increase in the thickness of workpiece and decreased as the distance between the top surface of the lower magnets and bottom surface of the workpiece increased.

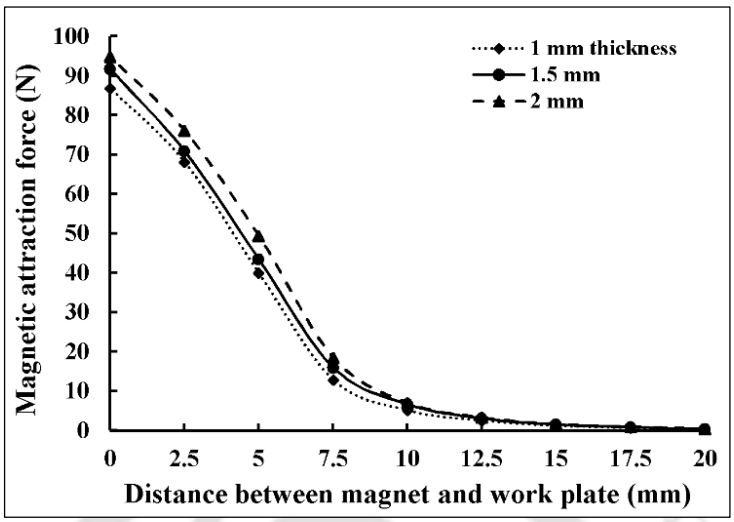

(a)

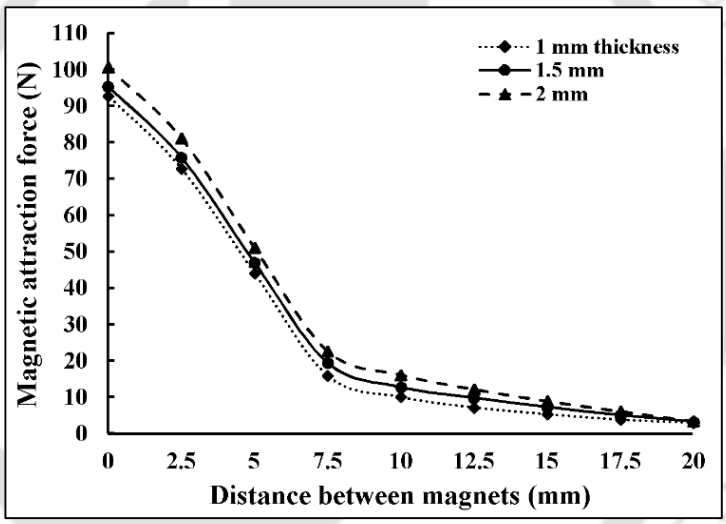

(b)

Figure 9.5 Variation of magnetic force with air gap for (a) mild steel and (b) stainless steel

The equations for magnetic force in terms of distance x were fitted using experimental data. The following fifth degree expressions provide the magnetic force as a function of distance x (in mm) between the top surface of the lower magnets and the bottom surface of the workpiece:

$$F_{ms1} = 0.0005\,x^5 - 0.0276\,x^4 + 0.5479\,x^3 - 4.0169\,x^2 - 0.1717\,x + 86.899, \quad (9.1)$$

$$F_{ms2} = 0.0004\,x^5 - 0.0232\,x^4 + 0.4676\,x^3 - 3.4231\,x^2 - 1.938\,x + 91.674, \quad (9.2)$$

$$F_{ms3} = 0.0004\,x^5 - 0.0239\,x^4 + 0.5025\,x^3 - 3.9385\,x^2 - 0.257\,x + 94.718, \quad (9.3)$$

$$F_{ss1} = 0.0005\,x^5 - 0.0305\,x^4 + 0.5918\,x^3 - 4.2291\,x^2 - 0.3236\,x + 92.887, \quad (9.4)$$

$$F_{ss2} = 0.0005\,x^5 - 0.0302\,x^4 + 0.5881\,x^3 - 4.222\,x^2 - 0.1721\,x + 95.455, \quad (9.5)$$

$$F_{ss3} = 0.0006\,x^5 - 0.0319\,x^4 + 0.6183\,x^3 - 4.442\,x^2 + 0.1279\,x + 100.8, \quad (9.6)$$

where F with subscripts denotes the magnetic force in N. In the subscripts, the letters indicate the work material and the number indicates the workpiece thickness in mm. The coefficients of determination for Eqs. (9.1–9.6) are 0.9989, 0.999, 0.9984, 0.9981, 0.9986 and 0.9985, respectively.

For simulation purpose, the force is considered to be corresponding to the initial settings. Actually, the force varies during the process due to changing air gap in-between the workpiece and magnets as well change in the temperature of the workpiece. These two effects are of opposing nature; hence assuming the constant value of force may not introduce much error. Table 9.2 shows the magnetic force at the fixed settings between the workpiece and magnets for workpieces of different thicknesses. It was observed that the force increases with the increase in the thickness (t) of the workpiece.

Table 9.2 Magnetic attraction force for different materials and thicknesses

For nonmagnetic material: Distance between magnets (x) = 15 mm For magnetic material: Distance between workpiece and magnet (x) = 10 mm		
Thickness (mm)	Magnetic force (N)	
	Mild steel	Stainless steel
1	5.5	5.6
1.5	5.6	7.4
2	6.94	9

9.3.2 Validation of FEM model

For both mild steel and stainless steel, the experiment and simulation temperature results were evaluated at bottom side for scan speeds of 1100 mm/min and 700 mm/min. Fig. 9.6 (a) and (b) shows experimental and simulation temperature profiles at the bottom surface centre point of the workpiece and the centre of laser irradiated line. There is a good agreement between experiment and simulation result.

For mild steel, the peak temperature difference between experiment and simulations was 28.7 °C and 42.4 °C for laser scan speeds of 700 mm/min and 1100 mm/min, respectively. The corresponding values for stainless steel are 26.5 °C and 33.8 °C, respectively. These values are based on the absorptivity value of 0.7. As the deviation between experimental and simulation results was small in all the cases, this value of absorptivity was considered to be appropriate.

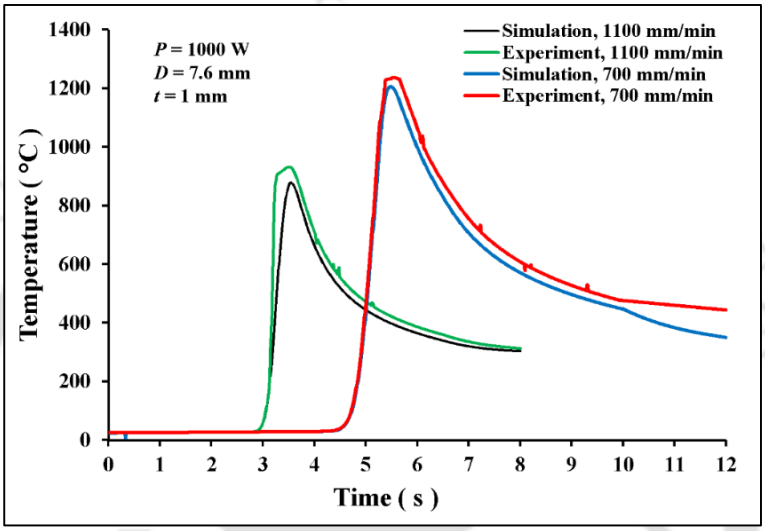

(a)

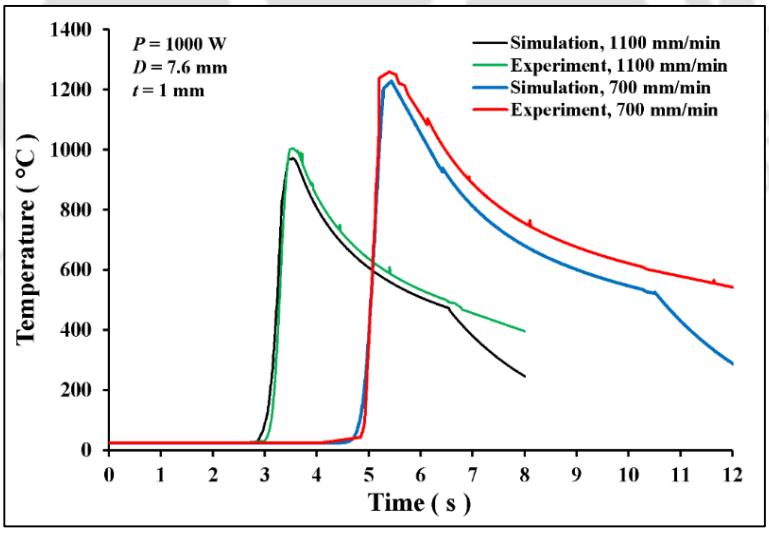

(b)

Figure 9.6 Simulated and experimental time histories of temperature for (a) mild steel and (b) stainless steel

The workpiece was bent due to the combined effect of laser beam irradiation and magnetic attractive force. Figures 9.7 and 9.8 show the experimental and simulated bend angles for 1 mm thickness mild steel and stainless steel workpieces, respectively at different scanning speeds. It was observed that the bending angle decreases with increase in scan speed for both materials. Figures 9.7 and 9.8 show the results for the following three cases: (i) magnetic force direction upward, (ii) magnetic force direction downward and (iii) no magnetic force. In a single scan, the achievable bend angle is in the range of 0.1º–3º in the case of temperature gradient mechanism (TGM), (Lawrence et al. 2001). In TGM, the bend angle was achieved towards the laser source direction, which was considered to be positive in this work. The results for laser bending without any external force is consistent with the literature. However, the application of magnetic force greatly enhances the bend angle.

Interestingly, the bend angle was greater when the magnetic force was upward than when it was downward. The first reason for this is that when the magnetic force was upward, TGM action and bending due to the force was in the same direction. The second reason was that, due to upward movement of the workpiece, the spot diameter decreases, leading to the concentration of more heat in smaller area, which in turn enhances the action of TGM.

For mild steel workpiece with upward force, the deviations between experimental and simulation results were 12%, 9.82%, 9.43%, 8.04%, and 5.26% for scan speeds of 1100, 1000, 900, 800 and 700 mm/min, respectively. The corresponding values were 13.5%, 10.2%, 9%, 7.4%, and 6.14% for downward magnetic force on mild steel workpiece. Without magnetic force, the corresponding deviations were 4%, 8.75%, 7.88%, 8% and 9.02%. For stainless steel, the corresponding deviations were13.64%, 9.52%, 3.85%, 3.05%, and 2.98% for upward magnetic force, 12.07%, 9.21%, 4.17%, 5.81%, and 3.7% for downward magnetic force and 5.26%, 9.89%, 5.56%, 6.38% and 3.45% without magnetic force. Thus, it can be said that there was a good agreement between the experimental and the simulation results.

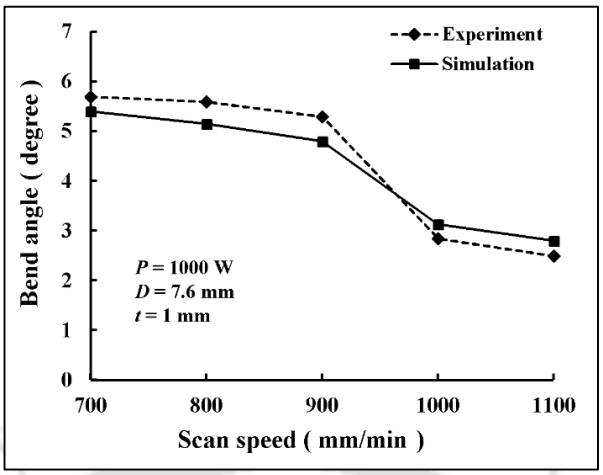

(a)

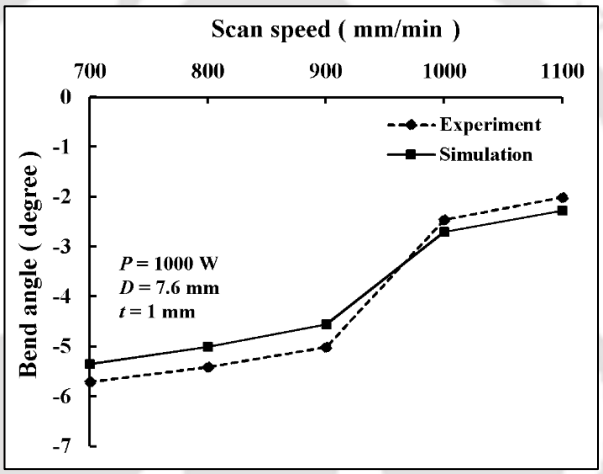

(b)

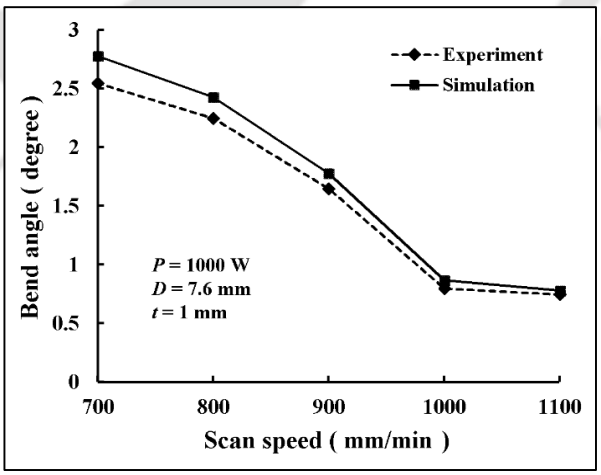

(c)

Figure 9.7 Bend angle results at various scan speed for mild steel: (a) upward magnetic force, (b) downward magnetic force and (c) without magnetic force

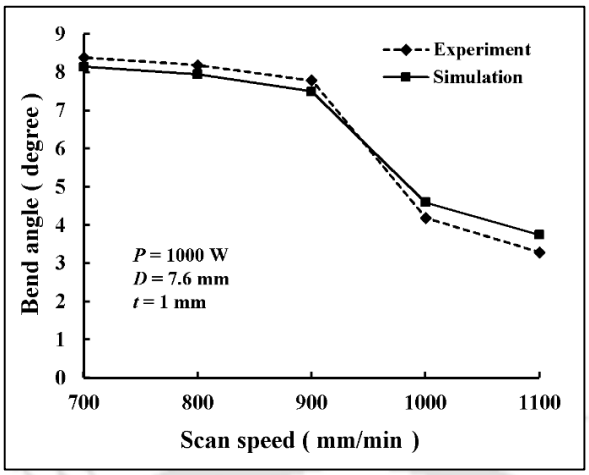

(a)

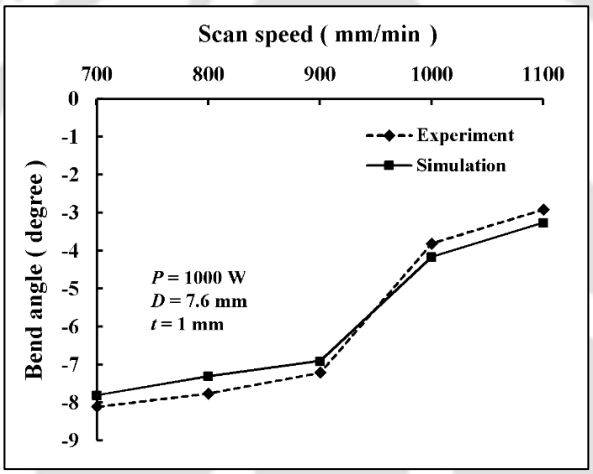

(b)

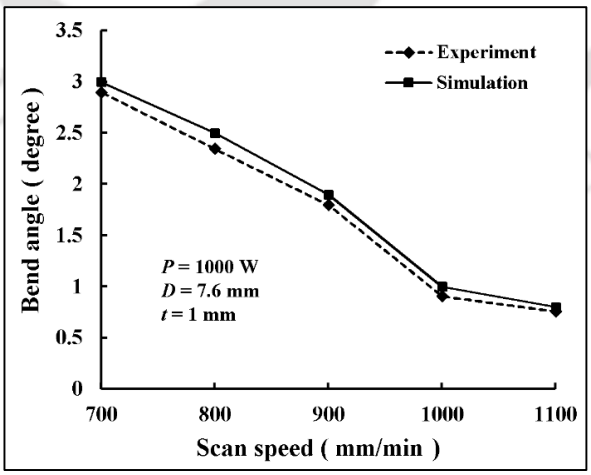

(c)

Figure 9.8 Bend angle results at various scan speed for stainless steel: (a) upward magnetic force, (b) downward magnetic force and (c) without magnetic force

Table 9.3 Deviations between experimental and simulated bend angles (with downward magnetic force)

Material	Scan speed (mm/min)	Thickness (mm)	Bend angle (degree)		
			Exp.	Sim.	Dev. (%)
Stainless steel	1100	1.5	–1.95	–2.20	12.8
	700	1.5	–6.75	–7.40	9.6
	1100	2	–1.60	–1.80	12.5
	700	2	–4.75	–5.20	9.5
Mild steel	1100	1.5	–1.75	–2.00	14.3
	700	1.5	–2.95	–3.26	10.5
	1100	2	–0.20	–0.18	10
	700	2	–0.47	–0.52	10.6

For 1.5 mm and 2 mm thickness workpiece, only two experiments were performed for each thickness at scan speeds of 700 mm/min and 1100 mm/min for both the materials. The magnetic force was acting downward. Table 9.3 shows the comparison of experimental results with the simulation results. A good agreement between the experiments and simulation reinforces the confidence in the modelling of the process.

9.3.3 Simulation results

Numerical simulations of laser bending (without magnetic force) as well as laser assisted bending processes (with upward and downward magnetic forces) were performed for 1.5 mm and 2 mm thick workpieces to determine the effect of material (mild steel and stainless steel) and magnetic force direction on bend angles. Figures 9.9 and 9.10 show the surface plots showing the dependency of bend angle on scan speed and sheet thickness. These plots have been obtained from FEM simulations.

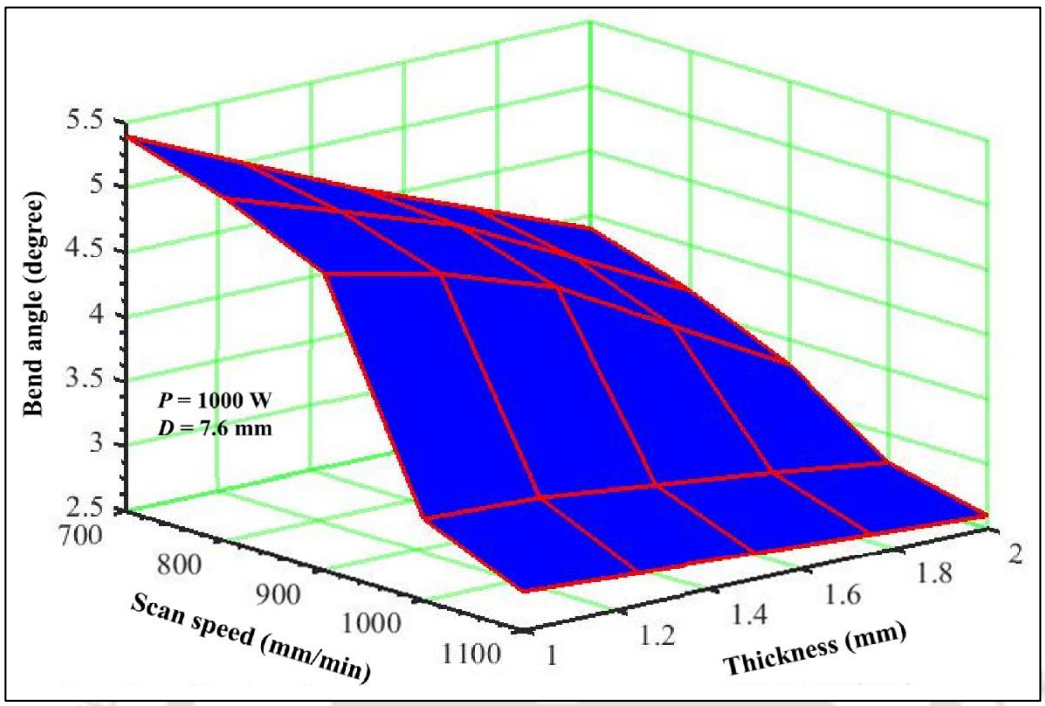

(a)

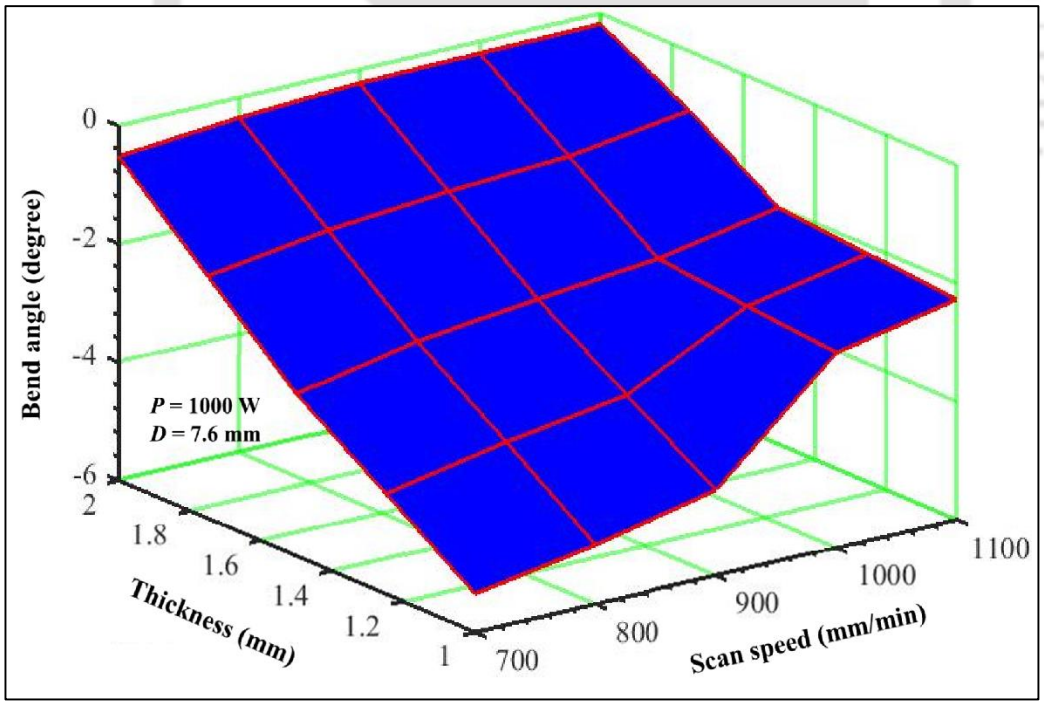

(b)

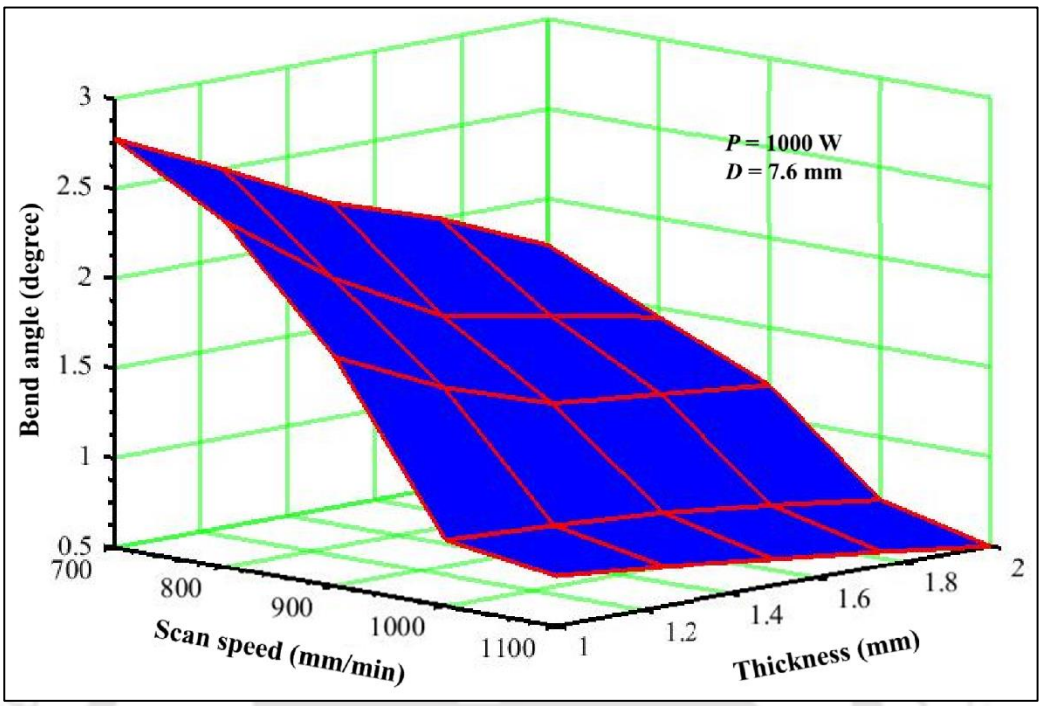

(c)

Figure 9.9 Laser bending of mild steel: (a) upward magnetic force, (b) downward magnetic force and (c) without magnetic force

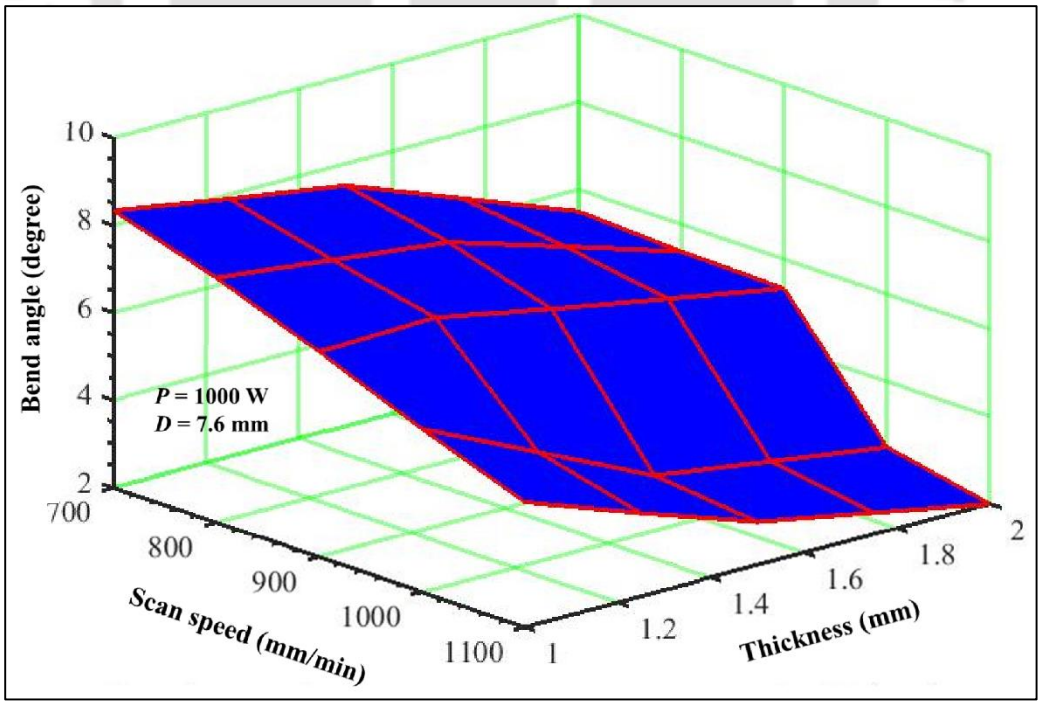

(a)

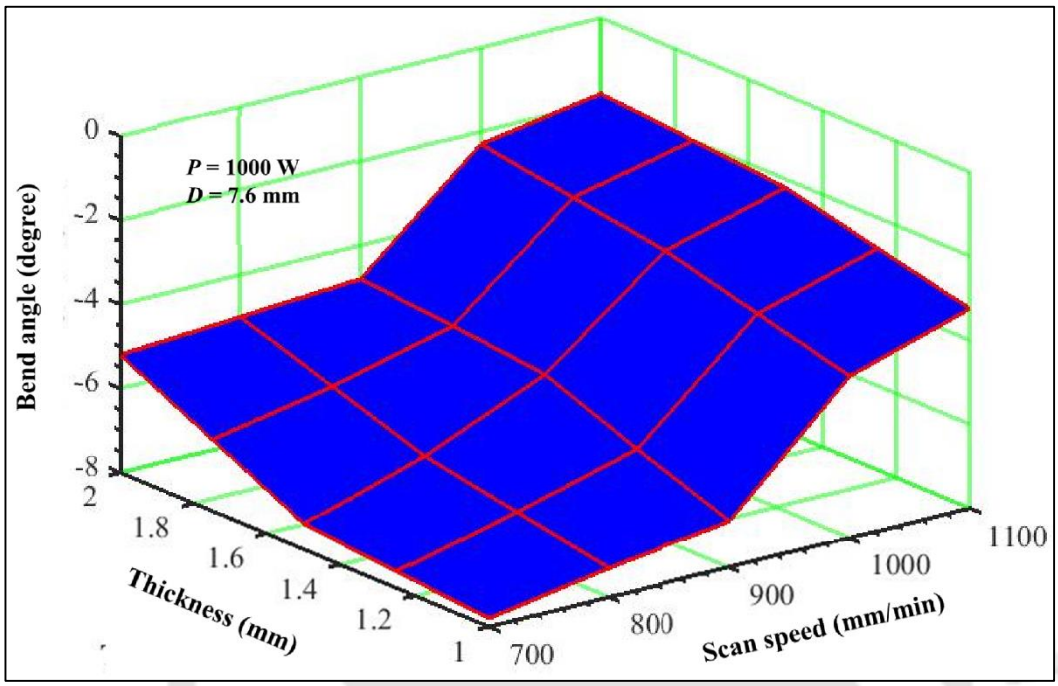

(b)

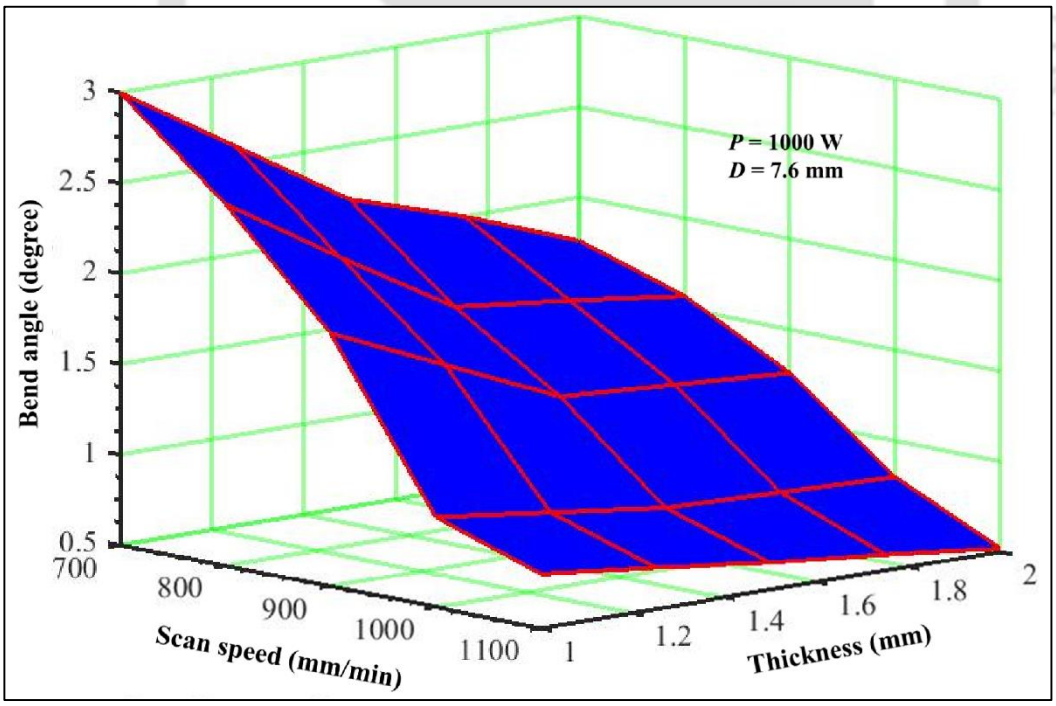

(c)

Figure 9.10 Laser bending of stainless steel: (a) upward magnetic force, (b) downward magnetic force and (c) without magnetic force

9.3.4 Edge effect

Edge effect is a performance parameter that is quantified in terms of the relative variation of the bend angle (RVBA) along the laser scan direction (width direction) as given in Eq. 3.6. The edge effect is more when the value of *RVBA* is higher, and vice-versa.

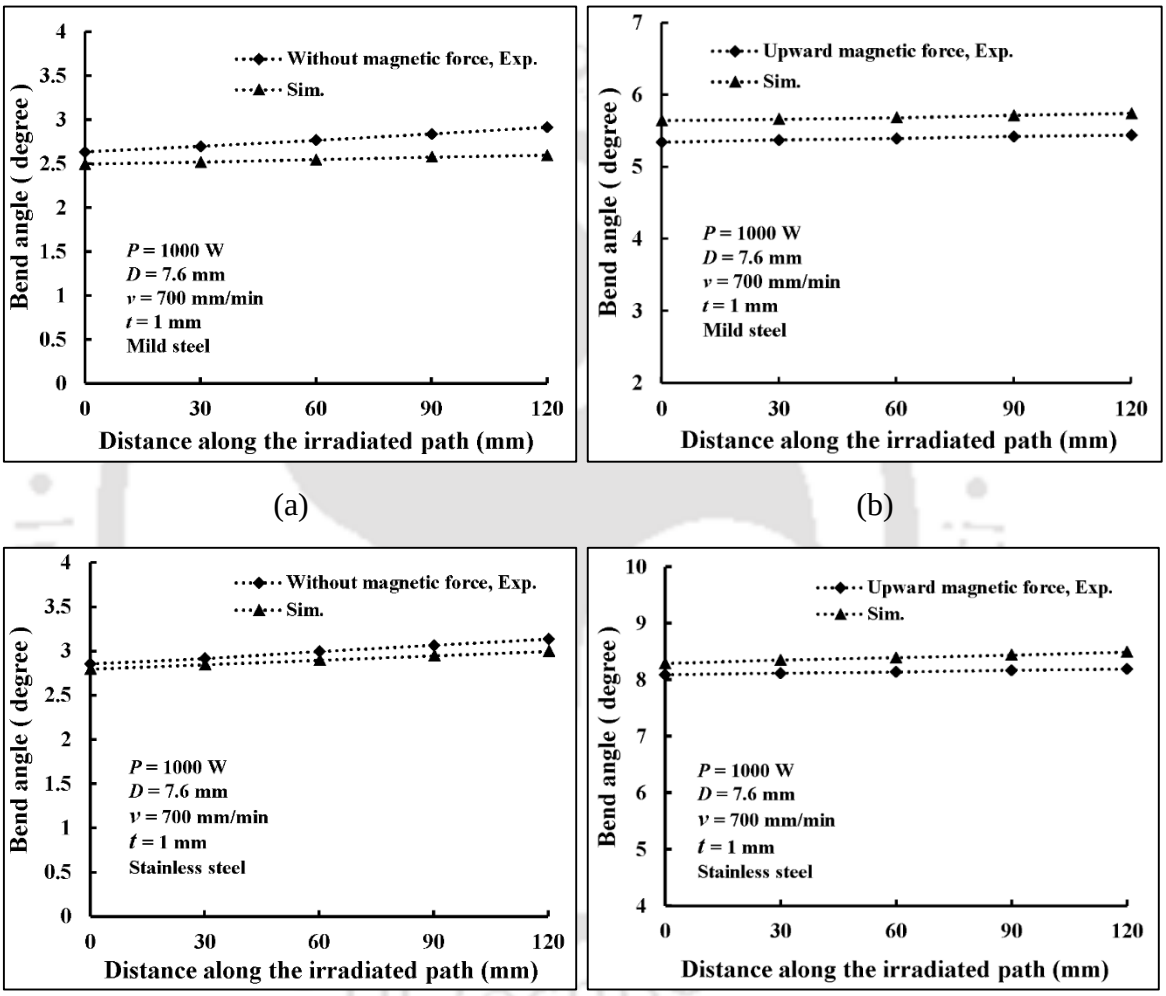

Figure 9.11 Variation of bend angle along the scan direction for (a) mild steel workpiece without magnetic force, (b) mild steel workpiece with upward magnetic force, (c) stainless steel workpiece without magnetic force and (d) stainless steel workpiece with upward magnetic force

Figure 9.11 shows the simulated and experiment bend angles along the laser scan directions. A good agreement is observed in-between simulated and experiment.

In order to see the variation of edge effect with scan speed, simulations were carried out. Figure 9.12 shows the simulated variation of edge effect with scan speed. The edge effect is lesser in laser assisted bending as compared to laser bending (without any magnetic force). This is due to better uniformity of the magnetic force. At low scan speed, the sheet got stuck with the magnets and it did not allow to move freely. In a way, magnets acted as fixture that restrained the movement of workpiece. Thus, uniform bend angle was obtained along the width direction.

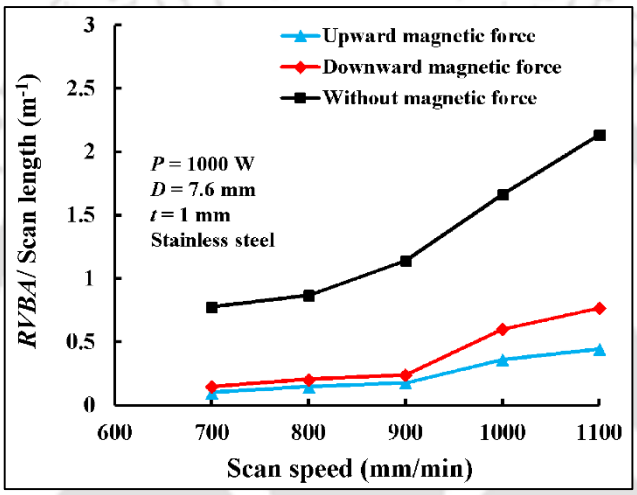

(a)

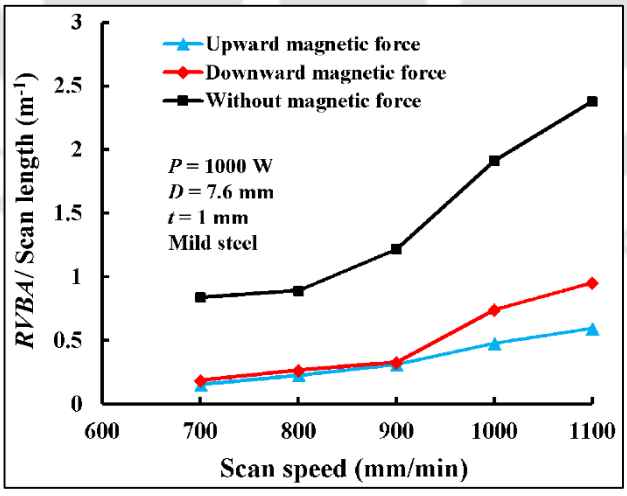

(b)

Figure 9.12 Effect of magnetic assisted bending on edge effect at different scan speeds for (a) stainless steel workpiece and (b) mild steel workpiece

9.3.5 Simulation of evolution of the bend angle with time

In simulations, the magnetic force is taken corresponding to initial settings of the workpiece and magnets. In practice, the bend angle evolves with time as shown in Figure 9.13. It kept increasing as the heating continued. Finally, there was some reduction in the bend angle due to springback when the workpiece was removed from the setup. The spring-back effect was less at low scan speeds due to high temperature of the workpiece.

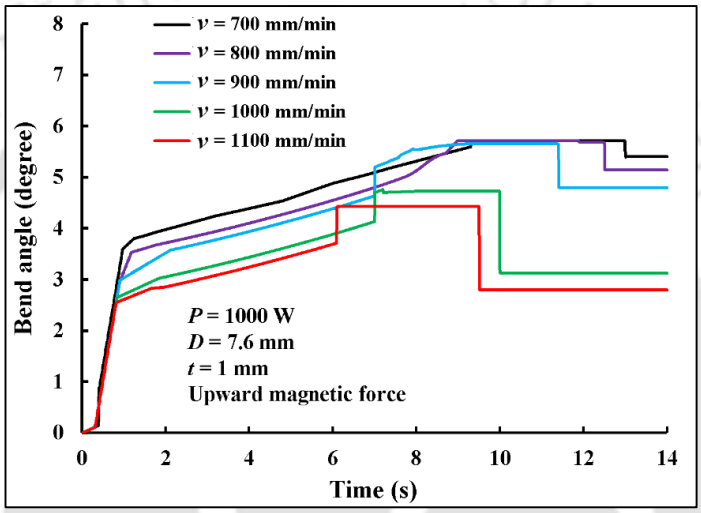

(a)

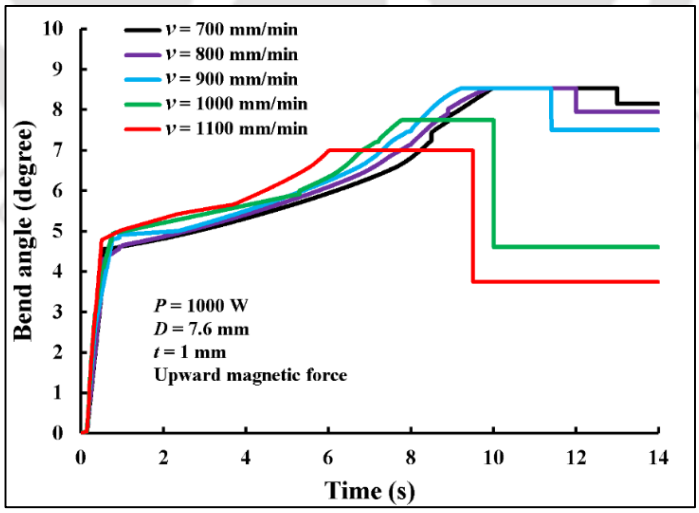

(b)

Figure 9.13 Evolution of bend angle with time in magnetically assisted bending as obtained by FEM simulation for (a) mild steel and (b) stainless steel at different scan speeds

The simulations presented in this work was taken into account of the spring-back effect, but not for the variation of magnetic force due to changing distance between the surface of the workpiece and magnets. It was also noted that as the gap between the workpiece and magnets increased causing an increase in the force, the temperature of the workpiece also increased which reduced the force. These two effects are of opposing nature and thus by taking the force value at initial setting, there may not be in much error. However, a detailed analysis can be carried out in future.

9.3.6 Microhardness

The hardness of mild steel and stainless steel raw workpieces were 130 and 152 HV, respectively. Figure 9.14 represents the variation of microhardness along perpendicular to laser scanning line of laser irradiated workpieces for different scan speeds. Three readings were taken along thickness direction at 0.25, 0.5, and 0.75 mm from top (irradiation side) and average result is reported. As a result of laser scanning without magnetic force for mild steel, the average microhardness values were 180.4, 174.1, 168, 163.8 and 161.8 HV for scan speeds of 700, 800, 900, 1000 and 1100, respectively as shown in Fig. 9.14(a). The corresponding values for stainless steel workpiece were 323.8, 295.5, 279.6, 259.2 and 249.8 HV, respectively (Fig. 9.14b). Obviously, the hardness is the maximum at and around the bend line. As the scan speed increases, the hardness decreases due to low amount of bending.

Figure 9.15 shows the variation of hardness along the thickness direction. As a result of laser irradiation of mild steel, the hardness at 0.25 mm below the top of surface reached to 189.1, 184.4 and 176.3 HV for upward magnetic force, downward magnetic force and without magnetic force, respectively as shown in Fig. 9.15 (a). The corresponding values for stainless steel workpieces were 344, 334.3 and 311.5 HV, respectively as shown in Fig. 9.15 (b). Microhardness near the top surface of the workpieces was greater than that which was near to the bottom surface for both mild steel and stainless steel workpieces. This was due to more heating and corresponding heat treatment near the top surface. It was also observed that hardness near the bottom surface was more for bending with downward magnetic force compared to bending with upward magnetic force and without magnetic force. Bending with downward

magnetic force created relatively higher compressive strains at the bottom side, which was responsible for increasing the microhardness.

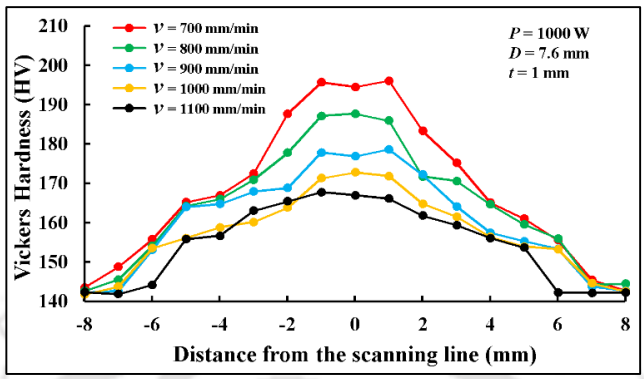

(a)

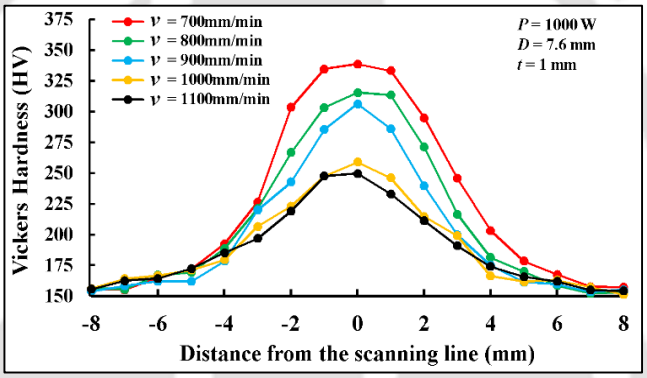

(b)

Figure 9.14 Average microhardness profile of laser irradiated workpiece: (a) mild steel and (b) stainless steel

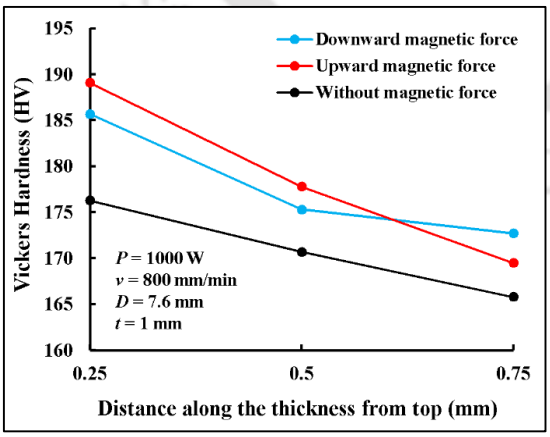

(a)

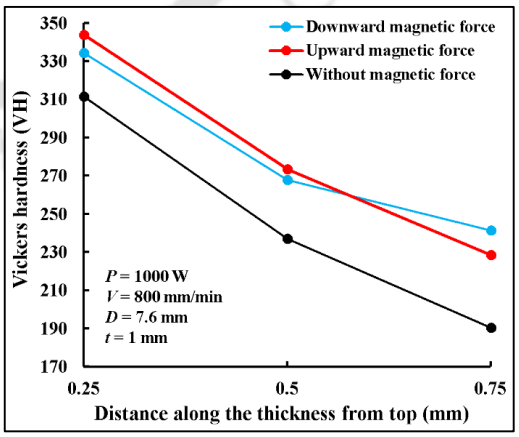

(b)

Figure 9.15 Average microhardness profile for downward magnetic force, upward magnetic force and without magnetic force for: (a) mild steel and (b) stainless steel

9.3.6 Temperature distribution

Figure 9.16 shows temperature on the top and bottom surfaces of workpiece. The temperature distribution at different scanning speed at 700, 800, 900 1000, and 1100 mm/min on particular laser power (1000 W) and laser beam diameter (7.6 mm). The temperature increased as the scan speed decreased. It was seen that the peak temperature at the top and bottom surface of workpiece reduced when the scan speed increased.

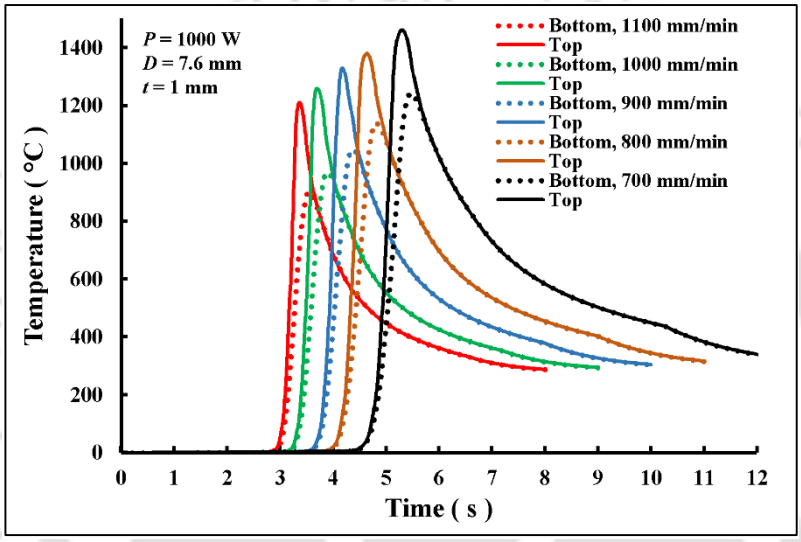

Figure 9.16 Effect of scanning speed on temperature distribution

A comparison of temperature among laser and laser assisted bending (with and without magnetic force) at top and bottom side of mild steel workpiece of thickness 1 mm is shown in Fig. 9.17. The peak temperature at the top and bottom surface centre point of the workpiece are equal in all cases (laser bending and laser assisted bending). That means, the magnetic force does not have any influence on the temperature distribution on the workpiece as shown in Fig. 9.17. To visualize the temperature profile for magnetic force assisted and without magnetic assisted laser bending, an offset delay of 1 s and 2 s was taken for down ward and upward magnet assisted bending to laser bending without magnetic force respectively, as shown in Fig. 9.17.

The effect of workpiece thickness on the temperature profile of top and bottom surface centre point is shown in Fig. 9.18. The peak temperature was increased with decrease in the workpiece thickness. The temperature gradient of the workpiece varied with different workpiece thickness at the particular laser power (1000 W), scan speed

(1000mm/min) and spot diameter (7.6 mm). The temperature gradient was 289, 384 and 518 ^{o}C for 1 mm, 1.5 mm and 2 mm, respectively. To visualise the temperature profile for three different workpiece thickness, an offset delay of 1 s and 2 s was taken for 1.5 mm and 2 mm to 1 mm workpiece thickness respectively, as shown in Fig. 9.18.

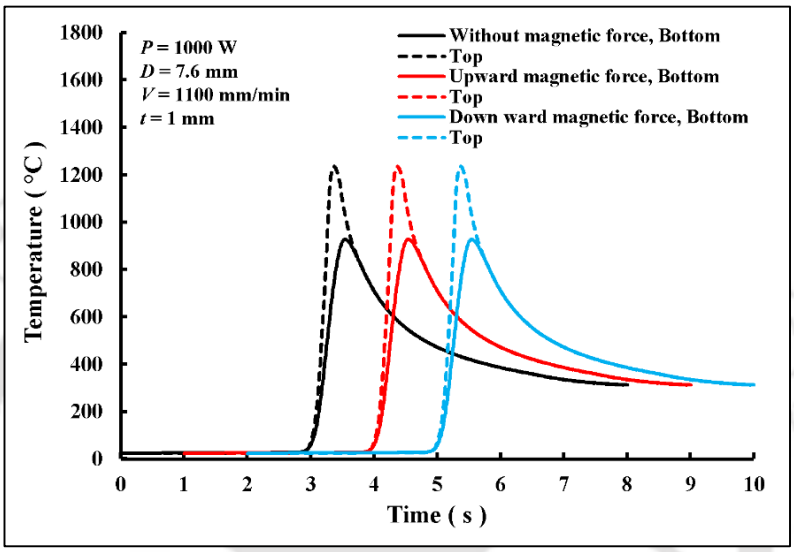

Figure 9.17 Temperature history for laser assisted and laser bending process

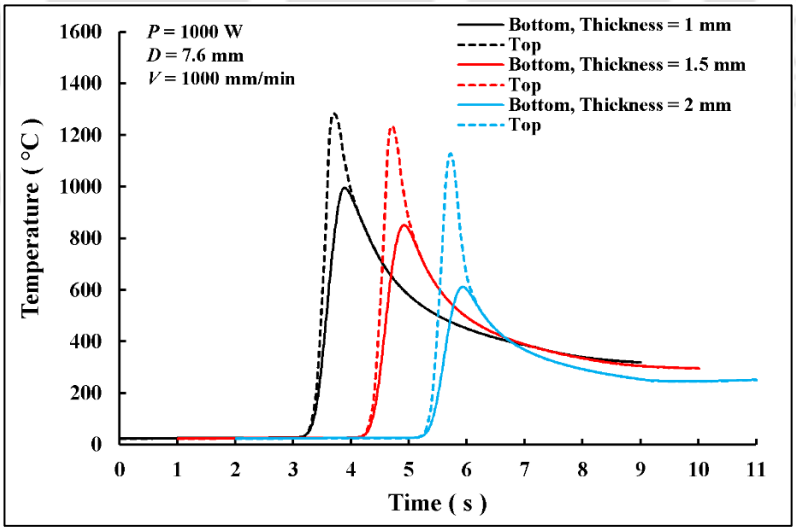

Figure 9.18 Temperature history for different thickness

9.3 Conclusion

In this work, a manufacturing process was proposed to obtain large bend angles by laser assisted bending with the application of magnetic force. The process can be used to bend magnetic as well as nonmagnetic materials. The following are the salient findings from this work:

- Application of magnetic force caused a two-fold enhancement in the bend angle. The bend angle was more when the directions of laser bending and the bending due to magnetic force coincided.
- The edge effect (the bend angle variation of bend angle along the width of the workpiece) was also studied. The bend angle along width was higher at the end of the scan path. The edge effect increased with the increase in the scan speed. At lower scan speed, the bend angle reached saturation as the workpiece got stuck with the magnets. This also reduced the edge effect. In general, the edge effect is lesser in magnetically assisted laser bending.
- Springback effect was lesser at low scan speed.
- Microhardness near the top surface of the workpiece was greater than that near the bottom surface for mild steel as well as stainless steel workpieces. Near the bottom surface, microhardness for laser bending with downward magnetic force was greater than that in laser bending with upward magnetic force or without any external force. This was due to relatively higher strains on the bottom side for laser bending with downward magnetic force.
- The magnetic force does not have any influence on the temperature distribution in the workpiece. The peak temperature at the top and bottom of workpiece are equal for laser and laser assisted bending.

One encouraging observation about the proposed laser assisted bending is that it could be simulated with reasonable accuracy, therefore this process can be easily accepted by the industries. Simulations were carried out using a FEM package and the magnetic force was taken corresponding to the initial settings. Effect of change in force due to deformation and temperature during the process was not taken into account. This may be considered in future.

Chapter 10

Epilogue

10.1 Introduction

Laser based bending is gaining popularity in many industrial sectors including aerospace, railway, shipbuilding and automobile. Literature reported that laser bending process has been investigated for many materials, such as metals, non-metals, ceramics, glasses, plastics and composites. However, the laser bending of small size sheet, strip plate, friction stir welded sheet and friction stir processing sheet as well as laser assisted bending by magnetic force were not explored systematically. Based on the research gap identified in the literature and to understand the robustness of the process, this work was carried out. In this thesis, experimental study and numerical simulations were carried out on the laser as well as laser assisted bending processes. The behaviour of material under laser based bending process were influenced by a combination of laser process parameters, workpiece geometry, workpiece material and the coating on the workpiece. The performance of a laser bending process should be assessed by its accuracy, repeatability, predictability and post-process quality of the product. The thesis attempted to do that by considering a number of variants of the process and applications. Salient findings and contributions are summarized for various subparts of the work in the following sections and overall conclusions have been presented. Finally, scope for future work is discussed.

10.2 Effect of Laser Parameters on Bending of Small Sized Sheet

The geometrical parameters like sheet thickness, length and width influence the bend angle. Most researchers have studied laser bending of large sized sheets. Based on the research gap, the effect of laser power, laser diameter, type of heat source (stationary and moving heat source) on small sized workpiece have been evaluated. The experimental and simulation result of small sized (of the order of 100 mm^2 surface

area) plate bending depicted that the bending angle is highly dependent on type of heat sources (stationary and moving). The stationary heat source could provide large bend angle (up to 4.5°). In the case of moving heat source, a bend angle of about 2.5° could be achieved in one pass in a 2 mm thickness steel workpiece. This bend angle is of same order as obtained in a bigger size sheet of the same thickness. The pattern of bend angle variation along width (scan direction) was some-what non-uniform in the case of stationary heat source as compared to moving heat source.

10.3 Effect of Single and Multi-pass on Laser Bending of Mild Steel Strips

The multi-pass laser bending of steel strips was studied experimentally and numerically. Effects of process parameters on bend angle, edge effect, flexure strength, temperature distribution, stress, plastic strain, microhardness and microstructure were investigated. Experimental results had a good agreement with numerical, i.e. finite element method (FEM) results due to inverse estimation of absorptivity. The edge effect on strip bending was very small as demonstrated experimentally and numerically. The flexural strength of laser scanned specimens increased. The microhardness values got increased with decrease in sample thickness and an increase in number of passes. This was attributed to formation of martensite and refined grains.

10.4 Effect of Laser Parameters as well as Welding Parameter on Laser Bending of Friction Stir Welded Sheets

Laser bending of friction stir welded aluminium alloy sheets was studied. Considering the difficulty in obtaining the temperature dependent material properties, an inverse methodology was employed. Heuristic optimization method was used to obtain the temperature dependent material properties based on the measurement of temperature at two locations during laser bending by an inverse method. The temperature dependent mechanical properties were also estimated inversely by comparing simulated and experimentally measured bend angles. Inversely determined temperature dependent material properties were used for FEM simulations of laser

bending of friction stir welded sheets. In simulations, material property and thickness variations in the weld zone was considered. The simulation results were validated with the experiments. The four scanning schemes were used for bending the friction stir welded sheets (along and across welding directions on the top and bottom surfaces). The highest bend angle was achieved when the scanning was carried out at the top (friction stirred) surface along the weld direction. It was observed that the welding parameters (tool rotation and welding speed) in friction stir welding had profound effect on bending behaviour.

10.5 Effect of Laser Absorptivity on Bending of Friction Stir Processed and Cement Coated Sheets

Laser bending of friction stir processed, cement-coated and uncoated raw sheets of aluminium alloy and mild steel was carried out. It was noted that friction stir processing roughened the surface and helped in getting larger bend angle due to increased absorptivity. Microhardness near the top surface of the sheet was greater than that near the bottom surface for both aluminium alloy and mild steel sheets; the microhardness increased with the number of passes. It is due to high temperature and large plastic deformation at the top surface. The bent friction stir processed sheets had higher microhardness compared to other sheets. For mild steel sheets, grain size before and after bending were studied. The grain size reduced from bottom surface to top surface of the sheet. The average grain size reduced with the number of laser passes. For friction stir processed sheet, the bend angle variation along the width (scan path), so-called edge effect, was smaller as compared to coated as well as uncoated sheets. It is possible to eliminate coating by friction stir processing, which may prove out to be a better environmentally-friendly option.

10.6 Laser Assisted Bending by Mechanical Load

In order to obtain, a high bend angle in a single pass laser assisted bending was studied by hanging weights at the free end of cantilevered sheet. The thermo-mechanical FEM modelling of the process was accomplished using a commercial package. However, many times, one simulation required about eight hours. Hence, an

artificial neural network (ANN) was carried out with output as bend angle and input as laser power, mechanical load, scan line distance and scan speed. The training data for ANN was obtained through FEM simulations. The ANN model made use of multi-layer perceptron as well as radial basis function judiciously. The network predicted most likely, upper and lower estimates of bend angle. Also, a method is suggested to find out the input parameters for a prescribed bend angle. Good predictability of the process is a strong requirement for the acceptability of the process in industry and this piece of work instils confidence to that aspect.

10.7 Laser Assisted Bending by Magnetic Force

In this piece of work, a manufacturing process was proposed to obtain large bend angles by laser assisted bending with the application of magnetic force. The process can be used to bend magnetic as well as nonmagnetic materials. The bend angle enhancement was more when the directions of laser bending and the bending due to magnetic force coincided. In general, the edge effect was lesser in magnetically assisted laser bending. Some springback effect was observed that lessened at low scan speed. Like in other laser based bending processes, here also, microhardness was higher at the top surface for mild steel as well as stainless steel.

10.8 Overall Conclusion

As the literature contains a number of studies on the bending of sheets using laser, this work focussed more on bending of small sized sheets, strips and friction stir welded sheets. It also attempted to enhance bend angle by assisting the laser bending with mechanical and magnetic loads. Attempt was also made to enhance the absorptivity of the workpiece. Study of mechanical properties after bending is also a major contribution of this thesis. Apart from experimental study, the process was studied through FEM and ANN simulations. It is encouraging to note that laser based bending could predict the bend angle with reasonable accuracy; this will help to increase its acceptability by industries.

10.9 Scope for Future Work

Although a lot of research findings are available on laser based bending in the literature including the present thesis, there are several issues that need further investigations. Some of these are as follows:

- FEM simulation requires a lot of computational time. There is a need to develop an efficient code for simulation of the process. At the same time, the code should have provision to predict the microstructure and mechanical properties of the product. Although some researchers have already done this, a generalized approach is missing. Different materials exhibit different kinds of behaviour, and a model developed for a particular material, say steel, may not work for another material, say magnesium alloy.
- There is a need to carry out more experimental investigation on the metallurgical aspects of different materials.
- This work has investigated laser bending of friction stir welded sheets. However, both the joined sheets were of same material. The work can be extended to laser bending of friction stir welded products comprising dissimilar materials and thicknesses.
- The present work explored laser assisted bending by using permanent magnetic force. The work can be extended to laser assisted bending by electromagnetic force to have better control on the process.
- The FEM model for laser assisted bending by using magnetic force needs upgradation as the present model makes some approximations.
- Some recent studies have observed that laser straightening of the bent sheets is not as easy as laser bending. It will be worthwhile to explore laser straightening.
- The laser forming of non-developable surfaces can be studied.
- Optimization of the laser bending process is also an interesting research area.
- The method of estimating temperature-dependent properties by inverse process is approximate. There is a need to develop a more robust method.

References

- Akinlabi, S.A., Pietra, F. and Akinlabi, E.T., 2015. Experimental and numerical investigation on laser beam forming of steel sheets. Proceedings of the Institution of Mechanical Engineers, Part L: Journal of Materials: Design and Applications, Vol. 229, No. 6, pp.455–471.
- Bammer, F., Schuöcker, D., Schumi, T., Holzinger, B. and Humenberger, G., 2011. A diode-laser-system for laser-assisted bending of brittle materials. Advances in Optical Technologies, 2011, pp.1–4.
- Barletta, M., Casamichele, L. and Tagliaferri, V., 2006. Line bending of Al_2O_3 coated and uncoated aluminium thin sheets. Surface and Coatings Technology, Vol. 201, Nos. 3–4, pp.660–673.
- Barletta, M., Gisario, A. and Guarino, S., 2009. Hybrid forming process of AA 6108 T4 thin sheets: modelling by neural network solutions. Proceedings of the Institution of Mechanical Engineers, Part B: Journal of Engineering Manufacture, Vol. 223, No. 5, pp.535–545.
- Bartkowiak, K., Dearden, G. and Watkins, K.G., 2004. 2-D Laser forming comparative study on Nd:Yag of titanium alloy Ti-6Al-4V. 23rd International Congress on Applications of Lasers and Electro-optics (ICALEO 2004), San Francisco, Vol. 97, pp.528.
- Behnagh, R.A., Besharati Givi, M.K. and Akbari, M., 2012. Mechanical properties, corrosion resistance, and microstructural changes during friction stir processing of 5083 aluminum rolled plates. Materials and manufacturing processes, Vol. 27, No. 6, pp.636–640.
- Bejan, A. and Kraus, A.D. (Eds.), 2003. Heat Transfer Handbook, Vol. 1, John Wiley and Sons, Hoboken, New Jersey, USA.
- Belghazi, H., El Ganaoui, M. and Labbe, J.C., 2010. Analytical solution of unsteady heat conduction in a two-layered material in imperfect contact subjected to a moving heat source. International Journal of Thermal Sciences, Vol. 49, No. 2, pp.311–318.

- Birnbaum, A.J., Cheng, P. and Yao, Y.L., 2007. Effects of clamping on the laser forming process, Journal of Manufacturing Science and Engineering, Vol. 129, No. 6, pp.1035–1044.
- Carey, C., Cantwell, W.J., Dearden, G., Edwards, K.R., Edwardson, S.P., Mullett, J.D., Williams, C.J. and Watkins, K.G., 2007. Effects of laser interaction with graphite coatings. Proceedings of the Laser Assisted Net Shape Engineering, Vol. 5, pp.673–686.
- Casalino, G. and Ludovico, A.D., 2002. Parameter selection by an artificial neural network for a laser bending process. Proceedings of the Institution of Mechanical Engineers, Part B: Journal of Engineering Manufacture, Vol. 216, No. 11, pp.1517–1520.
- Casamichele, L., Quadrini, F. and Tagliaferri, V., 2007. Process-efficiency prediction in high power diode laser forming. Journal of Manufacturing Science and Engineering, Vol. 129, No. 5, pp.868–873.
- Cavaliere, P. and De Marco, P.P., 2007. Friction stir processing of AM60B magnesium alloy sheets. Materials Science and Engineering: A, Vol. 462, No. 1, pp.393–397.
- Chakraborty, S.S., Maji, K., Racherla, V. and Nath, A.K., 2015a. Investigation on laser forming of stainless steel sheets under coupling mechanism. Optics and Laser Technology, Vol. 71, pp.29–44.
- Chakraborty, S.S., More, H., Racherla, V. and Nath, A.K., 2015b. Modification of bent angle of mechanically formed stainless steel sheets by laser forming. Journal of Materials Processing Technology, Vol. 222, pp.128–141.
- Chakraborty, S.S., More, H. and Nath, A.K., 2016. Laser forming of a bowl shaped surface with a stationary laser beam. Optics and Lasers in Engineering, Vol. 77, pp.126–136.
- Chan, K.C. and Liang, J., 2000a. Effect of microstructures on deformation behaviour of aluminium matrix composites. Laser Bending, Textures and Microstructures, Vol. 34, No. 1, pp.43–54.

- Chan, K.C. and Liang, J., 2000b. Laser bending of an Al6013/SiC_p aluminium matrix composite sheet. Journal of Materials Processing Technology, Vol. 100, No. 1, pp.214–218.
- Chandrasekaran, M., Muralidhar, M., Krishna, C.M. and Dixit, U.S., 2012. Online machining optimization with continuous learning. In Computational Methods for Optimizing Manufacturing Technology: Models and Techniques (pp. 85–110). IGI Global.
- Chang, C.I., Du, X.H. and Huang, J.C., 2007. Achieving ultrafine grain size in Mg-Al-Zn alloy by friction stir processing. Scripta Materialia, Vol. 57, No. 3, pp.209–212.
- Chehrghani, A., Torkamany, M.J., Hamedi, M.J. and Sabbaghzadeh, J., 2012. Numerical modeling and experimental investigation of TiC formation on titanium surface pre-coated by graphite under pulsed laser irradiation. Applied Surface Science, Vol. 258, No. 6, pp. 2068–2076.
- Chen, G., Xu, X., Poon, C.C. and Tam, A.C., 1998. Laser-assisted microscale deformation of stainless steels and ceramics. Optical Engineering, Vol. 37, No. 10, pp.2837–2843.
- Chen, G., Xu, X., Poon, C.C. and Tam, A.C., 1999. Experimental and numerical studies on microscale bending of stainless steel with pulsed laser. Journal of Applied Mechanics, Vol. 66, No. 3, pp.772–779.
- Chen, G. and Xu, X., 2001. Experimental and 3D finite element studies of CW laser forming of thin stainless steel sheets. Journal of Manufacturing Science and Engineering, Vol. 123, No. 1, pp.66–73.
- Chen, D.J., Xiang, Y.B., Wu, S.C. and Li, M.Q., 2002. Simulation and experiment of curve irradiated laser bending process of titanium alloy sheet. Materials Science and Technology, Vol. 18, No. 6, pp.673–676.
- Chen, D.J., Wu, S.C. and Li, M.Q., 2004a. Studies on laser forming of Ti-6Al-4V alloy sheet. Journal of Materials Processing Technology, Vol. 152, No. 1, pp.62–65.

- Chen, D., Wu, S. and Li, M., 2004b. Deformation behaviours of laser curve bending of sheet metals. Journal of Materials Processing Technology, Vol. 148, No. 1, pp.30–34.
- Chen, M.L., Jeswiet, J., Bates, P.J. and Zak, G., 2008. Experimental study on sheet metal bending with medium–power diode laser. Proceedings of the Institution of Mechanical Engineers, Part B: Journal of Engineering Manufacture, Vol. 222, No. 3, pp.381–389.
- Chen, J., Qi, Y., Shi, Y. and Bi, Z., 2010. An analytical model to predict bending angles in high-frequency induction heat forming. Proceedings of the Institution of Mechanical Engineers, Part C: Journal of Mechanical Engineering Science, Vol. 224, No. 3, pp.655–660.
- Cheng, P.J. and Lin, S.C., 2000a. An analytical model for the temperature field in the laser forming of sheet metal. Journal of Materials Processing Technology, Vol. 101, No. 1, pp.260–267.
- Cheng, P.J. and Lin, S.C., 2000b. Using neural networks to predict bending angle of sheet metal formed by laser. International Journal of Machine Tools and Manufacture, Vol. 40, No. 8, pp.1185–1197.
- Cheng, J. and Yao, Y.L., 2001. Cooling effects in multiscan laser forming. Journal of Manufacturing Processes, Vol. 3, No. 1, pp.60–72.
- Cheng, J. and Yao, Y.L., 2002. Microstructure integrated modeling of multiscan laser forming. Journal of Manufacturing Science and Engineering, Vol. 124, No. 2, pp.379–388.
- Cheng, J.G. and Yao, Y.L., 2004. Process synthesis of laser forming by genetic algorithm. International Journal of Machine Tools and Manufacture, Vol. 44, No. 15, pp.1619–1628.
- Cheng, P., Mika, D., Graham, M., Yao, Y.L. and Jones, M., 2005a. Laser forming of complex structures. The 1st International Workshop on Thermal Forming (IWOTF'05).
- Cheng, P., Yao, Y.L., Liu, C., Pratt, D. and Fan, Y., 2005b. Analysis and prediction of size effect on laser forming of sheet metal. Journal of Manufacturing Processes, Vol. 7, No. 1, pp.28–41.

- Cheng, P., Fan, Y., Zhang, J., Yao, Y.L., Mika, D.P., Zhang, W., Graham, M., Marte, J. and Jones, M., 2006. Laser forming of varying thickness plate—Part I: Process analysis. Journal of manufacturing science and engineering, Vol. 128, No. 3, pp.634–641.
- Cheng, G.J., Pirzada, D. and Ming, Z., 2007. Microstructure and mechanical property characterizations of metal foil after microscale laser dynamic forming. Journal of applied physics, Vol. 101, No. 6, pp.063108.
- Cui, G.R., Ma, Z.Y. and Li, S.X., 2009. The origin of non-uniform microstructure and its effects on the mechanical properties of a friction stir processed Al-Mg alloy. Acta Materialia, Vol. 57, No. 19, pp.5718–5729.
- Das, B. and Biswas, P., 2015. Effect of operating parameters on plate bending by laser line heating. Proceedings of the Institution of Mechanical Engineers, Part B: Journal of Engineering Manufacture, pp.1–8, DOI: 10.1177/0954405415612678.
- Dearden, G. and Edwardson, S.P., 2003. Some recent developments in two-and three-dimensional laser forming for ‘macro’ and ‘micro’ applications. Journal of Optics A: Pure and Applied Optics, Vol. 5, No. 4, pp.S8.
- Dehghani, K. and Mazinani, M., 2011. Forming nanocrystalline surface layers in copper using friction stir processing. Materials and Manufacturing Processes, Vol. 26, No. 7, pp.922–925.
- Deng, D. and Murakawa, H., 2006. Numerical simulation of temperature field and residual stress in multi-pass welds in stainless steel pipe and comparison with experimental measurements. Computational materials science, Vol. 37, No. 3, pp.269–277.
- Dieter GE., 1991. Engineering design: a materialistic and processing approach, 2nd edn. McGraw-Hill, New York.
- Dixit, U.S., Joshi, S.N. and Kumar, V.H., 2012. Microbending with laser. Micromanufacturing processes. CRC Press, Boca Raton, pp.283–303.
- Dixit, U.S., Joshi, S.N. and Kumar, V.H., 2013. Microbending with Lasers, Micromanufacturing Processes, edited by Jain, V.K. CRC Press, Boca Raton, Florida.

- Dixit, U.S., Joshi, S.N. and Kant, R., 2015. Laser forming systems: a review. International Journal of Mechatronics and Manufacturing Systems, Vol. 8, No. 3–4, pp.160–205.
- Dragos, V., Dan, V. and Kovacevic, R., 2000. Prediction of the laser sheet bending using neural network. In Circuits and Systems, 2000. Proceedings. ISCAS 2000 Geneva. The 2000 IEEE International Symposium on, Vol. 3, pp. 686–689, IEEE.
- Du, Y., Wang, X. and Silvanus, J., 2010. Improved BP network to predict bending angle in the laser bending process for sheet metal. Intelligent System Design and Engineering Application (ISDEA), 2010 International Conference on, Vol. 1, pp.839–843, IEEE.
- Dutta Majumdar, J. and Manna, I., 2011. Laser material processing. International materials reviews, Vol. 56, Nos. 5-6, pp.341-388.
- Dutta P.P., Dixit, U.S. and Kalita K., 2013. Experimental investigation on laser bending of mild steel coated with black enamel paint. In proceedings of national conference on manufacturing: Vision for Future, pp. 198–203.
- Dutta P.P., Dixit, U.S. and Kalita K., 2017. A strategy for achieving accurate bending by multi-pass laser line heating. International Journal of Mechatronics and Manufacturing Systems, Vol. 10, No. 4, pp. 277–298.
- Edwardson, S.P., Watkins, K.G., Dearden, G. and Magee, J., 2001. 3D laser forming of saddle shapes. Proceedings of Laser Assisted Net Shaping, pp.559–568.
- Edwardson, S.P., Abed, E., Bartkowiak, K., Dearden, G. and Watkins, K.G., 2006. Geometrical influences on multi-pass laser forming. Journal of Physics D: Applied Physics, Vol. 39, No. 2, p.382.
- Edwardson, S.P., Abed, E., Carey, C., Edwards, K.R., Dearden, G. and Watkins, K.G., 2007. Factors influencing the bend per pass in multi-pass laser forming. Proceedings of the 5th LANE, 1, pp.557–568.
- Edwardson, S.P., Griffiths, J., Dearden, G. and Watkins, K.G., 2010a. Temperature gradient mechanism: overview of the multiple pass controlling factors, Physics Procedia, Vol. 5, Part A, pp.53–63.

- Edwardson, S.P., Griffiths, J., Edwards, K.R., Dearden, G. and Watkins, K.G., 2010b. Laser forming: overview of the controlling factors in the temperature gradient mechanism. Proceedings of the Institution of Mechanical Engineers, Part C: Journal of Mechanical Engineering Science, Vol. 224, No. 5, pp.1031–1040.
- Eideh, A. and Dixit, U.S., 2013. November. A robust and efficient inverse method for determining the thermal parameters during laser forming. In Proceedings of National Conference of Recent Advancements in Mechanical Engineering. NERIST, Nirjuli, India (pp. 38–43).
- Eideh A., 2014. Determination of Parameters During Laser Bending by Inverse Analysis, M. Tech. Thesis, Department of Mechanical Engineering, IIT Guwahati, India.
- Eideh, A., Dixit, U.S. and Echempati, R., 2015. A simple analytical model of laser bending process, laser based manufacturing, in Joshi, S.N. and Dixit, U.S. (Eds.): 5th International and 26th National All India Manufacturing Technology, Design and Research AIMTDR 2014, Chapter 1, pp.1–15.
- Fan, Y., Cheng, P., Yao, Y.L., Yang, Z. and Egland, K., 2005. Effect of phase transformations on laser forming of Ti-6Al-4V alloy. Journal of Applied Physics, Vol. 98, No. 1, p.013518.
- Fan, Y., Yang, Z., Cheng, P., Egland, K. and Yao, L., 2007. Investigation of effect of phase transformations on mechanical behavior of AISI 1010 steel in laser forming. Journal of Manufacturing Science and Engineering, Vol. 129, No. 1, pp.110–116.
- Feng, A.H. and Ma, Z.Y., 2007. Enhanced mechanical properties of Mg–Al–Zn cast alloy via friction stir processing. Scripta materialia, Vol. 56, No. 5, pp.397–400.
- Folkersma, G., Brouwer, D. and Römer, G., 2016, Microtube laser forming for precision component alignment, ASME Journal of Manufacturing Science and Engineering, Vol. 138, No. 8, pp. 081012.
- Garg, A., Sastry, P.S., Pandey, M., Dixit, U.S. and Gupta, S.K., 2007. Numerical simulation and artificial neural network modeling of natural circulation boiling water reactor. Nuclear engineering and design, Vol. 237, No. 3, pp.230–239.

- Gautam, S.S., Singh, S.K. and Dixit, U.S., 2015. Laser Forming of Mild Steel Sheets Using Different Surface Coatings. In Lasers Based Manufacturing, 5th International and 26th All India Manufacturing Technology, Design and Research Conference, AIMTDR 2014, Edited by S.N. Joshi and U.S. Dixit Springer, New Delhi: pp. 17–39.
- Geiger, M., Vollertsen, F. and Deinzer, G., 1993. Flexible Straightening of Car Body Shells by Laser Forming. No. 930279, SAE Technical paper.
- Geiger, M. and Vollertsen, F., 1993. The mechanisms of laser forming. CIRP Annals-Manufacturing Technology, Vol. 42, No. 1, pp.301–304.
- Geiger, M., 1994. Synergy of laser material processing and metal forming. CIRP Annals-Manufacturing Technology, Vol. 43, No. 2, pp.563–570.
- Gisario, A., Barletta, M., Conti, C. and Guarino, S., 2011. Springback control in sheet metal bending by laser-assisted bending: Experimental analysis, empirical and neural network modelling. Optics and Lasers in Engineering, Vol. 49, No. 12, pp.1372–1383.
- Gisario, A., Barletta, M. and Venettacci, S., 2016. Improvements in springback control by external force laser-assisted sheet bending of titanium and aluminum alloys. Optics and Laser Technology, Vol. 86, pp.46–53.
- Gisario, A., Mehrpouya, M., Venettacci, S. and Barletta, M., 2017. Laser-assisted bending of Titanium Grade-2 sheets: Experimental analysis and numerical simulation. Optics and Lasers in Engineering, Vol. 92, pp.110–119.
- Gollo, M.H., Mahdavian, S.M. and Naeini, H.M., 2011. Statistical analysis of parameter effects on bending angle in laser forming process by pulsed Nd: YAG laser. Optics and Laser Technology, Vol. 43, No. 3, pp.475–482.
- Griffiths, J., Edwardson, S.P., Dearden, G. and Watkins, K.G., 2010. Finite element modelling of laser forming at macro and micro scales. PhysicsProcedia, Vol. 5, Part B, pp.371–380.
- Guan, Y., Sun, S., Zhao, G. and Luan, Y., 2005. Influence of material properties on the laser-forming process of sheet metals. Journal of Materials Processing Technology, Vol. 167, No. 1, pp.124–131.

- Guglielmotti, A., Quadrini, F., Squeo, E.A. and Tagliaferri, V., 2009. Laser bending of aluminum foam sandwich panels. Advanced engineering materials, Vol. 11, No.11, pp.902–906.
- Hao, N. and Li, L., 2003a. Finite element analysis of laser tube bending process, Applied Surface Science, Vol. 208, pp.437–441.
- Hao, N. and Li, L., 2003b. An analytical model for laser tube bending, Applied Surface Science, Vols. 208, pp.432–436.
- Hassan, K.A., Prangnell, P.B., Norman, A.F., Price, D.A. and Williams, S.W., 2003. Effect of welding parameters on nugget zone microstructure and properties in high strength aluminium alloy friction stir welds. Science and Technology of Welding and joining, Vol. 8, No. 4, pp.257–268.
- Hennige, T., Holzer, S., Vollertsen, F. and Geiger, M., 1997. On the working accuracy of laser bending, Journal of Materials Processing Technology, Vol. 71, No. 3, pp.422–432.
- Holzer, S., Arnet, H. and Geiger, M., 1994. Physical and numerical modelling of the buckling mechanism. In Laser assisted net shape engineering, proceedings of the LANE, Vol. 1, pp. 379–386.
- Hsieh, H.S. and Lin, J., 2004a. Laser-induced vibration during pulsed laser forming. Optics and Laser Technology, Vol. 36, No. 6, pp.431–439.
- Hsieh, H.S. and Lin, J., 2004b. Thermal-mechanical analysis on the transient deformation during pulsed laser forming. International Journal of Machine Tools and Manufacture, Vol. 44, No. 2, pp.191–199.
- Hu, Z., Labudovic, M., Wang, H. and Kovacevic, R., 2001. Computer simulation and experimental investigation of sheet metal bending using laser beam scanning. International Journal of Machine Tools and Manufacture, Vol. 41, No. 4, pp.589–607.
- Hu, Z., Kovacevic, R. and Labudovic, M., 2002. Experimental and numerical modeling of buckling instability of laser sheet forming. International Journal of Machine Tools and Manufacture, Vol. 42, No. 13, pp.1427–1439.

- Hu, J., Dang, D., Shen, H. and Zhang, Z., 2012. A finite element model using multi-layered shell element in laser forming. Optics and Laser Technology, Vol. 44, No. 4, pp.1148–1155.
- Hu, J., Xu, H. and Dang, D., 2013. Modeling and reducing edge effects in laser bending. Journal of Materials Processing Technology, Vol. 213, No. 11, pp.1989–1996.
- Jamil, M.C., Sheikh, M.A. and Li, L., 2011a. A study of the effect of laser beam geometries on laser bending of sheet metal by buckling mechanism. Optics and Laser Technology, Vol. 43, No. 1, pp.183–193.
- Jamil, M.S.C., Sheikh, M.A. and Li, L., 2011b. A numerical study of the temperature gradient mechanism in laser forming using different laser beam geometries. Lasers in Engineering, Vol. 22, Nos. 5–6, pp.413–428.
- Jamil, M.C., Fauzi, E.I., Juinn, C.S. and Sheikh, M.A., 2015. Laser bending of pre-stressed thin-walled nickel micro-tubes. Optics and Laser Technology, Vol. 73, pp.105–117.
- Ji, Z. and Wu, S., 1998. FEM simulation of the temperature field during the laser forming of sheet metal. Journal of Materials Processing Technology, Vol. 74, No. 1, pp.89–95.
- Jovic, S., Makragic, S. and Jovanovic, M., 2017. Parameters influence of laser forming on shaped surface by soft computing technique. Optik-International Journal for Light and Electron Optics, Vol. 142, pp.451–454.
- Kannatey-Asibu Jr, E., 2009. Principles of laser materials processing (Vol. 4). John Wiley and Sons.
- Kant, R. and Joshi, S. N., 2012a. Numerical simulation of laser bending of magnesium alloy AZ31B using FEM. Proc. of the International Conference IDDRG 2012, Vol. 2, pp.736–741.
- Kant, R. and Joshi, S. N., 2012b. Analysis of sheet-holding methods in laser bending process using FEM. Proc. of the 3rd Asian Symposium on Materials and Processing, ASMP - 2012, MCMTP6.

- Kant, R. and Joshi, S.N., 2013a. Numerical simulation of multi-pass laser bending processes using finite element method. In Proceedings of the 2nd international conference IRAM 2013, pp. 16–18.
- Kant, R. and Joshi, S.N., 2013b. Finite element simulation of laser assisted bending with moving mechanical load. International journal of mechatronics and manufacturing systems, Vol. 6, No. 4, pp.351–366.
- Kant, R. and Joshi, S.N., 2014. Numerical modeling and experimental validation of curvilinear laser bending of magnesium alloy sheets. Proceedings of the Institute of Mechanical Engineering Part B: Journal of Engineering Manufacture, Vol. 228, pp.1036–1047.
- Kant, R., Joshi, S.N. and Dixit, U.S., 2015a. An integrated FEM-ANN model for laser bending process with inverse estimation of absorptivity. Mechanics of Advanced Materials and Modern Processes, Vol. 1, No. 1, pp. 6.
- Kant, R., Joshi, S.N. and Dixit, U.S., 2015b, Research Issues in the Laser Sheet Bending Process, Chapter 4 in Materials Forming and Machining: Research and Development, edited by J. Paulo Davim, Woodhead Publishing, Cambridge, pp. 73–95.
- Kant, R. and Joshi, S.N., 2016. Thermo-mechanical studies on bending mechanism, bend angle and edge effect during multi-scan laser bending of magnesium M1A alloy sheets. Journal of Manufacturing Processes, Vol. 23, pp.135–148.
- Karthikeyan, L., Senthil Kumar, V.S. and Padmanabhan, K.A., 2013. Investigations on superplastic forming of friction stir-processed AA6063-T6 aluminum alloy. Materials and Manufacturing processes, Vol. 28, No. 3, pp.294–298.
- Kennedy, E., Byrne, G. and Collins, D.N., 2004. A review of the use of high power diode lasers in surface hardening. Journal of Materials Processing Technology, Vol. 155, pp.1855–1860.
- Kim, H.K. and Oh, S.I., 2001. Evaluation of heat transfer coefficient during heat treatment by inverse analysis, Journal of Materials Processing Technology, Vol. 112, pp. 157–165.

- Kohli, A. and Dixit, U.S., 2005. A neural-network-based methodology for the prediction of surface roughness in a turning process. The International Journal of Advanced Manufacturing Technology, Vol. 25, No. 1, pp.118–129.
- Kratky, A., 2007, May. Laser assisted forming techniques. In XVI International Symposium on Gas Flow, Chemical Lasers, and High-Power Lasers (Vol. 6346, p. 634615). International Society for Optics and Photonics.
- Kraus, J., 1997. Basic process in laser bending of extrusion using the upsetting mechanism. Laser Assisted Net Shape Engineering 2, Proceedings of the LANE, Vol. 97, pp.431–438.
- Kumar, V. and Dixit, U.S., 2017. Selection of process parameters in a single-pass laser bending process. Engineering Optimization, pp.1–16.
- Kyrsanidi, A.K., Kermanidis, T.B. and Pantelakis, S.G., 1999. Numerical and experimental investigation of the laser forming process, Journal of Materials Processing Technology, Vol. 87, No. 1, pp.281–290.
- Kyrsanidi, A.K., Kermanidis, T.B. and Pantelakis, S.G., 2000. An analytical model for the prediction of distortions caused by the laser forming process. Journal of Materials Processing Technology, Vol. 104, No. 1, pp.94–102.
- Labeas, G.N., 2008. Development of a local three-dimensional numerical simulation model for the laser forming process of aluminium components. Journal of materials processing technology, Vol. 207, No. 1, pp.248–257.
- Lambiase, F., 2012. An analytical model for evaluation of bending angle in laser forming of metal sheets. Journal of materials engineering and performance, Vol. 21, No. 10, pp.2044–2052.
- Lambiase, F. and Di Ilio, A., 2013. A closed-form solution for thermal and deformation fields in laser bending process of different materials. The International Journal of Advanced Manufacturing Technology, Vol. 69, Nos. 1–4, pp.849–861.
- Lambiase, F., Di Ilio, A. and Paoletti, A., 2013. An experimental investigation on passive water cooling in laser forming process, The International Journal of Advanced Manufacturing Technology, Vol. 64, Nos. 5–8, pp.829–840.

- Lambiase, F., Di Ilio, A. and Paoletti, A., 2015. Optimization of multi–pass laser bending by means of soft computing techniques. Procedia CIRP, Vol. 33, pp.502–507.
- Langlade, C., Roman, A., Schlegel, D., Gete, E. and Folea, M., 2016. Formation of a Tribologically Transformed Surface (TTS) on AISI 1045 steel by friction stir processing. Materials and Manufacturing Processes, Vol. 31, No. 12, pp.1565–1572.
- Lawrence, J., Schmidt, M.J. and Li, L., 2001. The forming of mild steel plates with a 2.5 kW high power diode laser. International Journal of Machine Tools and Manufacture, Vol. 41, No. 7, pp.967–977.
- Lawrence M. and Petterson A., 2002. Brain maker user's manual, 7th edn. California Scientific Software, Nevada City.
- Lee, K.C. and Lin, J., 2002. Transient deformation of thin metal sheets during pulsed laser forming. Optics and Laser Technology, Vol. 34, No. 8, pp.639–648.
- Li, W. and Yao, Y.L., 2000. Numerical and experimental study of strain rate effects in laser forming. Journal of Manufacturing Science and Engineering, Vol. 122, No. 3, pp.445–451.
- Li, W. and Yao, Y. L., 2001a. Numerical and experimental investigation of convex laser forming process. Journal of Manufacturing Processes, Vol. 3, No. 2, pp.73–81.
- Li, W. and Yao, Y. L., 2001b. Laser bending of tubes: mechanism, analysis and prediction. Journal of Manufacturing Science and Engineering, Vol. 123, No. 4, pp.674–681.
- Liechty, B.C. and Webb, B.W., 2008. Modeling the frictional boundary condition in friction stir welding. International Journal of Machine Tools and Manufacture, Vol. 48, No. 12, pp.1474–1485.
- Liu, C. and Yao, Y. L., 2002. Optimal and robust design of the laser forming process. Journal of Manufacturing Processes, Vol. 4, No. 1, pp.52–66.
- Liu, J., Sun, S. and Guan, Y., 2009. Numerical investigation on the laser bending of stainless steel foil with pre-stresses. Journal of materials processing technology, Vol. 209, No. 3, pp.1580–1587.

- Liu, F., Lin, X., Huang, C., Song, M., Yang, G., Chen, J. and Huang, W., 2011. The effect of laser scanning path on microstructures and mechanical properties of laser solid formed nickel-base superalloy Inconel 718. Journal of Alloys and Compounds, Vol. 509, No. 13, pp.4505–4509.
- Logothetis, N., 1992. Managing for total quality: from Deming to Taguchi and SPC. Prentice-Hall of India.
- Ma, Z.Y., 2008. Friction stir processing technology: a review. Metallurgical and materials Transactions A, Vol. 39, No. 3, pp.642–658.
- Ma, Z.Y., Mishra, R.S. and Liu, F.C., 2009. Superplastic behavior of micro-regions in two-pass friction stir processed 7075Al alloy. Materials Science and Engineering: A, Vol. 505, No. 1, pp.70–78.
- Magee, J. and De Vin, L.J., 2002. Process planning for laser-assisted forming. Journal of Materials Processing Technology, Vol. 120, No. 1, pp.322–326.
- Maji, K., Pratihar, D.K. and Nath, A.K., 2013. Analysis and synthesis of laser forming process using neural networks and neuro-fuzzy inference system. Soft Computing, Vol. 17, No. 5, pp.849–865.
- Maji, K., Pratihar, D.K. and Nath, A.K., 2014a. Laser forming of a dome shaped surface: Experimental investigations, statistical analysis and neural network modeling. Optics and Lasers in Engineering, Vol. 53, pp.31–42.
- Maji, K., Pratihar, D.K. and Nath, A.K., 2014b. Analysis of pulsed laser bending of sheet metal using neural networks and neuro-fuzzy system. Proceedings of the Institution of Mechanical Engineers, Part B: Journal of Engineering Manufacture, Vol. 228, No. 9, pp.1015–1026.
- Majumdar, J.D., Nath, A.K. and Manna, I., 2004. Studies on laser bending of stainless steel. Materials Science and Engineering: A, Vol. 385, No. 1, pp.113–122.
- Martin, R., 1979. Automated adjusting in precision engineering (German patent: Automatisiertesjustieren in der feinwerktechnik). Deutsches Patentamt, Offenlegungsschrift, Vol. 29, No. 18, pp.100.

- Mazhukin, V.I., Lobok, M.G. and Smurov, I., 2007. Transient effects in pulsed laser irradiation. Applied Surface Science, Vol. 253, No. 19, pp.7744–7748.
- McGrath, P.J. and Hughes, C.J., 2007. Experimental fatigue performance of laser-formed components. Optics and lasers in engineering, Vol. 45, No. 3, pp.423–430.
- Merklein, M., Hennige, T. and Geiger, M., 2001. Laser forming of aluminium and aluminium alloys—microstructural investigation. Journal of Materials Processing Technology, Vol. 115, No. 1, pp.159–165.
- Mishra, R.S., Mahoney, M.W., McFadden, S.X., Mara, N.A. and Mukherjee, A.K., 1999. High strain rate superplasticity in a friction stir processed 7075 Al alloy. Scripta Materialia, Vol. 42, No. 2, pp.163–168.
- Mishra, R.S. and Ma, Z.Y., 2005. Friction stir welding and processing. Materials Science and Engineering: R: Reports, Vol. 50, Nos. 1–2, pp.1–78.
- Mishra, A. and Dixit, U.S., 2013. Determination of thermal diffusivity of the material, absorptivity of the material and laser beam radius during laser forming by inverse heat transfer. Journal of Machining and Forming Technology, Vol. 5, Nos. 3–4 pp. 208–226.
- Morisada, Y., Fujii, H., Nagaoka, T., Nogi, K. and Fukusumi, M., 2007. Fullerene/A5083 composites fabricated by material flow during friction stir processing. Composites Part A: Applied Science and Manufacturing, Vol. 38, No. 10, pp.2097–2101.
- Mueller, S., Kruck, B. and Baudisch, P., 2013, April. LaserOrigami: laser-cutting 3D objects. In Proceedings of the SIGCHI Conference on Human Factors in Computing Systems (pp. 2585–2592). ACM.
- Nascimento, F., Santos, T., Vilaça, P., Miranda, R.M. and Quintino, L., 2009. Microstructural modification and ductility enhancement of surfaces modified by FSP in aluminium alloys. Materials Science and Engineering: A, Vol. 506, No. 1, pp.16–22.
- Ocana, J.L., Morales, M., Molpeceres, C., Garcia, O., Porro, J.A. and Garcia-Ballesteros, J.J., 2007. Short pulse laser microforming of thin metal sheets for MEMS manufacturing. Applied Surface Science, Vol. 254, No. 4, pp.997–1001.

- Okamoto, Y., Uno, Y., Ohta, K.I., Shibata, T., Kubota, S.I. and Namba, Y., 2000. Study on precision laser forming of plastic with YAG laser. Seimitsu Kogaku Kaishi/Journal of the Japan Society for Precision Engineering, Vol. 66, No. 6, pp.891–895.
- Okamoto, Y., Miyamoto, I., Uno, Y. and Takenaka, T., 2004. Deformation characteristics of plastics in YAG laser forming, Fifth International Symposium on Laser Precision Microfabrication, Vol. 5662, pp. 576-582, International Society for Optics and Photonics.
- Palani, I.A., Naikwad, S., Padmanabhan, R., Shanmugam, S. and Natu, H., 2015. Parametric Investigation in Laser Forming of 8 mm FE-410 Plate Using High Power CO_2 Laser and Its Bend Angle Prediction. Materials Today: Proceedings, Vol. 2, Nos.4–5, pp.2013–2021.
- Park, S., Lee, C.G., Han, H.N., Ma, N. and Chung, K., 2008. Surface friction stir method to improve formability and spring-back of AA5052-H32 sheets. International Journal of Material Forming, Vol. 1, No. 1, pp.261–264.
- Paunoiu, V., Squeo, E.A., Quadrini, F., Gheorghies, C. and Nicoara, D., 2008. Laser bending of stainless steel sheet metals. International Journal of Material Forming, Vol. 1, No. 1, pp.1371–1374.
- Pérez, J.A., González, M. and Dopico, D., 2010. Adaptive neurofuzzy ANFIS modeling of laser surface treatments. Neural Computing and Applications, Vol. 19, No. 1, pp.85–90.
- Pitz, I., Otto, A. and Schmidt, M., 2010. Simulation of the laser beam forming process with moving meshes for large aluminium plates. Physics Procedia, Vol. 5, Part B, pp.363–369.
- Pretorius, T., 2009. Laser Forming, The Theory of Laser Materials Processing, edited by Dowden, J., Vol. 119, pp. 281–314, Springer, UK.
- Qi, L. and Namba, Y., 2011. Precision laser adjustment using CW diode laser, Precision Engineering, Vol. 35, No. 1, pp.126–132.
- Quadrini, F., Guglielmotti, A., Squeo, E.A. and Tagliaferri, V., 2010. Laser forming of open-cell aluminium foams. Journal of Materials Processing Technology, Vol. 210, No. 11, pp.1517–1522.

- Ramulu, P.J., Narayanan, R.G. and Kailas, S.V., 2013. Forming limit investigation of friction stir welded sheets: influence of shoulder diameter and plunge depth. International Journal of Advanced Manufacturing Technology, Vol. 69, Nos. 9–12, pp. 2757–2772.
- Risbood, K.A., Dixit, U.S. and Sahasrabudhe, A.D., 2003. Prediction of surface roughness and dimensional deviation by measuring cutting forces and vibrations in turning process. Journal of Materials Processing Technology, Vol. 132, No. 1, pp.203–214.
- Romer, G.R.B.E. and Meijer, J., 2000. Inverse calculation of power density for laser surface treatment. Annals of the CIRP, Vol. 49, pp. 135–138.
- Roohi, A.H., Gollo, M.H. and Naeini, H.M., 2012. External force-assisted laser forming process for gaining high bending angles. Journal of Manufacturing Processes, Vol. 14, No. 3, pp.269–276.
- Roohi, A.H., Naeini, H.M., Gollo, M.H., Soltanpour, M. and Abbaszadeh, M., 2015. On the random-based closed-cell metal foam modeling and its behavior in laser forming process. Optics and Laser Technology, Vol. 72, pp.53–64.
- Rouquette, S., Guo, J. and Le Masson, P., 2007. Estimation of the parameters of a Gaussian heat source by the Levenberg-Marquardt method: Application of the electron beam welding. International Journal of Thermal Sciences, Vol. 46, pp. 128–138.
- Safdar, S., Li, L., Sheikh, M.A. and Liu, Z., 2007a. Finite element simulation of laser tube bending: Effect of scanning schemes on bending angle, distortions and stress distribution. Optics and Laser Technology, Vol. 39, No. 6, pp.1101–1110.
- Safdar, S., Li, L., Sheikh, M.A. and Liu, Z., 2007b. The effect of nonconventional laser beam geometries on stress distribution and distortions in laser bending of tubes. Journal of manufacturing science and engineering, Vol. 129, No. 3, pp.592–600.
- Safari, M. and Farzin, M., 2013. Experimental and numerical investigation of laser bending of tailor machined blanks. Optics and Laser Technology, Vol. 48, pp.513–522.

- Safari, M. and Farzin, M., 2014. A study on laser bending of tailor machined blanks with various irradiating schemes. Journal of Materials Processing Technology, Vol. 214, No. 1, pp. 112–122.
- Safari, M. and Farzin, M., 2015. Experimental investigation of laser forming of a saddle shape with spiral irradiating scheme. Optics and Laser Technology, Vol. 66, pp.146–150.
- Samm, K., Terzi, M., Ostendorf, A. and Wulfsberg, J., 2009, Laser-assisted micro-forming process with miniaturised structures in sapphire dies, Applied Surface Science, Vol. 255, No. 24, pp. 9830–9834.
- Sato, Y.S., Nelson, T.W., Sterling, C.J., Steel, R.J. and Pettersson, C.O., 2005. Microstructure and mechanical properties of friction stir welded SAF 2507 super duplex stainless steel. Materials Science and Engineering: A, Vol. 397, No. 1, pp.376–384.
- Scialpi, A., De Filippis, L.A.C., Cuomo, P. and Di Summa, P., 2008. Micro friction stir welding of 2024–6082 aluminum alloys. Welding International, Vol. 22, No. 1, pp.16–22.
- Sekban, D.M., Saray, O., Aktarer, S.M., Purcek, G. and Ma, Z.Y., 2015. Microstructure, mechanical properties and formability of friction stir processed interstitial-free steel. Materials Science and Engineering: A, Vol. 642, pp.57–64.
- Sharma, V., Gupta, Y., Kumar, B.M. and Prakash, U., 2016. Friction stir processing strategies for uniform distribution of reinforcement in a surface composite. Materials and Manufacturing Processes, Vol. 31, No. 10, pp.1384–1392.
- Sheikh, M.A. and Li, L., 2010. Understanding the effect of non-conventional laser beam geometry on material processing by finite-element modelling. Proceedings of the Institution of Mechanical Engineers, Part C: Journal of Mechanical Engineering Science, Vol. 224, No. 5, pp.1061–1072.
- Shen, Z.H., Zhang, S.Y., Lu, J. and Ni, X.W., 2001. Mathematical modeling of laser induced heating and melting in solids. Optics and laser technology, Vol. 33, No. 8, pp.533–537.

- Shen, H., Shi, Y., Yao, Z. and Hu, J., 2006. An analytical model for estimating deformation in laser forming. Computational Materials Science, Vol. 37, No. 4, pp.593–598.
- Shen, H., 2008. Mechanism of laser micro-adjustment. Journal of Physics D: Applied Physics, Vol. 41, No. 24, p.245106.
- Shen, H. and Yao, Z., 2009. Study on mechanical properties after laser forming. Optics and Lasers in Engineering, Vol. 47, No. 1, pp.111–117.
- Shen, H. and Vollertsen, F., 2009. Modelling of laser forming–An review. Computational Materials Science, Vol. 46, No. 4, pp.834–840.
- Shen, H., Ran, M., Hu, J. and Yao, Z., 2014. An experimental investigation of underwater pulsed laser forming. Optics and Lasers in Engineering, Vol. 62, pp.1–8.
- Shi, Y., Shen, H., Yao, Z., Hu, J. and Xia, L., 2006a. Application of similarity theory in the laser forming process. Computational Materials Science, Vol. 37, No. 3, pp.323–327.
- Shi, Y., Yao, Z., Shen, H. and Hu, J., 2006b. Research on the mechanisms of laser forming for the metal plate. International Journal of Machine Tools and Manufacture, Vol. 46, No. 12, pp.1689–1697.
- Shi, Y., Shen, H., Yao, Z. and Hu, J., 2007a. An analytical model based on the similarity in temperature distributions in laser forming. Optics and lasers in engineering, Vol. 45, No. 1, pp.83–87.
- Shi, Y., Shen, H., Yao, Z. and Hu, J., 2007b. Temperature gradient mechanism in laser forming of thin plates. Optics and Laser Technology, Vol. 39, No. 4, pp.858–863.
- Shi, Y., Hu, J. and Dong, C., 2011. Analysis of the geometric effect on the forming accuracy in laser forming. Proceedings of the Institution of Mechanical Engineers, Part B: Journal of Engineering Manufacture, Vol. 225, No. 10, pp.1792–1800.
- Shi, Y., Liu, Y., Yi, P. and Hu, J., 2012. Effect of different heating methods on deformation of metal plate under upsetting mechanism in laser forming. Optics and Laser Technology, Vol. 44, No. 2, pp.486–491.

- Shi, Y., Lu, X., Liu, Y. and Yi, P., 2013. Forming accuracy analysis of plate in multi-scanning laser bending process. Proceedings of the Institution of Mechanical Engineers, Part E: Journal of Process Mechanical Engineering, Vol. 227, No. 3, pp.225–228.
- Shi, Y., Zhang, C., Sun, G. and Li, C., 2016. Study on reducing edge effects by using assistant force in laser forming. Journal of Materials Processing Technology, Vol. 227, pp.169–177.
- Shichun, W. and Jinsong, Z., 2001. An experimental study of laser bending for sheet metals. Journal of Materials Processing Technology, Vol. 110, No. 2, pp.160–163.
- Shidid, D.P., Gollo, M.H., Brandt, M. and Mahdavian, M., 2013. Study of effect of process parameters on titanium sheet metal bending using Nd: YAG laser. Optics and Laser Technology, Vol. 47, pp.242–247.
- Shidfar, A., Jazbi, B. and Alinejadmofrad, M., 2012. Inverse estimation of pulse parameters of a time-varying laser pulse to obtain desired temperature at the material surface. Optics and Laser Technology, Vol. 44, pp. 1675–1680.
- Singh, K., Joshi, S.N., Ray, A.K. and Dixit, U.S., 2013a, August. A comparison of bend quality of mechanical and laser bending of mild steel. In Proceedings of National Symposium on Miniature Manufacturing in 21st Century (NSMMIC–2013), 16–18 August, IIT (BHU), Varanasi, India.
- Singh, K., Ray, A.K., Joshi, S.N. and Dixit, U.S., 2013b, November. Effect of lime and graphite grease coatings on the absorptivity of mild steel sheet in line heating by CO_2 laser. In Proceedings of national conference on recent advancements in mechanical engineering (pp. 8–9).
- Sonar, D.K., Dixit, U.S. and Ojha, D.K., 2006. The application of a radial basis function neural network for predicting the surface roughness in a turning process. The International Journal of Advanced Manufacturing Technology, Vol. 27, No. 7, pp.661–666.
- Sun, H., 1998. Thin lens equation for a real laser beam with weak lens aperture truncation. Optical Engineering, Vol. 37, No. 11, pp.2906–2914.

- Surekha, K., Murty, B.S. and Rao, K.P., 2009. Effect of processing parameters on the corrosion behaviour of friction stir processed AA 2219 aluminum alloy. Solid state sciences, Vol. 11, No. 4, pp.907–917.
- Tam, A.C., Poon, C.C. and Crawforth, L., 2001. Laser bending of ceramics and application to manufacture magnetic head sliders in disk drives, Analytical Sciences/Supplements, Vol. 17, pp.s419–s421.
- Tewari, A., Spowart, J.E., Gokhale, A.M., Mishra, R.S. and Miracle, D.B., 2006. Characterization of the effects of friction stir processing on microstructural changes in DRA composites. Materials Science and Engineering: A, Vol. 428, No. 1, pp.80–90.
- Thomson, G. and Pridham, M., 2001. Material property changes associated with laser forming of mild steel components. Journal of Materials Processing Technology, Vol. 118, No. 1, pp.40–44.
- Toros, S., Ozturk, F. and Kacar, I., 2008. Review of warm forming of aluminium–magnesium alloys. Journal of materials processing technology, Vol. 207, No. 1, pp.1–12.
- Ueda, T., Sentoku, E., Yamada, K. and Hosokawa, A., 2005. Temperature measurement in laser forming of sheet metal. CIRP Annals-Manufacturing Technology, Vol. 54, No. 1, pp.179–182.
- Ueda, T., Sentoku, E., Wakimura, Y. and Hosokawa, A., 2009. Flattening of sheet metal by laser forming. Optics and Lasers in Engineering, Vol. 47, No. 11, pp.1097–1102.
- Ueda, T., Wakimura, Y., Furumoto, T., Hosokawa, A. and Tanaka, R., 2011. Experimental investigation on laser flattening of sheet metal. Optics and Lasers in Engineering, Vol. 49, No. 1, pp.137–144.
- Valvi, S.R., Krishnan, A., Das, S. and Naryanan, G.R., 2015. Prediction of microstructural features and forming of friction stir welded sheets using cellular automata finite element (CAFE) approach. International Journal of Materials Forming, DOI 10.1007/s12289-015-1216-0.

- Van Elsen, M., Baelmans, M., Mercelis, P. and Kruth, J.P., 2007. Solutions for modelling moving heat sources in a semi-infinite medium and applications to laser material processing. International Journal of heat and mass transfer, Vol. 50, No. 23, pp.4872–4882.
- Vásquez-Ojeda, C. and Ramos-Grez, J., 2009. Bending of stainless steel thin sheets by a raster scanned low power CO_2 laser. Journal of Materials Processing Technology, Vol. 209, No. 5, pp.2641–2647.
- Venkadeshwaran, K., Das, S. and Misra, D., 2012. Bend angle prediction and parameter optimisation for laser bending of stainless steel using FEM and RSM. International Journal of Mechatronics and Manufacturing Systems, Vol. 5, Nos. 3–4, pp.308–321.
- Venkateswarlu, G., Davidson, M.J. and Tagore, G.R.N., 2012. Modelling studies of sheet metal formability of friction stir processed Mg AZ31B alloy under stretch forming. Materials and Design, Vol. 40, pp.1–6.
- Vivek, A., Kim, K.H. and Daehn, G.S., 2011, Simulation and instrumentation of electromagnetic compression of steel tubes, Journal of Materials Processing Technology, Vol. 211, No. 5, pp. 840–850.
- Vollertsen, F., Geiger, M. and Li, W.M., 1993. FDM and FEM simulation of laser forming: a comparative study. In Advanced technology of plasticity, Proceedings of the fourth international conference on technology of plasticity (pp. 1793–1798), Beijing, 19–24 September.
- Vollertsen, F. and Rodle, M., 1994. Model for the temperature gradient mechanism of laser bending. Proc. of the LANE'94, pp.371–378.
- Vollertsen, F., Komel, I. and Kals, R., 1995. The laser bending of steel foils for microparts by the buckling mechanism-a model. Modelling and Simulation in Materials Science and Engineering, Vol. 3, No. 1, pp.107–119.
- Vollertsen, F. and Sakkiettibutra, J., 2010. Different types to use laser as a forming tool. Physics Procedia, Vol. 5, pp.193–203.
- Walczyk, D.F. and Vittal, S., 2000. Bending of titanium sheet using laser forming. Journal of Manufacturing Processes, Vol. 2, No. 4, pp.258–269.

- Wang, Y. and Mishra, R.S., 2007. Finite element simulation of selective superplastic forming of friction stir processed 7075 Al alloy. Materials Science and Engineering: A, Vol. 463, No. 1, pp.245–248.
- Wang, X.Y., Xu, W.X., Xu, W.J., Hu, Y.F., Liang, Y.D. and Wang, L.J., 2011. Simulation and prediction in laser bending of silicon sheet. Transactions of Nonferrous Metals Society of China, Vol. 21, pp.s188–s193.
- Wang, X., Ma, X., Li, Z. and Wang, R., 2016. A study of thickening phenomenon in laser bending zone of a metal laminated plate. Procedia CIRP, Vol. 42, pp.454–459.
- Watkins, K.G., Edwardson, S.P., Magee, J., Dearden, G., French, P., Cooke, R.L., Sidhu, J. and Calder, N.J., 2001. Laser forming of aerospace alloys (No. 2001–01–2610). SAE Technical Paper.
- Woo, H.G. and Cho, H.S., 1999. Three-dimensional temperature distribution in laser surface hardening processes. Proceedings of the Institution of Mechanical Engineers, Part B: Journal of Engineering Manufacture, Vol. 213, No. 7, pp.695–712.
- Woodfield, P. L., Monde, M. and Mitsutake, Y., 2007. On estimating thermal diffusivity using analytical inverse solution for unsteady one-dimensional heat conduction, International Journal in Heat and Mass transfer, Vol. 50, pp. 1202–1205.
- Wu, D.J., Ma, G.Y., Liu, S., Wang, X.Y. and Guo, D.M., 2010a. Experiments and simulation on laser bending of silicon sheet with different thicknesses, Applied Physics A, Vol. 101, No. 3, pp.517–521.
- Wu, D., Zhang, Q., Ma, G., Guo, Y. and Guo, D., 2010b. Laser bending of brittle materials. Optics and Lasers in Engineering, Vol. 48, No. 4, pp.405–410.
- Xu W., Zhang L.C. and Wang X., 2013, Laser bending of silicon sheet: absorption factor and mechanisms, ASME Journal of Manufacturing Science and Engineering, Vol. 135, No. 6, pp.061005–7.

- Yang,Y.C., Wu, T.S. and Wei, E.J., 2007. Modelling of simultaneous estimating the laser heat flux and melted depth during laser processing by inverse methodology. International Communication in Heat and Mass transfer, Vol. 34, pp. 440–447.
- Yang, L.J., Tang, J., Wang, M.L., Wang, Y. and Chen, Y.B., 2010. Surface characteristic of stainless steel sheet after pulsed laser forming. Applied Surface Science, Vol. 256, No. 23, pp.7018–7026.
- Yanjin, G., Sheng, S., Guoqun, Z. and Yiguo, L., 2003. Finite element modeling of laser bending of pre-loaded sheet metals. Journal of Materials Processing Technology, Vol. 142, No. 2, pp.400–407.
- Yau, C.L., Chan, K.C. and Lee, W.B., 1998. Laser bending of lead frame materials. Journal of Materials Processing Technology, Vol. 82, No. 1, pp.117–121.
- Yilbas, B.S. and Akhtar, S.S., 2014. Laser bending of metal sheet and thermal stress analysis. Optics and Laser Technology, Vol. 61, pp.34–44.
- Yu, G., Masubuchi, K., Maekawa, T. and Patrikalakis, N.M., 2001. FEM Simulation of laser forming of metal plates. Journal of Manufacturing Science and Engineering, Vol. 123, No. 3, pp.405–410.
- Zahrani, E.G. and Marasi, A., 2013a. Modeling and optimization of laser bending parameters via response surface methodology. Proceedings of the Institution of Mechanical Engineers, Part C: Journal of Mechanical Engineering Science, Vol. 227, No. 7, pp.1577–1584.
- Zahrani, E.G. and Marasi, A., 2013b. Experimental investigation of edge effect and longitudinal distortion in laser bending process. Optics and Laser Technology, Vol. 45, pp.301–307.
- Zhang, X.R., Chen, G. and Xu, X., 2002. Numerical simulation of pulsed laser bending. Transactions-American Society of Mechanical Engineers Journal of Applied Mechanics, Vol. 69, No. 3, pp.254–260.
- Zhang, L., Reutzel, E.W. and Michaleris, P., 2004. Finite element modeling discretization requirements for the laser forming process. International Journal of Mechanical Sciences, Vol. 46, No. 4, pp.623–637.

- Zhang, X.R. and Xu, X., 2005a. Laser bending for adjusting curvatures of hard disk suspensions. Microsystem Technologies, Vol. 11, No. 11, pp.1197–1203.
- Zhang, X.R. and Xu, X., 2005b. Laser bending for high-precision curvature adjustment of microcantilevers, Applied Physics Letters, Vol. 86, No. 2, p.021114.
- Zhang, P., Yu, J. and Zheng, X., 2009. Deformation behaviors of laser forming of ring sheet metals. Tsinghua Science and Technology, Vol. 14, Supplement 1, pp.132–136.
- Zhou, J., Shen, H., Yu, X., Hu, J. and Yao, Z., 2013. On the competition between in-plane and out-of-plane deformations in laser thermal adjustment. Optics and Laser Technology, Vol. 45, pp.689–696.
- https://law.resource.org/pub/eur/ibr/en.1999.1.2.2007.html. Accessed on March 1, 2015.

Appendix

Appendix A

Important specification of field emission scanning electron microscope (FESEM)

Make	: Zeiss
Model	: Sigma
Specific chamber	: 330 mm Inner diameter, 270 mm height
Specimen weight	: up to 500 g tilted, up to 2000 g not tilted
Movement	: X = 125 mm, Y = 125 mm, Z = 50 mm
	T= –10° to +90°, R= 360°
Specific stage	: 5 axis motorized Cartesian
Chamber detector	: Inlense, SE-2, NEBSD
Magnification range	: 300× to 1000 k×

Appendix B

Important specification of CO_2 laser machine

Make	: Orion 3015 from LVD
Type	: GE FANUC HF excited CO_2 laser
Capacity	: 2.5 kW
Wave length	: 10.6 µm
Sheet size	: 3000 mm × 1500 mm
Maximum sheet weight	: 570 kg
X-axis travel	: 3080 mm
Y-axis travel	: 1555 mm
Z-axis travel	: 290 mm
Machine dimension	: 7975 mm × 2825 mm × 2200 mm
Total weight installation	: 11500 kg
Maximum position speed	
X-Y axis	: 100 m/min
Z-axis	: 15 m/min
Repetitive accuracy	: ± 0.02 mm
Position accuracy	: ± 0.05 mm/m
Controlling parameters	
CNC control	: GE FANUC 16 iLB with Pentium processor
Software	: CADMAN-L3D
Laser power	: 50–2500W
Output stability	: ±1% – ±2%
focal lens	: 5 to 7.5 inches focal length
Duty cycle	: 5 to 100%
Frequency	: Continuous wave, pulsed 1 to 2000
Laser gas composition	: He (60%), N_2 (35%), and CO_2 (5%) with 99.99% purity
Laser gas flow rate	: 10 liter/hour (for maximum power)
Assist gas (for cutting)	: Oxygen and nitrogen

Appendix C

Important specification of coordinate measuring machine (CMM)

Mark	: Carl-Zeiss
Measuring range (mm)	: 400 ×500 × 350
Over all dimensions (mm)	: 1415 ×1780 × 2470
Resolution (µm)	: 0.5
Maximum velocity (mm/sec)	: 400
Air requirements (kg/cm^2)	: 5.35
Machine weight (kg)	: 1540

Appendix D

Important specification of universal testing machine (UTS)

Model	: 8801
Make	: INSTRON
Capacity	: ±100 kN
Actuator stroke	: ±75 mm (±3 in)
Load cell height	: 97 mm (3.8 in)
Actuator fully retracted	: 63 mm (2.5 in)
Maximum daylight	: 1480 mm (58.3 in)
Column spacing	: 652 mm (22.1 in)
Column diameter	: 70 mm (2.1 in)
Table height	: 890 mm (35 in)
Overall width	: 920 mm (36.2 in)
Overall depth	: 546 (21.5 in)
Overall height (maximum)	: 2778 mm (109.4 in)
Weight	: 625 kg (1375 lb)

Appendix E

Important specification of optical microscope

Make	: Carl Zeiss
Model	: Axiotech-100HD,3D
Table movement	: 3-axis measuring system, reflect light measuring stage 75 mm × 55 mm × 50 mm
Tubes	: Binocular photo tube (siedentopf principle), 20°/23, 100 vis/100 doc
Camera	: Axio-Cam and Axiovision 4.8.2 software in built
Magnification range	: 500× to 5 k×

Appendix F

Important specification of microhardness tester

Make	: Buehler
Model	: Micromet-2101
Indentation force	: 1, 10, 50, 100, 300, 500, 2000 g force
Dwell time	: 5 to 60 s at interval of 5 s
Microscope Magnification	: 100× , 400×
Measurement of indentation	: Manual Filler eyepiece
Max. measurement length	: 175 microns
Max. Height of specimen	: 65 mm
Max. Depth of specimen	: 85 mm
Stage dimension	: 100 mm × 100 mm
Video port	: For photography and computerization
Power Supply	: AC 230 V

Appendix G

Important specification of non-contact profilometer

Mark	: Taylor Hobson
Model	: CCI-Lite
Magnification	: 20×
Precision(megapixel)	: 1
Power supply (V)	: 220
Focal distance (mm)	: 4.7
Field of view (mm)	: 0.825 × 0.825

Appendix H

Simulation and experimental results of bend angles

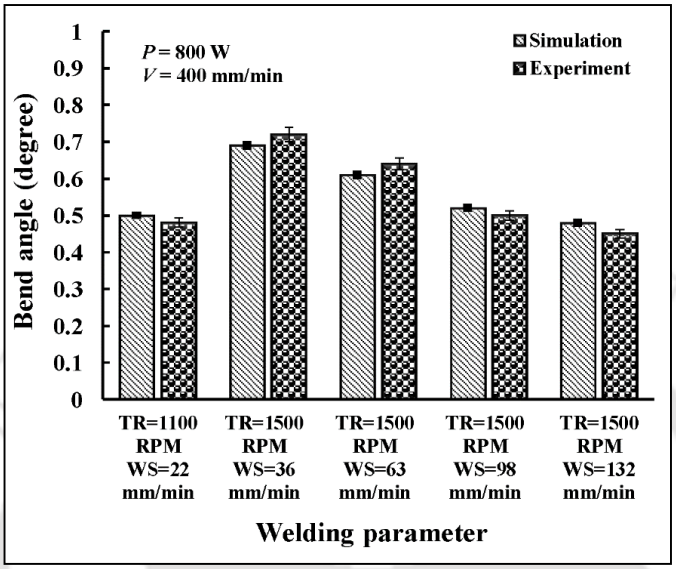

Figure Simulation and experimental results of bend angles for friction stir welded sheet (weld zone thickness 1.85 mm and scanning along weld direction on the bottom surface)

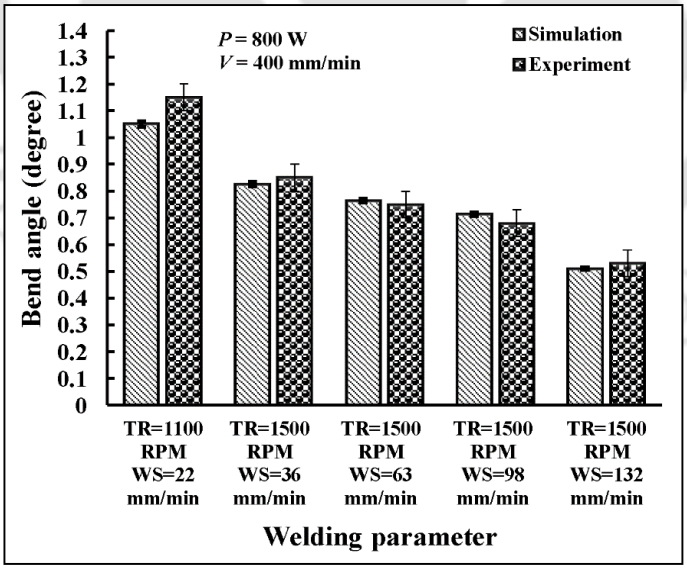

Figure Simulation and experimental results of bend angles for friction stir welded sheet (weld zone thickness 1.85 mm and scanning along weld direction on the top surface)

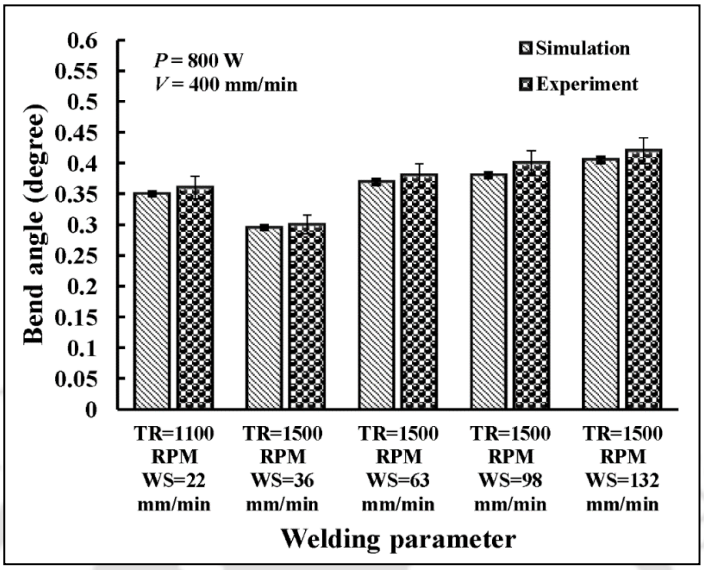

Figure Simulation and experimental results of bend angles for friction stir welded sheet (weld zone thickness 1.85 mm and scanning across weld direction on the bottom surface)

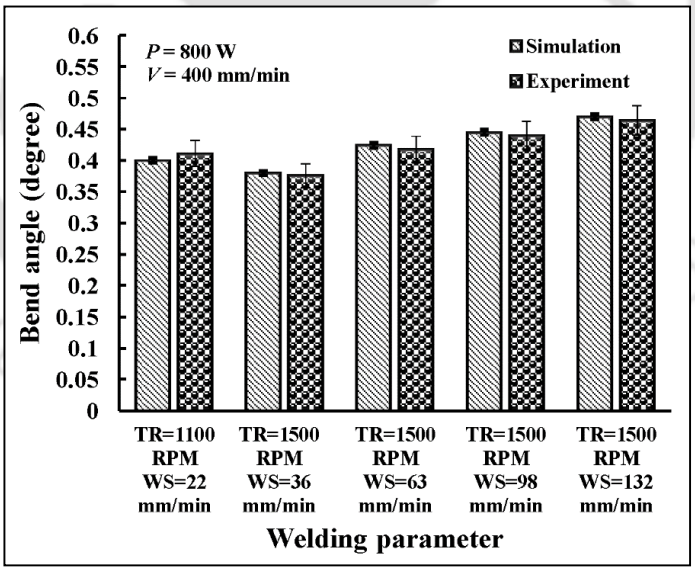

Figure Simulation and experimental results of bend angles for friction stir welded sheet (weld zone thickness 1.85 mm and scanning across weld direction on the top surface)

Publications from This Thesis

Journal Papers

1. Dixit, U.S. and Fetene, B.N., 2016. A finite element modelling of laser bending of friction stir welded aluminium 5052-H32 sheets. International Journal of Mechatronics and Manufacturing Systems, 9(3), pp. 215–236. DOI:org/10.1504/IJMMS.2016.079589.
2. Fetene, B.N., Shufen, R. and Dixit, U.S., 2016. FEM-based neural network modeling of laser-assisted bending. Neural Computing and Applications, in press. DOI:org/10.1007/s00521-016-2544-9.
3. Fetene, B.N., Dixit, U.S. and Liao, H., 2017. Laser bending of friction stir processed and cement-coated sheets. Materials and Manufacturing Processes, 32(14), pp. 1628–1634. DOI:org/10.1080/10426914.2017.1279321.
4. Fetene, B.N., Dixit, U.S. and Davim, J.P., 2017. Laser assisted bending by magnetic force. Journal of Engineering. June 2017, 11 pages. DOI:10.1049/joe.2017.0145.
5. Fetene, B.N., Kumar, V., Dixit, U.S. and Echempati, R., 2018. Numerical and experimental study on multi-pass laser bending of AH36 steel strips. Optics and Laser Technology, 99, pp. 291–300. DOI:org/10.1016/j.optlastec.2017.09.014.

Book chapter

1. Fetene, B.N., and Dixit, U.S., 2015. Finite Element Simulations of Laser Bending of Small Sized Sheets, in Laser Based Manufacturing: 5th International and 26th National All India Manufacturing Technology, Design and Research (AIMTDR) 2014, edited by S. N. Joshi and U. S. Dixit, pp. 41–53, Springer, New Delhi.

Conference Papers

1. Fetene, B.N. and Dixit U.S., 2014. Finite element simulations of laser bending of small sized sheets**,** 5th International & 26th All India Manufacturing Technology, Design and Research Conference (AIMTDR 2014), December 12th–14th, 2014, Indian Institute of Technology Guwahati, India.

2. Fetene, B.N. and Dixit U.S., 2015. A Finite element analysis of laser assisted mechanical bending of aluminium alloy sheets along with inverse determination of Input Parameters. 2nd National Conference on Emerging Technologies' Contribution in Promoting Defence and Industry (NCETCPDIC). Defence University, college of engineering, Bishoftu, Ethiopia, pp. 173−178.